Solidification and phase transformations in a dissimilar steel weld 18MND5/309L/308L : evolution of microstructure and mechanical properties

Fanny Mas

UNIVERSITÉ DE GRENOBLE

THÈSE

Pour obtenir le grade de

DOCTEUR DE L'UNIVERSITÉ DE GRENOBLE

Spécialité : **Matériaux, Mécanique, Génie civil, Electrochimie**

Arrêté ministériel : 7 août 2006

Présentée par

Fanny MAS

Thèse dirigée par **Yves BRECHET** et
codirigée par **Catherine TASSIN**

préparée au sein du **Laboratoire SIMaP**
dans **l'École Doctorale I-MEP2**

Solidification and phase transformations in a dissimilar steel weld 18MND5/309L/308L:
Evolution of microstructure and mechanical properties

Thèse soutenue publiquement le **19 décembre 2014,**
devant le jury composé de :

M. François MUDRY
Président de l'IRT M2P, Président
M. Jacques LACAZE
Directeur de recherche CNRS, CIRIMAT, Rapporteur
M. Mohamed GOUNE
Professeur, ICMCB, Rapporteur
M. Yves BRECHET
Professeur, Grenoble INP, Directeur de thèse
M^{me} Catherine TASSIN
Maître de Conférence, Grenoble INP, Co-directeur de thèse
M^{me} Aude SIMAR
Professeur, Université Catholique de Louvain, Examinateur
M. Ernst KOZESCHNIK
Professeur, Vienna University of Technology, Examinateur
M. François ROCH
Ingénieur chercheur, AREVA NP, Invité
M. Patrick TODESCHINI
Ingénieur chercheur, EDF R&D, Invité

Remerciements

Ça y est, la version définitive du manuscrit est bouclée mais il me reste une tâche de taille : trouver les mots justes pour vous remercier, vous qui avez fait de ces trois années de thèse une aventure exceptionnelle, métallurgiquement très enrichissante, et humainement très forte. Je tiens tout d'abord à remercier l'ensemble des membres de mon jury qui ont accepté de prendre part à ma soutenance, chacun apportant sa contribution à cette matinée de discussion scientifique. Merci à François Mudry qui a présidé ce jury avec beaucoup d'humour rendant l'atmosphère générale agréable et détendue. Merci à Jacques Lacaze et Mohamed Gouné pour le soin apporté à la relecture du manuscrit, vos remarques et suggestions m'ont permis de prolonger la réflexion et de soulever de nouvelles questions.

J'adresse un merci tout particulier à Yves Bréchet et Catherine Tassin qui m'ont fait confiance tout au long de cette thèse et qui ont su me transmettre leur passion pour la métallurgie physique. Yves, j'ai beaucoup apprécié le temps que tu as su trouver dans ton emploi du temps très chargé pour examiner avec moi les nombreuses problématiques scientifiques liées aux soudures bimétalliques. La grande diversité de ton expertise et la pertinence de tes suggestions ont guidé mes pas de jeune métallurgiste. Catherine, je te remercie pour m'avoir accompagné au jour le jour et pour avoir toujours répondu positivement à mes nombreuses sollicitations. Ton soutien et ton optimisme à toute épreuve m'ont aidée à ne pas baisser les bras dans les moments difficiles.

Cette thèse a été l'occasion de réunir les trois acteurs principaux du nucléaire Français autour d'un sujet commun : le vieillissement des LBM inox. Merci donc à EDF et Areva qui ont co-financé ce travail, mais également au CEA qui m'a permis de subtiliser un peu de son temps à son Haut-Commissaire. Je tiens à remercier tout particulièrement François ROCH qui a été à l'origine de ce sujet tout aussi complexe que passionnant et qui m'a fait confiance pour le mener à bien. Merci également à Miguel Yescas, Patrick Todeschini, Cécile Jardin et Jean-Paul Massoud qui ont accepté de se joindre à cette aventure. J'exprime également un grand merci à Gilles Perrin pour l'intérêt qu'il a porté à mon travail lors de nos nombreuses discussions mécaniques et métallurgiques à Grenoble comme à Paris.

Ces travaux de thèse ont donné lieu à de nombreuses collaborations, deux d'entre elles me sont particuliérement chères. La première m'a conduit chez nos voisins Wallons : tout d'abord merci à Aude Simar pour m'avoir initié à la rupture ductile et à sa modélisation. Ta gentillesse à mon égard et ton écoute ont été sources de motivation. J'ai énormément appris à ton contact et mon seul regret est de ne pas avoir commencé à travailler ensemble dès le début de ma thèse. J'espère que

nous aurons l'occasion d'interagir à nouveau, peut-être autour du soudage et/ou de la rupture des alliages d'alumminium ! La seconde collaboration a eu lieu dans la capitale autrichienne : merci à Ernst Kozeshnik et Yao Shan pour les nombreux échanges autour de la modélisation de la diffusion et de la précipitation. Merci pour votre accueil chaleureux lors de mes venues à Vienne. Même si la distance n'a pas facilité notre collaboration, je suis extrêmement reconnaissante pour le temps que vous avez consacré à développer les aspects numériques de ce problème complexe qu'est le couplage diffusion-précipitation.

Nombreuses sont les personnes qui ont consacré un peu (voire beaucoup) de leur temps à m'aider pour les caractérisations microstructurales et mécaniques de cette thèse. Je tiens à les remercier fortement :

- Nathalie Valle pour les mesures SIMS (Centre Public Gabriel Lippmann, Luxembourg)
- Emmanuel Rigal pour la fabrication de couples de diffusion par CIC (CEA, Grenoble)
- Cyril Cayron pour son aide à l'utilisation d'ARPGE (EPFL, Lausanne)
- Patrick Barges (Arcelor Mittal, Maizières) et Sophie Cazottes (INSA Lyon) pour les répliques extractives
- Laurent Artaud pour le montage de décarburation (SIMaP)
- Marion Descoins et Dominique Mangelink à la sonde atomique (IM2NP, Marseille)
- Marc Verdier à la naoindentation (SIMaP)
- Muriel Veron et Gilles Renou au MET (SIMaP)
- Eric Leroy au MET-FEG (ICMPE CNRS)
- Pierre Chemelle, Marie-Line Astier et Marc Mantel (Ugitech) pour les réponses toujours positives aux besoins de dépannage d'urgence (EBSD, répliques, analyse chimique)
- Guilhem Martin (SIMaP) pour la corrélation d'images mais avant tout pour son dynamisme et sa motivation sans faille qui m'ont énormément stimulé pour les dernières manips de la thèse.

Merci également à l'ensemble du personnel du CMTC pour les nombreux dépannages sur les outils de caractérisation, en particulier à Florence pour les nombreuses heures (jours) passées pour moi sur la microsonde et à Frédéric pour les nombreuses heures (jours) devant le FIB. J'ai aussi pu bénéficier de l'aide du pôle technique du laboratoire SIMaP qui a toujours répondu positivement à mes demandes les plus farfelues. Et surtout un grand **MERCI** à Alain pour les multiples découpes toujours réalisées en un temps record et dans la bonne humeur. Lors d'une expérience difficile et ambitieuse à l'ESRF, j'ai bénéficié du soutien d'une équipe de choc : merci à Marc, Stéphane, Guillaume, Mahmoud, Catherine et Cécile pour le réglage des PID jusque tard dans la nuit, pour les creusets cassés et le carbone évaporé. Mes remerciements vont également à Muriel pour les

escapades en banlieue parisienne et les heures passées dans le noir à Thiais. Mais ce sont surtout tes encouragements tout au long de ces trois ans, ainsi que tes nombreux conseils lors de la préparation de la soutenance qui m'ont aidée à avancer.

Au cours de ces trois ans, j'ai eu l'opportunité d'encadrer plusieurs stagiaires : merci à Aurélien, Jordi, Quentin et Patrice d'avoir accepté de parfois "faire la petite main". Ils ont beaucoup contribué aux résultats de cette thèse et m'ont aussi beaucoup appris sur le plan humain. Je souhaite ègalement saluer l'ensemble des membres du groupe PM, et en particulier mes amis thésards avec lesquels j'ai notamment partagé la bonne ambiance du midi, les parties de tarot endiablées et les footings pour décompresser. J'adresse un merci tout particulier à Laurent pour son aide précieuse au cours de ces trois années à travers nos nombreuses discussions métallurgiques (et moins métallurgiques) de fin de journée (ou de début de soirée). Merci également à Audrey et Nicolas qui ont fait du bureau 222 l'endroit le plus chouette du labo. Au programme : thé, gâteaux, bonbons accompagnés de discussions politiques (avec Nicolas) ou culinaires (avec Audrey) et parfois même métallurgiques. Bonne chance à vous deux pour la suite !

Pour finir mes remerciements vont aussi à tous ceux qui m'ont permis de me distraire, de m'évader de cette thèse trop souvent omniprésente. Merci à tous les copains (Pascal, Sophie, Mériem, Camille, Pauline, Quentin, Nico, Christine, Kilian, Frach) pour les sorties en montagne et les bonnes bouffes au retour. Merci à Papa et Maman pour leur soutien dans les moments difficiles, pour l'accueil à Marseille pendant la rédaction, ainsi que pour pour votre aide indispensable à la réussite du buffet. Merci à Camille et Martin pour les escapades en famille. Merci à Grand-Mère pour ton hospitalité à Lyon et les bons petits plats. Merci enfin à Yannick pour tous les bons moments passés à tes côtés.

Résumé étendu

Chapitre 1 - Introduction : motivations industrielles et scientifiques (p.7-14)

Contexte

Les soudures en aciers dissimilaires connues sous le nom de "liaisons bimétalliques inox" sont nombreuses au sein des réacteurs nucléaires français actuels. Elles permettent la connexion entre les gros composants de la centrale (cuve, pressuriseur, générateur de vapeur) en acier faiblement allié (16MND5, 18MND5, 20MND5) et les tuyauteries du circuit primaire en acier inoxydable (316L). Comme le montre la Figure 1, plusieurs couches de beurrage en acier inoxydable 309L et 308L sont d'abord déposées sur l'embout en acier faiblement allié, qui est ensuite soudé à une bague en acier 316L à l'aide d'un métal d'apport en acier inoxydable austénitique (308L). Le soudage homogène entre la bague intermédiaire et la tuyauterie peut ensuite être réalisé sur site.

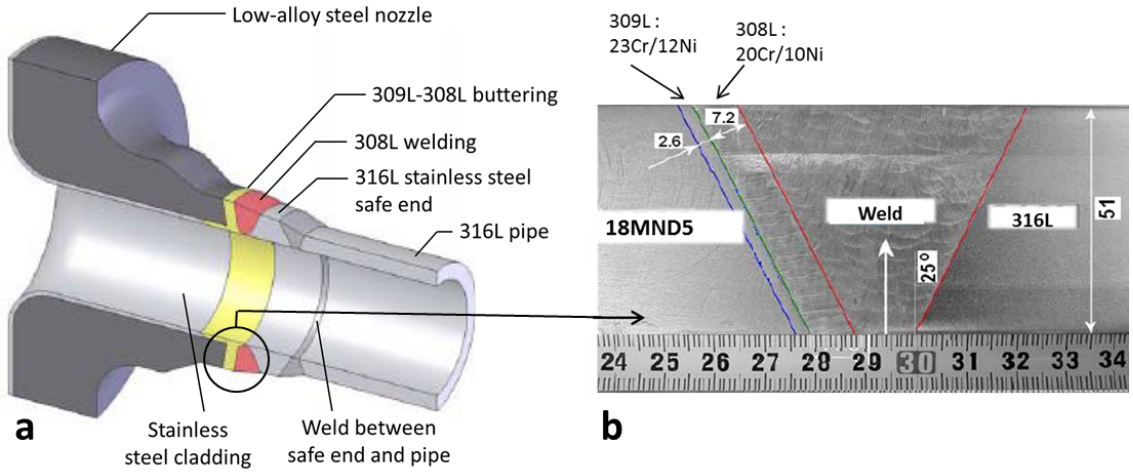

FIGURE 1: a- Représentation schématique d'une LBM entre un composant en acier faiblement allié et une tuyauterie en acier inox ; b- Macrographie mettant en évidence les interfaces entre alliages dissimilaires.

Le revêtement interne des composants en acier faiblement allié est un autre cas de soudage dissimilaire. Il a pour rôle d'assurer la protection contre la corrosion face à l'eau du circuit primaire.

Dans le contexte de l'extension de durée de vie des centrales nucléaires françaises, se pose

la question du vieillissement thermique de ces liaisons bimétalliques : comment les différentes microstructures présentes autour de l'interface évoluent-elles lorsqu'elles sont soumises à une température autour de 300°C pendant plusieurs dizaines d'années ? Les propriétés mécaniques de l'assemblage se dégradent-elles ? C'est pour répondre à ces problématiques qu'un projet d'ingénierie commun EDF-AREVA comprenant de nombreux essais mécaniques et caractérisations après vieillissement a été lancé fin 2011. Le travail de thèse qui va être décrit dans la suite a pour vocation de fournir un support scientifique à ce programme de R&D.

Matériaux et soudage

Pour des raisons pratiques, les soudures dissimilaires de cette étude ont été réalisées par soudage à l'arc sous flux de deux couches d'aciers inoxydables (309L et 308L sous forme de feuillards) sur une tôle en acier faiblement allié 18MND5. Elles sont donc représentatives du revêtement interne des gros composants de la centrale. La composition chimique du métal de base et des métaux d'apport est indiquée dans le Tableau 1 et les paramètres de soudage dans le Tableau 2. La tôle ainsi revêtue a été découpée en quatre blocs d'égales dimensions, l'un d'entre eux étant conservé à l'état brut de soudage. Le traitement thermique de détensionnement, dont le but est de relaxer les contraintes internes accumulées lors du soudage, a été appliqué aux trois autres. Il comprend les étapes suivantes :

- Chargement dans un four froid
- Montée en température : 30°C/h
- Maintien en température à 610°C pendant 8 heures
- Rampe de refroidissement : 25°C/h jusqu'à 300°C
- Refroidissement à l'air libre

Seul l'un des échantillons précédent a été conservé à l'état détensionné, des traitements de vieillissement accéléré à 400°C ont été appliqués aux deux autres : l'un pendant 5000 heures et l'autre pendant 10000 heures.

Tableau 1: Composition chimique des alliages en présence.

	C	**Si**	**Mn**	**Ni**	**Cr**	**Mo**	**Cu**
18MND5 (pds%)	0.199	0.219	1.623	0.635	0.231	0.479	0.114
309L (pds%)	0.021	0.359	1.698	12.57	23.66	0.068	0.023
308L (pds%)	0.011	0.152	1.671	10.43	20.04	0.014	0.025
	S	**P**	**Al**	**Co**	**Ti**	**N**	**Fe**
18MND5 (pds%)	0.0019	0.0048	0.028	0.011	<0.002	0.009	bal.
309L (pds%)	0.0077	0.0108	0.052	0.015	0.146	0.039	bal.
308L (pds%)	<0.0002	0.0133	0.026	0.007	<0.002	0.036	bal.

Tableau 2: Paramètres utilisés pour le soudage feuillard-flux

	1ère couche	**2ème couche**
Matériau d'électrode	309L	308L
Polarité	+ au feuillard	+ au feuillard
U (V)	27	27
I (A)	750 ± 20	750 ± 20
V (cm/min)	13.5 - 14.5	9.5 - 10.5
Hauteur de sortie du feuillard (mm)	28	28
Angle du feuillard (°)	90	90
Recouvrement (mm)	6	8
Température de pré-chauffage (°C)	130	Sans
Température inter-passe (°C)	< 200	< 100

Plan du manuscrit

Le travail de thèse est divisé en trois parties :

1. La première partie (chapitre 2) concerne la soudure 18MND5/309L/308L dans **l'état brut de soudage**. Elle a pour but d'étudier **la formation des microstructures au cours de la solidification** et de comprendre les transitions de phases observées dans le métal solidifié à partir de la ligne de fusion.

2. La seconde partie, qui comprend deux chapitres, est consacrée aux **transformations microstructurales qui se produisent au cours du traitement thermique de détensionnement.** Le premier chapitre (chapitre 3) décrit la **caractérisation détaillée** de la microstructure de part et d'autre de l'interface dans l'état traité thermiquement et sa comparaison avec l'état brut de soudage. Le second chapitre (chapitre 4) a pour objectif le **développement d'un modèle thermo-cinétique** couplant la diffusion dans un environnement multiconstitué à la cinétique de précipitation, dans le but de prévoir ces évolutions de la microstructure du joint soudé.

3. La troisième partie, également divisée en deux chapitres, s'intéresse aux **conséquences des transformations microstructurales** étudiées précédemment **sur le comportement méca-nique local.** Dans le premier chapitre (chapitre 5), différentes techniques expérimentales sont mises en place afin de fournir une **loi de comportement élasto-plastique pour chacune des zones d'intérêt.** Dans le dernier chapitre (chapitre 6), qui comprend des observations in-situ ainsi qu'une modélisation micro-mécanique, les mécanismes responsables de la **rupture ductile** dans la zone décarburée du métal de base et dans les couches d'acier inoxydable sont examinés.

Hormis une annexe consacrée aux études microstructurales et mécaniques menées sur les échantillons vieillis, le manuscrit s'est attaché à décrire et discuter le travail mené sur les états bruts et détension-

nés d'un point de vue microstructural et mécanique. En effet, il a été montré au cours de cette thèse qu'aucune transformation microstructurale n'intervenait au cours des traitements de vieillissement à 400°C. C'est pourquoi l'échantillon dans l'état détensionné a été considéré comme représentatif des soudures en service que l'on rencontre actuellement sur le parc nucléaire français.

Chapitre 2 - Evolution des mécanismes et microstructures de solidification (p.15-48)

Observations microstructurales

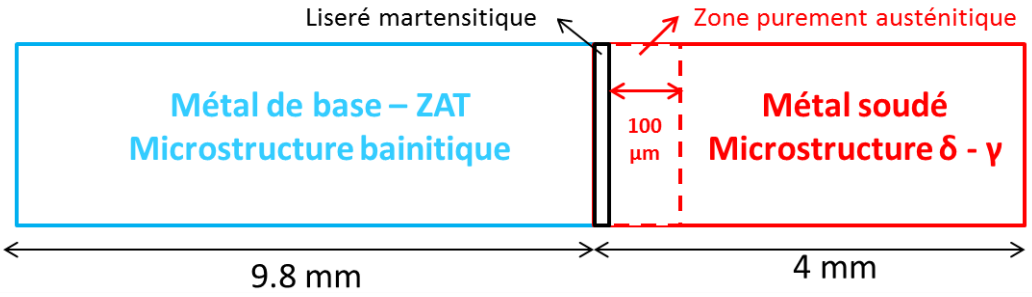

FIGURE 2: Représentation schématique de l'interface 18MND5/309L dans l'état brut de soudage.

Le soudage de deux aciers dissimilaires donne naissance à une grande variété de microstructures de part et d'autre de la ligne de fusion. Le schéma de la Figure 2 représente les différentes régions présentes autour de l'interface après dépôt de la première couche de beurrage en inox 309L. La microstructure de la zone affectée thermiquement du métal de base 18MND5 est de type bainitique avec de larges grains dans le premier millimètre. Un liseré de martensite d'épaisseur variable entre 5 et 200 μm et caractérisé par une forte dureté ($\approx$ 400 HV) est visible le long de la ligne de fusion. En s'éloignant de l'interface du côté métal fondu, on rencontre tout d'abord une zone purement austénitique s'étendant sur 70 μm, puis la structure biphasée $\delta-\gamma$ typique d'un acier inoxydable avec 18 pds.% de Cr et 9 pds.% de Ni. La ferrite δ résiduelle provient de la transformation incomplète de la ferrite primaire de solidification en austénite lors du refroidissement de la soudure. Ces évolutions microstructurales sont visibles sur les micrographies de la Figure 3. Elles sont accompagnées par des évolutions morphologiques puisque la solidification débute sous la forme d'un front plan au contact du métal de base, que celui-ci est ensuite déstabilisé sous forme de cellules qui deviennent ensuite des dendrites avec des ramifications secondaires.

Evolution de la composition et formation du liseré martensitique

Les évolutions microstructurales précédemment décrites sont associées à un gradient de composition depuis celle du métal de base jusqu'à celle du mélange entre le métal de base fondu et le métal d'apport 309L dans les proportions 20-80 % (voir Figure 4). Une zone de transition d'environ 70 μm de large a été mise en évidence. Elle est associée à l'existence d'une couche limite au fond du

bain liquide dans laquelle le mélange est partiel et le transport de solutés se produit essentiellement par diffusion. Les faibles teneurs en Cr et Ni dans le bain liquide au contact du métal de base sont responsables de la formation du liseré de martensite à l'interface lors du refroidissement suivant le soudage. En se basant sur des profils de concentration mesurés à la microsonde de Castaing et sur des formules empiriques donnant la température M_s de début de transformation martensitique en fonction de la composition, cette température a pu être calculée en fonction de la distance à la ligne de fusion. La variabilité de largeur du liseré martensitique a ainsi pu être reproduite.

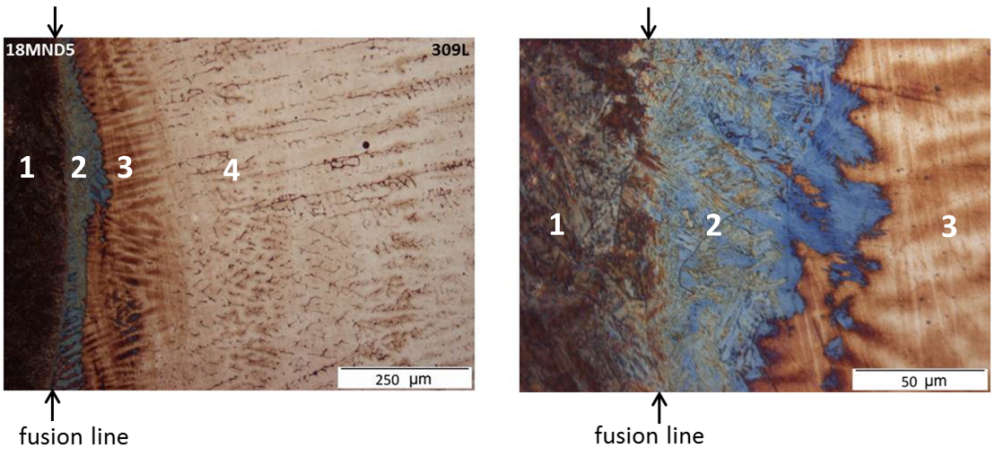

FIGURE 3: Interface entre le métal de base et le métal soudé austénitique dans l'état brut de soudage. L'attaque au Lichtenegger et Bloesch fait ressortir les différentes régions de la soudure : 1- ZAT du métal de base ; 2- liseré martensitique ; 3- zone purement austénitique ; 4- métal soudé biphasé δ-γ.

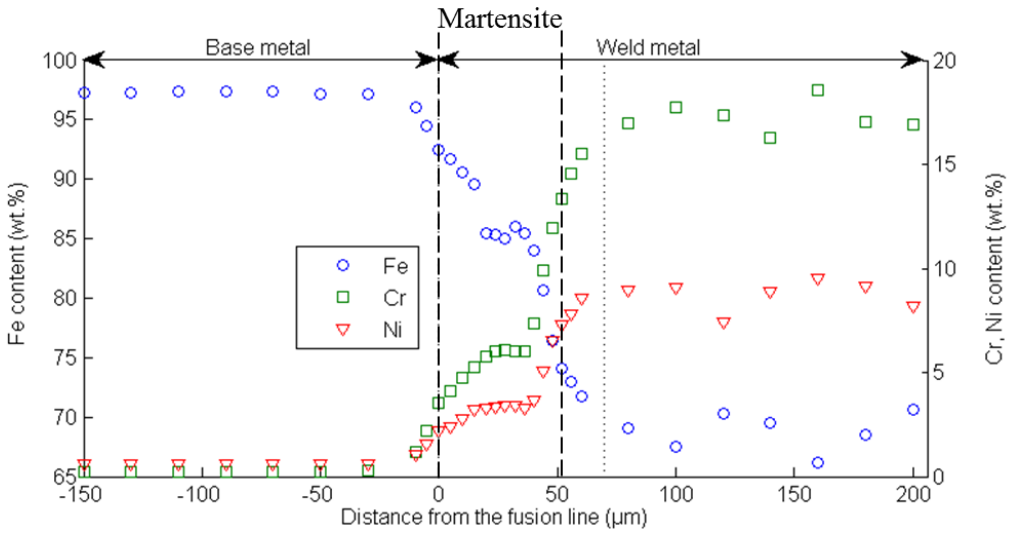

FIGURE 4: Profils de composition mesurés par microsonde sur une section transverse du joint soudé

Origine de la zone purement austénitique

Des mesures de micro-ségrégations dans la zone purement austénitique ont permis de montrer qu'une solidification primaire austénitique avait lieu dans cette région. D'autre part, une continuité des joints entre les anciens grains austénitiques du métal de base et les grains austénitiques nouvellement formés dans le métal soudé a été mise en évidence par des observations optiques après attaque chimique. Les orientations cristallographiques des anciens grains austénitiques ont été calculées à partir des orientations des variants martensitiques à l'aide du logiciel ARPGE [1, 2] en postulant une relation d'orientation de type Greninger-Troiano (GT). Comme le montre la Figure 5, une parfaite épitaxie a été trouvée à travers la ligne de fusion, conduisant à l'hypothèse d'une fusion métastable du métal de base sans germination de la phase δ, certainement à cause des fortes vitesses rencontrées en soudage.

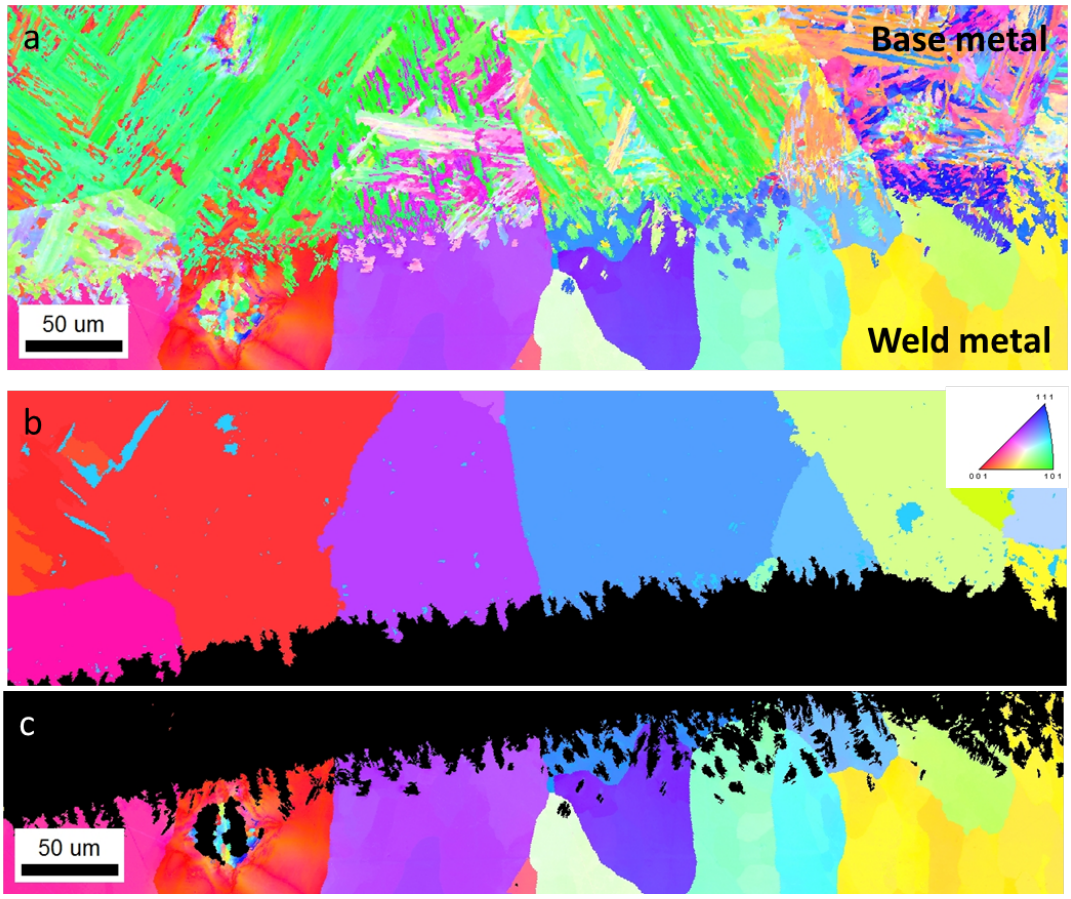

FIGURE 5: Résultats de la reconstruction des grains parents : a- Cartographie EBSD initiale ; b- Orientations des anciens grains austénitiques calculées à l'aide du logiciel ARPGE ; c- Orientations des grains austénitiques mesurées par EBSD du côté métal soudé.

Transitions du mode A au mode FA de solidification

Au-delà de la zone purement austénitique, le mode stable de solidification (c'est-à-dire ferrite primaire et austénite secondaire) est retrouvé après deux transitions successives :

- La ferrite apparaît d'abord dans l'espace inter-cellulaire de l'austénite (transition A $\rightarrow$ AF). Un calcul de type Scheil-Gulliver en deux étapes basé sur les évolutions de composition dans la zone de transition permet de prévoir la formation de ferrite dans le liquide résiduel de fin de solidification.

- Ensuite un modèle thermo-cinétique de compétition de croissance entre phases [3, 4, 5] est utilisé pour calculer la surfusion en pointe de dendrite pour la ferrite et l'austénite. Il démontre que les conditions présentes dans le bain fondu en termes de vitesse de solidification et de gradient thermique favorisent la croissance de la ferrite aux dépends de l'austénite (transition AF $\rightarrow$ FA).

Conclusions

La combinaison d'observations microstructurales et de mesures de composition à des modèles thermo-cinétiques a permis d'expliquer la grande variabilité des microstructures rencontrées autour de la ligne de fusion dans les soudures entre aciers dissimilaires. La diffusion y joue un rôle primordial car elle intervient dans la plupart des mécanismes invoqués : transport de solutés dans la couche limite à l'état liquide, déstabilisation du front plan, micro-ségrégations lors de la croissance cellulaire et dendritique, compétition de croissance entre ferrite et austénite. Les barrières à la germination d'origine cinétiques ont été quant à elles retenues pour justifier l'apparition d'une zone purement austénitique par croissance en épitaxie du métal solidifié sur le métal de base sans formation de phase δ.

Chapitre 3 - Caractérisation métallurgique de la diffusion du carbone et de la précipitation (p.49-80)

Mesures de la teneur en carbone

Comme l'on peut le voir sur la Figure 6, le traitement thermique de détensionnement entraîne de profondes transformations de la microstructure autour de la ligne de fusion : dissolution de la cémentite, disparition de la structure bainitique en lattes et croissance anormale des grains ferritiques du côté faiblement allié ; enrichissement en carbone et intense précipitation dans le liseré martensitique et la zone purement austénitique du côté métal soudé. La teneur en carbone en fonction de la distance à l'interface a été mesurée dans les états brut et détensionné à la fois par microsonde de Castaing et SIMS. Dans les deux cas, une approche quantitative reposant sur l'utilisation d'échantillons témoins ayant une teneur en carbone connue a été mise en place. Un bon accord entre les deux techniques a été obtenu, en particulier pour l'état détensionné. Elles y mettent en évidence un appauvrissement en carbone du métal de base sur 500 μm avec des teneurs fortement réduites (w(C)$<$0.015 wt.%) sur les 200 premiers micromètres correspondant à la zone à gros grains ferritiques. Deux pics de carbone sont détectés : l'un dans la martensite et l'autre dans l'austénite à l'interface avec la martensite (voir Figure 7). Les teneurs en carbone mesurées

dans l'austénite (maximum autour de 0.7 pds.%) sont peu communes pour un acier inoxydable. Ces variations locales de la teneur en carbone ont été confirmées par nano-indentation, les zones appauvries étant plus molles et les zones enrichies présentant une forte augmentation de leur dureté par rapport à l'état brut de soudage.

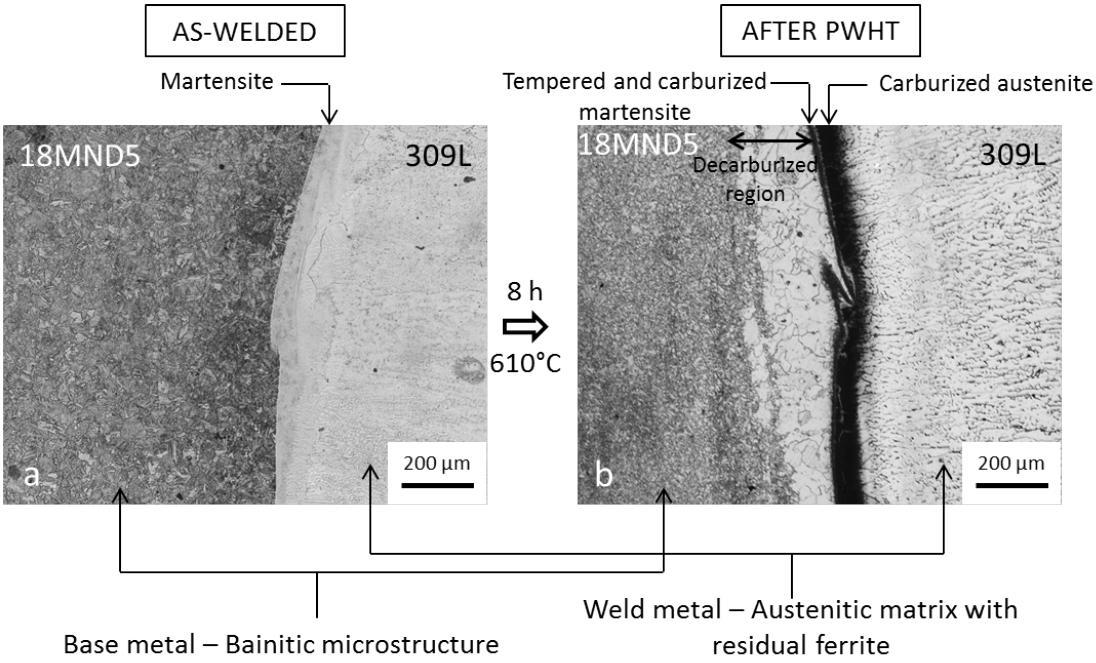

FIGURE 6: Micrographie optique de l'interface dissimilaire : a- dans l'état brut de soudage ; b- après traitement thermique de détensionnement.

Les mesures réalisées sur les états brut et intermédiaire (à la fin de la rampe de montée en température) ont montré que la diffusion du carbone est déjà amorcée lors du soudage et se poursuit pendant la montée en température. Ainsi le traitement thermique ne peut pas être réduit à sa partie isotherme de 8 h à 610°C uniquement.

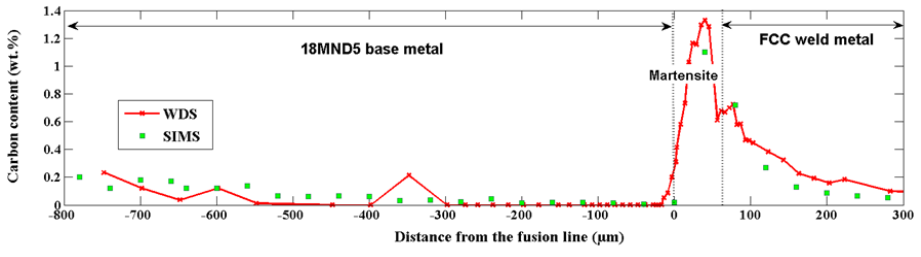

FIGURE 7: Mesure de la teneur en carbone en fonction de la distance à l'interface par microsonde et SIMS.

Nature et composition des précipités

Une identification systématique des carbures formés (voir Figure 8) a pu être menée en microscopie électronique à transmission assistée du procédé ACOM ("Automated Crystal Orientation Mapping"). De nombreux carbures de grande taille (jusqu'à 300 nm), à la fois $M_{23}C_6$ (structure

cubique) et M_7C_3 (structure hexagonale), ont été rencontrés dans le liseré martensitique, en particulier sur les joints de lattes. Dans la zone purement austénitique, une intense précipitation de petits carbures $M_{23}C_6$, cohérents avec la matrice FCC et alignés selon certaines directions préférentielles, a été mise en évidence. Seuls les joints de grains donnent lieu à une précipitation de carbures M_7C_3 dans l'austénite car ils constituent des court-circuits de diffusion pour le carbone. Des mesures EDS ont montré que tous ces carbures, bien que riches en chrome, incorporent une quantité non-négligeable de fer dans leur structure.

Lorsque l'on s'éloigne de l'interface dans le métal soudé, les liserés de ferrite δ résiduelle se décomposent par réaction eutectoïde ($\delta \rightarrow \gamma + M_{23}C_6$) lors du traitement de détensionnement. Comme le montre la Figure 9, les carbures $M_{23}C_6$ riches en Cr décorent l'ensemble des interfaces ferrite/austénite dans les deux couches en acier inoxydable (309L et 308L).

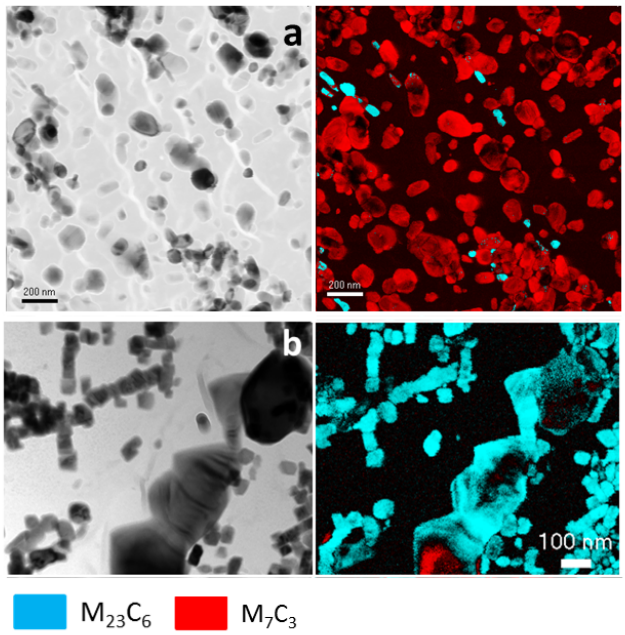

FIGURE 8: Cartographies de phases permettant l'identification des précipités a- dans le liseré martensitique ; b- dans la zone purement austénitique.

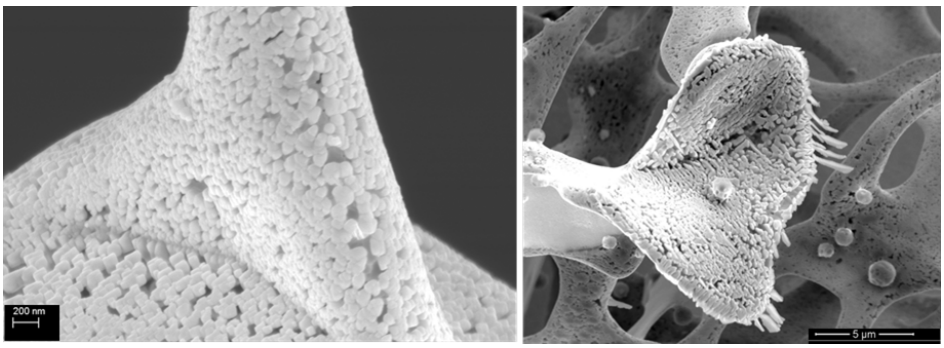

FIGURE 9: Images MEB montrant les carbures présents aux interfaces δ-γ dans l'état détensionné après dissolution des phases matrices δ et γ et extraction des précipités dans la couche de revêtement en 309L.

Quantification des carbures autour de l'interface

Des coupes sériées réalisées par faisceau d'ions focalisés et accompagnées d'une reconstruction 3D à l'aide du logiciel Avizo Fire® ont permis d'appréhender la forme des carbures et de quantifier l'évolution de leurs grandeurs caractéristiques (dimensions, densité, fraction volumique) au sein du liseré martensitique. Lorsque l'on s'éloigne du métal de base, on constate une progressive augmentation de la fraction volumique et du nombre de particules, tandis que la taille de ces dernières diminue. Cette évolution a été expliquée par une augmentation de la force motrice de germination lorsque la teneur en Cr augmente à l'intérieur du liseré martensitique.

Quant aux carbures présents dans l'austénite, ils ont été étudiés essentiellement au MET. En plus d'une population principale dont les dimensions sont de l'ordre de 60 nm, de petits clusters ($<$ 5 nm) ont également été observés.

Distribution des éléments entre matrice et précipités

Des mesures en sonde atomique tomographique (SAT) ont mis en évidence une importante sursaturation en carbone dans le liseré martensitique : non seulement le carbone y précipite, et cela dès la montée en température, mais de fortes teneurs ($\approx$ 0.1 pds.%) subsistent en solution solide. On est donc en présence d'une structure hors équilibre, le carbone dissout étant à priori disponible pour diffuser vers l'austénite. Dans l'état brut de soudage, les volumes analysés font ressortir une répartition hétérogène du carbone qui ségrègue sur des surfaces s'apparentant à des joints de lattes (voir Figure 10-a). De fortes teneurs en carbone en solution solide sont également mesurées dans la zone purement austénitique (jusqu'à 0.4 pds.% dans l'état détensionné).

Conclusions

Les nombreuses techniques expérimentales mises en œuvre dans ce chapitre ont permis de caractériser de manière détaillée et à différentes échelles la soudure bimétallique après détensionnement, considérée comme représentative de l'état en service. Ainsi les raisons des profondes transfor-mations microstructurales s'opérant au cours du traitement thermique ont été soulignées, et en particulier le rôle primordial du liseré martensitique. Ce dernier, en maintenant une part importante du carbone en solution, favorise ensuite son transport au sein de l'austénite.

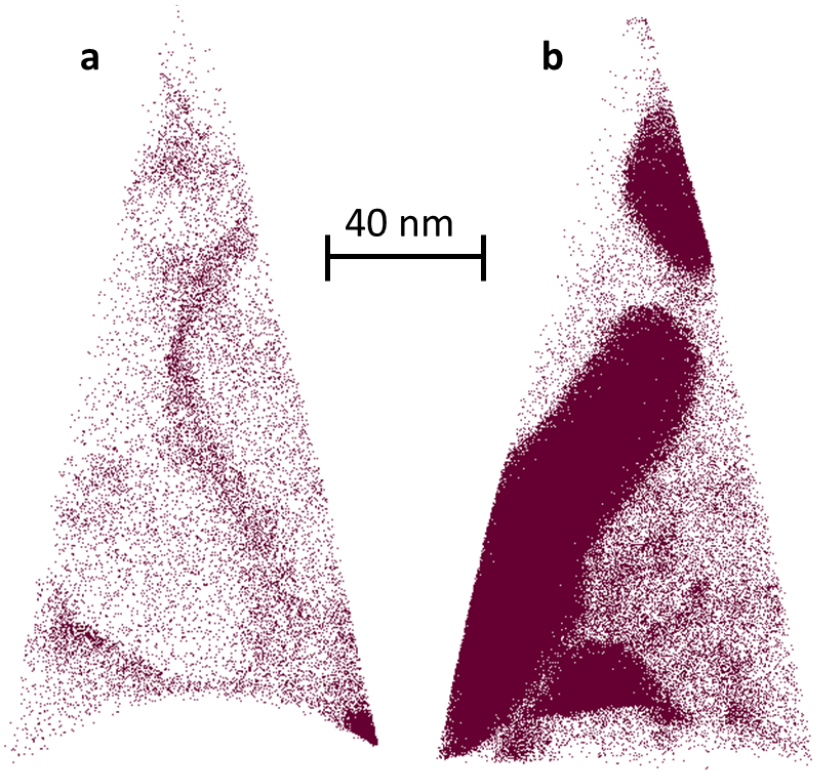

FIGURE 10: Distribution du carbone au sein de la martensite obtenue par SAT dans les états a- brut de soudage ; b- détensionné.

Chapitre 4 - Modélisation couplée de la diffusion du carbone et de la précipitation dans les soudures entre aciers dissimilaires (p.81-116)

Précipitation à l'équilibre

En se basant sur les modélisations existantes et communément utilisées pour simuler les traitements thermiques appliqués à des matériaux dissimilaires [6, 7, 8], un modèle couplant diffusion à longue distance dans un milieu multi-constitué et précipitation suivant l'équilibre thermodynamique a été implémenté au sein du logiciel MatCalc. Le gradient de potentiel chimique de l'ensemble des espèces présentes dans le système est considéré comme la principale force motrice pour la diffusion. La précipitation est supposée infiniment rapide devant la diffusion. Les résultats, présentés sur la Figure 11 à l'issue du traitement de détensionnement, montrent que si le profil en carbone est correctement reproduit dans la martensite, ce n'est pas le cas de l'austénite dans laquelle le carbone ne pénètre quasiment pas. Ceci s'explique par la grande stabilité des carbures $M_{23}C_6$ et M_7C_3 dans la martensite, ces derniers capturant la totalité du carbone disponible. En effet, la teneur en carbone en solution solide dans la martensite (considérée ici comme une BCC alliée) est maintenue à des niveaux trop faibles ($w(C)_{matrix} \approx 2.6 \times 10^{-5}$ pds.%) qui ne correspondent pas aux mesures en sonde atomique. Le profil expérimental en carbone n'a pu être reproduit qu'en augmentant fortement les

coefficients de diffusion, en particulier dans la zone purement austénitique (facteur multiplicatif de 400). Aucun argument physique raisonnable n'a pu être avancé pour justifier une telle augmentation.

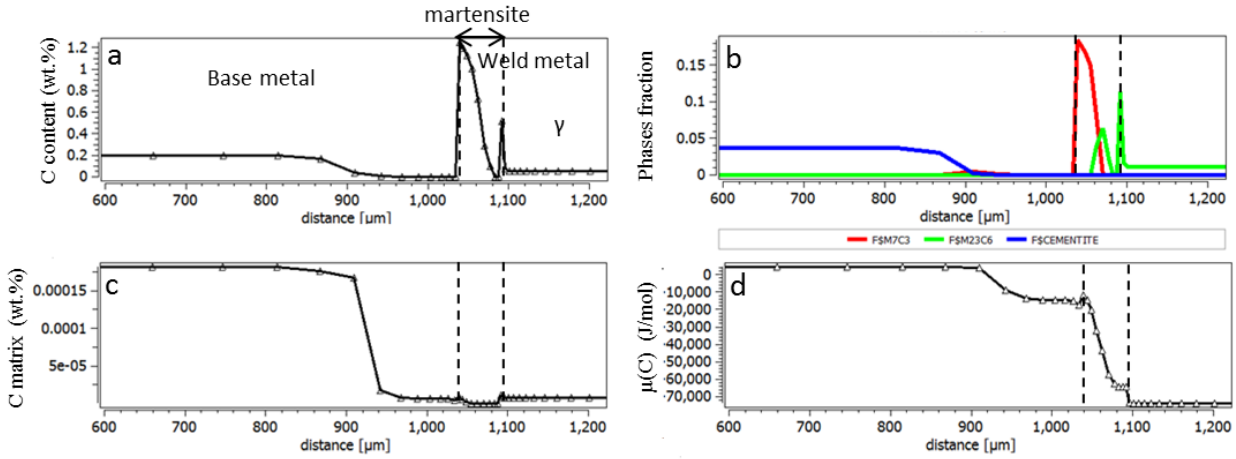

FIGURE 11: Resultats de la simulation anisotherme de la diffusion à travers le joint soudé avec précipitation à l'équilibre : a- teneur globale en carbone ; b- fraction volumique des précipités ; c- teneur en carbone dans la matrice ; d- potentiel chimique du carbone.

Prise en compte de la cinétique de précipitation

Face à l'échec de la démarche classique basée sur l'équilibre thermodynamique, un modèle prenant en compte la cinétique de précipitation a été développé. Le taux de germination a été calculé suivant la théorie classique étendue aux systèmes multi-constitués. Une approche en champ moyen basée sur le principe d'extremum thermodynamique a été appliquée pour la croissance/dissolution des précipités [9]. La population de carbures a été discrétisée en classes, chacune d'elle correspondant à une valeur du rayon et de la composition des précipités. Des grandeurs microstructurales telles que la taille de grains ainsi que la nature et le nombre de sites de germination, servent de données d'entrée à la modélisation [10]. Comme le montrent les graphiques de la Figure 12, le profil expérimental en carbone a pu être reproduit. Pour cela, il a fallu tenir compte de l'accélération de la diffusion par les joints de lattes dans les structures bainitiques et martensitiques (facteur multiplicatif de 8) ainsi que d'une importante énergie élastique générée par la formation de précipités dans une matrice martensitique en compression.

Conclusions

La prise en compte de la cinétique de précipitation au sein d'une simulation de diffusion à longue distance faisant appel aux bases de données thermo-cinétiques Calphad est une démarche novatrice. Même s'il subsiste des difficultés à la fois numériques et physiques qui doivent encore être surmontées, un tel couplage a permis :

- de tester l'effet d' un certain nombre de paramètres (nombre de sites de germination,

coefficients de diffusion, énergie d'interface, incompatibilité élastique entre matrice et précipités) sur la diffusion du carbone à travers le joint soudé.

- de mettre en évidence le rôle primordial du liseré martensitique dans le transfert de carbone depuis le métal de base jusque dans le métal soudé austénitique.
- d'identifier un jeu de paramètres permettant de reproduire le profil en carbone ainsi que les caractéristiques des précipités dans les différentes régions de la soudure.

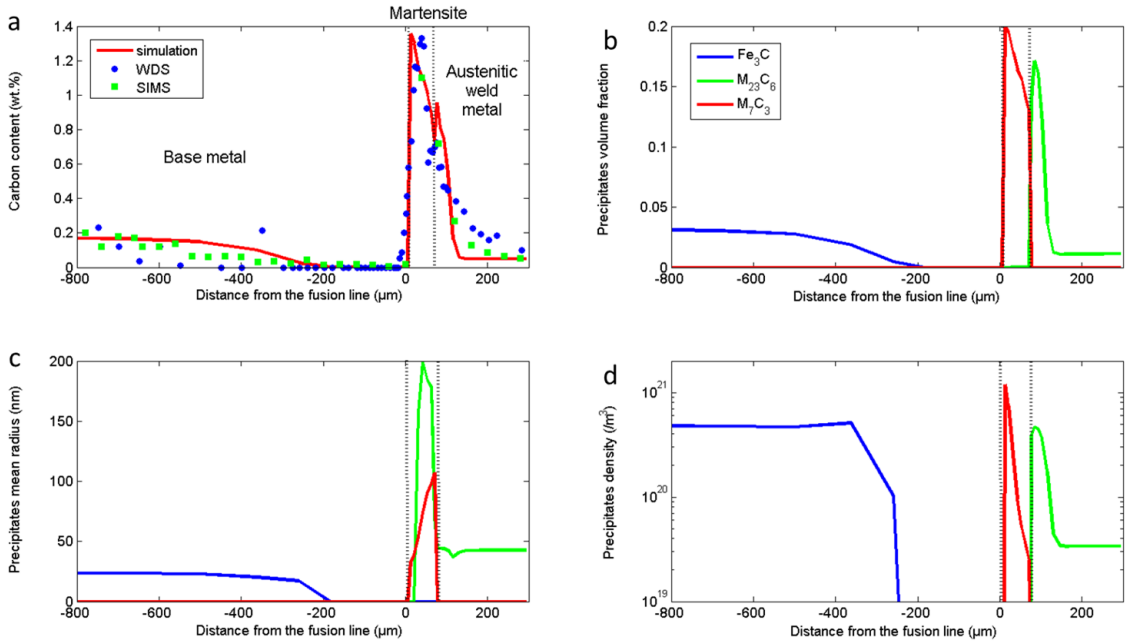

FIGURE 12: Resultats de la simulation anisotherme de la diffusion à travers le joint soudé tenant compte de la cinétique de précipitation : a- teneur globale en carbone ; b- fraction volumique ; c- rayon moyen et d- densité des précipités. Les principaux paramètres d'entrée de cette simulation sont les suivants : germination sur les côtés des joints de lattes dans les structures BCC, sur les dislocations dans la FCC, incompatibilité volumétrique de 0.19 entre matrice et précipités dans la martensite.

Chapitre 5 - Hétérogénéités dans le comportement élasto-plastique local (p.117-152)

Comme le montrent les profils de micro-dureté de la Figure 13, les transformations micro-structurales qui ont lieu au cours du traitement de détensionnement causent de profondes modifications des propriétés mécaniques de la plupart des régions autour de la ligne de fusion de la soudure. Le but de ce chapitre est de répondre aux questions suivantes :

- Quelles sont les conséquences des transformations microstructurales sur la répartition des déformations autour de l'interface ?
- Quelles lois de comportement élasto-plastiques régissent le comportement mécanique de chacune des régions ?

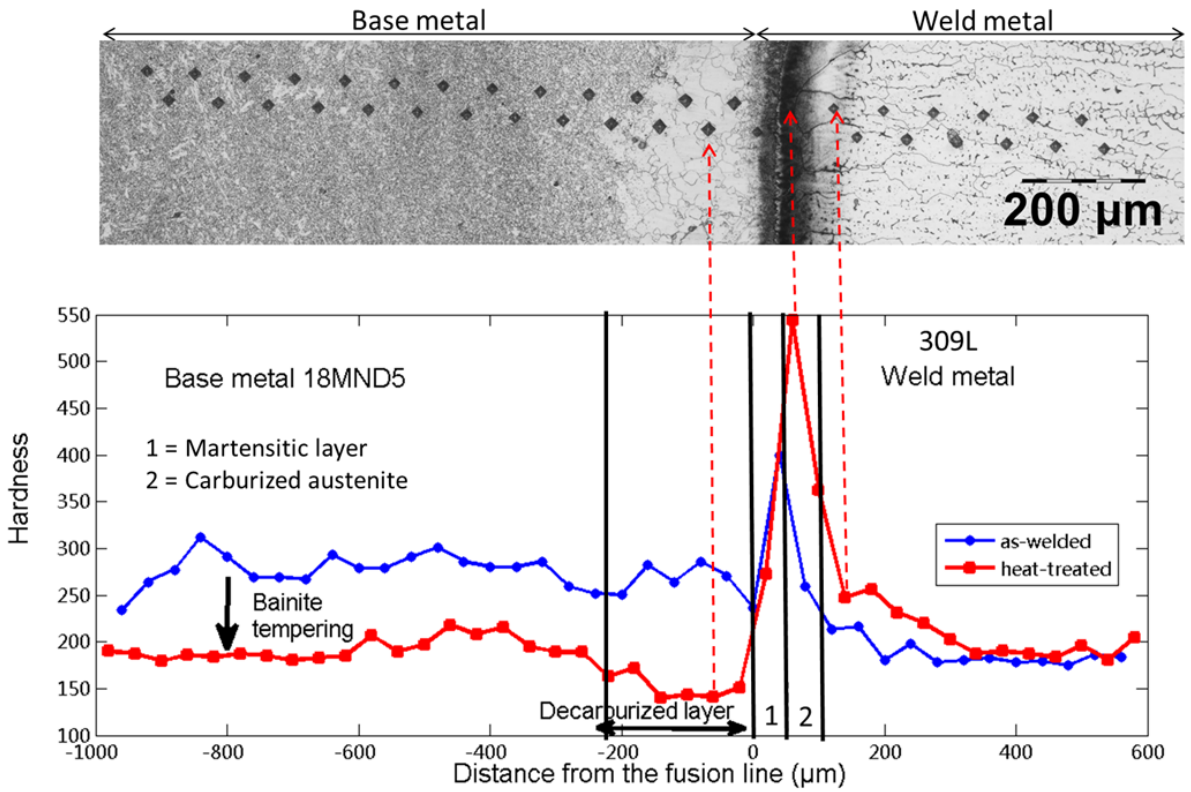

FIGURE 13: Profils de micro-dureté Vickers (100 g) sur une coupe transverse de la soudure dans les états brut de soudage et détensionné, la localisation des indents étant identifiée sur une micrographie optique de l'échantillon détensionné après attaque chimique.

Détermination des lois de comportement par zones

Plusieurs méthodes expérimentales ont été mises en œuvre afin d'accéder au comportement mécanique (limite d'élasticité et loi d'écrouissage) des différentes régions constituant la liaison bimétal-lique à l'état détensionné. Pour les zones suffisamment larges (zone affectée thermiquement du métal de base, couches de revêtement en acier inoxydable), des micro-éprouvettes (épaisseur 0.8 mm) ont été extraites par électro-érosion parallèlement à la ligne de fusion. Elles ont permis la réalisation d'essais de traction. Des essais de nano-indentation avec deux indenteurs suivant la méthode proposée par Bucaille [11] ont été utilisés pour estimer la limite d'élasticité et le coefficient d'écrouissage dans les zones d'épaisseur plus limitée (martensite, austénite carburée, zone décarburée). Bien qu'assez dispersés, les résultats permettent de générer des grandeurs locales jusqu'ici inac-cessibles.

Une attention particulière a été portée au métal de base décarburé par la fabrication de matériaux massifs équivalents en termes de taille de grains, teneur en carbone et dureté. Pour cela, deux démarches expérimentales ont été menées de front : décarburation du métal de base sous atmosphère H_2 humide ; traitement thermique prolongé d'un couple de diffusion 18MND5/inox 430 fabriqué par compression isostatique à chaud. Les zones décarburées massives ainsi créées ont ensuite été testées en traction. Il n'a pas été possible de déterminer un jeu unique de paramètres mécaniques pour la

zone décarburée. La comparaison des différentes méthodes a permis de générer des bornes supérieure (350 MPa par nano-indentation) et inférieure (200 MPa par décarburation en phase gaz) pour la limite d de la zone décarburée. Un coefficient d'écrouissage de 0.2 a été retenu car il était identique pour l'ensemble des échantillons massifs fabriqués.

Comportement mécanique global

Des essais de traction ont été réalisés sur la soudure complète dans les états brut et détensionné à l'aide d'éprouvettes prélevées perpendiculairement à la ligne de fusion. Une réduction de la limite d'élasticité ainsi qu'une augmentation de la ductilité sont observées dans l'état détensionné, certainement dues aux contraintes résiduelles accumulées pendant le soudage et ensuite relaxées lors du traitement thermique (voir Figure 14-a). Une simulation par éléments finis à l'aide du logiciel Abaqus a été conduite afin de modéliser le comportement élasto-plastique de la soudure en traction. Les lois de comportement précédemment déterminées ont été implémentées dans les différentes régions d'intérêt. Le comportement anisotrope du revêtement en acier inoxydable a été mis en évidence et la courbe contrainte-déformation expérimentale de la soudure globale n'a pu être reproduite qu'en introduisant le comportement moyen dans le sens travers des couches déposées (voir Figure 14-b). L'instabilité liée aux bandes de Lüders impliquées dans les premiers stades de déformation du métal de base a également pu être reproduite comme indiqué par les cercles noirs sur la Figure 14-b. Cependant les propriétés mécaniques de la zone décarburée n'ont pas d'influence sur le comportement élasto-plastique global. C'est pourquoi il a été nécessaire de procéder à des mesures plus locales.

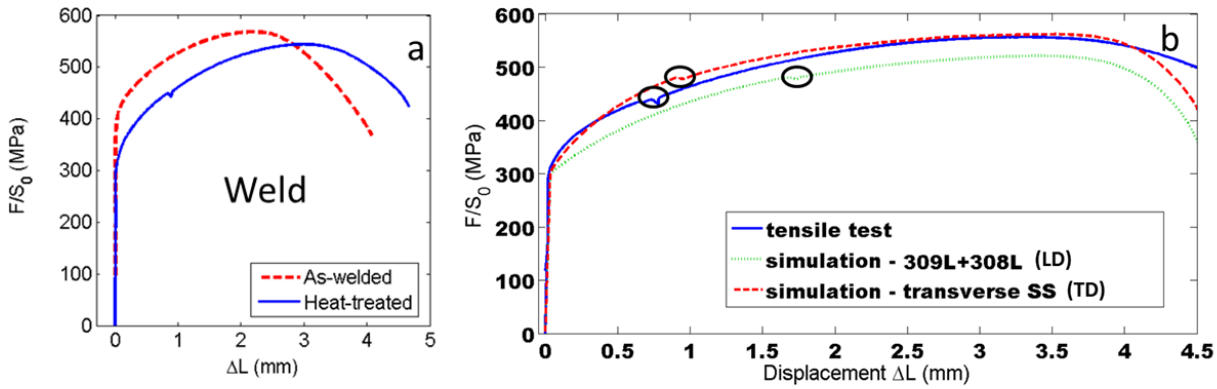

FIGURE 14: Comportement mécanique global de la soudure : a- courbes de traction expérimentales ; b- comparaison avec la simulation. LD fait référence à l'utilisation de lois de comportement déterminées dans le sens longitudinal pour les couches d'acier inoxydable, TD dans le sens transverse.

Hétérogénéités de déformation

Etant donné la grande diversité de microstructure présente de part et d'autre de l'interface, une forte variabilité de comportement mécanique est observée à l'échelle locale. Dans le but de quantifier la distribution des déformations entre les différentes régions lors d'une sollicitation mécanique globale, des micro-grilles en or ont été déposées à la surface d'une éprouvette de traction par des techniques de micro-lithographie. Après chaque incrément de déformation, des images MEB ont été réalisées et les champs de déformation ont été calculées par corrélation d'images en comparant à la situation initiale avant déformation. Les cartographies de déformation ainsi obtenues, dont deux exemples sont visibles sur la Figure 15, nous ont permis de déduire un certain nombre d'informations intéressantes :

- Les couches de revêtement en acier inoxydable sont les zones qui concentrent la majeure partie de la déformation, en accord avec leur faible limite d'élasticité et leur forte ductilité. Cependant, la déformation est hétérogène en leur sein : la partie proche des zones carburées étant fortement contrainte par ces dernières elle ne peut se déformer que faiblement.

- En plus de la zone décarburée à gros grains correspondant au métal de base fortement adouci sur 200 μm à partir de la ligne de fusion, une zone intermédiaire est mise en évidence. Cette dernière qui s'étend sur 300 μm subit des déformations plus importantes que le métal de base, certainement dues à une perte significative de carbone par diffusion, en accord avec les profils mesurés par SIMS et microsonde de Castaing (cf. Figure 7).

- La déformation dans la zone décarburée apparaît très hétérogène, certainement à cause d'effets microstructuraux liés à la taille importante des grains ferritiques dans cette région.

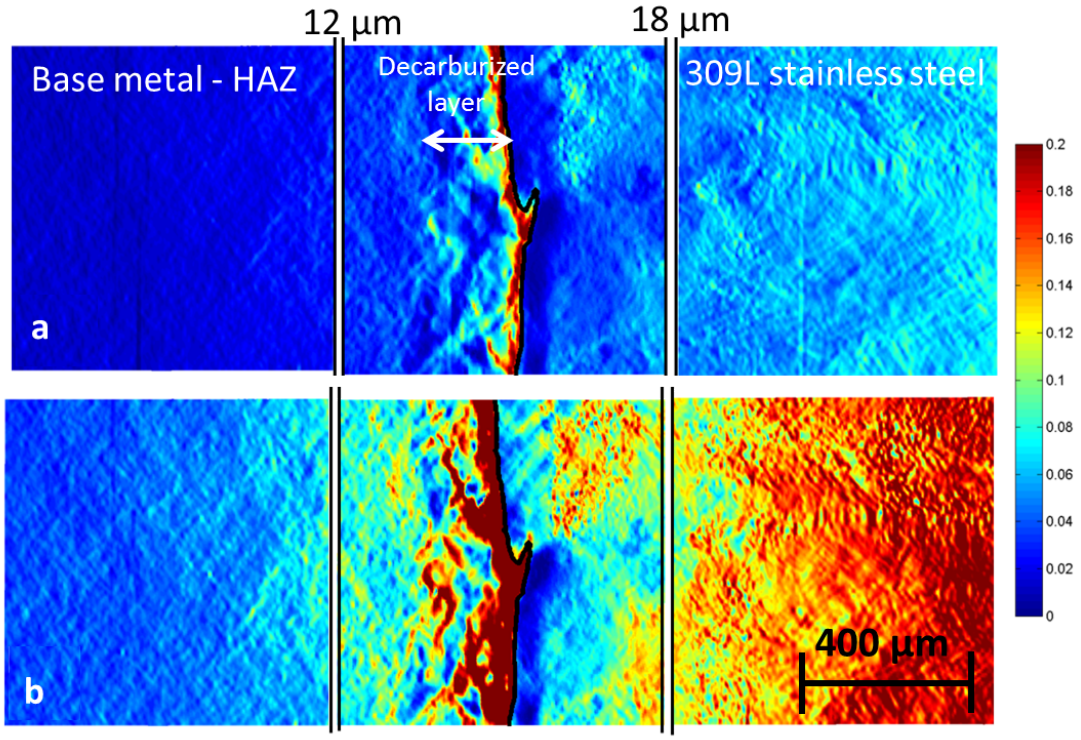

FIGURE 15: Déformation logarithmique suivant l'axe de traction mesurée par corrélation d'images pour différents incréments de déplacement : a- $\Delta L = 0.9$ mm, $\sigma = 480$ MPa; a- $\Delta L = 2.39$ mm, $\sigma = 548$ MPa

Les mesures expérimentales ont été comparées aux champs de déformation calculés, ce qui a permis de déterminer la limite d'élasticité de la zone décarburée (250 MPa). D'autre part, il a été nécessaire d'ajouter à la simulation une zone intermédiaire de 300 μm de large avec une limite d'élasticité à 300 MPa et un coefficient d'écrouissage de 0.2. De plus, la forme de la surface libre de l'éprouvette mesurée par profilomètrie a été correctement reproduite par la simulation.

Conclusions

Plusieurs méthodes ont pu être mises en œuvre pour estimer les propriétés mécaniques des différentes régions de la soudure. Les lois élasto-plastiques locales ont été confirmées voire ajustées par comparaison des champs de déformation mesurés par corrélation d'images à ceux calculés par la simulation. Les évolutions en termes de limite d'élasticité et de coefficient d'écrouissage à travers le joint soudé sont représentées sur la Figure 16. Elles pourront être utilisées comme données d'entrée pour des modèles mécaniques impliquant des géométries et sollicitations variées.

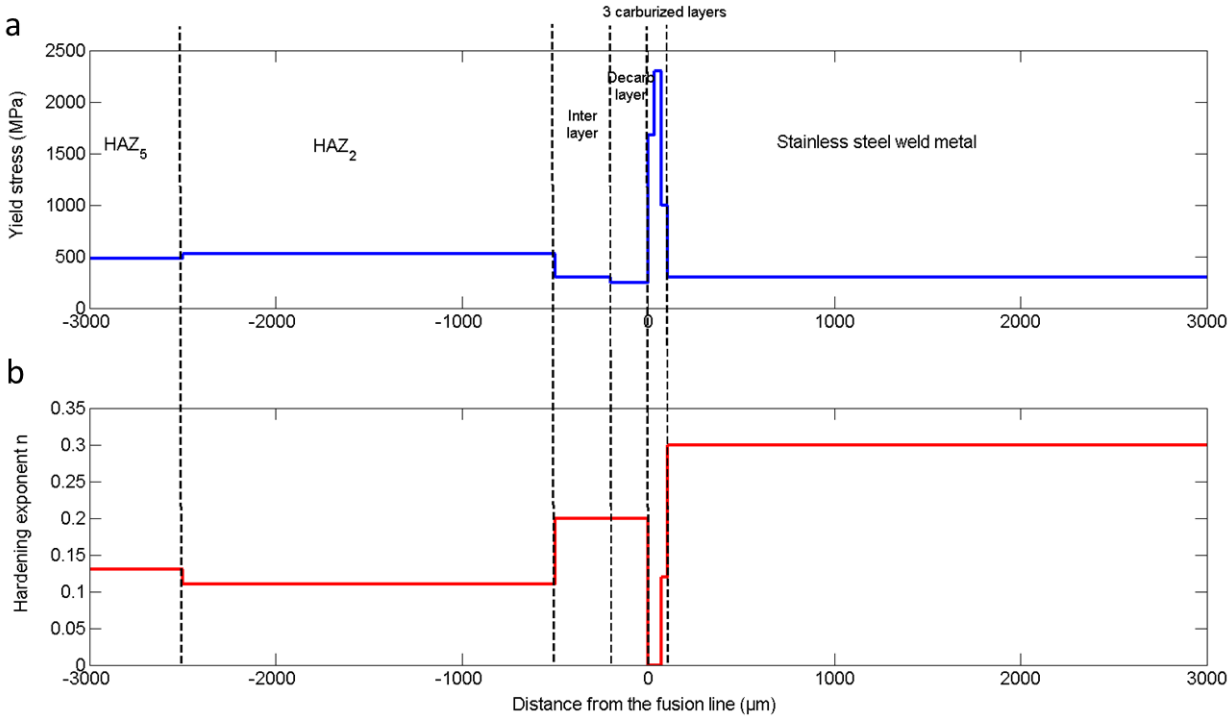

FIGURE 16: Evolution des propriétés plastiques autour de la ligne de fusion de la soudure à l'état détensionné en termes de a- limite d'élasticité et de b- coefficient d'écrouissage pour les différentes zones de la soudure (de gauche à droite) : ZAT du métal de base, zone intermédiaire, région décarburée, liseré martensitique, austénite carburée, métal soudé inoxydable.

Chapitre 6 - Endommagement ductile dans les zones molles du joint soudé (p.153-180)

Observations expérimentales

Les deux zones les plus molles de la liaison bimétallique, et donc susceptibles d'être endommagées par un mécanisme de rupture ductile à température ambiante comme en service, sont les couches de revêtement en acier inoxydable et le métal de base décarburé. Ces deux zones diffèrent fortement en ce qui concerne leur géométrie et les inclusions présentes pouvant servir de sites de germination pour l'endommagement. La zone décarburée est étroite (≈ 200 μm) et fortement contrainte par les zones dures qui l'entourent (martensite d'un côté, métal de base de l'autre). La triaxialité des contraintes, l'un des paramètres clés contrôlant la cinétique de croissance des cavités, y est particulièrement élevée (>1), notamment au contact du liseré martensitique. En revanche, cette zone est quasiment vierge en termes d'inclusions de taille significative. En effet, les carbures de cémentite ont été dissouts lors de la décarburation ; seuls subsistent quelques sulfures de manganèse. En ce qui concerne les couches d'acier inoxydable, elles sont larges (≈ 4 mm) et la contrainte générée par la partie carburée de l'austénite ne s'exerce qu'en son voisinage. En ce qui concerne les inclusions, elles sont nombreuses. On y trouve :

- les oxides de fin de solidification qui sont des particules sphériques dont le diamètre varie entre 250 nm et 5 μm.
- les interfaces δ-γ qui, dans l'état détensionné, sont décorées par un film quasi-continu de carbures.

Lors des essais de traction sur la soudure globale, la rupture a systématiquement lieu dans la deuxième couche de revêtement en 308L, dans l'état brut comme dans l'état détensionné. Néanmoins, comme le montre la Figure 17, on constate une diminution de la déformation à rupture, estimée par l'intermédiaire de la réduction de section, dans le cas de l'échantillon détensionné : 1.11 ± 0.13 contre 1.50 ± 0.036 dans l'état brut. Cette chute de ductilité est associée à l'existence de vides allongés sur le faciès de rupture, ceux ci n'étant pas présents dans l'état brut. Ces cavités sont attribuées à la germination de vides aux interfaces δ-γ (voir Figure 18-c), certainement fragilisées à l'état détensionné par la présence des carbures $M_{23}C_6$ formés par la décomposition eutectoïde de la ferrite δ.

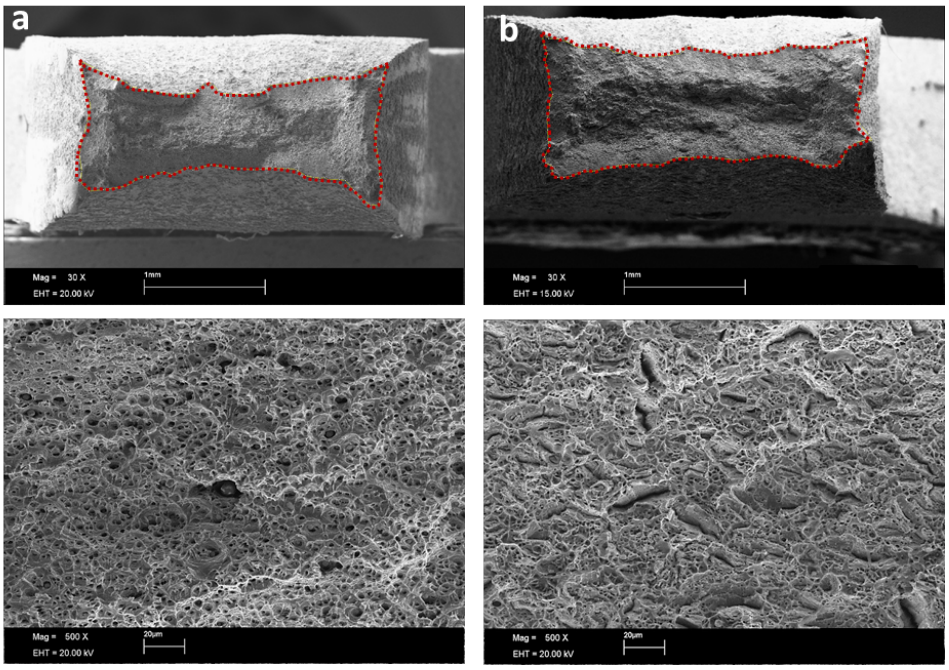

FIGURE 17: Surfaces de rupture dans l'acier 308L d'éprouvettes de traction à l'état a- brut de soudage ; b- détensionné.

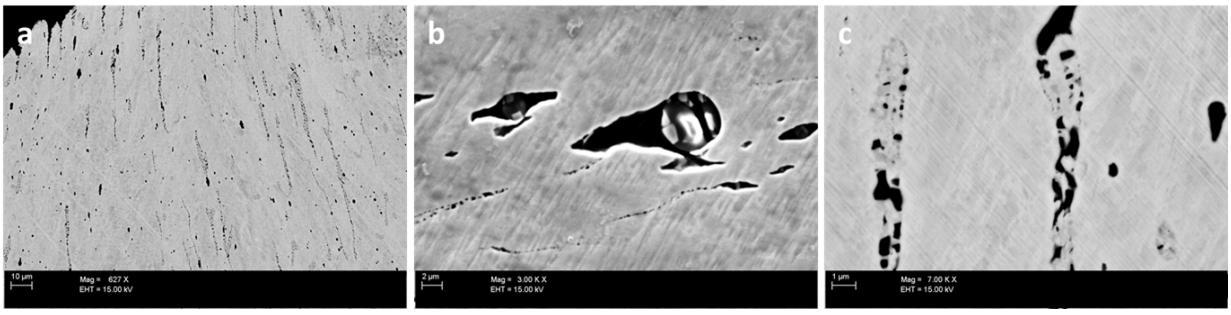

FIGURE 18: Micrographies MEB d'une coupe longitudinale à mi-épaisseur dans une éprouvette de traction à l'état détensionné rompue dans l'acier 308L : a- vue globale ; b- cavités ayant germées sur des oxides ; c- aux interfaces δ-γ.

Afin de provoquer la rupture dans la zone décarburée, des entailles circulaires centrées sur la région d'intérêt ont été ajoutées aux éprouvettes de traction. Les vides observés sur les surfaces de rupture sont plus larges : plusieurs dizaines de micromètres de diamètre contre seulement quelques micromètres dans le cas des aciers inoxydables. Cette observation est en accord avec la forte triaxialité et donc le fort taux de croissance attendu pour les cavités dans cette zone, ainsi qu'avec le nombre limité de sites de germination. D'autre part, une forte influence de la taille du liseré martensitique sur la déformation à rupture a été mise en évidence. Comme notifié dans le Tableau 3, lorsque le liseré martensitique est plus épais, la déformation à rupture est diminuée. Cette chute de ductilité semble être liée à l'augmentation de la triaxialité dans la zone décarburée au contact d'une zone dure plus épaisse.

Tableau 3: Evolution de la déformation à rupture dans la zone décarburée en fonction de l'épaisseur du liseré martensitique

Epaisseur du liseré martensitique	5 μm	35 μm	120 μm
Déformation à rupture	1.43	1.13	0.70

Modélisation micro-mécanique

Dans le but de calculer la déformation à rupture des différentes éprouvettes, un modèle micro-mécanique de rupture ductile développé par Pardoen et al. [12, 13] a été utilisé. Suivant le critère proposé par Beremin [14], la germination est enclenchée lorsque la contrainte principale aux interfaces particules/matrice atteint une valeur critique. Une extension du modèle de Gurson [15] tenant compte de l'évolution de la forme des cavités au cours de la déformation permet de calculer la croissance des vides. Le début de la coalescence correspond à la localisation de la déformation plastique dans l'espace inter-vides suivant le critère de Thomason [16]. Dans la présente étude, la déformation à rupture est considérée comme correspondant au début de la coalescence dans la région la plus endommagée, si bien que la déformation supplémentaire qui serait nécessaire pour rompre l'échantillon est supposée faible. La spécificité de l'approche choisie est le fait que l'écoulement plastique et l'endommagement soient découplés. Ainsi le calcul a lieu en deux temps : d'abord une simulation élasto-plastique de l'ensemble de l'éprouvette sous Abaqus de laquelle sont extraites les évolutions de la triaxialité et de la déformation plastique équivalente au cours du temps pour chacun des éléments du maillage, puis un calcul axisymétrique d'endommagement pour chacun des éléments susceptibles d'être endommagés. Ce dernier fournit la déformation équivalente locale au début de la coalescence, qui permet ensuite de remonter à l'incrément de déplacement global pour lequel la réduction de section doit être calculée à l'aide du modèle par éléments finis.

Ce modèle a été utilisé pour simuler la rupture ductile à la fois dans la zone décarburée et dans le revêtement inoxydable. Malgré une étude paramétrique basée sur la variation de nombreuses grandeurs mécaniques, l'effet de l'épaisseur du liseré martensitique sur la rupture dans la zone décarburée n'a pu être reproduit. Comme prévu, des niveaux de triaxialité plus élevés ont été obtenus dans le cas d'une martensite épaisse mais ils étaient associées à de faibles déformations plastiques, limitant ainsi la croissance des cavités. L'hypothèse de l'existence de sites de germination supplémentaires (points triples aux intersections des joints de grains notamment) qui ne seraient activés que par les valeurs de contraintes élevées présentes dans le cas d'une martensite épaisse a été émise. En revanche, le modèle capture bien l'effet d'une fragilisation des interfaces δ-γ sur la ductilité des couches de revêtement. En réduisant la contrainte critique de germination des cavités à ces interfaces de 3000 à 2300 MPa entre l'état brut et l'état détensionné, les déformations à rupture sont correctement prédites, à la fois pour les éprouvettes globales (perpendiculaires à l'interface) et pour les éprouvettes homogènes (parallèles à l'interface) prélevées dans les différentes couches de revêtement.

Conclusions

Ce chapitre a permis de mettre en évidence les paramètres déterminants pour le développement de l'endommagement et la rupture ductile dans les zones molles de la liaison bimétallique. On trouve parmi eux le degré de confinement de la région considérée ainsi que la quantité des sites potentiels de germination. L'effet du traitement thermique sur la microstructure a des conséquences directes sur la ductilité des différentes régions. L'adoucissement du métal de base sur une étroite bande décarburée conduit à la concentration des déformations dans cette zone. La décomposition de la ferrite δ en carbures provoque la fragilisation des interfaces et donc la germination de cavités à des niveaux de contraintes plus faibles.

Chapitre 7 - Conclusions et perspectives (p.181-190)

Le dernier chapitre reprend les principales conclusions des chapitres précédents en mettant en exergue les faits marquants de ce travail, dont les principaux sont énumérés ci-dessous :

- L'influence des mouvements de fluide dans le bain fondu sur l'irrégularité des microstructures d'interface a été mise en évidence.
- L'origine de la zone purement austénitique a été éclaircie.
- Un modèle thermo-cinétique couplant la diffusion à longue distance à la cinétique de précipitation a été développé. Il a permis de démontrer le rôle particulier joué par la martensite d'interface dans le transfert de carbone depuis le métal de base vers le métal soudé.
- La décomposition des résidus ferritiques présents dans le métal soudé austénitique a été observée et son influence sur la ductilité du revêtement a été démontrée.
- Des données microstructurales et mécaniques précises sur la zone décarburée ont été générées. Elles pourront ensuite être réutilisées dans le cadre de modélisations ultérieures.
- La stabilité des microstructures autour de l'interface ainsi que du comportement mécanique local a été constatée à 400°C, en comparaison avec celles à la fin du traitement de détensionnement.

Le manuscrit se termine en citant un certain nombre de perspectives qu'il serait possible de donner à un tel travail. Les principales concernent la modélisation, aussi bien microstructurale que mécanique. D'un point de vue thermodynamique, une amélioration de la description du liseré martensitique serait nécessaire afin de permettre le fort niveau de sursaturation en carbone mesuré dans cette région. Cela passe par la prise en compte du piégeage du carbone au sein de la matrice, sur des sites favorables énergétiquement tels que les joints de lattes et les dislocations. D'un point de vue mécanique, la prise en compte des gradients de contrainte/déformation comme force motrice pour le développement de l'endommagement permettrait un déplacement de la zone de rupture au sein de la zone décarburée. En effet, il est nécessaire que la rupture ait lieu à proximité du liseré martensitique pour qu'elle soit influencée par l'épaisseur de celui-ci.

Contents

Chapter 1

Introduction: industrial and scientific motivations

1.1 Industrial context

Dissimilar Metal Welds (DMW) that are the subject of this PhD thesis are common features of pressurized water nuclear reactors (see Fig. 1.1 for a global overview). They are principally located in the connections from the ferritic large components, this is the reactor pressure vessel, the steam generator (SG) and the pressurizer (PZR), to the austenitic main cooling lines of the primary circuit. The occurrence of this type of welds in the French nuclear power plants is summarized in Tables 1.1 and 1.2.

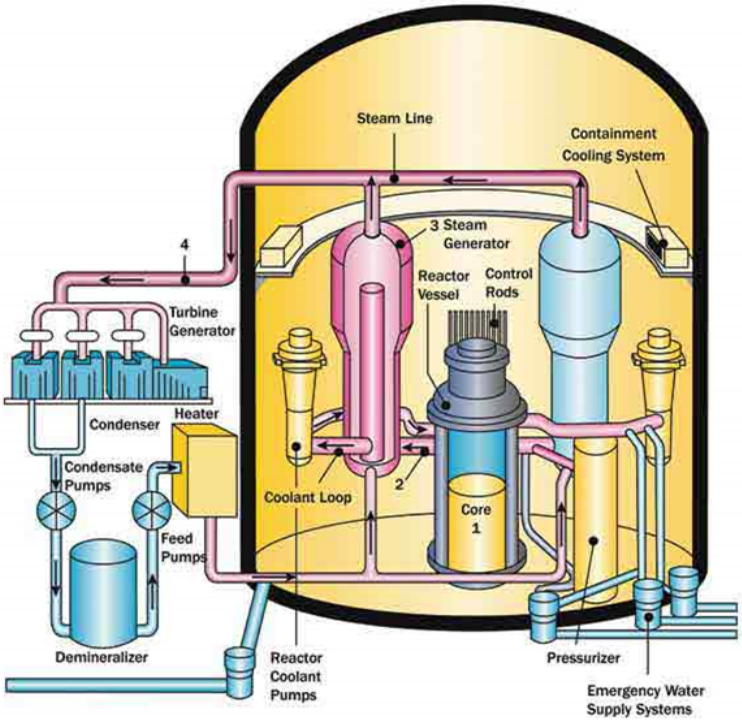

Figure 1.1: Schematic representation of a pressurized water reactor with its major components [17].

Table 1.1: Occurrence of the dissimilar steel welds in a French nuclear power plant.

Nuclear Plant	**DMW pressure vessel**	**DMW SG**	**DMW PZR**	**Total**
900 MW	6	6	6	18
1300 MW	8	8	6	22
N4	8	8	5	21

Table 1.2: Occurrence of the dissimilar steel welds in the French nuclear fleet.

Nuclear Units	**DMW pressure vessel**	**DMW SG**	**DMW PZR**	**Total**
900 MW	204	204	204	612
1300 MW	160	160	120	440
N4	32	32	20	84
Entire fleet	396	396	344	1136

The filler metal used in most of the dissimilar metal welds of the French fleet is austenitic stainless steel. The large components are made of a low-alloy steel (16MND5, 18MND5, 20MND5 in France or ASME/ASTM SA 508 Cl3 type in other countries) because of its good combination of mechanical properties. The ends of their nozzles are first "buttered" with several layers of austenitic stainless steels (309L and 308L) and then welded to the austenitic stainless steel "safe ends" with austenitic steel consumables (308L). These "safe ends" are intermediate rings which allow the on-site connection of the components to piping circuits of the plants by homogeneous welding. Such assembly is represented in Figure 1.2 and an enlargement around the dissimilar interfaces is provided in Figure 1.3 in the case of a steam generator. These DMW were initially fabricated manually by Shielded Metal Arc Welding (SMAW) and more recently have been manufactured using automated welding: Tungsten Inert Gas (TIG) for the buttering and Submerged Arc Welding (SAW) for the weld. Post-weld heat-treatment (PWHT) is then applied to temper the microstructure and reduce the residual stresses that develop in the heat-affected zone on the low-alloy side due to the welding process, the difference between thermal expansion coefficients of the alloys involved and the phase transformations. Other dissimilar welds are found in the primary circuit, including vessel penetrations welds and radial keys welds, which are made with Inconel 182 or 152 filler metals. However they will not be considered in this work. The internal cladding of the low-alloy steel components is also a case of dissimilar weld. Its role is to provide a good resistance to primary water corrosion.

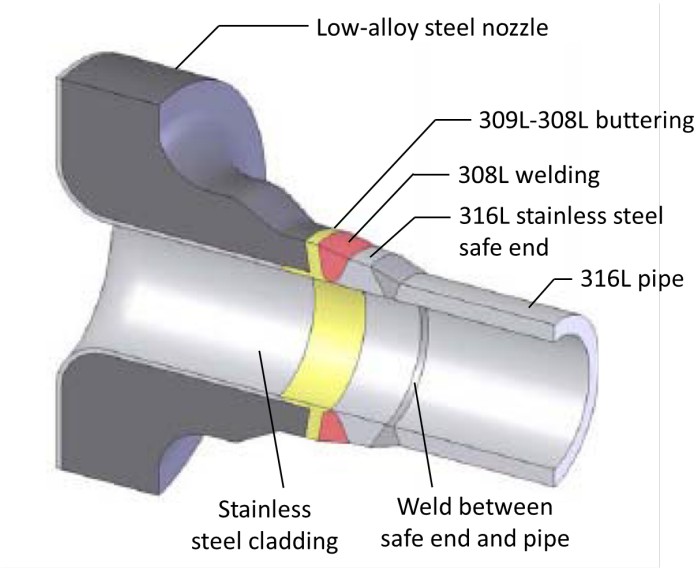

Figure 1.2: Schematic of a connection between a low-alloy steel component and a stainless steel pipe.

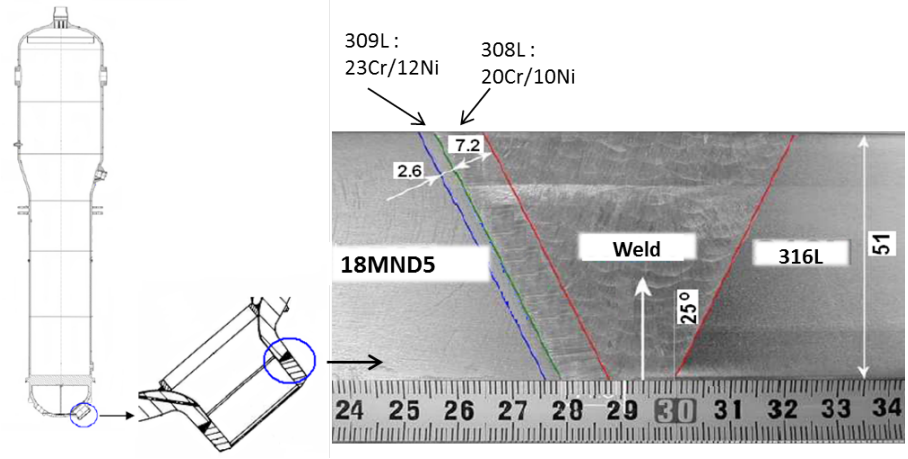

Figure 1.3: Geometry and constituents of a dissimilar steel weld in the case of a steam generator.

One particular feature of these welds is the variety of microstructures that can be obtained in the first buttering layer depending on the welding conditions, which can lead to different dilution ratios[1] within the same manufacturing program due to the manual nature of the process. From a practical point of view, the Schaeffler diagram can be used to predict the final microstructure as a function of the initial composition of the steel to be welded, the filler metal and the dilution ratio. 16MND5 low-alloy steel and 309L stainless steel have been located on the diagram of Figure 1.4 and the composition of the resulting weld deposit necessarily lies on the straight line joining both

[1]The dilution ratio corresponds to the proportion in which the base metal participates by its own melting to the elaboration of the fusion zone.

metals. The following microstructures have been reported for the first buttering layer when the dilution is increased [18]:

- Austenitic-ferritic with 5-6% ferrite for 20% dilution (relatively uncommon)
- Austenitic-ferritic with a low ferrite content (around 3%) for 24% dilution (very common)
- Purely austenitic for 30 % dilution (uncommon)
- Austenitic with small quantities of martensite for 35 % dilution (uncommon)
- Austenitic-martensitic for 40 % dilution (rare)

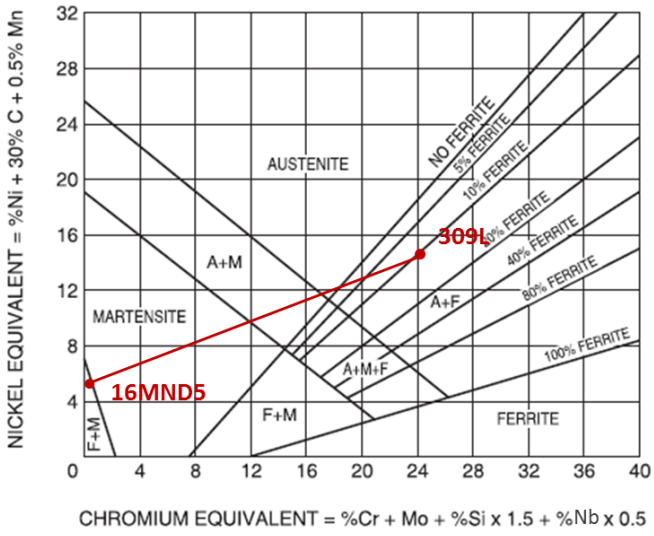

Figure 1.4: Schaeffler diagram where both 18MND5 low-alloy steel and 309L stainless steel have been located [19].

Given the service conditions, the question of thermal aging naturally arises: How do these different microstructures evolve in time when subjected to temperatures around 300°C for several decades? Are the mechanical properties going to degrade? In the context of plant life extension of the French nuclear fleet, a joint EDF-AREVA engineering project has been launched in 2011 to better understand this variety of encountered microstructures, their evolution during thermal aging and their impact on the mechanical properties of the welded joint. This PhD work was intended to provide a scientific support for the engineering program.

It is important to note that the stainless steel filler metals formerly used to weld low-alloy steels to stainless steels have now been suppressed from the design of the new European Pressurized Reactor (EPR). They have been replaced by nickel-base alloys (Inconel 52 and 82). Such a change was motivated by the following reasons:

- **Ease of fabrication** by reducing the number of intermediate layers necessary for welding
- **Elimination of the martensitic layer** at the fusion line and within the FCC region during the cooling subsequent to welding.
- **Decrease of the thermal expansion mismatch:**

$$\begin{cases} \lambda(16MND5) = 11.5 \times 10^{-6}/K \\ \lambda(309L) = 14.4 \times 10^{-6}/K \\ \lambda(I52) = 12.6 \times 10^{-6}/K \end{cases}$$

- **Delay of carbon diffusion** and consequently reduction of the size of the soft carbon-depleted zone in the HAZ and the hard carbon-enriched layer on the austenitic side, that may be created during the post-weld heat-treatment. In fact, the carbon solubility within the Ni-rich FCC matrix is lower than that in the Fe-rich one.

1.2 Base materials and weld production

For practical reasons it has been chosen to focus this study on DMW generated by the internal cladding of the ferritic components. In fact, the low-alloy steel is protected from corrosion by two layers of stainless steel: the first one in 309L, the second one in 308L. The process used for the reactor pressure vessel cladding is Submerged Arc Welding. Regarding the chemical and microstructural gradients across the interface, these particular DMWs are similar to those in connections between pipes and components. Nevertheless, as the cladding does not withstand high mechanical loads, the corresponding filler metals are not designed to have outstanding toughness properties. Therefore, the fracture properties in the austenitic stainless steel cladding which will be measured and modeled in the last part of this work cannot directly be applied to other dissimilar welds.

For this study we made use of a plate of 18MND5 (EDF RD MMC id.:T248) whose dimensions and thickness were 630 x 1200 mm^2 and 90 mm respectively. The flat strip electrode in stainless steel was 60 mm wide and 0.5 mm thick. The chemical compositions of the materials used for this work are listed in Table 1.3. For Al, Cr, Cu, Co, Fe, Mn, Mo, Ni, P, Si, and Ti, the contents have been determined by X-Ray Fluorescence (XRF) on Thermo-ARL9800, whereas for C and S combustion on LECO CS230 has been used. N was analyzed by combustion and conductibility on LECO TC400.

The welding parameters are indicated in Table 1.4. As can be seen in Figure 1.5, the molten pool and the arc zone are protected from atmospheric contamination by being "submerged" under a blanket of granular fusible flux consisting of silica and other oxides and fluorides. The coated metal plate was cut to extract four pieces whose dimensions were 135 x 630 x 90 mm^3. One of them (id.: 248B) was kept in the as-welded condition. The others were subjected to the post-welding heat-treatment in order to release the internal stresses according to the following steps:

- Charging in a cold furnace
- Heating ramp: 30°C/h
- Holding at 610°C for 8 hours
- Cooling ramp: 25°C/h until 300°C
- Air cooling

Among the heat-treated samples, one (id.: 248D) was put aside after the heat-treatment at 610°C, whereas the two others were subjected to an accelerated isothermal aging treatment at 400°C: one specimen (id.: 248V1) for 5000 hours and another one (id.: 248V2) for 10000 hours.

Table 1.3: Chemical compositions of the materials

	C	**Si**	**Mn**	**Ni**	**Cr**	**Mo**	**Cu**
18MND5 (wt%)	0.199	0.219	1.623	0.635	0.231	0.479	0.114
309L (wt%)	0.021	0.359	1.698	12.57	23.66	0.068	0.023
308L (wt%)	0.011	0.152	1.671	10.43	20.04	0.014	0.025
	S	**P**	**Al**	**Co**	**Ti**	**N**	**Fe**
18MND5 (wt%)	0.0019	0.0048	0.028	0.011	<0.002	0.009	bal.
309L (wt%)	0.0077	0.0108	0.052	0.015	0.146	0.039	bal.
308L (wt%)	<0.0002	0.0133	0.026	0.007	<0.002	0.036	bal.

Table 1.4: Parameters used for Submerged Arc Welding

	1st layer	**2nd layer**
Electrode Material	309L	308L
Polarity	+ at the strip electrode	+ at the strip electrode
U(V)	27	27
I(A)	750±20	750±20
V(cm/min)	13.5-14.5	9.5-10.5
Stick-out (mm)	28	28
Angle of the strip (°)	90	90
Overlapping (mm)	6	8
Pre-heating T (°C)	130	Without
Inter-pass T (°C)	<200	<100

Figure 1.5: Strip electrode welding process

1.3 Outline of the thesis

This PhD report is divided into three parts, going from welding to mechanical properties through phase transformations during heat-treatment:

1. The first part is dedicated to **understanding the diversity of microstructures** obtained in the vicinity of the 18MND5/309L interface after welding. The **reasons for their formation** and for the **transition from one to another** are investigated by combining experimental observations with thermo-kinetics calculations. It includes both the microstructure of the base metal affected by the welding thermal cycles and those of the weld metal that forms by solidification in the weld pool during cooling.

2. In addition to their industrial importance, dissimilar steel welds represent an ideal framework for fundamental studies aiming at understanding microstructure evolution kinetics. This is particularly true for the **phases transformations that occur during the post-weld heat-treatment** and that are a **combination of long-range diffusion and local precipitation** in materials with significant chemical gradients. This topic is the subject of the second part of the thesis, which is divided into two chapters. The first one is a complete characterization of the heat-treated microstructure and a comparison with the as-welded one to evaluate the consequences of the phase transformations in terms of carbon diffusion and carbides dissolution and precipitation. The goal of the second chapter is to develop a mesoscopic thermodynamic and kinetic model in order to fully couple diffusion in a multi-component system with precipitates nucleation, growth and coarsening. Several attempts to apply this model to the configuration of the dissimilar weld of interest have been made.

3. The consequences of the significant microstructural differences on the local mechanical behavior are examined in the third part, in particular the **local deformation** and **ductile failure** aspects. This part is divided into two chapters. The first one aims at determining **elasto-plastic constitutive laws** for each of the regions of the dissimilar weld in the post-weld heat-treated state via different experimental techniques. The second chapter, dedicated to the **ductile failure mechanisms in the weak zones of the weld**, includes both in-situ observations and damage modeling. In fact, the main concern for dissimilar steel welds integrity is the large difference of plastic behavior that exists on either side of the fusion line, that may cause stress concentration along the interfaces and therefore create a source of damage.

Each of the previously mentioned topics is addressed in terms of both experimental characterization and modeling. Since the three parts are self-sufficient, they can be read separately and all of them include their own experimental procedure and modeling approach. A literature review and a discussion are also included in each part.

Part I

The as-welded state

Chapter 2

Transitions in solidification mechanisms and microstructures

2.1 Literature review

2.1.1 A chemically graded assembly

When the welding process includes the melting of the two materials to be joined (such as in arc welding), chemical composition gradients have been reported in the vicinity of the interface between the base metal and the weld metal [20, 21, 22, 23]. They correspond to a zone where the composition varies continuously from that of the solid base metal to that of the liquid weld (homogeneous mixing of the molten base metal with the filler metal). Different designations have been used to refer to this region : "Intermediate Mixed Zone (IMZ)" [24, 25], "Partially Mixed Zone" [21], "Unmixed Zone" [26, 27, 28], "Filler Deficient Zone" [29], "Transition Layer" [30, 24]. Although this zone was first noticed by Savage [26] more than 40 years ago, the mechanisms for its formation have still not been completely clarified.

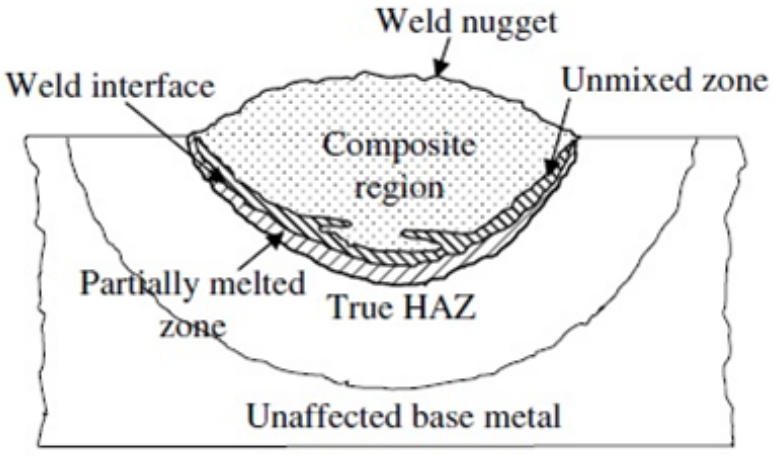

Figure 2.1: Schematic illustration of the different zones in a heterogeneous weld and the proposed terminology to identify these regions [26].

Ornath et al. [23] have attributed the compositional gradients to segregations during solidification, based on the hypothesis of a plane front solidification mode for the whole transition layer. According to them the irregular size of this layer within a same weld would be due to local changes in the solidification rate. However, most of the authors [21, 26, 29, 31, 24, 32] refer to fluid flow and the existence of a stagnant fluid layer in the molten pool at the interface with the solid substrate, where the fluid velocity approaches zero. This boundary layer would correspond to liquid base metal poorly stirred and in which diffusion in the liquid would be the predominant mechanism for solute mixing. As can be seen on Figure 2.1 this assumption has led Savage to propose a new terminology for the discrete regions encountered in a heterogeneous weld: going from the Heat-Affected Zone (HAZ) of the base metal towards the Composite Region formed by the convective mixing of base and filler metals, a Partially Melted Zone and an Unmixed Zone are successively met.

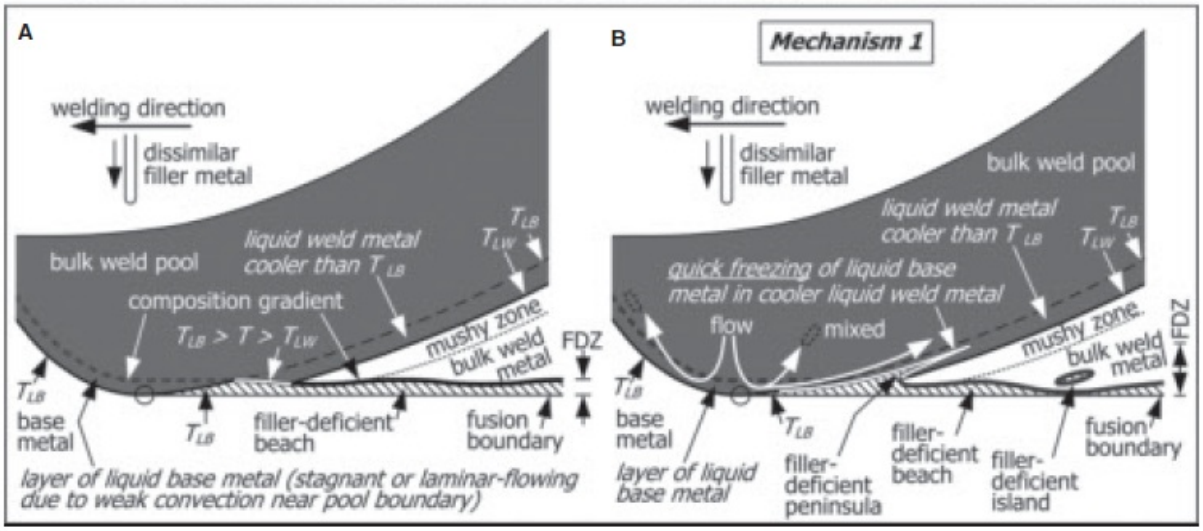

Figure 2.2: Formation of a fusion-boundary segregation when $T_{LW} < T_{LB}$ [29] A- Beach B- Beach, peninsula and island. Pool boundary is melting front before the circle and solidification front after.

Kou and Yang [29, 33] have considered the difference between the liquidus temperatures of the base metal (T_{LB}) and the weld metal (T_{LW}) as the main parameter governing the formation of the IMZ. In the case of a solute-rich filler metal, T_{LW} is lower than T_{LB} and the melting front is at T_{LB} whereas T_{LW} is the temperature of the solidification front. As shown in part A of Figure 2.2, a temperature below T_{LB} and above T_{LW} will make the filler-deficient layer solidify and create along the fusion line the feature often referred as beach in the literature [24]. The larger the temperature difference ($T_{LB} - T_{LW}$) is, the greater the chance for a thick filler-deficient zone to form. As shown in part B of Figure 2.2 the previous theory has also been applied to explain the formation of peninsulas, bays and islands when the convection is able to carry liquid base metal from the stagnant layer into the cooler liquid weld metal. These parts of liquid base metal will start

freezing quickly before much mixing occurs. Such turbulent behavior of the flow in the weld pool will result in the irregularities observed at the interface. However this explanation is only based on microstructural observations and no hydrodynamic model has been developed to forecast the size of the boundary layer as a function of the welding parameters. Some researchers have tried to eliminate the unmixed zone by improving convection in the weld pool. High-intensity ultrasonic [27] or electromagnetic [28] vibrations have been applied to induce a strong mixing of the molten base metal with the molten filler metal and thus eliminate the chemical gradients. Others [34] have been able to reduce the Intermediate Mixed Zone (IMZ) by increasing the buoyancy force (gravity level) by use of a centrifuge applying a net acceleration perpendicular to the weld pool surface up to eight times the terrestrial gravity.

2.1.2 Martensitic layer at the interface

In the welds between austenitic and ferritic steels, martensite is often reported to form at the interface, due to a combination of the rapid cooling subsequent to welding and the local chemical composition [20, 22, 35]. It constitutes a narrow band whose width can vary significantly within a given weld [23] because of local changes in the compositional gradient due to variations in fluid flow and cooling rate [21]. Most of the studies have based their phase identification on dilution calculations and the Schaeffler diagram only [22, 23]. High hardness (higher than 400 HV) has sometimes been measured in this transition layer [36, 25] and some authors have reported martensitic laths observed by means of Transmission Electron Microscopy [31, 37, 38]. This band of martensite is poorly revealed by Nital etching, which explains that it has often been named "light-etching zone" [20, 22, 35]. After having been tempered it seems to have no deleterious effect on the mechanical properties of the welded joint. However it can make the interface sensitive to hydrogen embrittlement during weld cooling to room temperature [30]. Indeed the hydrogen solubility is higher in austenite than in martensite. In order to limit hydrogen intake within the weld, both the flux and the filler metal have to be dried before use and the workpiece has to be preheated.

As can be seen on Figure 2.3, the martensitic layer width can be reduced by optimizing the composition of the filler metal, nickel-based alloys being known to limit the formation of martensite in comparison to stainless steel electrodes [30, 21, 31, 24, 35]. As it occurs inside the Intermediate Mixed Zone, the formation of martensite will be sensitive to the concentration profile. For a given base metal, high Ni content of the weld metal will result in steeper concentration gradients in the transition zone and so the austenite will be stabilized at a shorter distance from the interface. Moreover an increase in the carbon content of the base metal can also be suggested as carbon will be added to the liquid pool by melting of the base metal and so stabilize the austenitic phase during cooling. An increase in the welding speed will promote solidification before sufficient mixing and so martensite extension over larger distances.

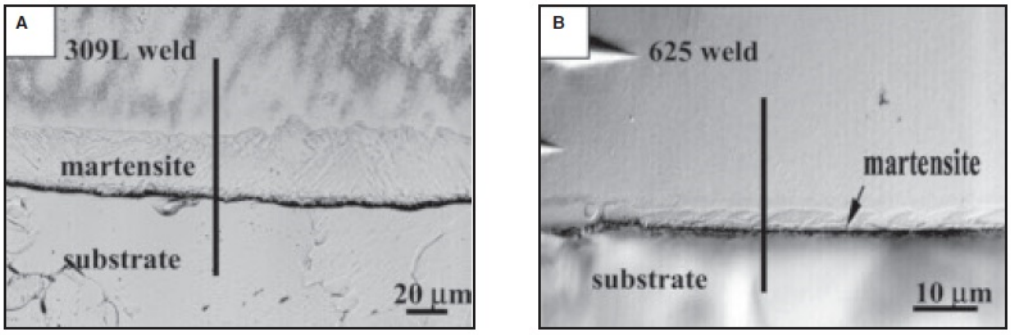

Figure 2.3: Martensitic layers observed in the welds A- A285 carbon steel/309L stainless steel B- A285 carbon steel/IN625 nickel-based alloy [21]

2.1.3 Solidification modes in stainless steel welds

The prediction of the solidification mode in stainless steel alloys is often based on the ternary Fe-Cr-Ni phase diagram. However non-equilibrium conditions prevailing during weld metal solidification and the presence of alloying elements other than Cr and Ni limit the use of such diagrams for determining the solidification sequence. Depending on the composition of the filler metal and the cooling rate, solidification can occur according to different modes that are displayed on Figure 2.4:

- **A mode:** primary austenite solidification without any ferrite.
  L $\rightarrow$ L+γ $\rightarrow$ γ
- **AF mode:** primary austenite solidification with formation of ferrite by eutectic reaction and Cr enrichment in the inter-dendritic space.
  L $\rightarrow$ L+γ $\rightarrow$ L+γ+δ $\rightarrow$ γ+δ
- **FA mode:** primary ferrite solidification followed by austenite formation both from the liquid and by solid-state ferrite decomposition. It is accompanied by Cr enrichment and Ni depletion in the core of the dendrites.
  L $\rightarrow$ L+δ $\rightarrow$ L+γ+δ $\rightarrow$ δ+γ
- **F mode:** primary ferrite solidification with possible nucleation and growth of austenite in the solid state into the ferrite (Widmanstatten austenite).
  L $\rightarrow$ L+δ $\rightarrow$ δ $\rightarrow$ δ+γ

As shown on Figure 2.4, the observation of the ferrite morphology together with the measurements of the composition profiles across the dendrites are really useful for determining both the primary solidification phase and the solidification sequence [39]. Several authors have studied the influence of initial composition and cooling rate on the solidification mode of stainless steels [40, 41, 42]. They usually calculate chromium and nickel equivalents according to Delong formulae [43]:

$$\begin{cases} Cr_{eq}=\%Cr + \%Mo + 1.5\%Si + 0.5\%Nb \\ \\ Ni_{eq}=\%Ni + 0.5\%Mn + 30\%C + 30\%N \end{cases}$$

and for given welding conditions determine the value of the Cr^{eq}/Ni^{eq} ratio at which transition from primary austenite to primary ferrite occurs.

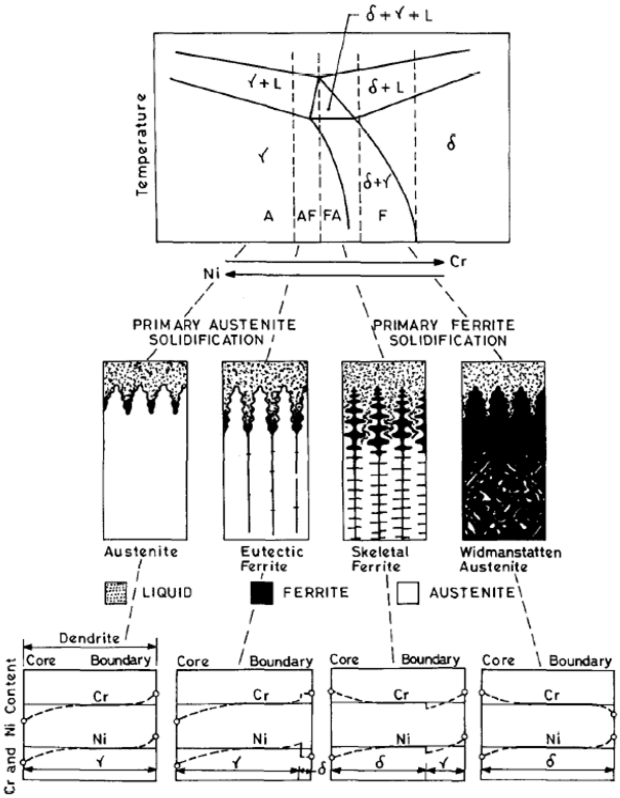

Figure 2.4: Locations of the four solidification modes on a constant iron section of the Fe-Cr-Ni phase diagram and the resulting room temperature microstructures [39].

In rapid cooling conditions, a significant departure from local equilibrium at the solid/liquid interface may occur. As a result, non-equilibrium structures and in some cases, partitionless solidification or plane front stabilization at extremely rapid growth rates can be observed [44]. It has often been experimentally demonstrated that steels, for which thermodynamics forecasts a primary δ-ferrite solidification, can be induced to solidify as metastable austenite by rapid cooling [45, 46, 47]. In the case of Fe-C-Al-Mn steels where the primary solidification microstructure is obscured by subsequent solid-state decomposition, time-resolved X-ray diffraction with a synchrotron radiation is used to in-situ track the δ to γ transition under high cooling rate conditions [48]. Such growth-controlled phase selection has been successfully treated by comparing the interface response of competing phases: the phase which develops the highest interface temperature for a given growth velocity will prevail [3, 4, 5]. The transition from stable ferrite to metastable austenite solidification can have serious consequences on weld integrity since it promotes solidification cracking. Indeed impurities such as phosphorous and sulfur have a higher solubility in the ferrite than in the austenite. In the case of a primary austenite solidification they are rejected within the inter-cellular space where they form liquid films with a low solidification temperature. During subsequent cooling micro-cracks may appear by contraction of the residual liquid while solidifying.

A characteristic feature of ferritic/austenitic welds is the occurrence of a Type II grain boundary[1] that has been shown to be prone to premature cracking, especially in hydrogen-rich environments. Several reasons have been invoked for its formation. On the one side, Nelson et al. [49] observed Bain-type orientation relationships between BCC and FCC through the fusion line and proposed the Type II GB would result from the migration of the γ (base metal)/FCC (weld metal) interface upon cooling during the $\delta \rightarrow \gamma$ transformation of the base metal. On the other side, Wu et al. [50] performed a systematic study by varying the composition and microstructure of the weld overlay. They associated Type II GB with a change in the solidifying phase from δ to γ in the case of primary δ solidification, and with a film of impurities rejected ahead of the growing solid in the case of primary γ solidification.

This literature review has provided valuable insight into the microstructural features that are usually encountered in the dissimilar steel welds. It constitutes a starting point for the observation of the 18MND5-309L interface, whose main goal will be to highlight the high variability of microstructures in the vicinity of the fusion line and discuss the reasons for such an evolution over short distances.

2.2 Experimental methods

2.2.1 Microstructural investigation

For this part focused on solidification during welding, only one layer of 309L was deposited on the 18MND5 base metal plate in order not to be subjected to subsequent thermal effects associated with other deposits next to or above the initial one. Preheating of the piece to be welded and drying of the flux material have been performed to minimize the hydrogen content in the deposited metal and so the risk of premature cracking. The chemical compositions of the base materials are those of Table 1.3 and the welding parameters those given for the first layer in Table 1.4.

Transverse and longitudinal cross-sections were prepared for metallographic analysis. Nital etchant (4% HNO_3 in methanol) was applied for revealing the microstructure of the base metal. Concerning the weld metal, two types of etching were used: Lichtenegger and Bloesch chemical solution (100mL H_2O, 20g NH_4HF_2, 1g $K_2S_2O_5$) and an electrolytic etchant (50% H_2O, 50% HNO_3, 1.2V, 20 mA/cm^2). Both are sensitive to the level of microsegregations: the first one has been chosen for its ability to color the phases with respect to their composition whereas the second one can be combined with Nital etching as it reveals the solidification microstructures in the stainless steel without affecting the low-alloy steel. Both optical and scanning electron microscopy were used to image the microstructural features of interest.

[1] Grain boundary (GB) which forms parallel to the fusion line, next to it on the weld metal side.

2.2.2 Composition measurements

Composition profiles were measured by both Wavelength Dispersive Spectroscopy (WDS) and Energy Dispersive Spectroscopy (EDS). These two techniques are based on the excitation of characteristic X-ray photons under the electron beam. WDS was preferred for its spectral resolution well-adapted to accurate quantification whereas EDS was chosen when very small space steps were necessary.

The WDS measurements were performed on an Electron Probe Micro-Analyzer CAMECA SX50 equipped with the SamX software, with an accelerating voltage of 16 kV and a probe intensity of 600 nA. WDS allowed an accurate quantification as the signal was compared with the ones of reference samples made of the pure metals, using the PAP $\Phi(\rho z)$ method [51]. Corrections for atomic number, matrix absorption and fluorescence were taken into account. Measurements were performed on the reference samples just before the analysis on the specimen of interest, in the same conditions.

EDS on a Jeol JSM 6400 SEM equipped with a Brucker AXS SDD detector was chosen for the measurements of inter-cellular and dendritic microsegregations with a step of 0.5 μm. It is a semi-quantitative method as the use of reference samples is replaced by comparison with pre-recorded spectra. No measurement was performed for carbon and nitrogen. When necessary, their local content was evaluated based on a dilution coefficient d[2] calculated on the Ni profile, Cr being potentially subjected to evaporation during welding and to additions from the flux.

2.2.3 Study of the orientation relationships

Electron back-scattered diffraction (EBSD) analysis was used to study the orientation relationships (OR) between the solid substrate and the weld metal. The samples were prepared by classical mechanical grinding and polishing techniques, the last step consisting of prolonged polishing in a colloidal silica suspension to remove residual cold-working. The EBSD patterns were acquired on a JEOL 7001F SEM under the following conditions: an acceleration voltage of 20 kV, a specimen tilt of 70°, a working distance of 20 mm and a scan step varying between 1 μm and 400 nm on an hexagonal grid. Kikuchi patterns were automatically analyzed using OIM^{TM} software. Automatic reconstruction of the parent grains orientation was performed with the ARPGE software developed at CEA, Grenoble. A detailed description of this program can be found in the references [1, 2]. Of particular interest in this software is the fact that there is no need for any residual parent phase for achieving the reconstruction. The method is based on the fact that the orientational variants (daughter crystals in OR with a parent crystal) and the operators (transformations between variants) have the algebraic structure of a groupoid whose composition table acts as a crystallographic signature of the transition. After a specified orientation relationship was postulated between parent and product phases, the product grains were identified based on a criterion on the misorientation angle and a minimum number of pixels per grain. For the parent grains reconstruction the program

[2] $w(C,x) = d(x) * w(C,18MND5) + (1 - d(x)) * w(C,309L)$ with $d(x) = (w(Ni,x) - w(Ni,309L))/(w(Ni,18MND5) - w(Ni,x))$, w(X,x) being the mass content of element X at the distance x from the fusion line.

checks if the misorientations between neighboring daughter grains are close to the theoretical operators and if the composition of these operators is in agreement with the theoretical groupoid composition table. The calculation proceeded in two steps: first a nucleation step with a low tolerance angle (3° in our case) and then a growth step with a larger tolerance angle (6°). When at least four orientationnal variants are present within the daughter grains and there exists an orientation relationship between parent and daughter grains, ARPGE usually reconstructs 80 to 90 % of the map during the nucleation step. Then the anglar tolerance is automatically increased (from 3 to 6°) to obtain the whole reconstruction. The GenOVa program [52] was used to simulate theoretical pole figures assuming a given OR between the daughter and parent grains. They were then compared with the experimental ones created by post-treatment of the EBSD maps with the OIM^{TM} software.

2.2.4 Thermodynamic calculations and DSC measurements

Thermodynamic calculations, both phase equilibria and solidification under modified Scheil-Gulliver conditions, were performed with ThermoCalc® software [53] together with the TCFE6 database [54] dedicated to iron-based alloys. In the Scheil-Gulliver method the fraction and composition of all phases during solidification are calculated step by step by applying local equilibrium at interface. The main assumption is the very slow, and therefore negligible, diffusion of substitutionnal species in the solid phases. In our calculations with the modified Scheil-Gulliver method, back diffusion for carbon and nitrogen only as well as ferrite to austenite transformation were allowed.

Differential Scanning Calorimetry (DSC) experiments were conducted on the low-alloy steel with a Setaram Multi HTC calorimeter to determine the temperatures at which phase transitions occur. The samples ($\simeq$ 4 x 4 x 12 mm^3 size and 1550 mg weight) were placed in an alumina crucible with high-purity argon flow as protective atmosphere. They were first heated up to 1400°C at a rate of 5°C per minute and after 15 minutes at 1400°C, they were subjected to a ramp of 2°C per minute up to 1520°C, temperature for which the whole sample should be liquid. A base line calibration run was performed before experiment.

2.3 Results

2.3.1 Overview of the diversity of microstructures around the fusion line

The following schematic (see Fig. 2.5) represents the different regions around the 18MND5-309L interface in the as-welded state. Each of them will be described in detail below.

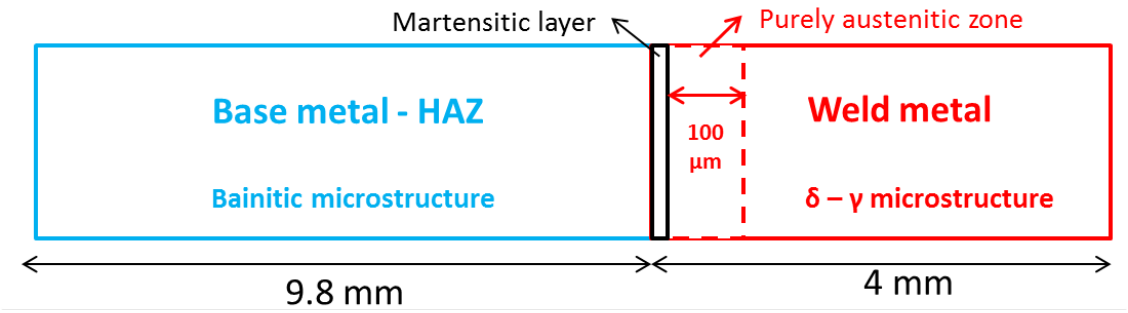

Figure 2.5: Schematic of the 18MND5-309L interface in the as-welded state.

2.3.1.1 The base metal 18MND5

The Heat Affected Zone (HAZ) of the base metal which spans over 9.8 mm has a bainitic microstructure (ferritic laths and cementite carbides). Coarse grains are visible in the first millimeter from the fusion line (Fig. 2.6-b) where the high temperatures encountered during the welding cycle have allowed grain growth. Further away from the interface (see Figure 2.6-c) the grains are smaller as recrystallization has taken place without significant grain growth. The positions of the isothermal curves inside the HAZ and the thermal cycle at different locations can be calculated following the method described below:

- Temperature calculation using Rosenthal's equation in the case of a distributed heat source without any consumable electrode [55]:

$$T - T_0 = \left(\frac{qvL}{\rho c\sqrt{4at\pi}}\right)\exp\left(\frac{-z^2}{4at}\right)\left[\mathrm{erf}\left(\frac{y+L}{\sqrt{4at}}\right) - \mathrm{erf}\left(\frac{y-L}{\sqrt{4at}}\right)\right] \tag{2.1}$$

  y being the direction along the width of the electrode and z along the depth of the weld pool. The meaning and value of the parameters needed for the calculation are summarized in Table 2.1.

- Determination of the location of the fusion line both experimentally (measurement on a transverse section of the weld, see Fig. 2.6-a) and numerically (solving Equation 2.1 for $T < T_f = 1508°\mathrm{C}\ \forall \mathrm{t}$).

- Calculation of the offset on the position of the fusion line due to the melting of the consumable electrode and correction of the calculated isotherms according to this shift.

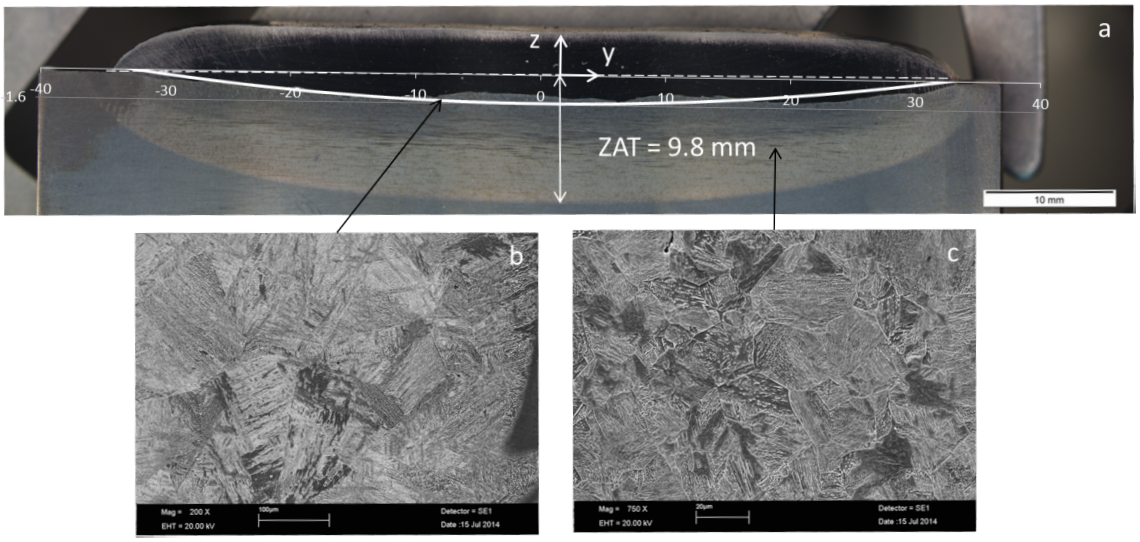

Figure 2.6: a- Transverse cut of the mono-layer weld allowing to locate both the fusion line (white solid line) and the HAZ. Microstructure of the base metal b- at the fusion line. c- at 4 mm from the fusion line.

Table 2.1: Parameters used for the calculation of the temperature cycles by means of Equation 2.1.

U	Arc voltage	27 V
I	Intensity	750 A
η	Arc efficiency	0.8-0.95
q	Power of the source (W)	UI/η
v	Welding speed	2.33 mm/s
$\mathbf{T_0}$	Preheating temperature	130°C
$\mathbf{T_f}$	18MND5 melting temperature	1508°C
2L	Width of the strip electrode	60 mm
ρ**c**	18MND5 heat capacity	4.6 mJ/mm^3/°C [56]
a	18MND5 thermal diffusivity	6.43 mm^2/s [56]

Of particular interest are the Ac1 (temperature at which the formation of austenite begins on heating) and Ac3 (temperature at which the microstructure is fully austenitic) isotherms. Ac1 position defines the limit of the HAZ. Given the high heating and cooling rates encountered in welding, phase transformations are retarded leading to 820°C (instead of 720°C) and 900°C (instead of 820°C) for Ac1 and Ac3 respectively [57, 58]. Figure 2.7 displays their calculated position: an arc efficiency of 0.86 is chosen as it leads to a good agreement for the depth of the HAZ at the center of the pool (y=0). Its global shape is approximately reproduced (see Fig 2.7). The value of the efficiency (<1) is due to the fact that part of the heat power of the arc is used for the melting of the flux and the consumable electrode. This method also allows to calculate the thermal cycle at each location in the solid base metal and then deduce an estimate of the heating rate and thermal gradient at the solid/liquid interface: 212°C/s and 1.5 x 10^5 °C/m, respectively.

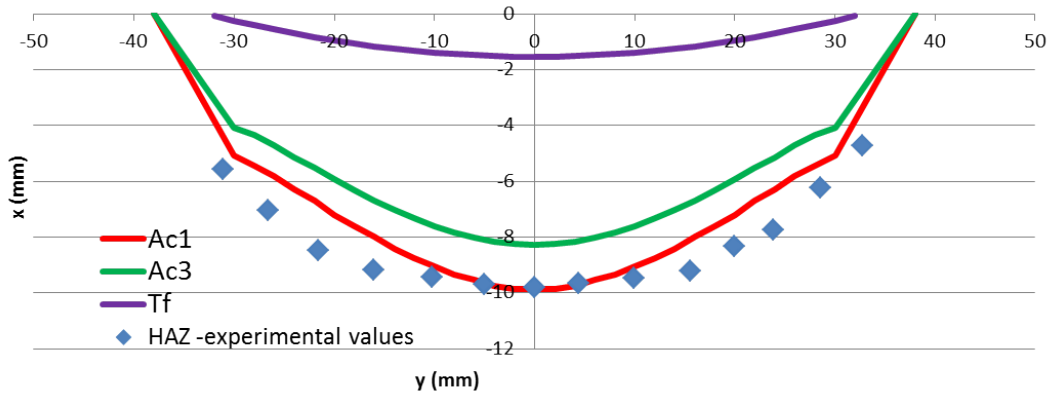

Figure 2.7: Calculated positions of Ac1 and Ac3 isotherms for an arc efficiency of 0.86 and comparison with experimental measurements for the HAZ size.

2.3.1.2 The interfacial martensitic layer

The observations conducted at the fusion line revealed the presence of a martensitic layer all along the interface. In agreement with the information from the literature (see Section 2.1.2) it is characterized by the following main features:

- It is perfectly revealed by Lichtenegger and Bloesch etchant as a blue lathy layer in between the brown ferritic base metal and the orange weld metal (see Fig. 2.8).
- Its width is extremely irregular varying from 5 to 200 μm which arises from the turbulent fluid flow in the weld pool (see Fig. 2.9).
- In the as-welded state, its micro-hardness is found to be around 400 HV whereas those of the adjacent base metal and austenitic weld are 300 HV and 180 HV respectively.
- Its width can be estimated by calculating the martensitic start temperature M_s as a function of the distance from the fusion line thanks to the following empirical formulae:
  - **For the low-alloy steels** (with no alloying elements whose content is higher than 5wt.%) [59]
    $M_s(°C) = 561 - 474w\%(C) - 33w\%(Mn) - 17w\%(Cr) - 17w\%(Ni) - 21w\%(Mo)$
  - **For the alloyed steels** (Cr content lower than 14wt.%) [60]
    $M_s(°C) = 635 - 474w\%(C) - 33w\%(Mn) - 17w\%(Cr) - 17w\%(Ni) - 21w\%(Mo)$
  - **For the stainless steels** [61]
    $M_s(°C) = 502 - 810w\%(C) - 13w\%(Mn) - 12w\%(Cr) - 30w\%(Ni) - 6w\%(Mo)$

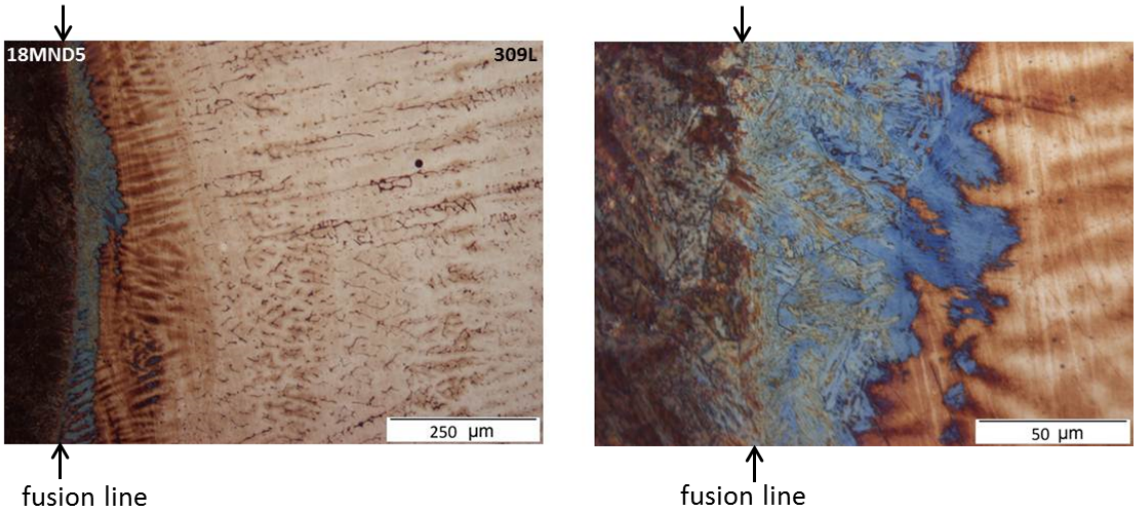

Figure 2.8: Interface between 18MND5 base metal and austenitic weld metal after Lichtenegger and Bloesch etching.

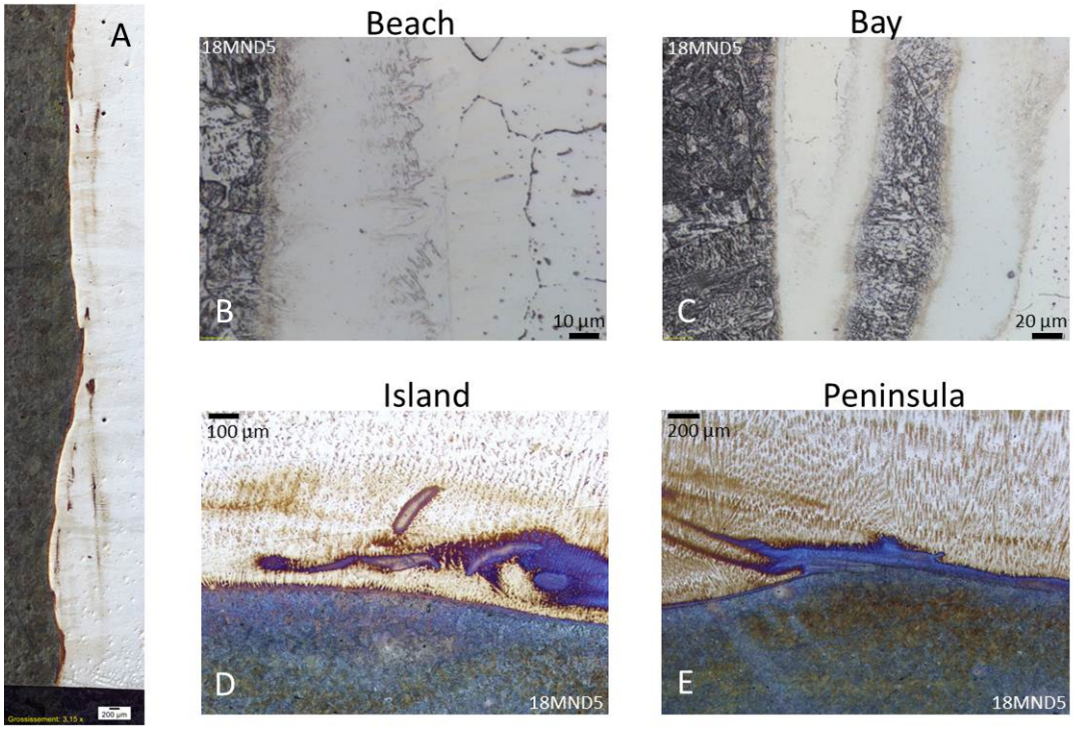

Figure 2.9: Microstructural features encountered at the interface between the 18MND5 base metal and its stainless steel cladding A- General view of the interface after Lichtenegger and Bloesch etching. B and C- Beach and bay after Nital+Nitric acid etching. D and E- Island and peninsula after Lichtenegger and Bloesch etching.

2.3.1.3 The austenitic weld metal

Starting from the martensitic layer, one meets first a fully austenitic zone and then a two-phase $\delta-\gamma$ microstructure typical of a stainless steel with 18 wt.% Cr and 9 wt.% Ni. The fully austenitic zone (A) spreads over 70 μm, as can be seen in Figure 2.10-a. The successive steps allowing the transition from a single phase γ to a two-phase (δ+γ) microstructure will be detailed in Section 2.3.3.

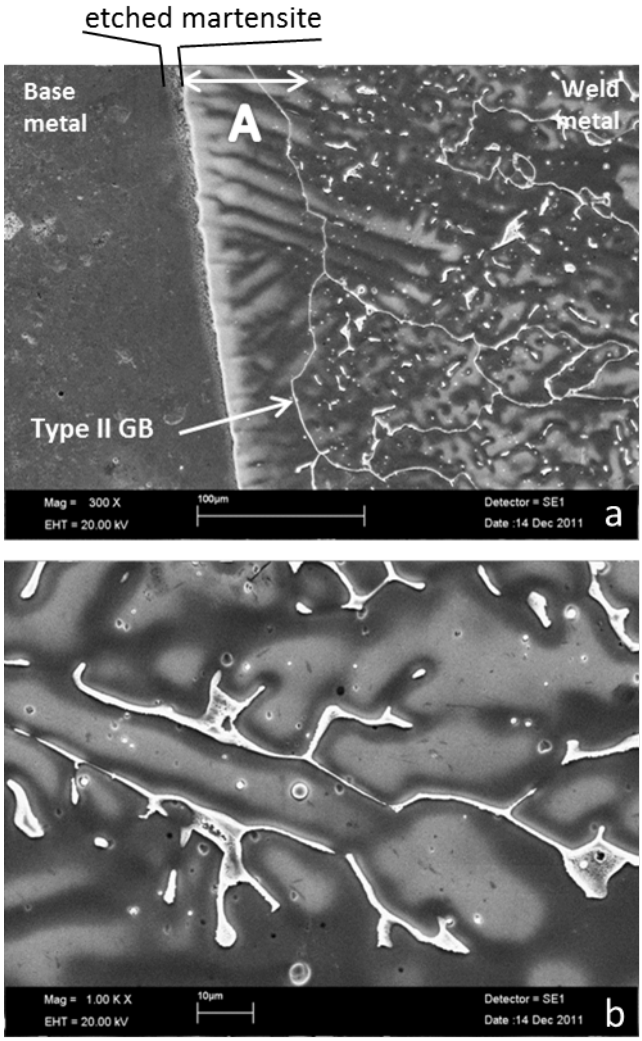

Figure 2.10: SEM micrograph of the weld microstructure after electro-nitric etching. a) Global view where plane front to cells transition is visible and the extent of the purely austenitic zone (A) is marked by a double arrow. b) Duplex microstructure at 200 μm from the fusion line with δ-ferrite (in white) embedded in the austenitic matrix, both types of γ phase are visible: austenite from solidification (in light gray) and austenite from δ decomposition (in dark gray).

2.3.2 Compositional evolution in the boundary layer

Composition profiles were measured around the fusion line by WDS on a transverse section of the weld and are plotted in Figure 2.11 for Fe, Ni and Cr. The profiles can be divided into three distinct

parts, from the left (base metal) to the right (austenitic coating): a flat plateau corresponding to the part of the base metal which remained solid during welding, then the transition zone in which composition gradients take place and finally a quasi-flat part which can be associated with the homogeneous mixing of the molten metals in the weld pool by convection. The compositions measured on the last plateau (on the right of the profile) correspond to the mixing of the molten base metal with the filler metal in proportions 20-80 %, which is in agreement with the remolten width. In the transition zone the composition profile has been refined with one measurement every 5 μm to precisely capture variations occurring over short distances. Concerning Ni and Cr contents, they first increase over 10 μm, then stabilize over 20 μm and finally increase again. This zone can be associated with the boundary layer in which mixing is partial, as convection is weak and liquid diffusion is the main active mechanism. Fluid motion and solute transport are the phenomena usually mentioned to explain composition evolution in dissimilar welds. But solidification segregations have to be added to completely describe the complex shape of the profile in the transition layer.

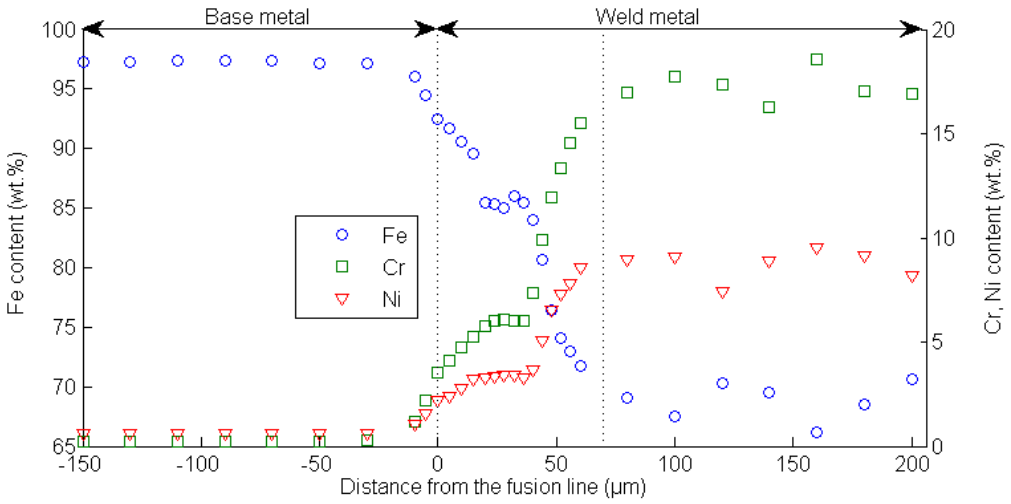

Figure 2.11: Composition profiles measured by WDS on a transverse section of the weld. The origin of the x-axis (0 on the plot) has been taken at the end of the base metal.

Depending on the location in the weld along the interface, the concentration profile can vary significantly as shown in Figure 2.12 where two regions have been chosen for WDS measurements of the substitutional species across the interface. The first one presents a narrow band of martensite (Fig. 2.12-A) whereas the second (Fig. 2.12-B) displays a larger interfacial layer. For both of them the evolution of the M_s temperature with the distance from the fusion line was calculated and a good agreement was observed with the width of the martensitic layer revealed by etching. The narrow martensite is associated with steep gradients in the IMZ whereas the formation of a large layer is enabled by smoother compositional changes. Therefore upper limits for martensite formation can be deduced in terms of alloying elements concentration: around 14 % for Cr and 7.5 % for Ni.

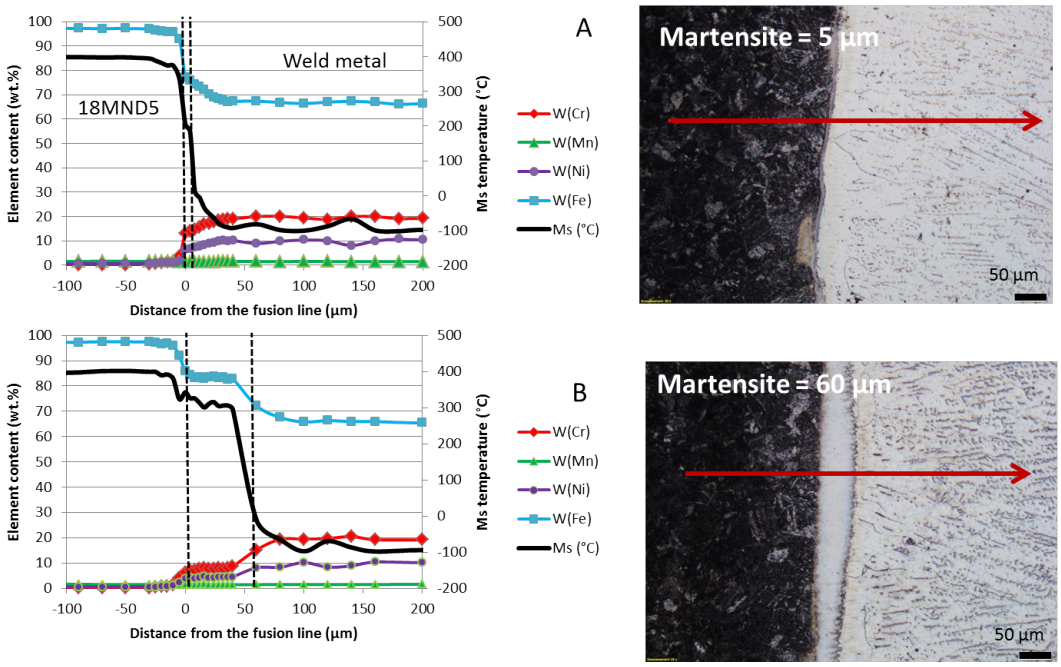

Figure 2.12: Relation between the size of the martensitic layer measured on optical micrographs and the slope of the composition profiles obtained by WDS: A- in the case of a narrow martensite; B- in the case of a thick martensite.

2.3.3 Morphological evolution and change in the solidification mode

The transition layer is not only the place of compositional gradients but it is also subjected to a progressive increase of the solidification velocity which has to be zero in contact with the solid substrate. As a consequence, there is an evolution of the solid/liquid interface's morphology: it begins with a planar front which gets destabilized, goes on by a cellular growth and as the solidification velocity keeps increasing, cells evolve into dendrites, the secondary arms improving the redistribution of solutes between solid and liquid phases. This transition is clearly visible in Figure 2.10-a. The microstructure of Figure 2.10-b (visible beyond 150 μm from the fusion line) is typical of a primary ferrite solidification: the core of the dendrites is made of residuals of δ-ferrite embedded in an austenitic matrix. Two types of austenite are found: the one formed from the liquid at the end of solidification and which constitutes the external shell of the dendrite, the other one formed at lower temperature when δ-ferrite decomposes. As can be seen in Figure 2.13, the transition from pure γ phase to $\gamma+\delta$ is progressive: some δ phase first nucleates in the inter-cellular space in between the γ cells.

In order to determine the first phase to solidify from the liquid, microsegregation profiles were measured by EDS, both in the purely austenitic zone and further away from the interface where dendrites of δ phase are found. The results are shown in Figure 2.14 and reveal two distinct types of solidification:

- The **first plot** (Figure 2.14-a), measured across the cells is **typical of a primary austenite solidification**: it presents a segregation of chromium in the inter-cellular space with a curved

profile inside each cell whereas the nickel profile is flat in the interior of the cells.

- On the contrary, the **second plot** (Figure 2.14-b), measured across the two-phase dendrites, is **typical of a primary ferrite solidification** followed by its regression: Cr segregations are observed in the center of the dendrites and the Ni profile is also curved as both types of austenite have different compositions. The one formed from the liquid is enriched in nickel whereas the one formed from the ferrite is enriched in chromium.

These results are in good agreement with the values of the partition coefficients presented in Table 2.2, calculated for the compositions of interest at the liquidus temperature for both types of solidification. Thus these results clearly evidence the evolution of the solidification mode, from first **single phase austenite** (A mode) towards **primary austenite with ferrite as second phase** (AF mode) and finally **primary ferrite with austenite as second phase** (FA mode), using the common denomination found in the literature [62].

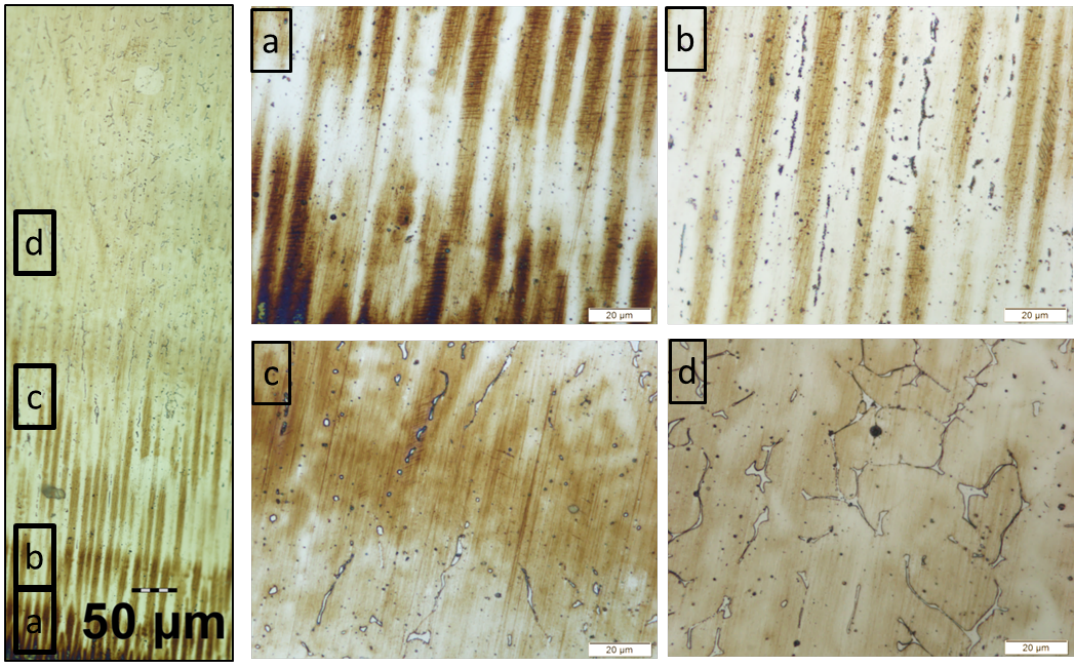

Figure 2.13: Optical micrographs of the weld metal after Lichtenegger and Bloesch etching. Global view with the evolution of the solidification mode on the left. a- Cellular A mode. b- Cellular AF mode. c- FA mode (transition between cellular and dendritic growth). d- Dendritic growth with FA mode.

Table 2.2: Partition coefficients of nickel and chromium calculated for the composition of the transition zone where the microsegregation profiles were measured for the following global composition: w(C)=0.052%, w(Cr)=18%, w(Mn)=1.6%, w(Mo)=0.16%, w(N)=0.03%, w(Ni)=9%, w(Si)=0.7%

	k(Cr)	**k(Ni)**
Primary FCC	0.86	1.00
Primary BCC	1.03	0.76

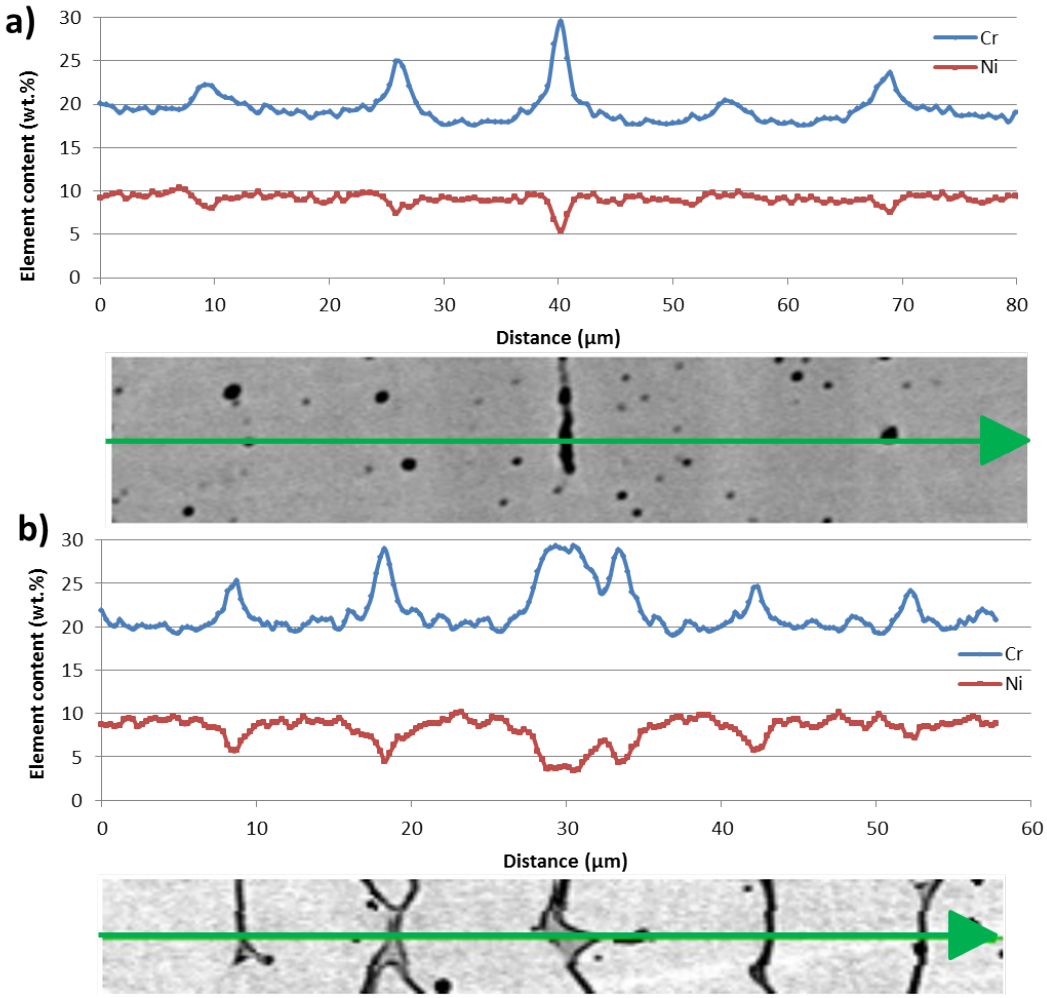

Figure 2.14: Cr and Ni profiles measured by EDS. a- Across the austenitic cells. b- Across the two-phase dendrites

2.3.4 Orientation relationship between base and weld metals

A careful examination of the fusion line on etched samples revealed a continuity between the former austenitic grain boundaries of the base metal and the newly formed austenitic grain boundaries of the weld metal. It can be seen in Figure 2.15 where this feature has been underlined by arrows. This seemed to indicate that the austenitic region of the weld has grown by epitaxy on the austenite grains of the base metal.

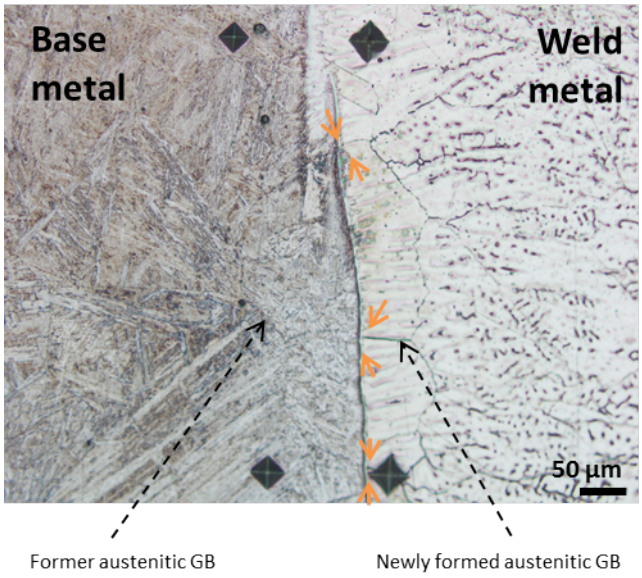

Figure 2.15: Optical micrograph of the weld (x 200) after a two-step etching: Nital and Electro-nitric. Arrows are superimposed to highlight the continuity of the grain boundaries (GB) across the fusion line.

For verifying these observations, an EBSD study of the orientation relationships (OR) between the base and the weld metals was conducted. Due to rapid cooling subsequent to welding, the base metal at the interface has a bainitic microstructure and no residual austenite was found to enable a direct comparison of its orientation with the one of the adjacent grain in the weld. For several austenitic grains of the weld lying along the fusion line, the <100> pole figure was compared with the <100> and the <110> pole figures from a set of martensitic laths formed from a single austenitic grain located in the base metal, just across the interface. One example is presented in Figure 2.16-a,b,c and for all the grains tested each martensitic variant has one of its <100> and <110> directions lying around one of the <100> directions of the opposite austenitic grain. This is typical of a Bain transformation and indicates that there is a high probability for the former austenitic grain (from which the martensitic laths have grown) to have the same orientation as the adjacent FCC grain which formed from the liquid weld. The exact OR was then determined by comparing the experimental and simulated <100> and <110> pole figures of martensite crystal orientations inside a single austenite grain. The better match was obtained with the crystallographic correspondence proposed by Greninger and Troiano (GT) [63] and is displayed in Figure 2.16-c,d. The GT transformation is intermediate between the well-known Kurdjumov-Sachs (KS) [64] and Nishiyama-Wassemann (NW) [65] ORs. Its Euler angles (ϕ_1, ψ, ϕ_2) are 2.7,

46.6 and 7.5 ° respectively. This OR, which is implemented into ARPGE software, was postulated for the reconstruction of the parent austenitic grains on the base metal side and the results are shown in Figure 2.17. The orientations calculated in the base metal (Figure 2.17-b) are in perfect agreement with the ones recorded in the austenitic grains of the weld metal, just across the fusion line (Figure 2.17-c).

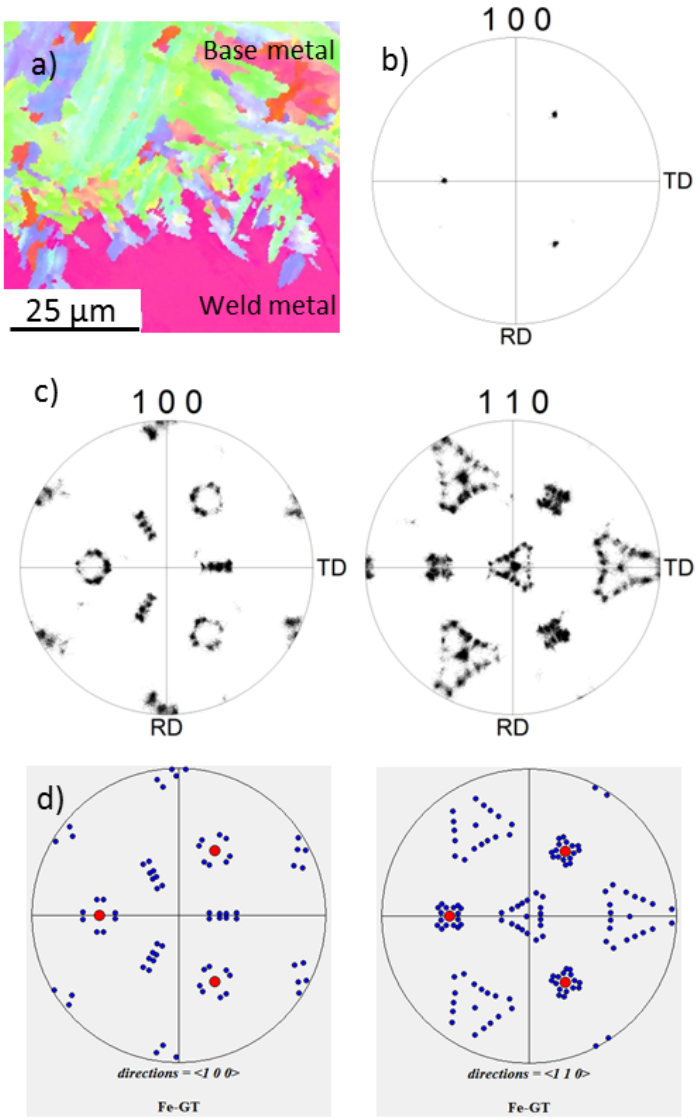

Figure 2.16: a- EBSD map of some martensitic laths in the base metal and the adjacent austenitic grain in the weld. b- Experimental <100> pole figure from the austenitic grain. c- Experimental <100> and <110> pole figures from the martensitic laths. d- Simulated poles figures, red dots being the <100> directions of the parent austenitic grain and blue dots being the directions of the 24 martensitic variants obtained assuming the GT orientation relationship.

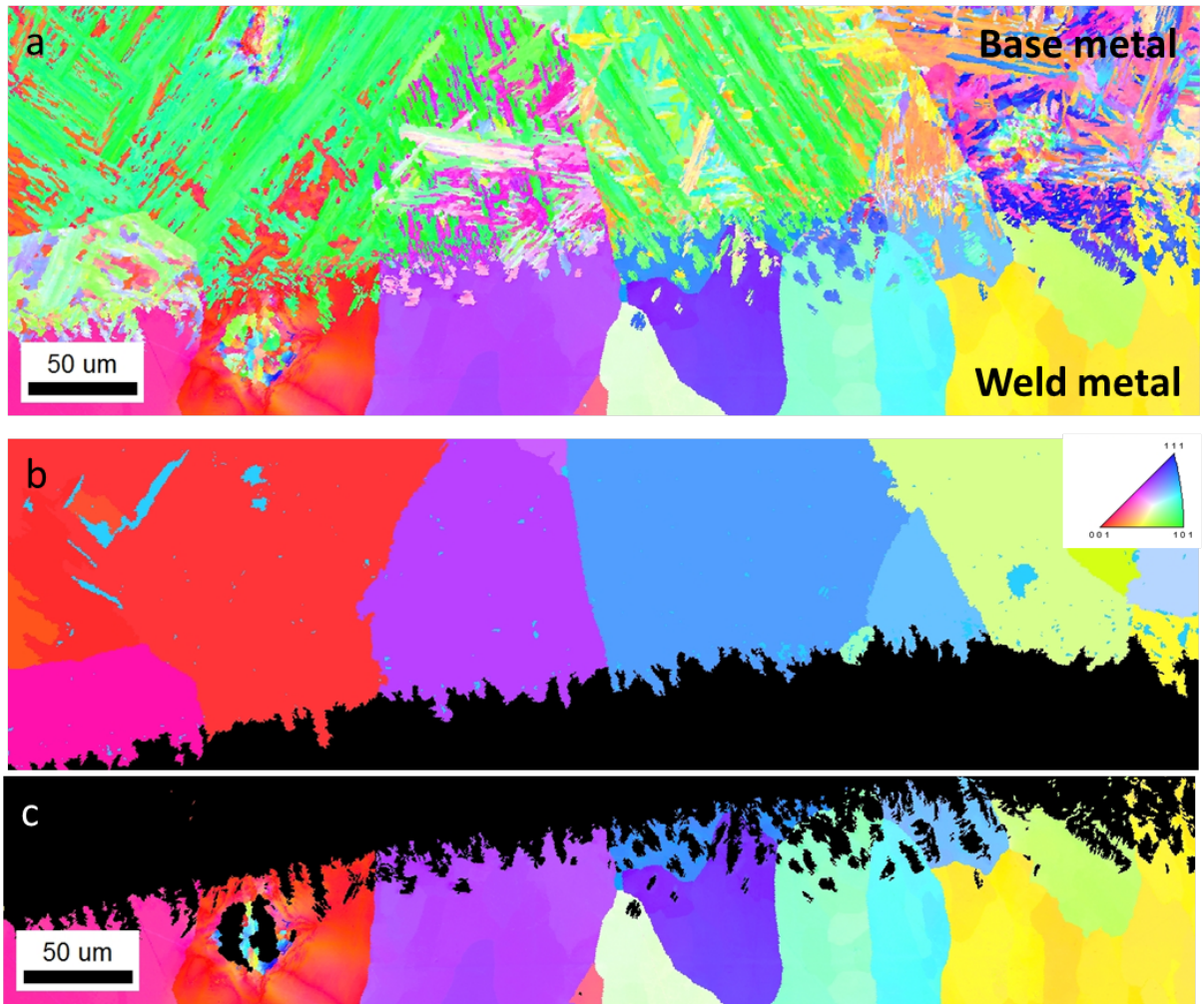

Figure 2.17: Results of the parent grains reconstruction with ARPGE software in a region where the martensitic layer at the interface was thin ($\approx 5\mu$m, as in Fig. 2.15). a- Initial EBSD map around the interface. b- Crystallographic orientations of the former austenitic grains on the base metal side, calculated by ARPGE. c- Crystallographic orientations of the austenitic grains on the weld metal side, measured by EBSD.

2.4 Discussion

2.4.1 Solute transport in the liquid boundary layer

The chemical gradients observed over 70 μm from the fusion line into the weld have been attributed to insufficient mixing of the liquid and the existence of a boundary layer upon contact with the solid base metal. As the main force acting in the weld pool is electromagnetic [66], an order of magnitude for the maximal fluid velocity can be obtained by $U = \sqrt{jBL/\rho}$. All the parameters needed for the calculation are defined and evaluated in Table 2.3; more details can be found in Appendix A. It leads to a value between 47 and 81 mm/s for U which is a realistic order of magnitude by comparison with the results of CFD calculations for different arc welding techniques in the absence of surface tension driven flow [67, 68]. Solute transport in the liquid pool is governed by equation 2.2 which includes both diffusion and convection:

$$\frac{\partial C}{\partial t} = D\nabla^2 C - \overrightarrow{U}.\overrightarrow{\nabla C} \tag{2.2}$$

where C is the solute content and U the velocity of the fluid. If we consider the permanent regime for solute transport ($\frac{\partial C}{\partial t} = 0$), the diffusive boundary layer ($\delta_c = (DL\delta_v/U)^{1/3}$ with $\delta_v = \sqrt{\mu L/\rho U}$ being the hydrodynamic boundary layer [69]) can be estimated. In our case a value between 64 and 84 μm is found (depending on the characteristic length chosen for the weld pool), which is in good agreement with the width of the zone with compositional gradients on the WDS profile.

Table 2.3: Parameters used for the estimation of the size of the boundary layer.

I (A)	Intensity	750
ρ **(kg/m^3)**	Liquid steel density	6350 [70]
j (A/m^2)	Current density	2 x 10^5
B (T)	Magnetic field	3.5 x 10^{-3}
L (mm)	Characteristic length of the weld pool	20-60
μ **(Pa.s)**	Dynamic viscosity of liquid steel	2.5 x 10^{-3} [70]
D (m^2/s)	Interdiffusion coefficient in the liquid	1.5 x 10^{-9}

According to our knowledge, the process of surfacing a metal sheet by Submerged Arc Welding with a strip electrode has been the subject for a multi-physics modeling only once[3] [66]. Such a model includes both heat conduction and convection by taking into account the heat production from the arc plasma and its dissipation through the flux and the liquid metal, together with the different forces acting on the fluid (buoyancy, electro-magnetic forces, arc pressure).

[3]This lack of information has to be related with the difficulty to observe and monitor velocity and temperature in the weld pool as it is covered by the granular flux.

2.4.2 Plane front solidification

The solidification of the weld pool begins from the part of the solid base metal which has not been molten during welding. Thus the velocity of the solid/liquid interface is equal to zero at the bottom of the molten bath and then increases when the solidification front moves away from the base metal. The evolution of the solidification velocity V with the distance from the fusion line can be determined by simple geometrical considerations on the longitudinal cut of Figure 2.18 which corresponds to the location of the WDS profile of Figure 2.11. It illustrates a fusion line configuration which is believed to be representative of the generic shape of the molten bath. As shown by Equation 2.3, the solidification rate V for a point M with the coordinates (X,Y) is found by projection of the velocity of the electrode $\overrightarrow{V_b}$ on the direction perpendicular to the solidification front at M:

$$V = V_b \cos(\theta) = \frac{V_b Z'(X_M)}{\sqrt{1 + Z'(X_M)^2}} \tag{2.3}$$

with $Z'(X_M)$ being the derivative of the coordinate Z with respect to the coordinate X.

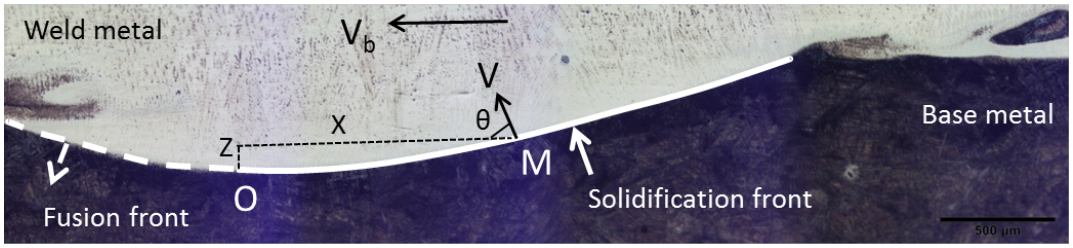

Figure 2.18: Optical micrograph of a longitudinal section in a single-layer weld.

At low velocities, the solidification front is planar with solute rejection occurring in the liquid in front of the interface. In a homogeneous system, the plane front solidification can be divided into two parts: first, a transient regime during which the solute content in the solid increases and then a steady-state regime characterized by solidification at the nominal composition [71, 72]. Beginning at the fusion line on the WDS profile of Figure 2.11 and moving towards the weld metal, one observes first an increasing part and then a plateau, which could be attributed to the transient and steady-state regimes of the plane front solidification respectively. Nevertheless, solidification occurs in the present case in a non-homogeneous liquid due to the partially mixed zone, preventing from a clear conclusion on the location of this first transition.

Then, solidification velocity increases even more and the solid/liquid interface changes its morphology to allow for sufficient solute exchange. It corresponds to the transition from plane front to cells [73, 44]. In order to determine its location in the weld, the constitutional undercooling criterion for a ternary alloy (Fe-Cr-Ni) was applied [74]:

$$V \geq V_c = G[\frac{D_{11}k_1}{m_1 C_1^{\infty}(k_1 - 1)} + \frac{D_{22}k_2}{m_2 C_2^{\infty}(k_2 - 1)}] \tag{2.4}$$

The meanings and the values for the parameters used for the calculation are summarized in Table 2.4; they have been extracted from TCFE6 and MOB2 databases [54] for the Cr and Ni contents

of the composition plateau. The critical thermal gradient and solidification velocity were estimated by measuring the cells spacing ($\lambda_1 = 9$ μm) and combining the empirical formula determined on type 310 stainless steel: $\lambda_1 = 80(GV)^{-0.33}$ [62] with Equation 2.4. The critical velocity V_C for plane front destabilization is found to be 180 μm/s with $G = 4 \times 10^6 K/m$ and is reached at about 30 μm from the fusion line as obtained from Equation 2.3. This distance is of the same order of magnitude as the end of the plateau observed on the WDS profile. It is of particular interest to notice that the calculated distance for the end of the plane front solidification is smaller than the region with chemical gradients on the WDS profile. Contrary to what was postulated by Ornath et al. [23], the transition zone includes the domain with planar solidification but cannot be explained by segregations during planar solidification only.

Table 2.4: Thermodynamic and kinetic parameters used for the application of the constitutional undercooling criterion in the case of an austenitic solidification of a ternary Fe-Cr-Ni alloy (1=Cr, 2=Ni). The Ni and Cr concentrations are those measured by WDS (Fig. 2.11) on the intermediate plateau between 15 and 30 μm from the fusion line.

Inter-diffusion coefficient of Cr in the liquid $-D_{11}-$	$1.5 \times 10^{-9} m^2/s$
Inter-diffusion coefficient of Ni in the liquid $-D_{22}-$	$1.5 \times 10^{-9} m^2/s$
Nominal composition in Cr $-C_1^\infty-$	6.1 wt.%
Nominal composition in Ni $-C_2^\infty-$	3.3 wt.%
Liquidus slope for Cr $-m_1-$	-300K/wt.%
Liquidus slope for Ni $-m_2-$	-155K/wt.%
Liquidus temperature $-T_L-$	1780K
Mass partition coefficient of Cr $-k_1-$	0.87
Mass partition coefficient of Ni $-k_2-$	0.93

2.4.3 Origin of the purely austenitic zone

From the fusion line, the first solidification mode encountered is austenitic. The phases expected to form at high temperature were predicted by equilibrium thermodynamic calculations for both the compositions of the base metal and the purely austenitic zone in the weld metal. The input data in terms of local composition measured by WDS as well as the results in terms of volume fractions of phases as a function of the temperature are presented in Figure 2.19. On the one hand, the primary solidification phase in the austenitic zone should be δ-ferrite (Fig. 2.19-a), whereas the measurement of the microsegregations across the cells have proven a primary austenitic solidification. On the other hand, the fusion of the base metal should proceed in three steps with δ-ferrite being the last phase to melt (Fig. 2.19-b). The melting sequence predicted by thermodynamics is:

- $\gamma \rightarrow Liquid$
- $\gamma \rightarrow Liquid + \delta$ (peritectic reaction)
- $\delta \rightarrow Liquid$

which is identified by the dotted arrow on the isoplethal section of the phase diagram of Figure 2.19-d. It is important to notice that the δ-phase exists only in presence of the liquid and over a narrow range of temperature (about 20°C).

This fusion sequence was confirmed at low heating rate by differential scanning calorimetry measurements (Figure 2.20) which show a two step melting with a first peak corresponding to the decomposition of the austenite in ferrite and liquid, and a second one to the melting of the δ-phase. The temperatures determined by DSC are really close to the ones calculated with ThermoCalc® and TCFE6: 1514°C versus 1509°C for the calculated liquidus, 1470°C versus 1467°C for the calculated solidus and 1492°C versus 1486°C for the appearance of δ upon heating. Of course the heating rate was rather low (2°C/min) to achieve solid-liquid transformations near equilibrium, which is far from the conditions met during welding. The continuity of the grain boundaries across the fusion line and the perfect match for the orientations of the austenitic grains on both sides of the interface can have two origins: either an epitaxial growth of the weld metal on an austenitic substrate during solidification or a phase boundary migration during the subsequent $\delta \rightarrow \gamma$ solid-state phase transformation, as proposed by Nelson and al [49]. Taken into account that the solidification of the weld near the interface has been identified as austenitic from the microsegregation profiles (Figure 2.14-a), this led to the conclusion that the base metal was austenitic when solidification of the liquid weld took place in contact with it. This suggests that the high heating rates encountered during the welding process did not allow the nucleation of the δ-phase and lead to a metastable fusion of the base metal in a single step: $\gamma \rightarrow Liq$ (Fig. 2.19-c). In this configuration only austenitic grains would be directly in contact with the molten liquid, which makes easier their growth by epitaxy upon cooling after melting. A second case of non-equilibrium melting is also possible for a temperature above T_0 [4] (= 1491.51°C for γ and liquid, calculated with ThermoCalc® [53]) and a high heating rate [75]. The calculated To-temperature (marked by a red solid line in Figure 2.19-d) is close to the one measured by DSC (1492°C) for the appearance of δ. This supports the possibility of a metastable melting without partitioning of the austenitic base metal. Either of these two possibilities (melting of the substrate with or without partitioning) can explain the presence of the purely austenitic zone adjacent to the fusion line. Considering a gradient of 4×10^6 K/m in the liquid pool and the metastable extension of the γ liquidus (green dotted line in Fig. 2.19-d), a mushy zone of 10 μm is expected. However it was never observed, which is in favor of a metastable melting without partitioning at T_0.

[4] T_0 is the temperature at which the Gibbs free energy of the liquid and the solid γ are equal.

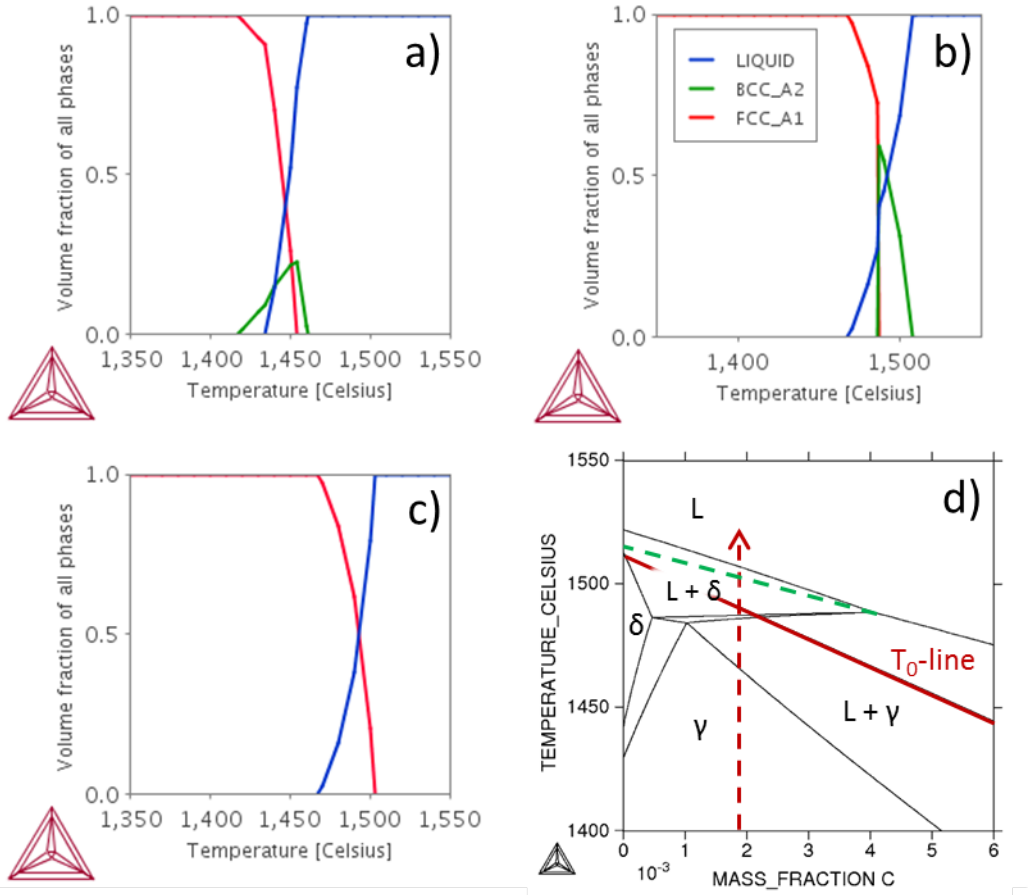

Figure 2.19: Phase equilibria at high temperature calculated with ThermoCalc® and the TCFE6 database a- for the fuly austenitic zone (w(C)=0.08%, w(Cr)=14%, w(Mn)=1.2%, w(Mo)=0.24%, w(N)=0.027%, w(Ni)=7.8%, w(Si)=0.59%) b,c- for the low-alloy steel substrate (w(C)=0.18%, w(Cr)=0.2%, w(Mn)=1.4%, w(Mo)=0.3%, w(N)=0.009%, w(Ni)=0.7%, w(Si)=0.4%), case b being the full equilibrium and case c the metastable one when the BCC phase is suppressed. d- Isoplethal section of the phase diagram for 18MND5, the composition of interest being identified by an arrow, T_0 temperature by a red solid line and the extension of the γ liquidus by a green dotted line.

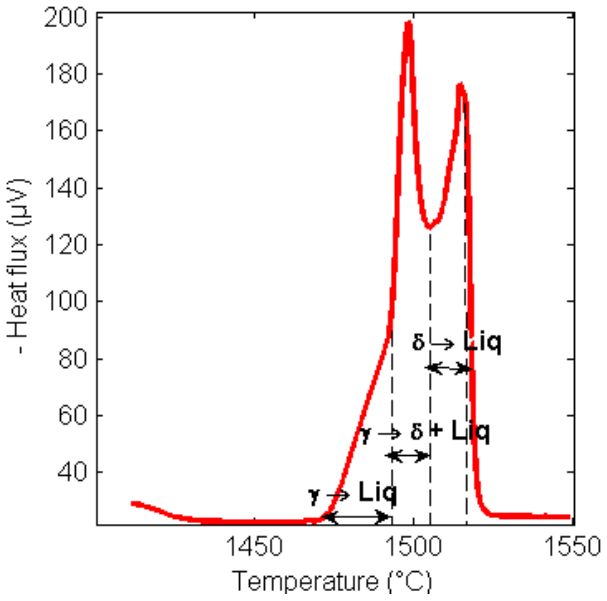

Figure 2.20: DSC measurements for the low-alloy steel base material (heating rate = 2°C/min)

2.4.4 Formation of ferrite in the inter-cellular space

In between the purely austenitic zone (without any δ-ferrite) and the two-phase region (where δ lays in the center of the dendrites), an intermediate area has been observed where ferrite is present in the inter-cellular spaces. It means that it has formed at the end of solidification, from the last liquid remaining in between the austenitic cells. The location of this transition from the A-mode to the AF-mode can be forecast by mean of a two-step modified Scheil-Gulliver calculation. Starting from the destabilization of the plane front (at 30 μm from the fusion line), solidification according to Scheil hypotheses was simulated for each local composition of the plot of Figure 2.11. The contents in Mo, Mn and Si are not shown but were also measured by WDS, whereas C and N were estimated by dilution calculations. In the first application of the modified Scheil-Gulliver model, only the FCC phase and the liquid were allowed to form, the ferritic phase being rejected from the calculations to reproduce the growth of austenitic cells. Interrupting the calculation after 95% of the liquid has solidified allowed extracting the composition of the 5% remaining liquid[5] to serve as initial condition in the second modified Scheil calculation. This one was conducted without any constraint on the phases allowed to form in order to simulate the free solidification of the last liquid in between the austenitic cells. Depending on the composition of the 5% remaining liquid, it can lead either to a primary-ferrite or a primary-austenite solidification. For the first 20 micrometers from the beginning of the cellular growth, primary austenite solidification was found, which means that no ferrite formed in the inter-cellular space. However the progressive increase in ferrite-stabilizing elements in the last droplets of liquid is responsible for the appearance of ferrite in between the cells and then the change in primary phase of solidification. Two examples of the method employed

[5]Calculations have also been performed for 2 and 1% remaining liquid and the results in terms of phase selection are unchanged.

here are displayed in Figure 2.21, one before the transition (A mode in Figure 2.21-a,b) and the other after (AF mode in Figure 2.21-c,d). Thus the transition from A to AF mode of solidification was found to occur at about 50 μm from the fusion line, which is of the same order of magnitude as the microstructural observations (Figure 2.10-a). This transition has been predicted by means of thermodynamical arguments only, based on the evolution of the local composition. In agreement with the local equilibrium condition, ferrite has been considered to appear as soon as its formation allowed reducing the Gibbs free energy of the system, by comparison with the situation without any ferrite.

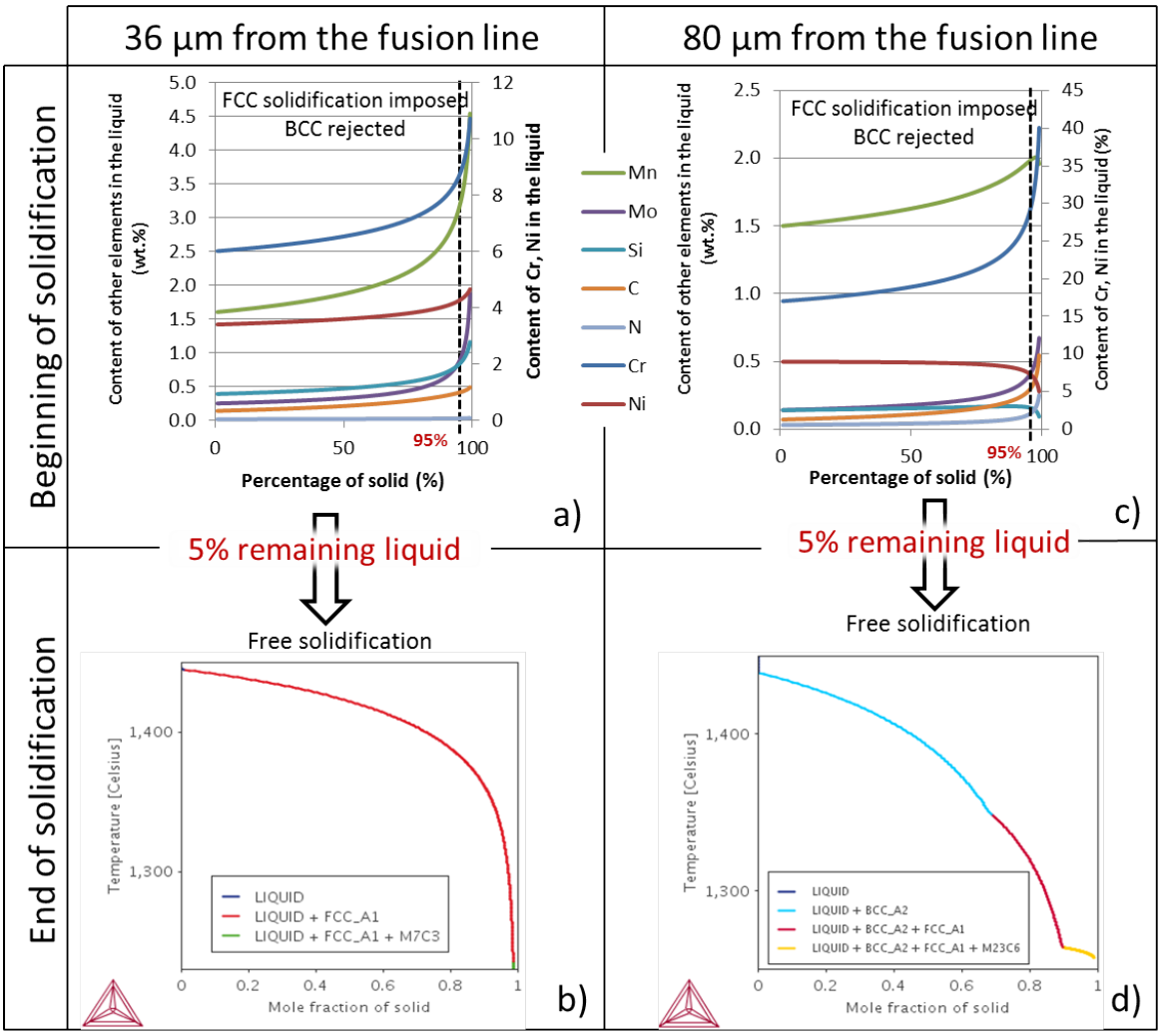

Figure 2.21: Results of solidification calculations using a modified Scheil-Gulliver model: a- Solidification with BCC rejected for the local compositions at 36 μm from the fusion line: w(Cr)=6% ; w(Ni)=3.4% ; w(Mn)=1.6% ; w(Mo)=0.25% ; w(Si)=0.39% ; w(C)=0.14% ; w(N)=0.016%. b- Free Solidification for the 5% remaining liquid at 36 μm from the fusion line. c- Solidification with BCC rejected for the local compositions at 80 μm from the fusion line: w(Cr)=17% ; w(Ni)=9% ; w(Mn)=1.5% ; w(Mo)=0.14% ; w(Si)=0.14% ; w(C)=0.07% ; w(N)=0.03%. d- Free solidification for the 5% remaining liquid at 80 μm from the fusion line.

2.4.5 Growth competition between ferrite and austenite

Once ferrite has nucleated in the inter-cellular spaces, a growth competition takes place and there is a need to predict which phase, ferrite or austenite, will grow at the expense of the other. We showed that the conditions present in our system, both in terms of compositions and solidification velocity, do not allow metastable austenite to continue growing and that ferrite will finally prevail. For that we made use of a dendrite growth model, first developed by Kurz et al. [3], extended to multi-component system by Bobadilla et al. [4] and applied to conditions of high solidification velocities by Rappaz et al [5]. The model is based on the calculation of the undercooling at the tip of a growing dendrite, the phase with the higher tip temperature having the higher growth rate. This dominating phase will preceed the solidification front of the other one. As shown in Equation 2.5, three terms have been included in the calculation of cell tip undercooling: the effects of solute species, thermal gradient and capillarity:

$$T_p = T_L + \sum_i m_i(C_i^* - C_i^0) - \frac{GD}{V} - \frac{2\Gamma}{R} \tag{2.5}$$

where T_L is the liquidus temperature, m_i the liquidus slope for element i, C_i^* and C_i^0 the liquid and nominal composition for element i respectively, G the thermal gradient, D the liquid interdiffusion coefficient, V the solidification velocity, Γ the Gibbs-Thomson parameter and R the tip radius. Estimating the solutal contribution requires the knowledge of the concentration fields around the growing cell. As displayed in Equation 2.6, the tip was approximated by a paraboloïd and Ivantsov solution [76] was applied to obtain the amount of solute build-up at the solid-liquid interface:

$$\begin{cases} C_i^* = \frac{C_i^0}{1-(1-k)I_v(P)} \\ \\ \text{with } P = \frac{VR}{2D} \text{ and } I_v(P) = Pexp(P)\int_P^\infty \frac{exp(-u)}{u}du \end{cases} \tag{2.6}$$

P being the solutal Peclet number. According to the marginal stability criterion of Mullins and Sekerka [77] which was extended to multicomponent systems by Coates et al. [74], the radius of curvature of the growing tip was taken equal to the shortest wavelength which makes the plan front unstable. The value of 8×10^5 K/m for the thermal gradient (G) was calculated from the growth velocity (V) and the cooling rate (ϵ) and is of the same order of magnitude as the data from the literature for welding in the absence of surface tension driven flow [67, 78]. The cooling rate was estimated to be around 160 K/s by measuring the secondary dendrite arm spacing at the cells to dendrites transition ($\lambda_2 = 6.5$ μm, $V = 200$ μm/s) very close to the appearance of ferrite. The following empirical formula was used: $\lambda_2 = 25(\epsilon)^{-0.28} = 25(GV)^{-0.28}$ [62]. The calculation was performed for a quaternary system Fe-Ni-Cr-C whose compositions are those encountered in the weld at the location where ferrite is found in the inter-cellular space. The parameters used for the tip growth calculation are listed in Table 2.5, the thermodynamic ones being extracted from the TCFE6 database and the kinetic ones from the MOB2 database. Such a model allowed us to obtain the temperature at the tip of both phases δ and γ as a function of the solidification velocity, as shown in Figure 2.22. A vertical line has been drawn to mark the value of the welding speed,

which represents the maximum solidification velocity that can be reached in the weld pool. For the compositions and the velocity encountered in the present process, the ferritic tip will always be warmer than the austenitic one. This confirms that, once δ has nucleated, the conditions in the weld pool will favour its growth at the expense of γ and that a transition from AF mode to FA mode will take place. This conclusion is in agreement with the optical micrograph of Figure 2.23 where one can notice a continuity between the ferrite nucleated in the inter-cellular location and the one in the intra-dendritic position. It is the proof that inter-cellular ferrite serves as nucleus for the intra-dendritic one, which then becomes the primary phase to solidify.

Table 2.5: Physical, thermodynamic and kinetic parameters used for the calculation of the tip temperature for $w(Cr) = 15.6$ wt.% ; $w(Ni) = 8.3$ wt.% and $w(C) = 0.05$ wt.%

	Ferrite ($\Phi = \delta$)	**Austenite** ($\Phi = \gamma$)
Liquidus temperature T_L^Φ **(K)**	1745	1736
Liquidus slope for Cr m_{Cr}^Φ **(K)**	-0.75	-4.18
Liquidus slope for Ni m_{Ni}^Φ **(K)**	-5.8	-0.78
Liquidus slope for C m_C^Φ **(K)**	-108.5	-58.5
Partition coefficient of Cr $k_{Cr}^{\Phi/L}$	1	0.85
Partition coefficient of Ni $k_{Ni}^{\Phi/L}$	0.78	1
Partition coefficient of C $k_C^{\Phi/L}$	0.12	0.34
Diffusion coefficient in the liquid D (cm^2/s)	1.5×10^{-5}	1.5×10^{-5}
Surface tension (mJ/m^2)	260 [4]	358 [4]
Molar volume at $\mathbf{T_L^\Phi}$ (cm^3/mol)	7.52 [4]	9.03 [4]
Molar entropy of fusion $(J/mol/K)$	5.79	6.63
Thermal conductivity $(J/s/m/K)$	30 [4]	30 [4]

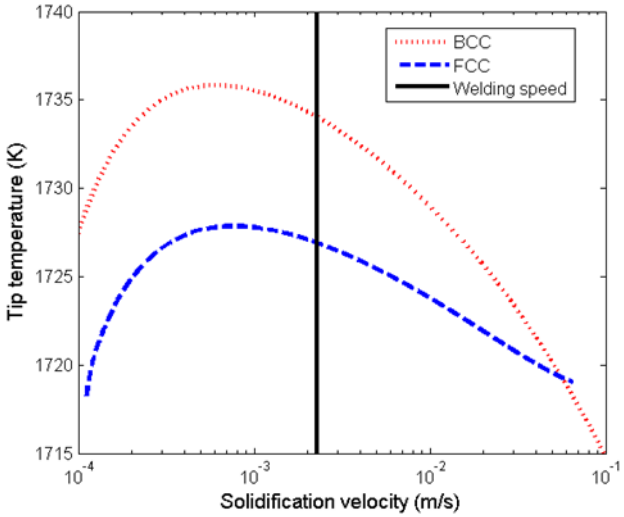

Figure 2.22: Results of the growth competition in terms of tip temperature as a function of solidification velocity

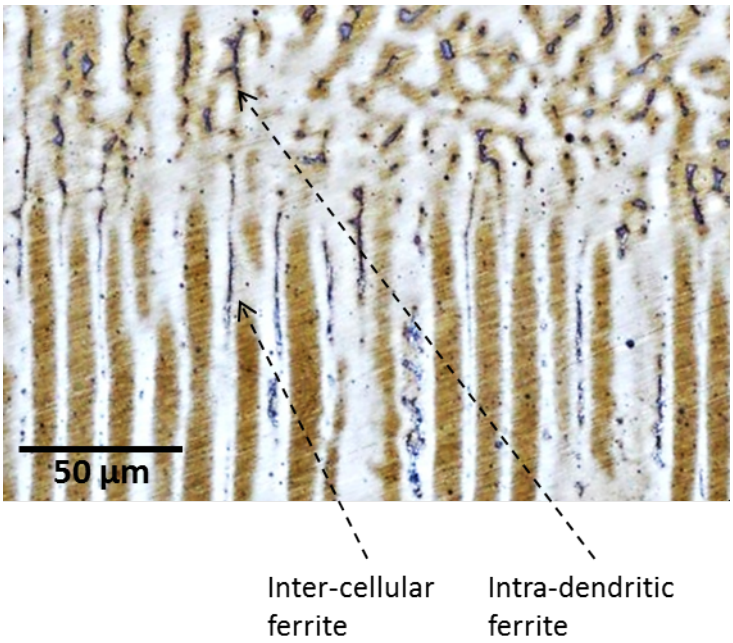

Figure 2.23: Optical micrograph showing the continuity between the inter-cellular ferrite and the intra-dendritic one (transition AF $\rightarrow$ FA)

2.5 Summary and conclusions

This part has been devoted to the study of the as-welded state of a mono-layer specimen, which corresponds to the deposition of the first 309L layer on the 18MND5 base metal. It is of primary importance as it will serve as initial state for the deposition of the subsequent layers and the following post-welding heat-treatment.

The large variety of microstructures detected over a limited distance on either side of the fusion line (around 1 mm) is the main reason for the phase transformations under long-range diffusion that take place during the PWHT (see Part II) and the resulting heterogeneities in local mechanical behavior (see Part III).

Based on the WDS profiles measured across the interface in the dissimilar steel weld between the 18MND5 low-alloy ferritic steel and the 309L austenitic stainless steel, solidification mechanisms and microstructures evolution have been investigated:

1. Between the solid base metal that has not melted and the liquid weld metal that has been homogenized by convection, **an intermediate transition layer** has been observed ($\approx$ 70 μm wide). It is the place for **three types of evolutions**, that is in terms of composition, solid-liquid interface morphology and primary solidification mode. Chemical gradients in this zone first originate from an **insufficient mixing in the liquid boundary layer** at the bottom of the weld pool.

2. Then, **plane front solidification** with successively transient and permanent regimes causes solute rejection ahead of the solid-liquid interface and is responsible for modifying the composition profile. In terms of phases formation, the predominant role of the base metal as solid substrate has been highlighted. The **perfect epitaxy** between the former austenitic grains in the base metal and the new ones in the weld suggests a **metastable fusion of the low-alloy steel.**

3. The stable solidification mode predicted by thermodynamic calculations (FA mode) is recovered after **two main transitions:**

   - first, the formation of ferrite in the inter-cellular space **(A $\rightarrow$ AF transition)**
   - and then, the growth competition between ferrite and austenite **(AF $\rightarrow$ FA transition)**

   Thanks to simple thermodynamic and kinetic considerations, the locations for these transitions have been predicted and agree well with the microstructural observations.

From the base metal to the austenitic weld metal through the intermediate martensitic band, the microstructures resulting from the welding of dissimilar steels 18MND5/309L have been described and understood in this section. The complex phase transitions that result from the metastable melting of the base metal are summarized in Figure 2.24.

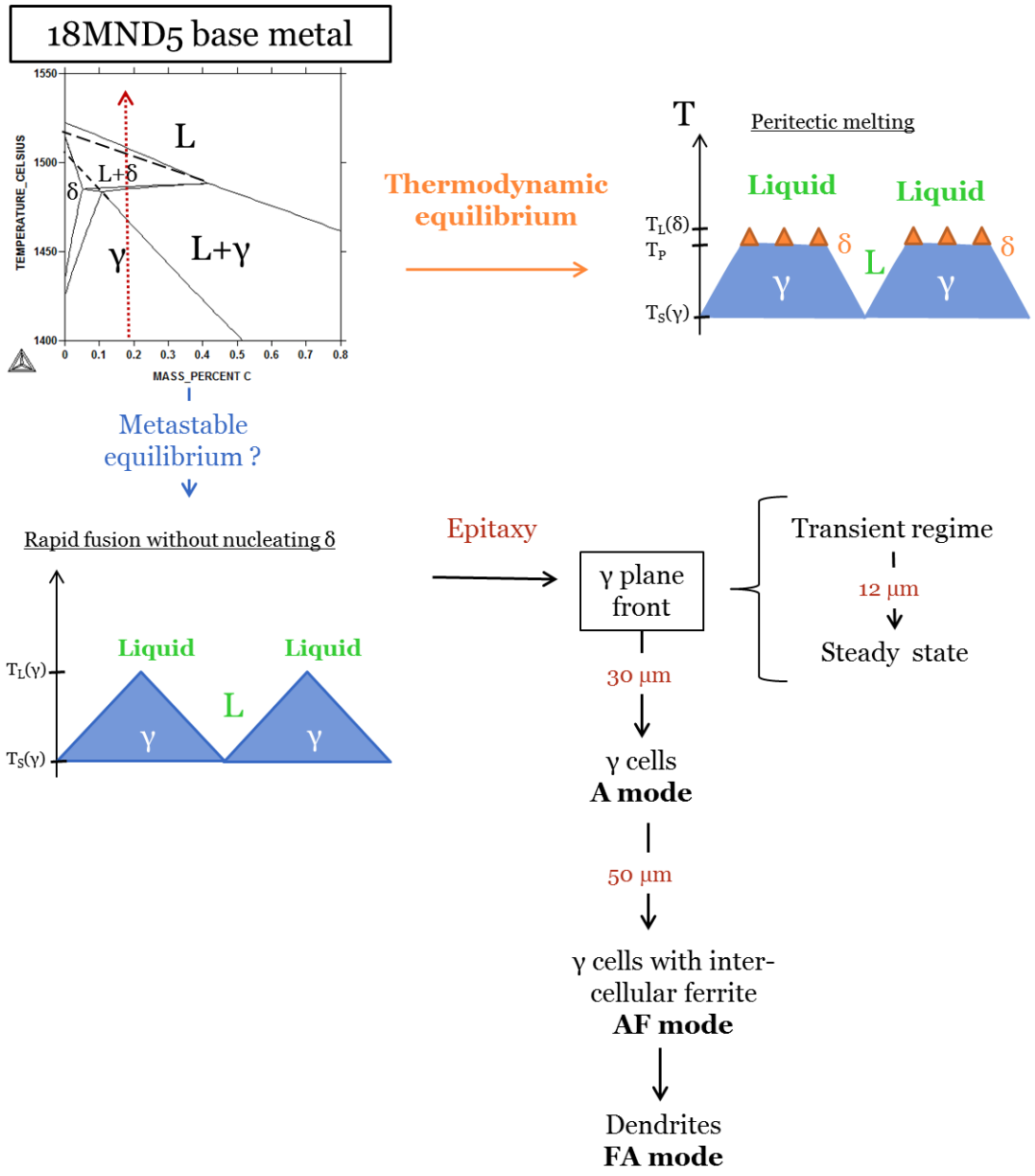

Figure 2.24: Summary of the phase transitions occurring during the solidification of the weld metal and resulting from the metastable melting of the base metal.

Part II

Carbon diffusion and precipitation during post-welding heat-treatment

Chapter 3

Metallurgical characterization of coupled carbon diffusion and precipitation in dissimilar steel welds

3.1 Introduction

Dissimilar metal welds (DMW) provide a paradigm for coupled long-range diffusion and local precipitation occurring during post-welding heat-treatment (PWHT) in chemically heterogeneous materials. In addition to their industrial importance, they provide an interesting challenge to understand microstructure evolution kinetics. The most widely encountered DMWs are those between two ferritic steels with different chromium contents [79, 80] and those between a low-alloy ferritic steel and an austenitic stainless steel [81, 82]. Even in the case of similar carbon content in both steels, carbon is found to diffuse from the low-alloyed to the high-alloyed side. A case of uphill diffusion is even reported [83] as in the well-known Darken's experiment [84]. In all cases, the driving force for carbon diffusion is the carbon activity gradient between both steels, which cannot be described by carbon concentration only. This diffusion often results in significant microstructural changes around the fusion line: carbides dissolve on the low-alloy side and create a soft decarburized zone whereas the high-alloy part is hardened by carburization and carbides precipitation.

Several characterization tools can be combined to investigate carbon migration and the resulting local microstructural transformations. Optical Microscopy (OM) and Scanning Electron Microscopy (SEM) along with microhardness allow the characterization of the size of the affected regions for different alloys combinations [85, 86]. Electron Probe Micro-Analysis (EPMA) and SIMS provide the carbon profile across the fusion line [87, 88, 89], and TEM coupled with Energy Dispersive Spectrometry (EDS) gives access to the precipitation sequence based on crystallography and chemistry of the carbides [79, 90]. Chromium and molybdenum-rich carbides are generally found to precipitate on the high-alloyed side. The microstructures on both sides of the interface highly depend on the type of steels and the tempering temperature. They greatly influence the amount of carbon redistribution through the interface due to the higher diffusivity of carbon into the ferritic

matrix than in the austenite. In the case of ferritic-austenitic welds at the temperature of post-weld heat-treatment, the carbon-depleted zone always spans a greater extent than the carbon-enriched part [83, 91]. When low-alloy steel is welded using nickel-base filler metals, a reduction of size of both the carburized and decarburized regions is observed [85, 36]. This is due to the reduced diffusivity of carbon in the Ni-matrix.

As carbon is a crucial element in steel metallurgy and its distribution into an alloy has important consequences on the mechanical properties, significant efforts have been devoted to the challenge of its quantification in the recent years. Even if they remain delicate (especially because of the risk of contamination) several methods such as Electron Energy Loss Spectroscopy in a TEM [92, 93], SIMS nano-analysis [94], Field Emission Electron Probe Microanalysis [95, 96] and Atom Probe Tomography (APT) [97, 98] have been successful in measuring carbon at a local scale (in matrix phases as well as in precipitates). In the case of perfectly flat interfaces as in coatings and diffusion bondings, quantitative carbon profiles are often obtained by Glow Discharge Optical Spectroscopy (GDOS) [99, 100]. Except for APT, carbon quantification is based on the use of standards with controlled microstructure and known carbon content.

The goal of this chapter is to investigate carbon diffusion occurring during post-weld heat-treatment of the welds produced by Submerged Arc Welding and exhibiting the specific three-phase configuration described in Part I: low-alloy bainitic base metal / martensitic layer / high-alloy austenitic weld metal. The main objectives of this experimental work can be summarized as follows:

1. Accurately **measure the carbon content** on both sides of the fusion line in the as-welded and heat-treated conditions.

2. Quantitatively investigate the **microstructural changes** occurring in the same region during PWHT, and especially characterize the **precipitates** in terms of crystallography, chemistry, morphology, volume fraction and size distribution.

3. Evaluate carbon and other main **elements** (Fe, Cr, Ni, Mn, Mo, Si) **distribution between matrix and precipitates** within each region of the weld.

4. Understand how the presence of a **martensitic layer** influences the extent of carbon diffusion.

3.2 Experimental procedure

3.2.1 Carbon content measurements

As surface contamination is the major problem in carbon concentration measurements, a particular attention was paid to the samples preparation: they were mechanically polished just before their introduction into the analysis chamber using alumina suspension for the final stage followed by ultrasonic cleaning in distilled water.

Wavelength Dispersive Spectrometry (WDS) measurements were performed with a Ni/C multilayer monochromator (2d=9.5 nm) on a CAMECA SX50 electron microprobe equipped with the SAMx software. The following conditions were used: accelerating voltage of 16 kV, counting time of 40 s and beam current of 900 nA which allowed sufficient counting statistics in the case of low carbon levels ($<$ 0.02 wt.%) and a measurement every 4 μm without any contamination. A liquid nitrogen cooling trap together with a low-pressure oxygen jet onto the specimen allowed reducing the carbon contamination arising from the cracking of residual organic molecules by the electron beam. Quantitative analysis required the use of the calibration curve method described in ISO standard 16592 [101] which postulates a linear relationship between the intensity of the C Kα peak and the carbon content in the probed volume. The samples used as references were a piece of electrolytic iron and various Fe-C solid solutions obtained by quenching from the high temperature austenitic domain [102] with carbon contents varying from 6.5×10^{-4} (measured by combustion) to 0.99 wt.%. An example of calibration curve is provided in Figure 3.1-a. One should notice that the straight line does not pass through the origin, which denotes the presence of residual carbon contamination inside the chamber.

Secondary ion mass spectrometry (SIMS) measurements were carried out on the same samples. This technique has the advantage to be less sensitive to surface contamination since the samples can be cleaned (sputter cleaning) inside the chamber before analysis. SIMS experiments were carried out on a modified CAMECA IMS-6f instrument using a Cs^+ primary bombardment (impact energy of 5.5 keV) to enhance C^- emission. The pressure in the chamber was around 10^{-8} mbar during the whole experiment. In the image mode, the focused Cs^+ primary ion beam (diameter smaller than 1 μm, intensity of 200 pA) was scanned across an area of (400×400) μm^2 to acquire images with a size of 256×256 pixels. The mass resolution $\Delta M/M$ was 300 and the time necessary to acquire one image around 100 s. This approach was only qualitative and allowed obtaining images of the carbon distribution across the weld. For quantitative measurements of carbon, in-depth profiles were performed. The focused Cs^+ beam (current of 7 nA) was scanned across a zone of (50×50) μm^2 and the C^- secondary ions were collected from a circular area (diameter of 8 μm) with one measurement every 40 μm. With the same reference samples as those used for WDS, a calibration line was established (Fig. 3.1-b) that allowed quantitative measurements of the carbon concentration across the weld interface.

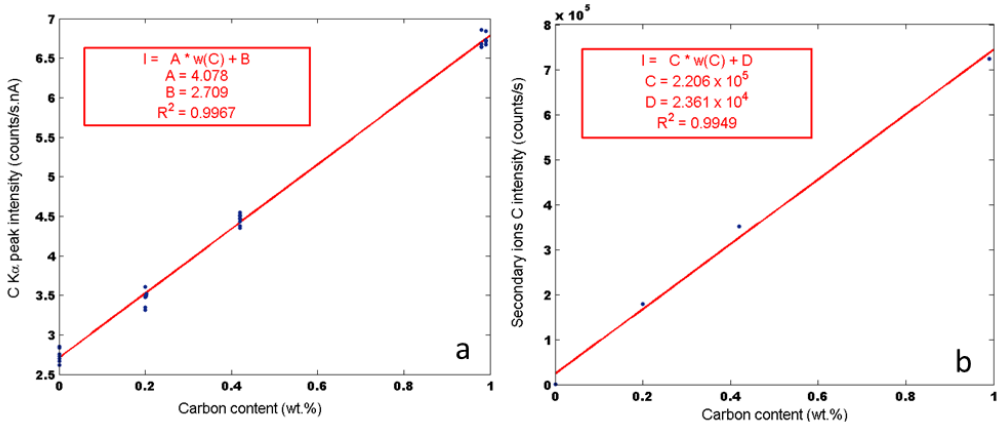

Figure 3.1: Calibration curves for the quantification of the carbon content by a- WDS and b- SIMS.

3.2.2 Nanoindentation

Nanoindentation was chosen as an indirect method to probe the local carbon content in the different regions around the interface. The continuous stiffness method [103, 104] (superimposed oscillation of 2 nm at 45 Hz) allowed monitoring the elastic modulus and the hardness as a function of the indentation contact depth. More details about this technique are provided in Section 5.3.1.2. In fact carbon enrichment leads to an increase of the local hardness whereas carbon depletion is usually accompanied by a local softening. Using a Berkovich three-sided diamond pyramid as indenter, profiles were performed on transverse sections of the weld with a minimum distance between two consecutive locations of 4 μm (indentation depth of 200 nm). For all measurements, a steady state corresponding to a hardness plateau was reached after 150 nm of indenter penetration. Local hardness was taken as the mean value between 180 and 190 nm.

3.2.3 Precipitates identification

Specimens for TEM observations were either thin foils prepared by Focused Ion Beam (FIB) milling in predefined areas or extraction replicas. Samples for precipitates extraction were first ion-etched with a Gatan PECS (Precision Etching and Coating System) [105] and then sputter-coated with a 25 nm thick layer of carbon in the same device. The carbon film was scored with a scalpel into 1 mm squares located at the region of interest and the sample was immersed for one hour in a solution of 5% bromine in methyl alcohol. This led to the dissolution of the matrix (ferrite, tempered martensite [1] or austenite) and allowed extracting the precipitates embedded in the carbon films floating on the solution. The replicas were deposited on TEM mesh grids and examined on a FEI Tecnai F20 TEM operating at 200 kV.

The TEM was equipped with a NANOMEGAS unit (Astar model) which allowed automated orientation and phase mapping [106, 107]. Selected areas were scanned by the electron beam in

[1] In what follows, we will continue designating as martensite the intermediate layer with a lathy microstructure, even if it has been tempered during the welding of the second cladding layer and the subsequent post-weld heat-treatment.

the nano-diffraction mode with a step size of 4 nm. At each step, the diffraction pattern was recorded with an acquisition speed of 34 frames per second. A 10 μm C2 (condenser diaphragm) aperture and a camera length of 100 mm were used. Given a crystallographic structure, numerical diffraction patterns were produced for every possible set of Euler's angles within ranges limited by the symmetry of the material. Identification was then performed off-line by a template matching algorithm [108]. In addition to phase and orientation maps, the software calculates the degree of matching of a given template by the following correlation index:

$$Q(i) = \frac{\sum_{j=1}^{n} P(x_j, y_j) T_i(x_j, y_j)}{\sqrt{\sum_{j=1}^{n} P^2(x_j, y_j)} \sqrt{\sum_{j=1}^{n} T_i^2(x_j, y_j)}} \tag{3.1}$$

where the experimental pattern is represented by the intensity function P(x,y) while every template is given by the function $T_i(x, y)$. The summation is extended over the n non-zero dots contained in the template. The higher Q_i is, the better is the match between the experimental diffraction pattern and the template i. The degree of confidence of a given solution (that can be used either in terms of phase or orientation) is characterized by a reliability index R defined as follows:

$$R = 100(1 - \frac{Q_2}{Q_1}) \tag{3.2}$$

where Q_1 and Q_2 refer to the two highest values of Q_i for distinct solutions. If R is high (typically higher than 15), it means that there exists a match clearly better than all the others and thus the solution is safe.

3.2.4 Carbides quantification

The size (3D), morphology and distribution of the precipitates inside the martensitic layer of the post-weld heat-treated sample have been investigated by Focused Ion Beam (FIB) tomography. By means of a SEM-FIB Zeiss NVISION40 CrossBeam® with a 54° angle between the electron and ion beams, slices were cut every 10 nm with a Ga^+ beam current of 700 pA and an accelerating voltage of 30 kV. A layer of carbon with a thickness of 1.5 μm was deposited on the top of the volume of interest to reduce curtaining during milling due to microstructural heterogeneities. Fiducial marks were made by ion milling on the deposit to facilitate alignment and control of the slices thickness. A U-pattern was first milled around the region of interest to prevent shading of the signal used for imaging and minimize redeposition effects. The sample was tilted at 54° in order to mill a perfect planar surface. A secondary electrons in-lens detector operated under a tension of 5 kV was used for imaging at a working distance of 5.1 mm. The image field of 20 x 15 μm^2 with a digitalization of 2048 x 1536 pixels combined with the 10 nm step in depth allowed a voxel size of 10 nm^3. 3D reconstruction and visualization were performed by means of Fiji® and Avizo Fire 6.2® softwares. With the conditions chosen for imaging, the carbides and the martensitic laths appeared in dark and bright gray respectively (Fig. 3.16). When performing statistics on the carbides population, all particles with a volume smaller than 8000 nm^3 ($2 \times 2 \times 2 \times \ pixels^3$) were considered as noise and eliminated.

In the area where the serial sectioning was performed the martensitic layer had a thickness of 35 μm and 5 stacks of about 1 μm in thickness (100 images) were analyzed at different locations in order to capture the changes affecting the carbides population. This method could not be applied to the carbides in the austenitic matrix as their size is too small (R<20 nm): for this population the analysis was limited to BF (Bright Field) and DF (Dark Field) images acquired on a Jeol 3010-LaB_6 transmission electron microscope on thin foils prepared by FIB in planes either parallel or perpendicular to the fusion line.

3.2.5 Elements distribution

Atomic level microstructural observations were performed by atom probe tomography in order to understand how carbon and the main substitutional elements were distributed between precipitates and matrix in both the martensitic layer and the fully austenitic zone at the different stages of heat-treatment. It also allowed imaging and quantifying chemical segregations that exist around the defects (dislocations and subgrain boundaries) within the matrix. Specimens, which have to be sharp needles with a small tip diameter (around 20 nm) were prepared by Focused Ion Beam (FEI Helios dual-beam) using the lift-out technique and annular milling with a Ga^+ ion beam.

For APT measurements, the small tip is brought to a high DC voltage (5-20 kV), thus inducing a very high electrostatic field, just below the point of atoms evaporation. Under laser pulsing, few atoms are evaporated from the surface by field effect and are projected onto a high sensitivity detector which simultaneously measures the time of flight t_v of the ions and the (X,Y) position of the impact. Knowing the evolution of the electric field applied to the sample, the nature of the ion, more precisely its charge over mass ratio, can be determined by:

$$\frac{m}{n} = \frac{2eVt_v^2}{L^2} \tag{3.3}$$

where -ne is the charge of the ion, m its mass, V the electrical potential and L the distance between the tip and the detector. By progressively removing atoms from the tip and reconstructing their initial position, a 3D image of the material is obtained at the atomic scale.

APT acquisitions were performed using the LEAP 3000X HR local probe (Im2np laboratory in Marseille) with a wavelength of 532 nm. Sample evaporation was carried out at 50 K using 100 kHz laser picoseconds pulses of 0.7 nJ energy. During analysis, the evaporation rate was kept between 0.005 and 0.007 ions per pulse under a vacuum pressure of 1.4×10^{-11} Torr. Data reconstruction was done with the IVAS^{TM} software.

3.3 Results and discussion

3.3.1 Carbon profile across the fusion line

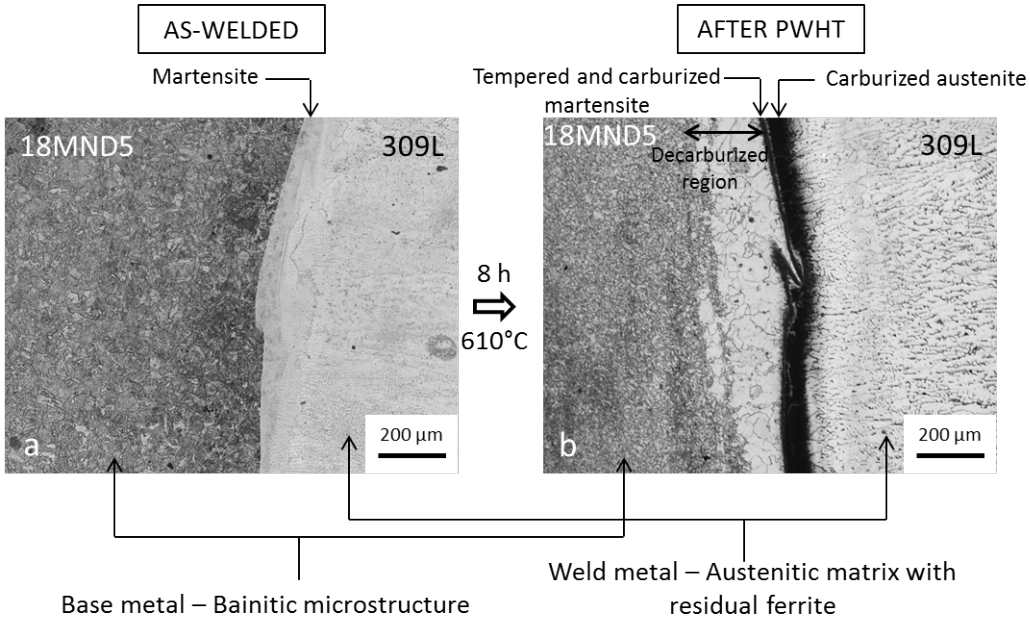

Figure 3.2: Optical micrograph of the dissimilar interface after a two-step etching : Nital (5% HNO_3 in methyl alcohol) and electro-chromic (10 g CrO_3 in H_2O, 6V, $1A/cm^2$). a- As-welded and b- post-weld heat-treated states.

The initial microstructure of the weld is recalled on Figure 3.2-a. As previously mentioned, it can be divided into 3 zones: the base metal 18MND5 with a bainitic microstructure (ferrite laths and Fe_3C carbides), then an intermediate martensitic layer whose width varies between 5 and 200 μm depending on the location along the fusion line, and finally the austenitic weld metal. As seen in Part I, the microstructure on the weld metal side in contact with the martensite is fully austenitic, residual δ-ferrite appearing only after approximately 100 μm from the fusion line. When subjected to the heat-treatment at 610°C this microstructure is dramatically modified as a result of carbon diffusion from the base metal towards the weld metal. As shown on Figure 3.2-b, decarburization of the base metal leads to the formation of a zone with large ferrite grains which spans over 200 μm. These grains have a rounded shape typical of abnormal grain growth which can be explained by the simultaneous carbides dissolution and grain boundaries migration. On the weld side, carbon diffuses to both the interfacial martensite and the purely austenitic zone (black layer of Fig. 3.2-b). The dark aspect of the carburized regions results from carbides precipitation. Whatever the width of the martensitic band (that encounters tempering during holding at 610°C), the carburization into austenite spreads over about 70 μm.

Quantitative measurements of the evolution of the carbon content were performed by both WDS and SIMS. A very good agreement between the results of these two techniques was obtained for the heat-treated sample (Fig. 3.3-a). Starting from the fusion line towards the base metal, a zone almost entirely depleted in carbon ($w(C) < 0.015$ wt.%) was characterized over a distance of 200

μm corresponding to the region were large ferrite grains are observed. Then the carbon content progressively increases to reach the nominal content of the low-alloy steel at about 500 μm from the fusion line ($w(C) = 0.20$ wt.%). On the weld metal side, two maxima of the C content are detected: one into the tempered martensite with a maximum carbon content of 1.3 wt.% and another one into the austenite with a maximum C level of 0.8 wt.%. The carburized zone width in the austenite is around 70 μm. Both carbon measurements agree well with the extent of the phase transformations observed in the heat-treated microstructure (see Figure 3.2-b). Images of the C^- intensity acquired by SIMS on a post-weld heat-treated sample are displayed on Figure 3.4. Although not quantitative they allow mapping the distribution of carbon through the weld and confirm the extent of both carburized and decarburized regions.

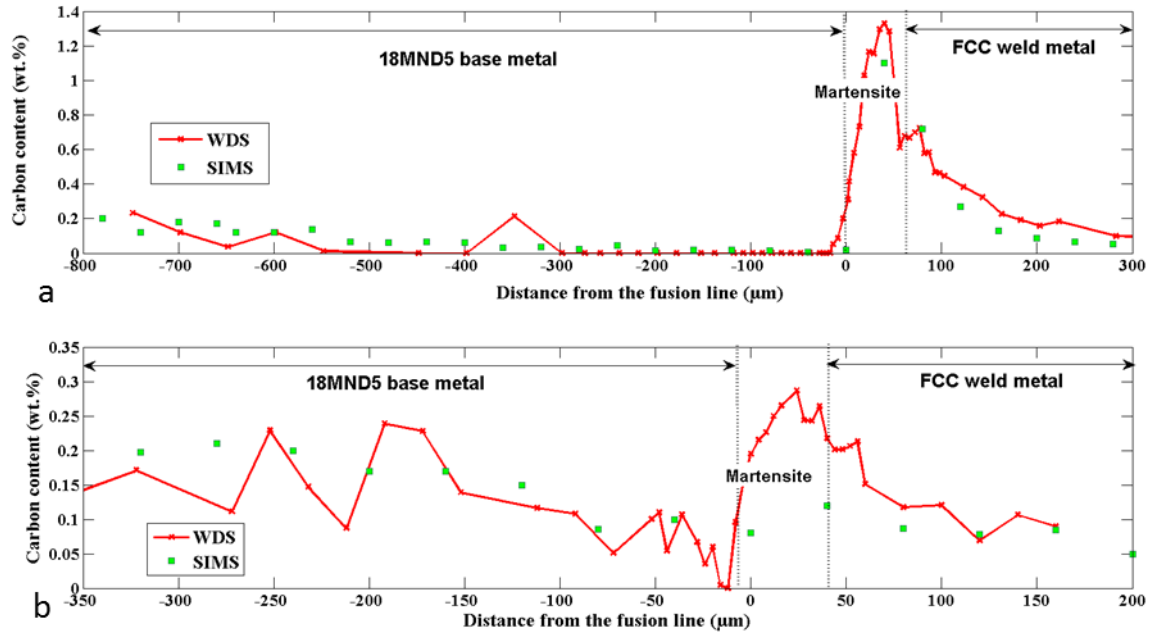

Figure 3.3: Carbon content as a function of the distance from the fusion line, measured by WDS and SIMS in a- the heat-treated state and b- the as-welded state.

The two techniques used here appear to be complementary. WDS allows a better spatial resolution that is particularly appropriate to capture variations occuring over a limited space scale, as it is the case in the as-welded condition and for the carbon enrichment of martensite and austenite in the heat-treated sample. The size of the probed volume ($<1\ \mu m^3$)[2] is also responsible for the small singularities detected in the base metal as it is sensitive to cementite precipitates (around 200 nm in size). WDS also has the advantage of allowing a simultaneous quantification of the substitutional elements, which is not the case in SIMS where Cr and Fe are better measured as positive ions. WDS allowed to confirm that no diffusion of the substitutional elements took place at 610°C, as the Cr, Ni, Mn, Mo, Si profiles were identical in the as-welded and heat-treated states. This is in agreement with the low diffusion coefficients for substitutional elements in the BCC matrix at 610°C. Considering chromium ($D_{CrCr} = 1.9 \times 10^{-24} m^2/s$ according to TCFE6 database), a mean

[2]Estimated by Monte-Carlo simulations for a 16 kV electron beam on an iron sample

diffusion distance ($X = 2\sqrt{Dt}$) of 0.47 nm is obtained after 8h at 610°C. On the other side, SIMS is able to detect very low carbon contents (such as 0.004 wt.% in the present case) thanks to its high sensitivity and strong limitation of surface contamination. It is particularly adapted for quantifying residual carbon within the decarburized layer, which is not possible by WDS as such low carbon contents do not emerge from the surface contamination. Since the quantitative approach with SIMS could only be applied in the in-depth profiling mode with steps of 40 μm, this method appeared to be well suited for variations occuring over larger distances, as it is the case for the decarburization of the base metal in the heat-treated sample. The resulting profile in this zone is quite smooth because the area of analysis (8 μm in diameter) allows measuring a global composition and is not influenced by the two-phase microstructure (ferrite + carbides) of the base metal.

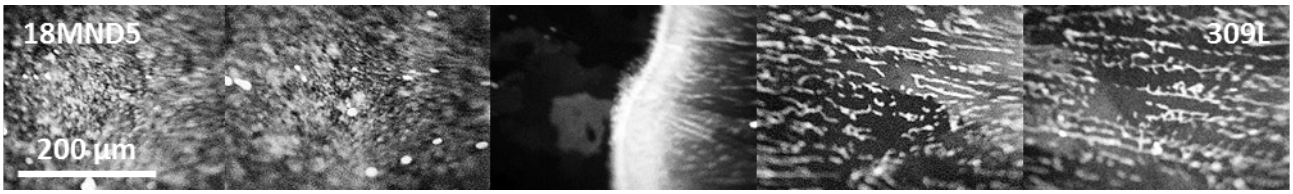

Figure 3.4: Carbon intensity maps obtained by SIMS on the heat-treated state, white areas being carbon-rich and black ones carbon-poor. The dendrites on the weld metal side appear in white since carbides form by δ-ferrite decomposition during the heat-treatment (see Section 3.3.2.3). The sputter cleaning leads to blurred edges of the images mainly on the 18MND5 side

For the as-welded sample (Fig. 3.3-b) the agreement between SIMS and WDS is not as good as that for the post-weld heat-treated one. The variations of the carbon content are expected to happen only over short distances, which makes the quantification by SIMS profiling less relevant with the analytical conditions used (average C content measured on a surface of 8 μm in diameter with a step of 40 μm). The WDS profile revealed that some carbon diffusion already occurs during the welding of the two stainless steel layers (309L over 18MND5 and then 308L above) as the carbon levels in the weld are higher than the ones expected by simple dilution. Moreover a decrease of the C content over 200 μm in the 18MND5 steel is visible.

One of the sample was subjected to an interrupted heat-treatment in order to characterize the state of the weld at the end of the heating ramp before the temperature plateau. It was retrieved from the furnace and quenched as soon as the temperature had reached 610°C. Significant carbon diffusion has already taken place during the heating ramp as evidenced by the decarburization of the base metal over 80 μm and the dark aspect of the martensitic layer on Figure 3.5-a (to be compared with the as-welded condition in Fig. 3.2). Moreover two C peaks were detected on this intermediate state by WDS, one in the martensite at 0.5 wt.% and another in the austenite around 0.2 wt.%, together with a reduced carbon content over 80 μm in the HAZ.

As a complement to carbon measurements, nanoindentation profiles were performed with a spatial resolution similar to the one achieved by WDS. From a macroscopic point of view, a decrease in hardness is observed after heat-treatment on the low-alloy side due to the tempering of the

bainitic microstructure and the carbon depletion within the first 500 μm of the HAZ close to the fusion line. As mentioned previously in the case of carbon quantification by WDS, the size of the nanoindentation probe results in some dispersion on the low-alloyed side (between 2.4 and 3.5 GPa in the heat-treated 18MND5 steel) caused by the heterogeneities of the microstructure. The reduction in hardness in the decarburized region with large ferrite grains is limited but the scatter is highly reduced (variations between 2.37 and 2.70 GPa) as expected for an homogeneous microstructure. Concerning the martensitic layer at the fusion line, its hardness shows almost no significant evolution after heat-treatment, the carbon enrichment being probably counterbalanced by the tempering of the microstructure. However the local strength of the purely austenitic zone is deeply modified and increases from 4 to 8 GPa over 60 μm. This huge rise of the local hardness can be related to carbon intake, either in supersaturation into the FCC matrix or as a dispersion of small precipitates.

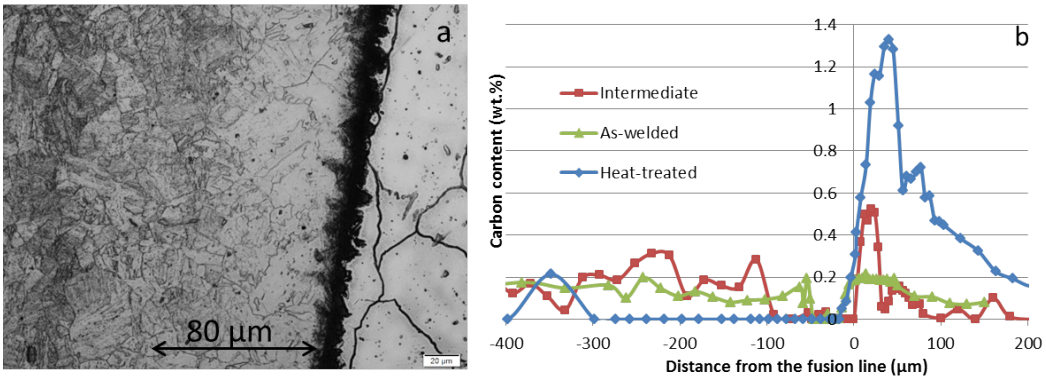

Figure 3.5: Intermediate state at the end of the heating ramp. a- Microstructure after Nital + Electrochromic etching. b- Carbon profile measured by WDS, the as-welded and heat-treated states have been added for comparison.

3.3.2 Nature and composition of the precipitates

3.3.2.1 In the martensitic layer

FIB thin foils extracted perpendicular to the fusion line from both the as-welded and heat-treated samples revealed quasi no precipitates in the as-welded state whereas an intense precipitation of large carbides (size up to 300 nm - Figure 3.7-a) was observed after heat-treatment. Two types of carbides were identified after 8 hours at 610°C: $M_{23}C_6$ and M_7C_3 (M stands for Fe, Cr, Ni, Mn essentially) which are typically found in high alloyed martensitic steels [109]. $M_{23}C_6$ carbides were detected as a cubic structure (Fm-3m space group) with a cell parameter of 10.68 Å whereas M_7C_3 were identified with an hexagonal cell (P63mc space group) with a and c parameters equal to 14.01 and 4.53 Å respectively [110]. Long streaks along the $< 110 >$ and $< 1\bar{1}0 >$ directions on the selected area electron diffraction (SAED) patterns from the M_7C_3 carbides were frequently observed. As mentioned in the literature [111], these anisotropic spots are due to stacking faults in planes perpendicular to the basal plane.

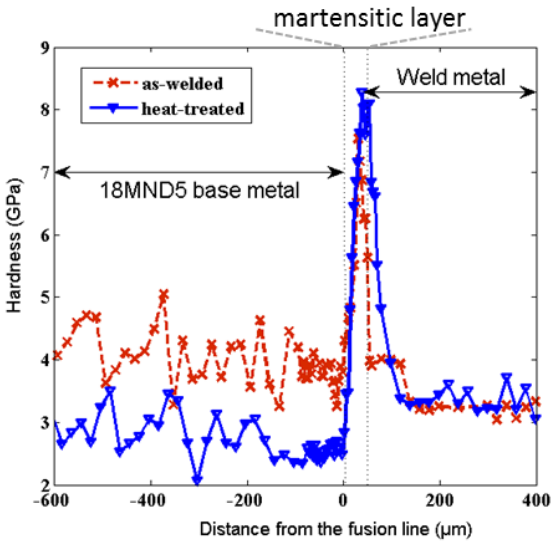

Figure 3.6: Nanoindentation profiles through the welding interface in the as-welded and heat-treated samples. The dotted line at 0 μm corresponds to the fusion line whereas the one at 50 μm defines the interface between martensite and austenite.

The systematic crystallographic mapping performed with Astar system on carbon extraction replicas allowed capturing the evolution in nature of the carbides throughout the martensitic layer: mainly M_7C_3 were found next to the low-alloy side (Figure 3.8-a) whereas both M_7C_3 and $M_{23}C_6$ were present at the extremity adjacent to the austenitic region (Figure 3.8-b). This change in the carbides population can be related to the evolution of the carbon content from 1.3 to 0.7 wt% (Fig. 3.3-a). Indeed a decrease in the carbon concentration destabilizes the M_7C_3 precipitates (high C/M ratio) leading to the formation of $M_{23}C_6$ (lower C/M ratio). It is shown on the plot of Figure 3.9-a, from the volume fractions of precipitates in the tempered martensite (BCC matrix) calculated by minimization of the total Gibbs free energy (local equilibrium approach) with the MatCalc software [113], that both Cr-rich carbides can coexist within a carbon content range from 0.68 to 1.35 wt.%.

Carbon extraction replicas allowed measuring the content in substitutional elements by TEM-EDS without the contribution of the X-Ray signal from the matrix. The results which are averages over 20 precipitates in the same zone are displayed in Table 3.1 and show a significant incorporation of iron into the carbides. It can be explained by the limited chromium content (around 11 wt.% in martensite) together with its low diffusion coefficient at 610°C ($D_{Cr} = 7 \times 10^{-19} m^2/s$ in the BCC matrix[3]).

[3]Value extracted from the mc-fe.ddb database of the MatCalc software

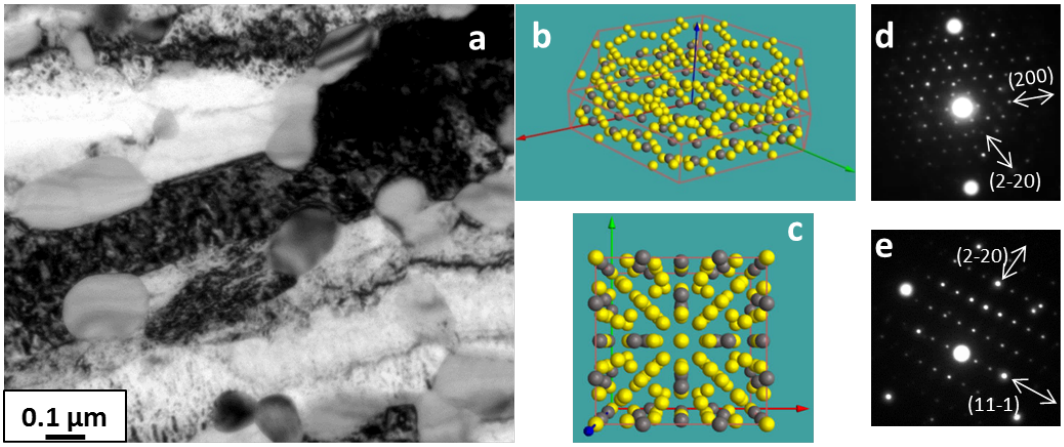

Figure 3.7: Carbides in the tempered martensitic layer after heat-treatment. a- Bright Field TEM image b- Unit cell of M_7C_3 from [112] c- Unit cell of $M_{23}C_6$ from [112] d- SAED pattern of M_7C_3 (zone axis [001]) e- SAED pattern of $M_{23}C_6$ (zone axis $[11\bar{1}]$).

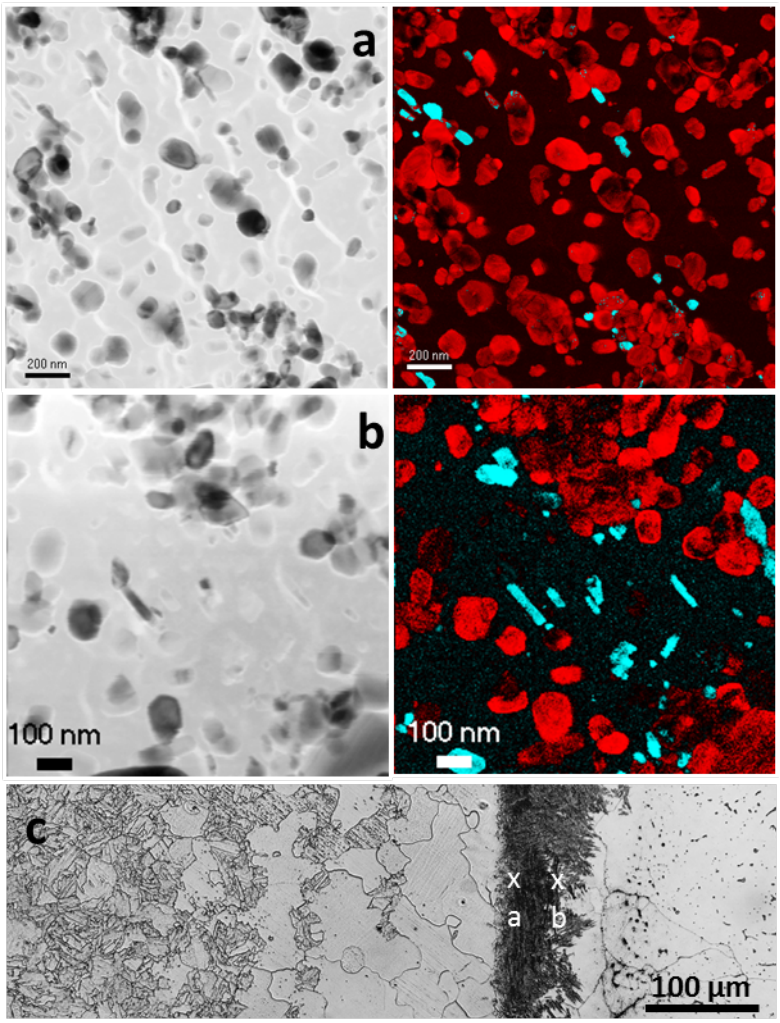

Figure 3.8: Carbides identification in the tempered martensitic layer by ACOM (superimposition of phases and reliability), M_7C_3 shown in red, $M_{23}C_6$ in blue. a- Next to the interface with the base metal. b- Next to the interface with the austenitic weld metal. c- Optical micrograph of the heat-treated interface with the localization of observations a and b.

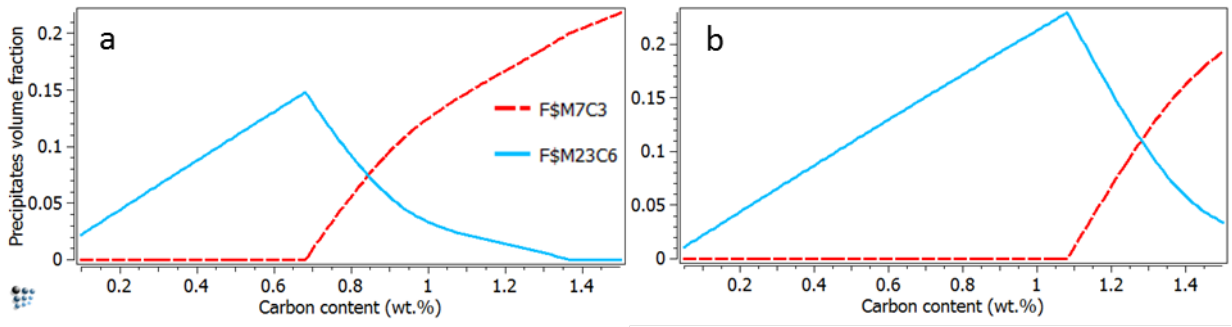

Figure 3.9: Precipitates volume fractions at 610°C calculated as a function of the global carbon content (MatCalc software [113], mc-fe.tdb database [114]) a- For the tempered martensitic layer: w(Cr)=11% ; w(Ni)=6% ; w(Mn)=1.5% ; w(Si)=0.5% ; w(Mo)=0.3% b- For the austenitic weld metal: w(Cr)=18% ; w(Ni)=9% ; w(Mn)=1.2% ; w(Si)=0.8% ; w(Mo)=0.2%.

3.3.2.2 In the fully austenitic region

Numerous carbides were extracted from the first micrometers (less than 10 μm) of the austenite adjacent to the martensitic layer and identified by ACOM as shown on Figure 3.10: only small $M_{23}C_6$ carbides (less than 60 nm in size) were observed within the grains but large carbides identified either as $M_{23}C_6$ or M_7C_3 were found aligned along the grain boundaries (GB). Referring to the plot of Figure 3.9, a carbon content higher than 1.1 wt.% is necessary for the formation of M_7C_3 in this zone. The size and nature of these GB particles underline the role played by the grain boundaries as shortcuts for carbon diffusion. However the effect of the GBs on the global carbon diffusion in the austenite is limited in the present case as the grains are large and elongated (50 μm wide). In fact, enhanced carbon diffusion from the GBs to the grain interior and associated precipitation spans over less than 3 μm as can be seen on SEM image of Figure 3.11. The fact that some large carbides on the GBs are partly indexed as $M_{23}C_6$ and partly as M_7C_3 seems to indicate that there could be a direct transformation from one carbide (with the lower C/M ratio) to the other (with a higher C/M ratio) when the local carbon content increases by long-range diffusion. As can be seen in Table 3.1, carbides in the austenite also incorporate significant quantities of iron, nickel and manganese in their structure.

Table 3.1: Substitutional elements contents in the carbides (in u-fraction[4]) measured by TEM-EDS.

	U-frac(Cr)	**U-frac(Fe)**	**U-frac(Mn)**	**U-frac(Ni)**
M_7C_3 in martensite	0.61	0.34	0.044	-
$M_{23}C_6$ in martensite	0.61	0.34	0.041	0.006
M_7C_3 along GBs in austenite	0.65	0.32	0.027	0.006
$M_{23}C_6$ in austenite	0.60	0.36	0.021	0.021

[4] $u_k = \frac{x_k}{\sum_S x_k}$ where x_k is the molar fraction of element k, the summation being taken over the substitutional elements only.

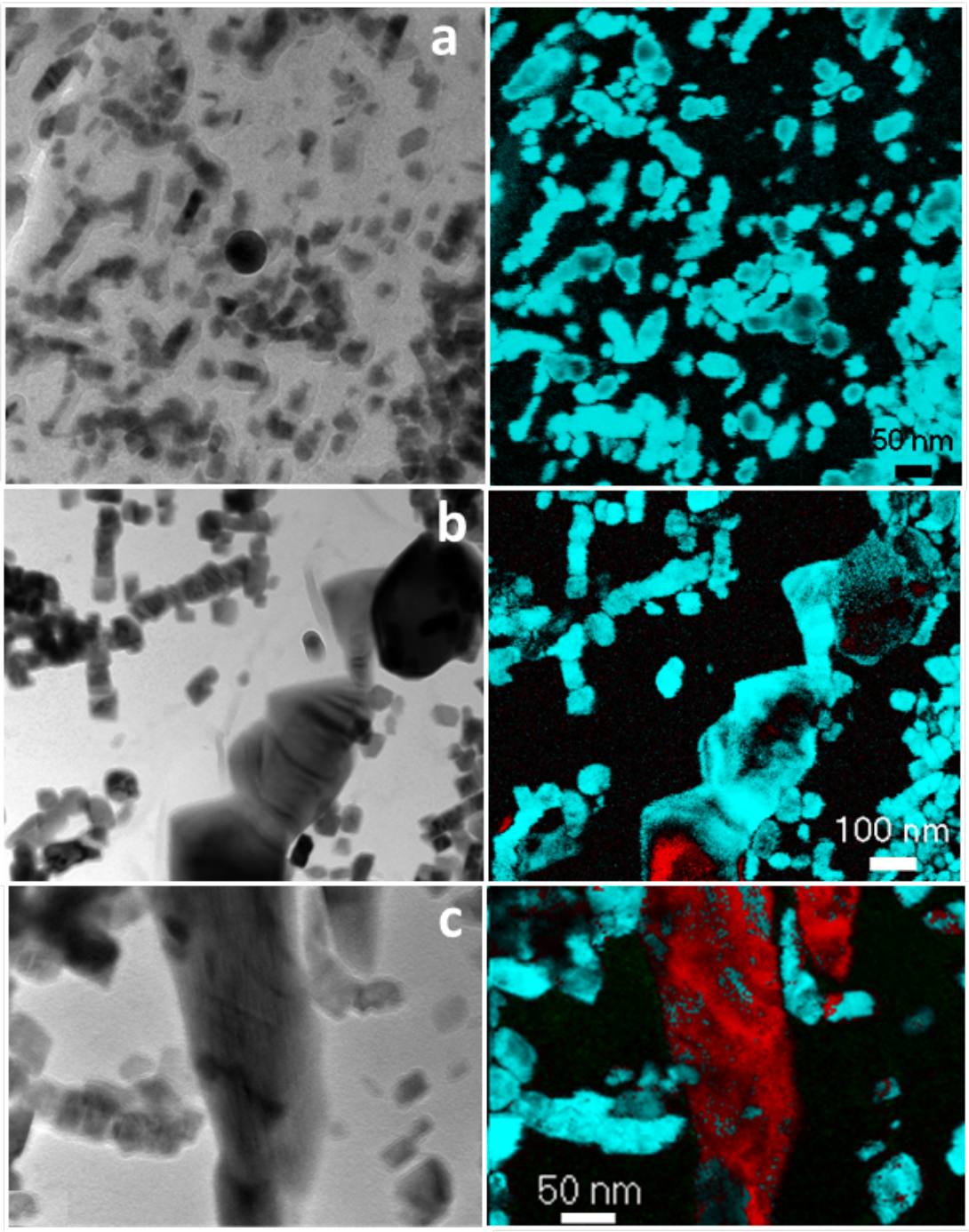

Figure 3.10: Carbides identification in the austenitic weld metal (at about 5 μm from the martensite), M_7C_3 shown in red, $M_{23}C_6$ in blue. a- Inside the grains, b and c- At grain boundaries.

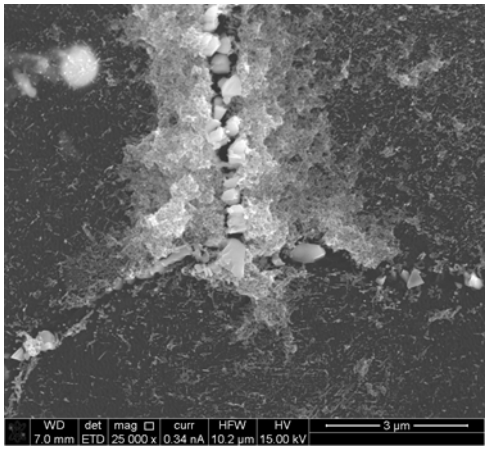

Figure 3.11: SEM image of carbide precipitates on a carbon extraction replica showing intense precipitation at grain boundaries in austenite.

3.3.2.3 In the $\delta - \gamma$ weld metal

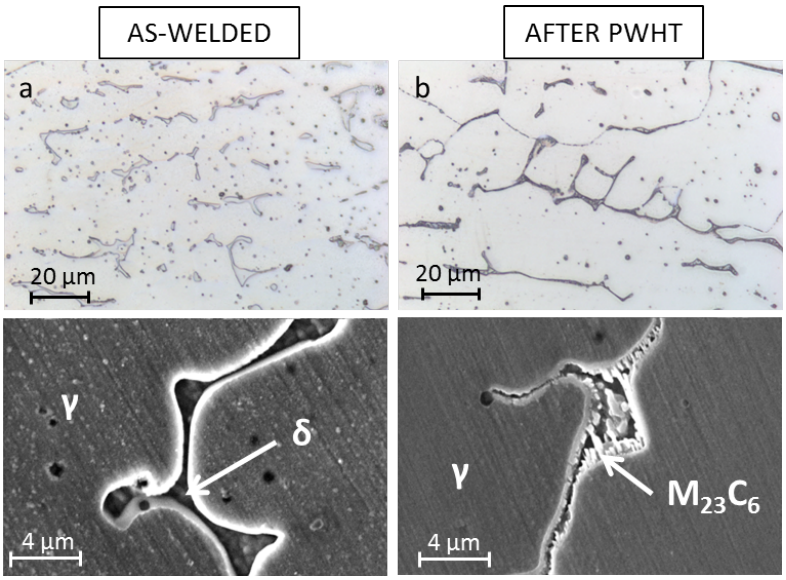

Figure 3.12: Optical and SEM micrographs of residual ferrite on the weld metal side after electro-chromic etching. a- In the as-welded condition, b- In the post-weld heat-treated state.

Austenitic stainless steels with primary ferrite solidification are widely chosen as filler metals as they reduce the risk of premature failure of the weld in comparison with the case of stainless steels with a primary austenite solidification [115, 116]. However the small amount of residual δ-ferrite is a non-equilibrium phase at room and service temperatures and may decompose into carbides and/or various intermetallic phases [117, 118, 119]. In the present case, δ was found to decompose during the post-weld heat-treatment into carbides. EDS profile of Figure 3.13 displays a periodic alternating of Cr-rich and Cr-poor regions along the $\delta - \gamma$ interfaces, which is an evidence of a lamellar eutectoïd reaction:

$$\delta \rightarrow \gamma + carbides \tag{3.4}$$

As shown on the micrographs of Figures 3.12 and 3.13, the preferential sites for carbides nucleation are the $\delta - \gamma$ interfaces. EDS analyses revealed that these carbides are enriched in chromium and molybdenum, elements that are known to segregate into the ferritic phase during solidification and the subsequent solid-state $\delta \rightarrow \gamma$ transformation. Concerning carbon, it is mainly dissolved into the austenitic matrix and has to diffuse towards the interface.

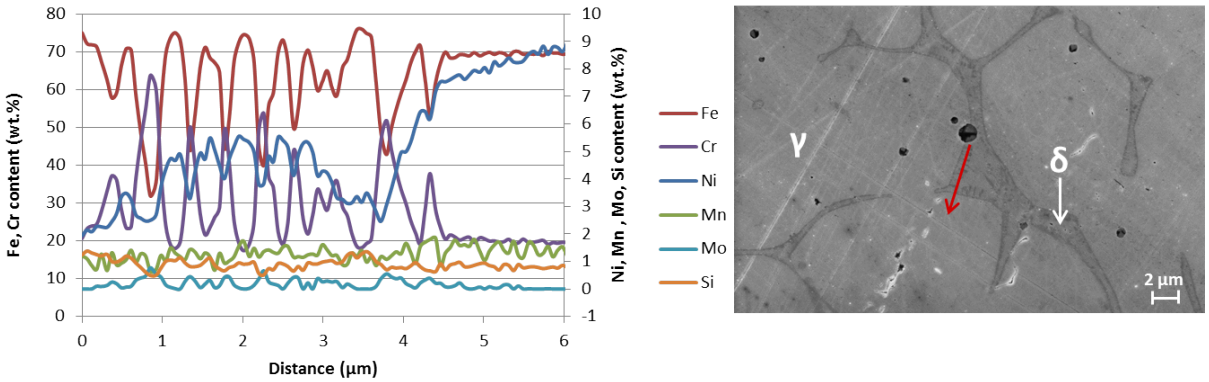

Figure 3.13: EDX profile along the δ-γ interface in the heat-treated specimen.

TEM allowed identifying the carbides as $M_{23}C_6$, which are certainly favored by their cristallographic similarity with the austenitic matrix. Low misorientations ($<2°$) relative to the cube-on-cube relationship were found between the carbides and the FCC matrix:

$$\{100\}_\gamma \parallel \{100\}_{M_{23}C_6}$$
$$< 100 >_\gamma \parallel < 100 >_{M_{23}C_6}$$

The comparison of the ACOM maps of Figure 3.14 highlights that the decomposition reaction has reached a higher degree of completion in the 309L than in the 308L. This can be related to a higher carbon content in the 309L layer than in the 308L one due to the mixing with the molten base metal ($w(C) = 0.2\%$) during welding. The fraction of transformed ferrite at the end of the post-weld heat-treatment was estimated based on several phase maps obtained with the ACOM technique on thin foils specimens. The results are reported in Table 3.2. Carbon extraction replicas were performed in the 309L layer and the dissolution of both δ and γ matrices revealed the 3D morphology of the carbides: they appeared to have small cubic shapes (200 nm in size) and to entirely cover the $\delta - \gamma$ interfaces to the point of forming a continuous self-standing network (see Fig. 3.15). Such arrangement might have a deleterious effect on the weld ductility as this quasi-continuous film of carbides could provide an easy path for crack propagation.

Table 3.2: Fraction of δ-ferrite which has decomposed into carbides measured on ACOM maps.

	309L	**308L**
Fraction of decomposed ferrite	18.6%	10.9%

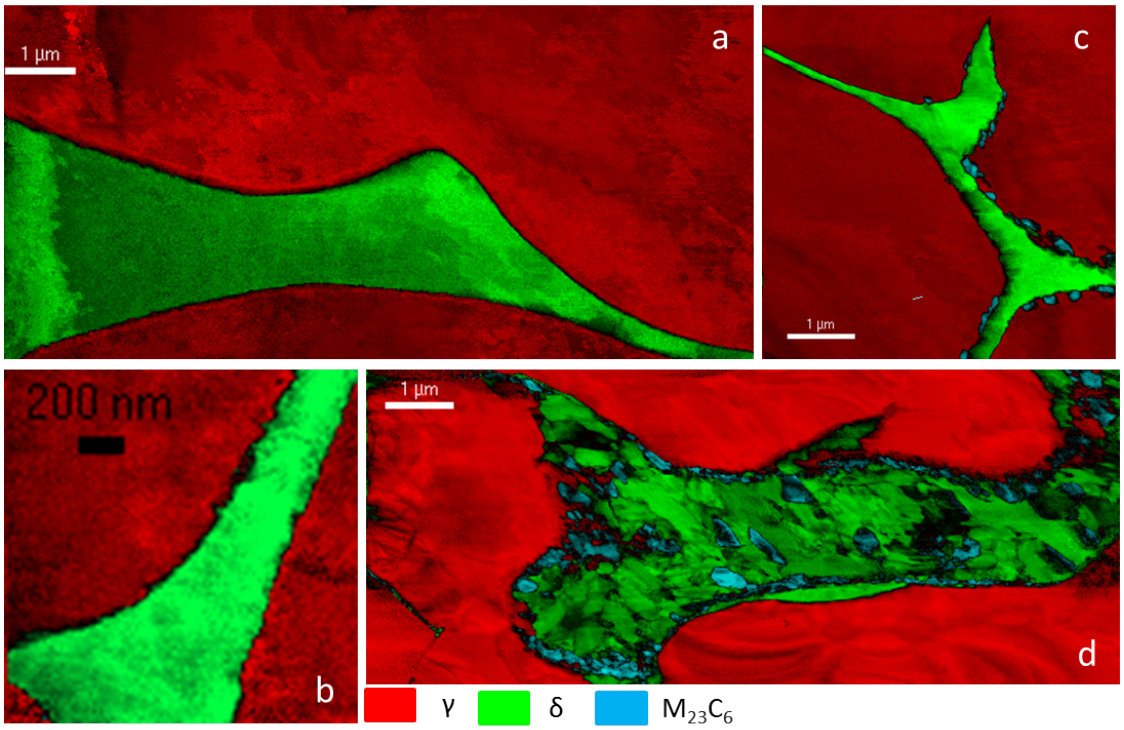

Figure 3.14: ACOM maps consisting of the superimposition of phases identification and reliability (low values in black) around residual δ-ferrite in the as-welded specimen a- in the 308L layer, b- in the 309L layer, and in the heat-treated sample c- in the 308L layer, d- in the 309L layer.

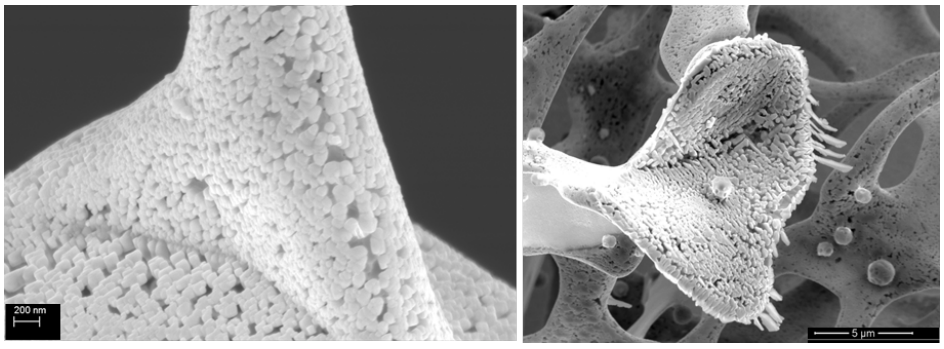

Figure 3.15: SEM micrographs of carbides retrieved from the matrix by carbon extraction replicas performed in the 309L layer.

3.3.3 Evolution of the carbides population around the interface

3.3.3.1 In the martensitic layer

Serial sectioning with FIB was applied inside martensite in the post-weld heat-treated sample since it allows 3D reconstitution over large areas with sufficient magnification to image medium-size particles (voxel size of 10 nm^3). Larger particles were mainly found on the lath boundaries whereas small carbides were rather observed in their interior (Figure 3.16-a). This preferred location is in agreement with both, heterogeneous nucleation (energetically favored in disordered regions) and easy growth by enhanced diffusion of elements along the subgrain boundaries. This leads to fairly elongated shape for the carbides that are better represented as cylinders and plates than spheres (see Figure 3.16-b).

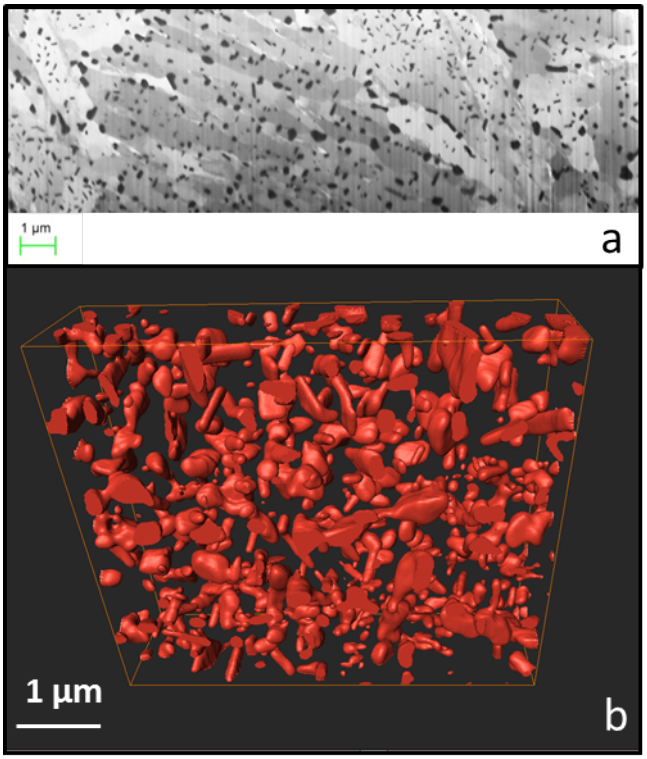

Figure 3.16: Serial cutting with FIB into the tempered martensitic layer. a- SEM image of the microstructure (laths in light grey + carbides in black and dark grey) and b- 3D carbides reconstruction with Avizo®.

Going from the fusion line towards the austenite across the tempered martensitic layer (35 μm wide), one observes an evolution in the carbides population: the mean size of the precipitates decreases (Figure 3.17-a,b) whereas their volume fraction and their density increase (Figure 3.17-c,d). At first glance, the quasi-constant volume fraction of carbides for the three last series (from 16 to 28 μm) might be surprising as it is associated with a continuous decrease of the global carbon content. Nevertheless it should be noticed that the nature of the precipitates also changes from M_7C_3 to $M_{23}C_6$. For each slice (corresponding to different locations inside the martensitic band) we divided the particles into 3 classes according to their size: the percentage of large particles (radius more than 50 nm) decreases with the distance from the base metal whereas the small carbides

(radius less than 25 nm) become more and more numerous (see Figure 3.18). This evolution of the precipitates through the martensitic layer is quite unusual. In the case of the nitriding of stainless steels, large precipitates are found in the interior of the sample whereas a high density of small particles is present at the surface [120]. In the present case, the decrease of the precipitates size within the martensitic layer might be related to the driving force for precipitates nucleation which increases when the Cr content increases.

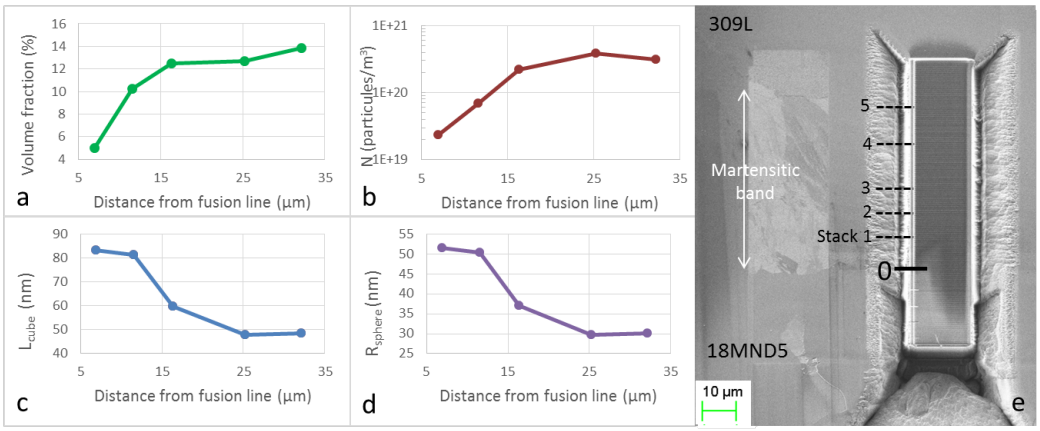

Figure 3.17: Characteristic parameters of the carbides population in the tempered martensitic band as a function of the distance from the fusion line, as obtained from FIB tomography. a- Volume fraction; b- number of particles; c- mean dimension with the assumption of cubic precipitates (volume $V = L^3_{cube}$) d- mean radius with the assumption of spherical precipitates ($V = \frac{4}{3}\Pi R^3_{sphere}$). e- Localization of the stacks inside the martensitic layer.

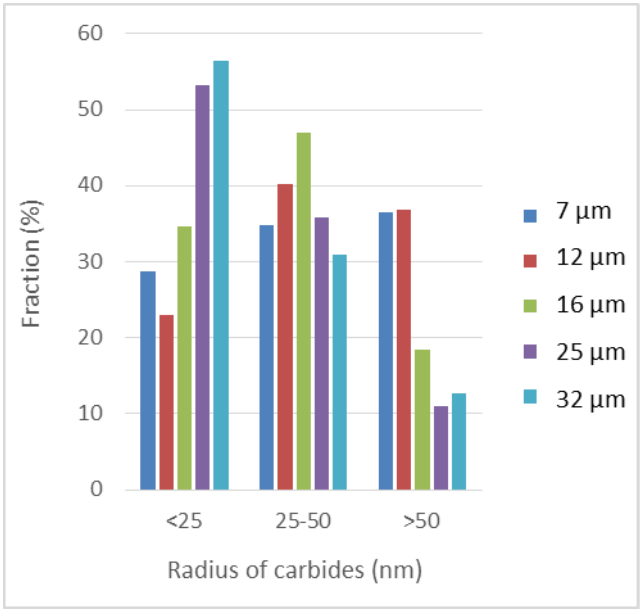

Figure 3.18: Size distribution of the carbides in the tempered martensite, at several distances (from 7 to 32 μm) from the fusion line (FIB tomography).

3.3.3.2 In the fully austenitic region

As the carbon replicas systematically broke at short distances from the martensite, certainly due to the high quantity of particles accumulated in this zone, carbides extraction had only been efficient in the first micrometers of austenite (< 10 μm) next to the martensitic layer. Thus, FIB thin foils removed both perpendicular and parallel to the fusion line were employed to investigate the evolution of the carbides population in the austenite. In agreement with the observations on replicas (see Figure 3.10) numerous $M_{23}C_6$ carbides around 60 nm in size were found in the near surroundings of the martensite/austenite interface on the FCC side. Cube-on-cube orientation relationship between these carbides and the austenitic matrix was observed:
$< 001 >_{M_{23}C_6} // < 001 >_{FCC}$ (see indexation of the diffraction patterns in Fig. 3.19-c and -i). As can be seen on Figure 3.19-h some of the particles display a cubic shape and seem to be aligned along prefered directions.

At intermediate distances from the fusion line (see Figure 3.19-e, at 15 μm from the fusion line) two distinct populations are visible. Large cubic carbides seem concentrated along some characteristic features that could be dislocations, and in between what looks like dislocations cells decorated by cubic precipitates (diameter of the cells around 1 μm), a large amount of very small clusters can be seen (radius less than 5 nm). The large precipitates are not coherent with the matrix (see indexation of the diffraction pattern in Fig. 3.19-f), which is in agreement with a nucleation on defects and a larger size. The small ones are numerous and may result from homogeneous nucleation. Either there exists a high driving force for nucleation due to a large carbon intake into the austenitic matrix during the temperature plateau at 610°C or they precipitate during the subsequent cooling (which lasts several hours between 610°C and room temperature) with quasi no diffusion and so a limited growth of the particles.

Further away from the fusion line (see Figure 3.19-h, at 35 μm from the fusion line), the carbides systematically have a cubic morphology and are aligned along particular crystallographic directions. This can be compared to the growth of γ' precipitates in Ni-Al alloys. When precipitates nucleate coherently with the matrix phase, differences in lattice parameters create elastic distortions in their neighborhood. Sphere to cube shape transition together with regular spatial arrangement along the least dense directions of the FCC matrix ((100) less rigid than (110) and (111)) have been shown to reduce these coherency stresses [121, 122]. Hence it corresponds to an energetically favored configuration. Moreover such a high density of carbides combined with their regular spatial organization could be responsible for a significant strengthening of the austenitic matrix (visible on Figure 3.6).

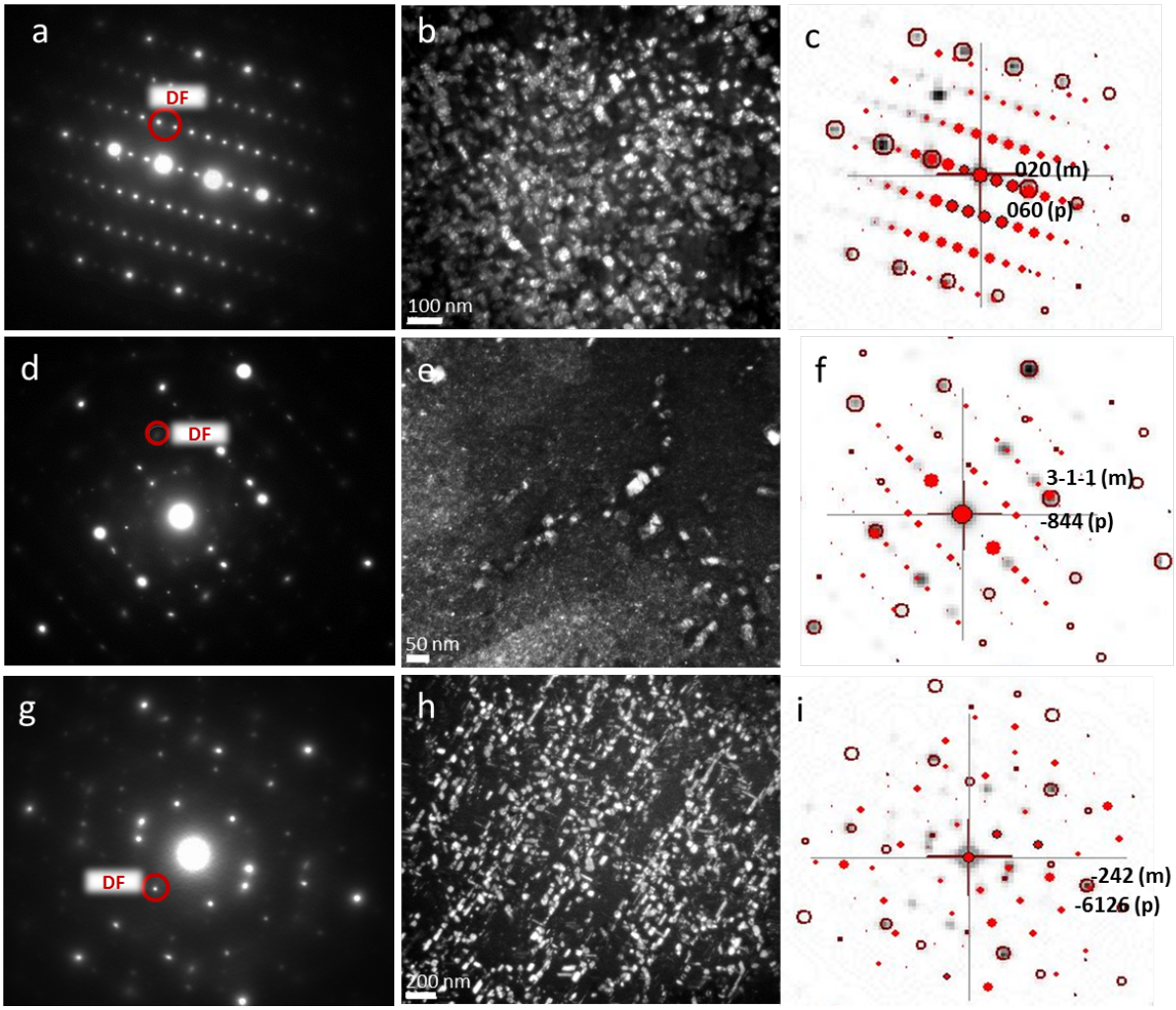

Figure 3.19: $M_{23}C_6$ carbides in carburized austenite. a- Diffraction pattern taken at 5 μm from the interface with martensite. b- DF image resulting from the area selection displayed on a). c- Indexation of the diffraction pattern ([102] zone axis) with open circles for the dots from the matrix (m) and filled circles for the ones from the precipitates (p). d- Diffraction pattern taken at 15 μm from the interface with martensite. e- DF image resulting from the area selection displayed on d) showing a second population of very fine precipitates. f- Indexation of the diffraction pattern ([215] zone axis for the matrix and [213] for the precipitates). g- Diffraction pattern taken at 35 μm from the interface with martensite. h- DF image resulting from the area selection displayed on e) showing the alignment of the precipitates. i- Indexation of the diffraction pattern ([214] zone axis).

3.3.4 Elements distribution within matrices and precipitates

3.3.4.1 In the tempered martensitic layer

Atom probe tomography reconstitution of volumes extracted from the tempered martensitic layer at different stages of the heat-treatment (as-welded, intermediate state at the end of the heating ramp, end of the heat-treatment) are displayed on Figure 3.21. Chromium and molybdenum-rich carbides with increasing size are clearly visible. In order to enable comparison between the three states, it was necessary to extract the APT samples from the exact same location within a martensitic layer with the exact same width. This was verified a posteriori by comparing the global nickel content of each APT specimen (5.0, 4.4 and 5.1 at.% in the as-welded, intermediate and heat-treated conditions, respectively). Of primary importance is the fact that some carbides already exist in the as-welded state and that precipitation goes on during the heating ramp. Therefore the post-weld heat-treatment can certainly not be reduced to a temperature plateau of 8 hours at 610°C, as both carbon diffusion (see Figure 3.5) and phase transformations occur during the transient phases. Iso-concentration surfaces were used to create matrix/precipitate interfaces and evaluate the mean compositions on both sides of these interfaces.

Concerning carbon, three main facts need to be reported:

1. The increase of the global carbon content in the tempered martensite associated with an increase of the precipitates dimensions does not lead to a complete depletion of the matrix. This means that carbon is not totally consumed by carbides nucleation and growth, and that a significant part of it remains interstitially dissolved in the matrix (see Table 3.3), and thus is available for diffusion towards the austenite.

2. Carbon within the matrix phase was found to be heterogeneously distributed. As shown in Figure 3.20-a, carbon-rich surfaces were encountered in the as-welded state and might correspond to carbon segregations along both dislocations and subgrain boundaries of the martensitic microstructure. As a logical consequence, the carbides in the intermediate and final stages of the heat-treatment were found to have elongated shapes in agreement with their preferential growth along subgrain boundaries (see Fig. 3.16-a) and the 3D reconstitution performed by FIB (see Fig. 3.16-b). In Figure 3.20-b, one of the carbides in the heat-treated state displays an elongated shape as if it had preferentially grown along a defect.

3. The carbon content in the precipitates measured by APT does not correspond to the normal stœchiometry of the carbides dictated by their crystallography. For $M_{23}C_6$ carbides, the carbon content is expected to be around 20.7 at.% whereas it should be at 30 at.% for M_7C_3 carbides. Contents lower than 20.7 at.% were found in the as-welded and intermediate states and between 20.7 and 30 at.% at the end of the heat-treatment. Such an underestimation of the carbon content within carbides is quasi-systematically present in the examples of the literature when carbides were analyzed by APT [123, 124, 125]. Several reasons can be provided to explain this discrepancy:

- Compared to metallic atoms, carbon has a high ionization energy (11.26 eV versus from 6.8 to 8.15 eV for the metallic elements encountered in the bimetallic weld). As a result, carbon will require a higher local electric field to evaporate, which may lead to its retention to the specimen surface and then the simultaneous evaporation of molecular ions. The carbides will remain as protuberances at the surface before evaporating at once. This causes multiple events on the detector and depending on its "dead time", the detection efficiency for carbon might be lowered [124]. Indeed carbon was detected as multiple peaks on the mass spectrum (C^{3+}, C^{2+}, C^{+}, C_3^{2+}, C_2^{+}, C_3^{+}, MoC^{2+}, CrC^{+}) which confirms that the previously described phenomenon certainly happens in the present case.
- When a molecular ion is field evaporated from a specimen surface, it may dissociate during the travel towards the detector. After the dissociation, one or several daughter ions continue traversing the remainder potential drop and result in inferring mass-charge ratios different from the original one. Such dissociation that can happen anywhere on the way to the detector will create species whose signature will be lost within the spectrum noise [126]. Neutral atomic species can also be generated during molecular ion dissociation and participate to data loss.

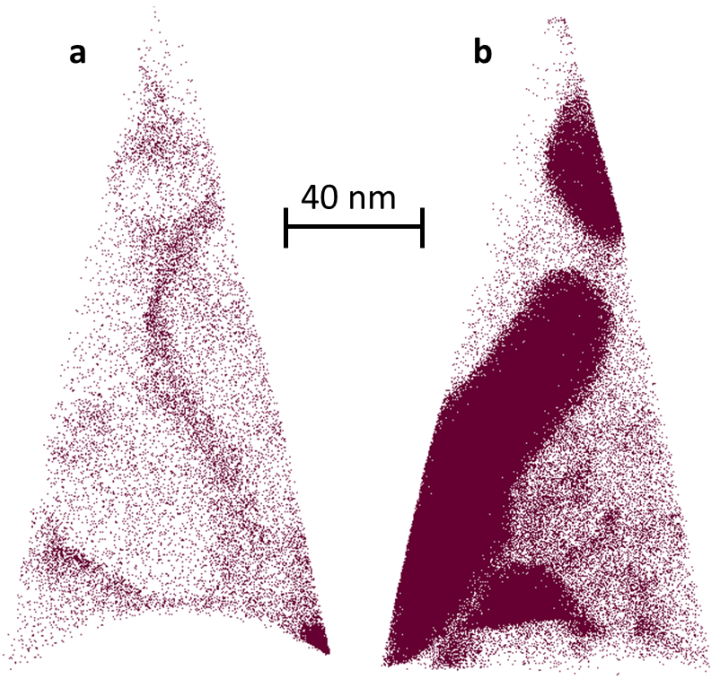

Figure 3.20: Carbon distribution within the tempered martensite a- in the as-welded condition, b- in the heat-treated state.

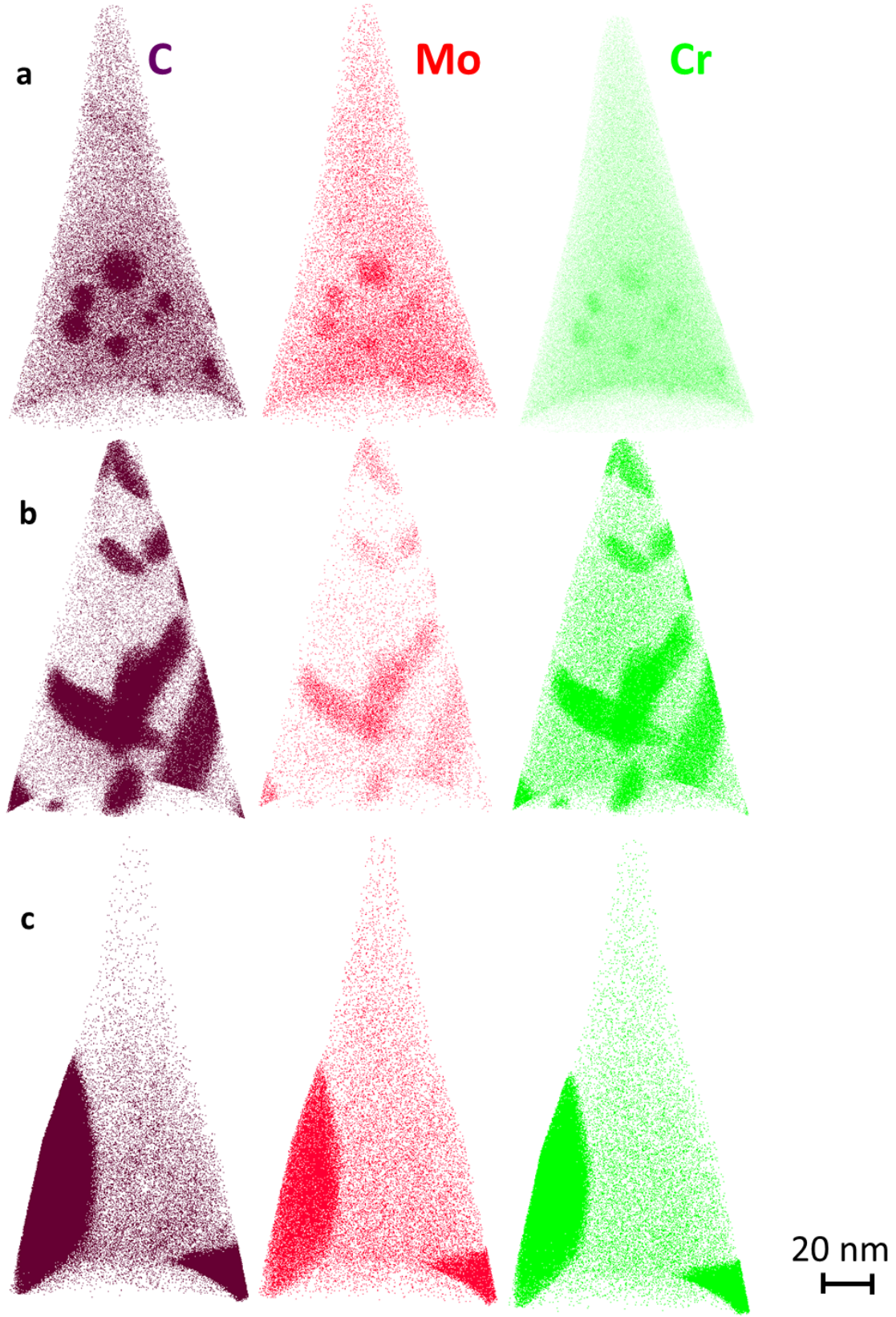

Figure 3.21: APT volumes from the martensitic layer a- in the as-welded state, b- in the intermediate state (end of the heating ramp), c- in the heat-treated condition.

As shown in Tables 3.3 and 3.4, precipitation of Cr and Mo-rich carbides is associated to a significant decrease of their content into the matrix. During the first stage of the heat-treatment (until the beginning of the temperature plateau) the carbides enrich in chromium (from 0.47 to 0.59 u-fraction). In the following part of the heat-treatment including the temperature plateau at 610°C, its content within both precipitates and matrix decreases (from 0.59 to 0.41 u-fraction in the precipitates): a possible interpretation is that a point has been reached where chromium becomes limiting. The growth of precipitates could then only continue by adapting their stoechiometry, and especially by including more iron in their structure. The Cr/Fe ratio in the precipitates is found to first increase from 1.02 to 1.79 during the heating-ramp, and then decrease to 0.84 at the end of the heat-treatment. However this tendency has to be considered with extreme caution as it is also affected by the fact that the samples could not exactly be prepared from the exact same location within the martensitic zone. As already shown by the EDS measurements with TEM on extraction replicas (see Table 3.1), the precipitates also incorporate a significant quantity of iron and manganese. Surprisingly higher chromium contents were measured by TEM within the precipitates (around 0.6 u-fraction). This might be due to the fact that in APT measurements a non-negligible part of the chromium within the precipitates evaporates as molecular ions with carbon, especially CrC^+. Therefore chromium is probably subjected to the same loss as carbon during evaporation. Concerning nickel and silicium, they are systematically rejected from the precipitates (see their low contents in Table 3.4), which is made easier by a faster diffusion at high temperatures.

Table 3.3: Composition of the matrix phase in the martensitic layer evaluated by means of iso-concentration surfaces to delimit the particles in the as-welded, intermediate (end of the heating ramp) and heat-treated states. Only the elements with a global content higher than 0.08 at.% were taken into account in this table.

Matrix	**As-welded** at.% (wt.%)	**Intermediate** at.% (wt.%)	**Heat-treated** at.% (wt.%)
C	0.36 (0.08)	0.44 (0.10)	0.45 (0.10)
Cr	10.83 (10.23)	3.53 (3.32)	1.49 (1.40)
Fe	81.24 (82.40)	89.12 (90.04)	90.19 (90.83)
Mn	1.43 (1.43)	1.08 (1.07)	1.67 (1.65)
Mo	0.17 (0.30)	0.036 (0.06)	0.07 (0.13)
Ni	4.73 (5.04)	4.63 (4.92)	5.21 (5.51)
Si	1.05 (0.54)	0.97 (0.49)	0.76 (0.38)

Table 3.4: Compositions of the precipitates (in u-fraction) in the martensitic layer evaluated by means of iso-concentration surfaces to delimit the particles in the as-welded, intermediate (end of the heating ramp) and heat-treated states.

Carbides	**As-welded (u-fraction)**	**Intermediate (u-fraction)**	**Heat-treated (u-fraction)**
Cr	0.47	0.59	0.41
Fe	0.46	0.33	0.49
Mn	0.018	0.030	0.053
Mo	0.015	0.017	0.024
Ni	0.030	0.029	0.019
Si	0.006	0.005	0.001

3.3.4.2 In the fully austenitic region

Atom probe tomography volumes were also prepared from the fully austenitic zone at 20 μm from the interface with martensite in the post-weld heat-treated state (zone equivalent to the one observed by TEM in Figure 3.19-e). As shown on Figure 3.22 where both atoms and iso-concentration surfaces are represented, the few precipitates found were enriched in chromium and molybdenum. Mean compositions displayed in Table 3.5 indicated that a large amount of carbon remained in solid solution into the matrix where the carbon content (1.7 at.%) was much larger than the equilibrium solubility of carbon in the Fe-Cr-Ni alloys at 610°C (0.008 at.% calculated with MatCalc). This enhanced carbon solubility could be explained either by slow precipitation kinetics or by tensile residual stresses which would result in a local expansion of the FCC lattice. The hydrostatic stress necessary to cause such equilibrium displacement was evaluated around 1030 MPa by [127]:

$$C_C^\gamma = C_{0,C}^\gamma exp(\sigma \frac{V_C}{RT}) \tag{3.5}$$

where C_C^γ is the carbon content in austenite measured by APT, $C_{0,C}^\gamma$ the equilibrium C content, σ the hydrostatic stress, V_C the molar volume of carbon in austenite, T the absolute temperature and R the universal gas constant. As previously, the carbon content within the precipitates is certainly underestimated (11.7 instead of 20.7 at.% for $M_{23}C_6$ carbides). As in the martensitic region, nickel and silicium are rejected into the matrix.

When iso-concentration limits were reduced to 4 and 18.5 at.% for C and Cr respectively, small clusters or at least concentrations fluctuations were evidenced. These segregations can be related to the small bright spots observed on the DF TEM image of Figure 3.19-f. Despite the presence of these small clusters, C and Cr contents within the austenitic matrix are only slightly reduced: from 0.4 to 0.38 wt.% for C, and from 15.9 to 15.8 wt.% for Cr.

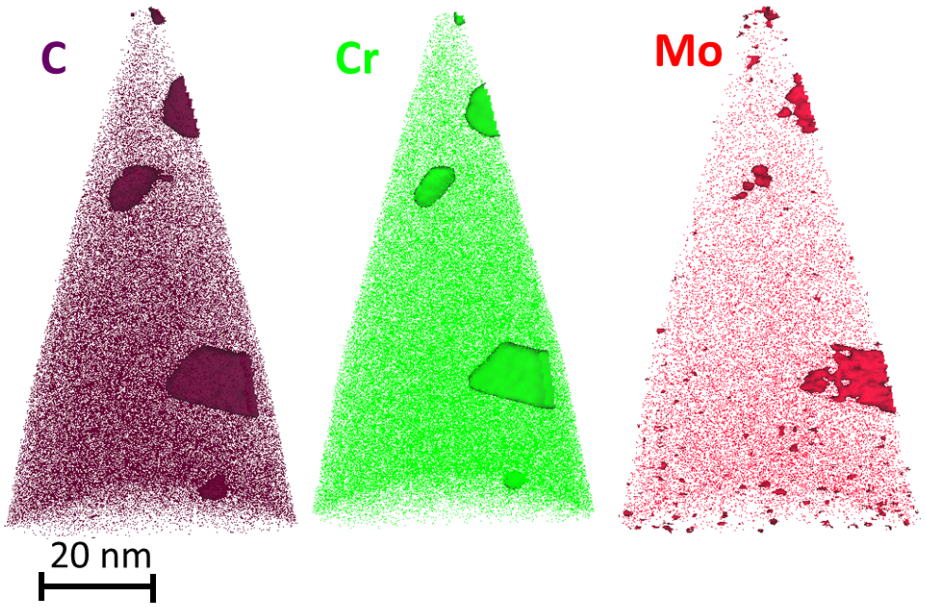

Figure 3.22: APT volume from the fully austenitic zone at 20 μm from the interface with martensite in the heat-treated condition. The iso-concentration surfaces are set to 8.75 at.% for C, 30 at.% for Cr and 0.8 at.% for Mo.

Table 3.5: Compositions of both matrix and precipitates evaluated by means of iso-concentration surfaces to delimit the particles. Only the elements with a global content higher than 0.08 at.% were reported in this table.

	Global composition at.% (wt.%)	**Matrix composition** at.% (wt.%)	**Precipitates composition** at.% (wt.%)
C	1.8 (0.4)	1.7 (0.4)	11.7 (2.9)
Cr	16.8 (16.1)	16.6 (15.9)	45.8 (48.4)
Fe	70.5 (72.6)	70.8 (72.8)	35.8 (40.6)
Mn	1.5 (1.5)	1.6 (1.6)	1.3 (1.5)
Mo	0.1 (0.2)	0.09 (0.2)	1.0 (2.0)
Ni	7.9 (8.6)	7.9 (8.5)	3.8 (4.5)
Si	1.2 (0.6)	1.2 (0.6)	0.4 (0.2)

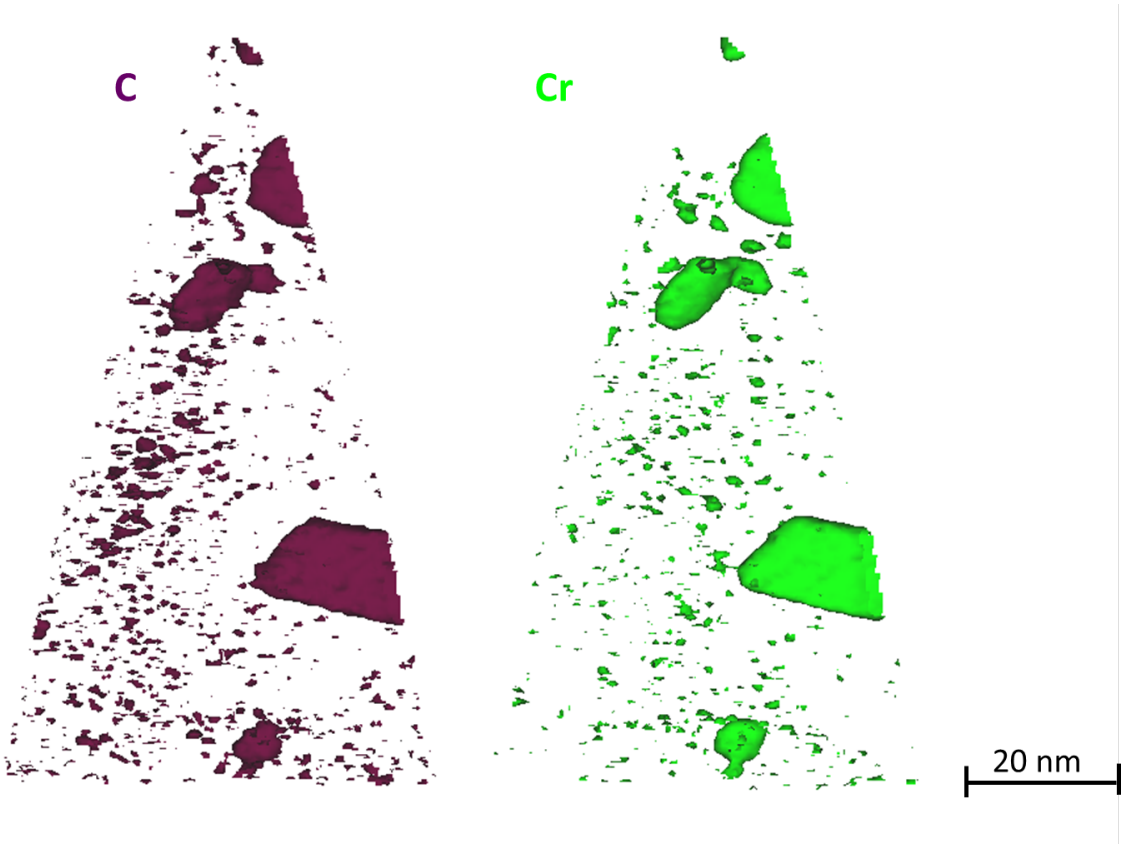

Figure 3.23: Iso-concentration surfaces for C and Cr with limits set at 4 and 18.5 at.% respectively.

3.4 Summary and conclusions

The following main conclusions can be drawn based on the results obtained from this experimental study:

1. Concerning the characterization techniques, the **combination of WDS, SIMS and nano-indentation** has allowed measuring the evolution of the carbon distribution through the ferritic / martensitic / austenitic regions near the fusion line of a dissimilar steel weld. The same reference samples were used for both SIMS and WDS, with the **quantitative results being in good agreement, especially for the heat-treated sample.** The development of a quantitative method for carbon measurements with SIMS has allowed detecting contents as low as 0.004 wt.% in the decarburized layer. WDS and nanoindentation were well adapted to capture fine and very local variations whereas SIMS was preferred for quantifying compositional changes occuring over larger scales. Concerning precipitation, **ACOM** revealed to be a powerful tool to systematically **identify a large number of carbides** based on their crystallography. **Serial cutting with FIB** associated with 3D reconstruction was efficient to follow the evolution of the main particles features in the case of the medium-size precipitates present in the martensite. **Atom probe tomography** allowed quantifying the distribution of carbon and the main substitutional elements between matrix and precipitates. By this

technique, a significant amount of carbon, heterogeneously distributed, was evidenced within the matrix of the martensitic layer.

2. Concerning the heat-treatment, carbon diffusion accompanied by precipitation of small carbides was found to already initiate during welding. Then, it goes on during the heating ramp to the 610°C holding temperature with carbon enrichment of the martensitic layer together with nucleation and growth of carbides. Carbon diffusion into the austenite occurs mainly during the temperature plateau at 610°C, which is in agreement with a low carbon diffusion coefficient in the FCC matrix at lower temperatures. Therefore the dissimilar welds of this study are subjected to a **complex thermal history that cannot easily be simplified** as carbon diffusion and precipitates evolution occur at temperatures lower than 610°C.

3. Carbon diffusion from the low-alloy to the high-alloy side was found to create large microstructural heterogeneities over short distances. Decarburization of the base metal resulted in the formation of a **narrow soft band made of large ferrite grains in contact with a hardened region** (martensite + carburized austenite). The evolution of the local hardness in the surroundings of the interface gave a first insight into the local mechanical heterogeneities that exist in such welds. Localization of the plastic deformation and a state of triaxial stress are expected to occur in the decarburized layer during mechanical loading.

4. The **interfacial martensitic band** present in between the low-alloy steel and the austenitic stainless steel was found to behave as a **sink for carbon**, in accordance with the huge carbon chemical potential difference that exists initially with the 18MND5 base metal (see Figure 4.9-d). During the heat-treatment a significant quantity of carbon passes through this intermediate zone. Even if most of it precipitates (mainly with Cr atoms) inside the martensitic layer, a non-negligible part remains in solid solution and is available to diffuse towards the austenite driven by the high chemical potential gradient across this second interface. This **dual behavior** can be related to the value of the diffusion coefficient for carbon in this zone: not only it is higher in BCC matrix than in FCC ($D_C(400°C, BCC) \approx 25 \times D_C(610°C, FCC)$), but it can also be enhanced along lattice defects such as subgrain boundaries and dislocations. In fact, **carbon segregation around subgrain boundaries** was evidenced by atom probe analyses in the as-welded sample.

5. After the post-welding heat-treatment, the **carbon concentration in the purely austenitic zone** has reached **very high values** (up to 0.8 wt.%), which are completely unusual for stainless steels. Precipitation of coherent $M_{23}C_6$ cubic carbides together with a dense population of very small clusters (radius $<$ 5 nm) led to a high level of local strengthening.

Chapter 4

Modeling coupled carbon diffusion and precipitation in dissimilar steel welds

4.1 State of the art

4.1.1 Modeling of diffusion

4.1.1.1 Some elements of diffusion in multicomponent alloys

Obtaining simple analytical solutions for the description of diffusion-controlled phase transformations is only possible under strong simplifying assumptions, such as the geometry of the precipitating phases, their fixed stœchiometry, and a linear coupling between fluxes and concentration gradients. Moreover most of the known analytical solutions are derived for binary systems. However, in practice, modern materials are a combination of multiple elements in order to meet the requirements imposed by their industrial service environment. In steel, at the very least, carbon (interstitial) and another element (any of the metallic substitutionals) provide two components with vastly different diffusivities. The well-known Fick's law which relates the mass flux to the gradient of chemical composition via the proportionality coefficient D relies on the absence of chemical interaction between the species. As demonstrated by Darken [84] with uphill diffusion experiments, this relation cannot be directly applied to multicomponent alloys in which some elements can diffuse against their own composition gradient. However it can be generalized in the framework of irreversible thermodynamics which assumes a linear coupling between fluxes and forces and allows for interactions between elements via their contribution in the chemical potential of each other. Therefore, the real driving force for diffusion is the chemical potential gradient of all the species present in the system and Onsager's equation [128] should be used:

$$J_k^K = -\sum_{i=1}^{n} L_{ki} \nabla \mu_i \tag{4.1}$$

J_k^K is the flux of species k in $mol.m^{-2}.s^{-1}$ in the lattice-fixed frame of reference.
μ_i is the chemical potential of species i in $J.mol^{-1}$
L_{ki} is a kinetic factor related to the diffusion of species k under the gradient of chemical potential

of i. The matrix L being symetric, $L_{ik} = L_{ki}$.

In the lattice-fixed frame of reference (also known as Kirkendall's frame of reference [129] which is linked to an atomic plane) the net flux of atoms is counterbalanced by the flux of vacancies and the kinetic factor of species k under its own chemical potential gradient L_{kk} can be expressed as the product $M_k C_k$ of its mobility and concentration. Moreover the coupling between species being weak in this framework, the non-diagonal terms of equation 4.1 can be neglected [130]:

$$J_k^K = -L_{kk}^K \nabla \mu_k = -M_{kk} C_k \nabla \mu_k \tag{4.2}$$

For pratical reasons, diffusion is rather studied in a frame attached to one end of the sample which moves relative to the lattice-fixed frame of reference [131]. The most common one (number-fixed frame of reference) is defined by:

$$\sum_{k=1}^{s} J_k' = 0 \tag{4.3}$$

The summation is performed over the substitutional elements only, as they are considered as solely responsible for the volume of the material and equation 4.3 expresses the balance in the number of species crossing a given surface. The fluxes in this new frame J_k' must take into account its velocity v relative to the Kirkendall's frame:

$$J_k' = J_k^K - v\frac{x_k}{V_m} \tag{4.4}$$

with x_k being the molar fraction of species k and V_m the molar volume considered as equal for all substitutional elements.
Combining equations 4.3 and 4.4, the velocity can be deduced:

$$v = \frac{V_m u_k}{x_k} \sum_{i=1}^{s} J_i^K \tag{4.5}$$

$u_k = \frac{x_k}{\sum_{i=1}^{s} x_i}$ being the site fraction of element k, $i = 1..s$ standing for substitutional elements only. The diffusivities in the frame of interest can then be obtained knowing the ones in the lattice-fixed frame which can be assessed experimentally as they depend on mobilities and concentrations only:

$$J_k' = J_k^K - u_k \sum_{i=1}^{s} J_i^K = -\sum_{i=1}^{n} L_{ki}' \nabla \mu_i \tag{4.6}$$

$$\begin{cases} L_{kj}' = (\delta_{jk} - u_k) L_{jj}^K \\ \text{for the substitutional elements} \\ L_{Ij}' = -u_I L_{jj}^K \\ \text{for I interstitial and j substitutional} \end{cases}$$

It is important to notice that the factors L_{kj}' depend on composition via the site fraction u_k. It is often convenient to describe the diffusion process in terms of concentration gradients like in Fick's law. Applying the chain derivation rule and using the spatial coordinate z, one finds [132]:

$$J_k' = -\sum_{i=1}^{n} L_{ki}' \sum_{j=1}^{n} \frac{\partial \mu_i}{\partial C_j} \frac{\partial C_j}{\partial z} = -\sum_{j=1}^{n} D_{kj}' \frac{\partial C_j}{\partial z} \tag{4.7}$$

with $D'_{kj} = \sum_{i=1}^{n} L'_{ki} \frac{\partial \mu_i}{\partial C_j}$ being the intrinsic diffusion matrix.
As the n concentration gradients are not independent, mass conservation allows reducing the summation to:

$$J'_k = \sum_{j=1}^{n-1} D'^{n}_{kj} \frac{\partial C_j}{\partial z} \tag{4.8}$$

$$\begin{cases} D'^{n}_{kj} = D'_{kj} - D'_{kn} \\ \text{if j is a substitutional element} \\ D'^{n}_{kj} = D'_{kj} \\ \text{if j is an interstitial element} \end{cases}$$

with D'^{n}_{kj} being the reduced intrinsic diffusion matrix in the number-fixed frame of reference. The summation of equation 4.8 underlines that in a multicomponent environment, the diffusion of each element is influenced by all the others present in the system. Each term of the intrinsic diffusion matrix is made of two different contributions:

- **the kinetic contribution** L'_{ki} which depends on **concentration** and **mobility** whose determination requires the use of a kinetic database.
- **the thermodynamic contribution** $\frac{\partial \mu_i}{\partial C_j}$ which corresponds to the **second derivative of the Gibbs free energy relative to concentrations** whose determination requires the use of a thermodynamic database.

Thus solving a diffusion problem in a multicomponent environment means finding a solution to the following system of partial differential equations:

$$\begin{cases} \frac{\partial C_k}{\partial t} = \frac{\partial}{\partial z}(-J'_k) \\ \\ J'_k = -\sum_{j=1}^{n-1} D'^{n}_{kj} \frac{\partial C_j}{\partial z} \end{cases} \tag{4.9}$$

The mathematical concepts of diffusion that have been presented in the current section serve as basis for the different models that will be discussed in details later in this chapter.

4.1.1.2 The Calphad approach

The Calphad method whose first developments date from more than forty years now, aims at modeling the multicomponent multi-phase behavior of real materials. The latter are characterized by complex chemical interactions that cannot be described by neither the regular nor the ideal solution approximations. Only the basic principles of the method will be reviewed in the present section and the readers are encouraged to refer to comprehensive textbooks on that topic for further details [133, 134]. The idea of this approach is to represent the Gibbs free energy as a function of pressure, temperature and concentrations with adjustable coefficients that have to be optimized to represent a dedicated set of experimental data. The power of the method stems from the fact that calculations for multicomponent alloys can be performed from data assessed on different binary and ternary systems. For instance, the excess Gibbs energy G^{EX} which is due to non ideal chemical

behavior is generally represented by a series of Redlich-Kister polynomials [135] which take into account all attractive and repulsive interactions between the component atoms in each phase:

$$G^{EX} = \sum_{i,j} X_i X_j (X_i - X_j)^n . P_{ij}^n \tag{4.10}$$

where X_i, X_j are the mole fraction variables, n an exponent which is limited in practice to 3 and P_{ij}^n the weighting parameters that are stored into the dedicated thermodynamic databases. Moreover various models have been developed to account for phases with multiple sublattices, magnetic properties and order-disorder transitions. This technique has the advantage to allow the prediction of the stable phases and their thermochemical properties in regions of the phase diagrams where neither experimental nor theoretical information is available, and also applies to metastable phases that may appear during the course of a phase transformation.

Initially aiming at the prediction of phase diagrams, the Calphad approach was then extended to include transport and describe transformation kinetics. The atomic mobilities were modeled in a similar way as the Gibbs free energies. However experimental measurements of interdiffusion coefficients in materials with more than three elements are quite challenging and thus reliable diffusion data are rather scarce. That is why models allowing to extrapolate diffusivities in high order systems from experimental data obtained on lower order systems are particularly helpful. The physical parameter stored in kinetic databases is the logarithm of the atomic mobility [136]:

$$RTln(RTM_i) = RTln(M_i^0) - Q_i \tag{4.11}$$

Both the activation energy $-Q_i$ and the logarithm of the frequency factor $RTln(M_i^0)$ will in general depend on temperature, pressure and composition. The composition dependency of these two parameters is represented with a linear combination of the values at each end-point of the composition space and a Redlich-Kister expansion:

$$\Phi_B = \sum_i x_i \Phi_B^i + \sum_i \sum_{j>i} x_i x_j [\sum_{r=0}^{m} {}^r\Phi_B^{i,j} (x_i - x_j)^r] \tag{4.12}$$

where Φ_B represents $RTln(M_i^0)$ or $-Q_i$. The term Φ_B^i is the value of Φ_B for pure i and the term $\Phi_B^{i,j}$ represents binary interaction parameters of the order r. They are obtained by an optimization procedure called assessment which takes into account the available experimental and theoretical data. It has been chosen to store the mobilities rather than the interdiffusion coefficients because they are less numerous: n mobilities versus $(n-1)^2$ interdiffusion coefficients for a n-element system. The reduced diffusivity matrix can then be calculated from the mobilities through:

$$D_{kj}'^n = \sum_{i=1}^{n-1} (\delta_{ik} - u_k) x_i M_i (\frac{\partial \mu_i}{\partial x_j} - \frac{\partial \mu_i}{\partial x_n}) \tag{4.13}$$

where δ_{ik} is the Kronecker symbol and μ_i the chemical potential of element i whose derivatives with respect to composition require the access to thermodynamic data. That is why a kinetic database always need to be associated to a thermodynamic one.

4.1.1.3 Macroscopic models for long-range diffusion with precipitation

In the problem we are dealing with in this thesis, we have to consider both a macroscopic chemical gradient for diffusion, and a local driving force for precipitation. That is why emphasis will be put on existing models which combine long-range diffusion and phase transformations, especially precipitates formation or dissolution in a material subjected to a carbon or nitrogen flux. Such coupling is relevant in many practical cases such as carburization of Ni-Cr alloys [6, 7] or stainless steels [137, 138], gaseous nitriding [139, 120], carbon diffusion in welds between dissimilar steels [7, 140, 87, 79] and gradient sintering of cemented cutting tools [141].

The work of Bongartz [6] in order to predict the carburization of Ni-based alloys in atmospheres with a high carbon activity is pioneer in this field. Although it is based on the Fick's law for carbon diffusion and the kinetic and thermodynamic parameters are adjusted to fit the experimental results, its approach for combining long-range diffusion and precipitation has been retained up to now. By long-range diffusion one means that the diffusion distances in the multi-phase material are large compared to the distances between precipitates. The model consists in dividing the calculation at each time step into two parts (see Fig. 4.1): a first step of diffusion limited to the matrix phase followed by a step of precipitation. In the second part, the composition at which each carbide should appear is deduced from its equilibrium constant K and compared to the global composition after diffusion. A system of equations is then solved to obtain the carbon quantity removed from the matrix by each type of precipitate and then, a new step of diffusion can be performed. The main feature of this approach is its ability to take into account an unlimited number of carbides likely to form. For instance, Bongartz et al. forecast the precipitation of M_7C_3, M_2C, M_6C, $M_{23}C_6$ and M_3C_2 in alloy Ni-25Cr-12Co-10Mo carburized at 850°C for 1000 hours [6]. Not only the global carbon profile can be calculated but also its distribution between solid solution and precipitates.

Beside simplified empirical approaches [88, 142], the development of modern computational thermodynamics and kinetics has allowed building more sophisticated and realistic models as the one of Engström [7] referred to as "dispersed system simulation". It is nowadays mainly used to predict phase formation and concentration profiles as a result of long-range interdiffusion. The original two-stage method of Bongartz [6] was kept for the dispersed system calculation which offers the advantage to rely on thermodynamic and kinetic data determined independently of the system of interest. In the diffusion step, the diffusivity in the matrix was multiplied by a labyrinth factor (taken equal to the square of the volume fraction of the precipitates f^2) to include the fact that the diffusion paths could be partly blocked by the dispersed particles. In the equilibrium step, the volume fraction and composition of each phase (matrix and precipitates) are obtained by minimization of the Gibbs free energy of the system. The whole numerical procedure was implemented into the DICTRA software [143] linked with Thermo-Calc® for the calculation of the chemical potentials, with use of appropriate databases.

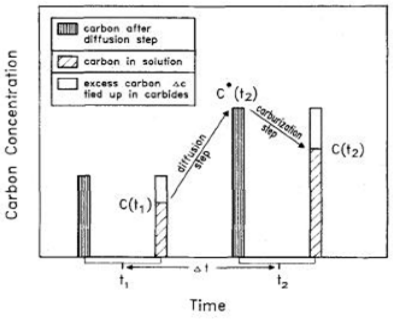

Figure 4.1: Principle of the diffusion-precipitation calculation in Bongartz's model at one grid point between the times t_1 and t_2 [6].

This approach was successfully applied to carbides formation during the carburization of Ni-Cr alloys [7] and high-temperature diffusion of carbon in a joint between a low-alloy steel and a stainless steel [8]. In both cases good agreement with the experimental observations was found. Nevertheless such models are restricted to cases with diffusion occuring in a unique and continuous matrix phase. To treat the case of a ferritic/austenitic weld at the temperature of interest, each steel has to be placed in a separate cell with a fixed interface in between [140] (see Fig. 4.2). At each time step, a condition of local equilibrium at this interface allows finding the common chemical potential for each element that is then applied as boundary condition for the subsequent diffusion calculation in each cell.

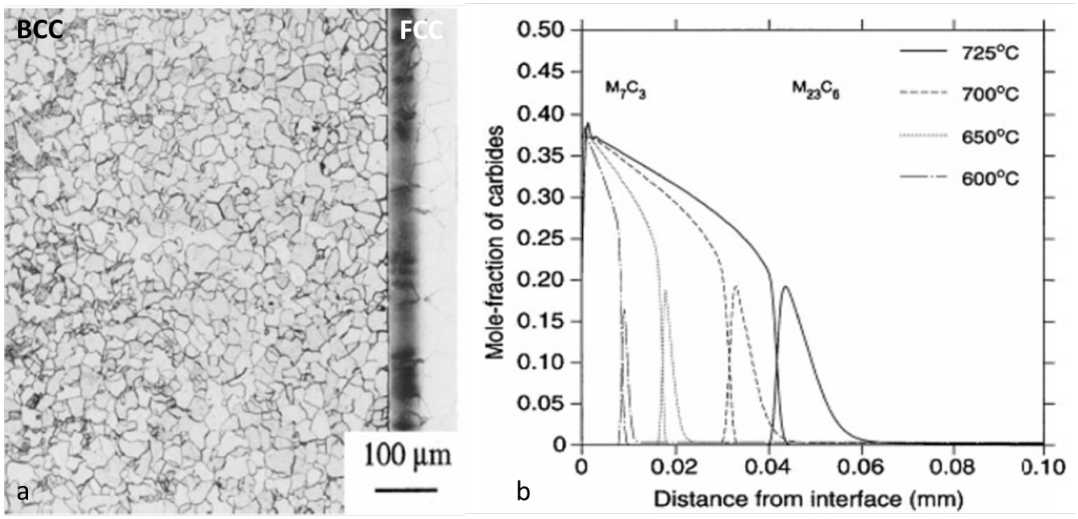

Figure 4.2: Diffusion couple between a low-alloy steel and a stainless steel annealed at 650°C for 100 h. a- Microstructure after etching. b- Results of the simulation in terms of mole fraction of carbides in the stainless steel as a function of the distance from the interface for different temperatures of heat-treatment [8].

Later the homogenization approach was developed to handle diffusion in multiphase systems, especially for the case of Fe-Cr-Ni $\alpha + \gamma$ diffusion couples [144, 145]. The 1D space was divided into slices in which local equilibrium holds and instead of the mobility in a single matrix phase, an effective mobility was obtained by averaging over all the phases in which diffusion occurs. In the lattice-fixed frame of reference the problem is therefore transformed into diffusion in an effective single phase governed by the following equation:

$$J_k = -\frac{1}{V_m}(M_k u_k)\frac{\partial \mu_k}{\partial r} = -\frac{1}{V_m}\Gamma_k^*\frac{\partial \mu_k}{\partial r} \tag{4.14}$$

where M_k, u_k, and μ_k are the mobility, the u-fraction and the chemical potential of component k, respectively. The local kinetic properties are determined by the choice of the function Γ_k^* which is calculated as the average of the product $M_k^\Phi u_k^\Phi$ (transport capacity of element k by the phase Φ) over all the phases Φ. Several homogenization functions (Wiener bounds, Hashin-Shtrikman bounds) have been implemented and are available into the software DICTRA [143]. This model has been successful in predicting the thickness of the thin fcc layer that appears after annealing a $\alpha + \gamma/\gamma + \alpha$ diffusion couple for 100 h at 1100°C [144]. However the application of this model at lower temperatures (T<800°C) is not fully satisfying in some cases where the hypothesis of local equilibrium does not give the right amount of phases, especially for stainless steels.

All the models described above are relatively easy to use as they only need temperature, global composition, thermodynamic and kinetics databases as inputs. However they are based on the assumption that local equilibrium is established at each space node in each time step. Phases formation and dissolution are considered as immediate and the kinetics of precipitation is not taken into account.

4.1.2 Modeling the precipitation kinetics

Precipitation is a special case of phase transformation when the daughter phase consists of particles whose size is very small (from few nanometers to few micrometers) in comparison to the one of the parent phase generally called matrix phase. The precipitation sequence is usually divided into three different stages [10]:

- **Nucleation:** It is a stochastic process during which local fluctuations in temperature and/or composition allow nuclei to form. During this stage the number density of particles with a critical radius r^* increases with time.

- **Growth:** It is a deterministic process during which new atoms bind to the initial nucleus leading to an increase of both the mean radius and the volume fraction.

- **Coarsening:** Once the equilibrium volume fraction has been reached, small precipitates dissolve under the curvature-induced pressure called Gibbs-Thomson effect. The volume fraction remains nearly constant whereas the number density of particles decreases and the mean radius increases.

4.1.2.1 Nucleation: early stages of decomposition

The driving force for microstructural changes during precipitation of a new phase from the supersaturated solid solution is the reduction of the free energy that, for a spherical nucleus of radius r, can be written as:

$$\Delta G(r) = \frac{4}{3}\Pi r^3(\Delta g_{ch} + \Delta g_{el}) + 4\Pi r^2\gamma \tag{4.15}$$

The first term ($\Delta g_{ch}<0$) is the chemical part and represents the gain of free energy on forming the particle. The two others are detrimental (>0) as Δg_{el} is the strain energy term and the last one the energy necessary to form a new interface (γ being the interfacial energy). The resulting ΔG versus the size of the cluster r is plotted in Figure 4.3 and passes through a maximum for $r = r^*$. Clusters of radius r^* are in unstable equilibrium with the solid solution and only those with a radius larger than r^* are predicted to grow. The associated critical free energy called activation barrier for nucleation is:

$$\Delta G^* = \frac{16\Pi}{3}\frac{\gamma^3}{(\Delta g_{ch} + \Delta g_{el})^2} \tag{4.16}$$

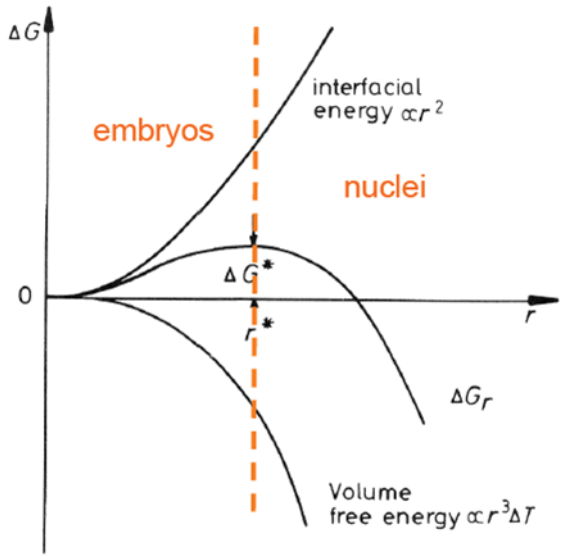

Figure 4.3: Schematic of the free energy changes associated with precipitate formation as a function of cluster radius r.

The Classical Nucleation Theory (CNT) extended to multi-component systems leads to the following expression for the nucleation rate [10, 146]:

$$J = \frac{\partial N}{\partial t} = N_0 Z\beta^* exp(\frac{-\Delta G^*}{kT})exp(\frac{-t}{\tau}) \tag{4.17}$$

T being the absolute temperature, k the Boltzmann constant and t the time. N_0 represents the

total number of potential nucleation sites. The Zeldovich factor Z [147] takes into account that there remains some probability to dissolve for a nucleus slightly larger than the critical size. This thermodynamic quantity is given by:

$$Z = [\frac{-1}{2\Pi kT}\frac{\partial^2 \Delta G}{\partial n^2}|_{n=n*}]^{1/2} = [\frac{a^6}{64\Pi^2 kT}\frac{(\Delta g_{ch} + \Delta g_{el})^4}{\gamma^3}]^{1/2} \tag{4.18}$$

n is the number of atoms in the nucleus, the derivative of ΔG being taken at the critical nucleus size n^*. The last term of equation 4.18 corresponds to the calculation of the second derivative in the case of a spherical nucleus, a being the inter-atomic distance. The atomic attachment rate β^* in Equation 4.17 takes into account the diffusive transport of atoms and its expression for multi-component systems was proposed by Svoboda et al. [9]:

$$\beta^* = \frac{4\Pi r^{*2}}{a^4 V_m}[\sum_{i=1}^{n}\frac{(C_{ki} - C_{0i})^2}{C_{0i}D_{0i}}]^{-1} \tag{4.19}$$

C_{ki} and C_{0i} are the concentrations of element i in the precipitate with index k and in the matrix, respectively. D_{0i} is the diffusivity of element i in the matrix. τ is the incubation time for nucleation:

$$\tau = \frac{1}{2\beta^* Z^2} \tag{4.20}$$

4.1.2.2 Growth kinetics

Multi-component problem formulation (restriction to 2 phases)

Let's consider a multi-component system with a precipitate β growing into a matrix phase α. Inside both phases, the flux of each element i is related to the chemical compositions by the modified Fick's first law:

$$\begin{aligned} J_i^\alpha &= -\sum_{j=1}^{n-1} D_{ij}^\alpha \nabla C_j^\alpha \\ J_i^\beta &= -\sum_{j=1}^{n-1} D_{ij}^\beta \nabla C_j^\beta \end{aligned} \tag{4.21}$$

However at the precipitate/matrix interface the fluxes $J_i^{\alpha\beta}$ (into the precipitate) and $J_i^{\beta\alpha}$ (into the matrix) are unbalanced. They are compensated by the motion of the phase boundary at the velocity v satisfying the mass balance equation:

$$J_i^{\alpha\beta} + J_i^{\beta\alpha} = (C_i^{\beta\alpha} - C_i^{\alpha\beta}).v \tag{4.22}$$

where $C_i^{\beta\alpha}$ and $C_i^{\alpha\beta}$ are the interfacial compositions on the precipitate and matrix side, respectively, $J_i^{\alpha\beta}$ the flux into the phase boundary and $J_i^{\beta\alpha}$ the one out of the phase boundary. Thus solving

the moving boundary problem means determining the 2(n-1)+1 unknowns, (n-1) compositions on each side of the interface and 1 velocity of the phase boundary. However mass balance provides only (n-1) equations and an additional hypothesis is needed. The most common one is the local equilibrium hypothesis which assumes fast interfacial reactions and so negligible chemical potential gradients across the phase boundary, providing the n missing equations:

$$\mu_i^{\alpha\beta} = \mu_i^{\beta\alpha} \tag{4.23}$$

Although the moving boundary problem is fully determined in the case of 2 phases, analytical solutions can only be obtained for a binary alloy, the interfacial compositions being fixed by a unique equilibrium tie-line [148].

Exact solution of the multi-component growth (DICTRA's approach)

Contrary to the case of a binary alloy, it is no longer possible to determine a unique interfacial composition for higher-order systems. In fact there is an infinite number of tie-lines satisfying the local equilibrium composition for 2 phases in contact. In the DICTRA software [143] the operative tie-line is determined iteratively taken into account the need of a unique value for the velocity v of the interface and the diffusion properties of the different species. It is important to emphasize the complexity of such a procedure as the operative tie-line is continuously evolving during the course of the precipitation reaction. However this rigorous approach has been successful in predicting the temporary existence of metastable precipitates [149] as well as the various growth regimes of fast and slow reactions and the transition between them [130]. As illustrated on Figure 4.4, the simultaneous and competitive growth of cementite, $M_{23}C_6$ and M_7C_3 was studied in ferritic Fe-Cr-C alloys [150, 132] and the effect of a change in global composition was investigated (see Fig. 4.4-a,b,c). In the case of Fe-7.3Cr-0.12C a regime of local equilibrium without partitioning of the substitutional elements (LENP) takes place at the early stages and cementite grows with the same Cr/Fe ratio as the matrix (see Fig. 4.4-d). In such simulations no nucleation is considered (a small nucleus is placed in each cell in the initial state) but the effect of interfacial energy on growth can be added.

The full calculation of the coupling between long-range diffusion and interface movement is computationally expensive and is limited to a small number of interacting precipitates. That is why simplified models adapted to a faster resolution by numerical methods have been developed. With this in mind, J. Ågren's group has chosen to replace the full calculation of the diffusion fields around and inside the precipitates by suitable analytical profiles and has obtained a good agreement with the DICTRA simulations for the growth rate of $M_{23}C_6$ carbides in ferritic alloys [151]. This approach has been implemented into the software TC-PRISMA [152].

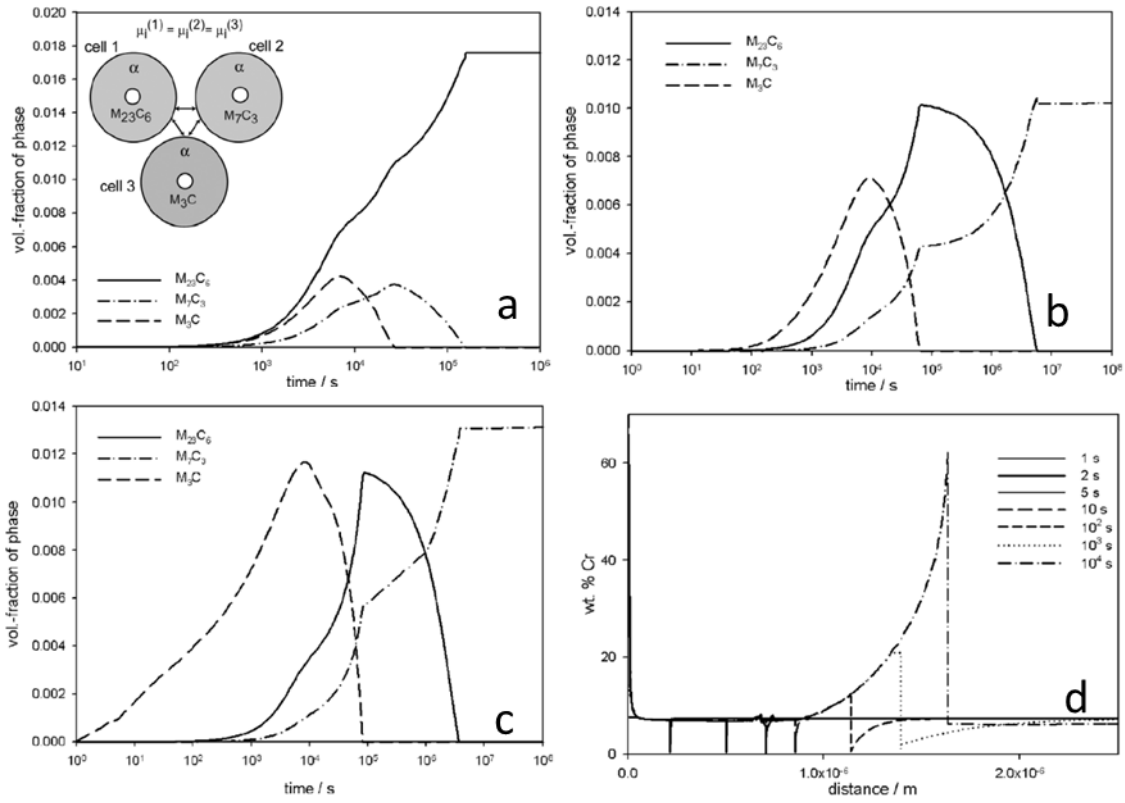

Figure 4.4: Results of DICTRA simulations [132] for the competitive growth of M_3C, $M_{23}C_6$ and M_7C_3 carbides a- in Fe-12Cr-0.1C at 1053 K. b- in Fe-7.3Cr-0.1C at 1053 K. c- in Fe-7.3Cr-0.12C at 1053 K. d- Cr profile in Fe_3C in the early time steps of the simlation c.

Mean-field treatment of precipitation growth (MatCalc's approach)

The present section will give a brief review of the SFFK model [9]. It is a mean-field approach based on the Onsager's thermodynamic extremum principle [153, 154] to derive the evolution equations for the precipitates radius and composition. It postulates that a thermodynamic system evolves along the particular kinetic path where maximum entropy is produced. If we consider a n-component system with m randomly distributed precipitates with spherical diffusion fields, its total Gibbs free energy G can be written as:

$$G = \sum_{i=1}^{n} N_{0i}\mu_{0i} + \sum_{k=1}^{m} \frac{4\Pi r_k^3}{3}(\lambda_k + \sum_{i=1}^{n} C_{ki}\mu_{ki}) + \sum_{k=1}^{m} 4\Pi r_k^2 \gamma_k \tag{4.24}$$

N_{0i} is the number of moles of element i in the matrix and μ_{0i} the associated chemical potential. λ_k is the elastic strain energy due to lattice misfit, C_{ki} the concentration of element i in the precipitate k and μ_{ki} the associated chemical potential. γ_k denotes the energy associated to the interface between precipitate k and the matrix. The first term of equation 4.24 corresponds to the Gibbs free energy of the matrix, the others to the Gibbs free energy of the precipitates (elastic, chemical and

interfacial contributions). During a precipitation reaction, the total Gibbs free energy is decreased until equilibrium is reached. In the SFFK model three dissipative processes Q are considered:

- **the migration of interfaces** with mobilities M_k

$$Q_1 = \sum_{k=1}^{m} \frac{4\Pi r_k^2 \dot{r_k^2}}{M_k} \tag{4.25}$$

  $\dot{r_k}$ being the rate of growth of the radius of precipitate k.

- **the diffusion of all components in the precipitates**

$$Q_2 = \sum_{k=1}^{m}\sum_{i=1}^{n} \int_0^{r_k} \frac{RT}{C_{ki}D_{ki}} 4\Pi r^2 j_{ki}^2 dr = \sum_{k=1}^{m}\sum_{i=1}^{n} \frac{4\Pi RT r_k^5}{45 C_{ki}D_{ki}} \dot{C_{ki}^2} \tag{4.26}$$

  j_{ki} being the diffusive flux of element i inside the precipitate k and R the universal gas constant.

- **the diffusion of all components in the matrix**

$$Q_3 = \sum_{k=1}^{m}\sum_{i=1}^{n} \int_{r_k}^{Z} \frac{RT}{C_{0i}D_{0i}} 4\Pi r^2 J_{ki}^2 dr \tag{4.27}$$

  J_{ki} being the diffusive flux of element i from the precipitate k into the matrix and Z a characteristic length between two precipitates. Such an expression is based on the assumption that the distance between the individual precipitates is sufficiently large and their diffusion fields do not overlap.

By maximizing the Gibbs free energy dissipation rate $\dot{G}$, a decoupled system of linear equation is obtained for the growth rate $\dot{r_k}$ and the rate of change of chemical composition $\dot{C_{ki}}$ of each precipitate:

$$\sum_{i=1}^{n-1} A_{ij} \dot{y_j} = B_i \tag{4.28}$$

where the variable $\dot{y_j}$ represents the rates $\dot{r_k}$ and $\dot{C_{ki}}$ as well as the Lagrange multipliers due to the stoechiometric constraints of the precipitates. For more details concerning the maximization procedure and the exact values of the coefficients A_{ij} and B_i the interested reader should refer to [10, 155]. It is important to notice that no interfacial composition is calculated by this mean-field model, only mean compositions of matrix and precipitates are considered in the evolution equations.

When the equilibrium phase fraction is reached, there still remains a driving force for precipitates distribution rearrangement driven by curvature-induced pressure also called Gibbs-Thomson effect [156]. As the solute content in the matrix at the interface with a precipitate depends on the size of the particle, a solute flux occurs from the small precipitates to the larger ones. Consequently the latter grow at the expenses of the smaller ones, allowing a release of excess interfacial energy. This stage referred to as coarsening or Ostwald ripening reduces the precipitate number density while the mean radius is increasing. The SFFK approach includes both growth and coarsening that often occur simultaneously.

4.1.2.3 Special features included in the MatCalc software

The software package MatCalc [113, 9, 157] was employed for the diffusion and phase transformations simulation embedded in this work. Some of its main specific characteristics will be briefly described in this section.

Heterogeneous nucleation

The number of potential nucleation sites (N_0 in equation 4.17) together with their type highly depend on the microstructure of interest and their choice greatly influences the course of precipitation. If homogeneous nucleation is considered, every substitutional atom of the bulk can serve as a nucleation site ($N_0 = N_A/\nu^\alpha$ where N_A is the Avogadro number and ν^α the molar volume). However in most cases, nucleation occurs on defects such as dislocations, grain or subgrain boundaries. Their disordered nature facilitates microscopic fluctuations and diffusion while their disappearance when the precipitate grows leads to an energy gain for the system. In the MatCalc software a realistic microstructure representation was developed with grains and subgrains being approximated by an arrangement of tetrakaidecahedra (14-sided polyhedra) as shown in Figure 4.5. Their shape allows filling space with a minimum volume loss and a minimum surface area. They can also be shrunk or stretched to simulate martensitic laths (see Fig. 4.5-b,c). Nucleation can occur on their faces (2-dimensional), their edges (1-dimensional) or their corners (0-dimensional). Concerning dislocations, the number of sites along them can be estimated by ρ/a where ρ is the dislocation density and a the mean atomic distance. For each type of nucleation sites, the detailed calculation and mathematical expression of their number as a function of the microstructural parameters can be found in reference [10].

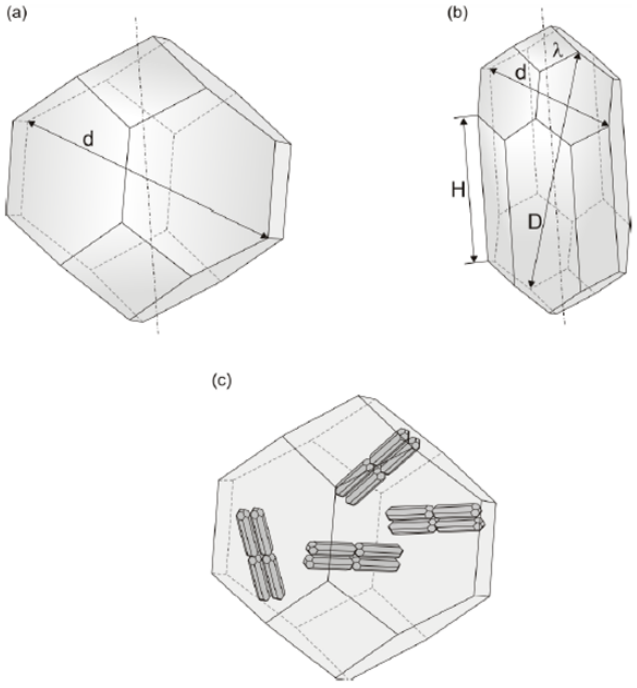

Figure 4.5: Tetrakaidecahedra used in MatCalc to describe the matrix microstructure and determine the number of potential nucleation sites, a- symmetric grain b- elongated grain c-grain and subgrains [10].

Each growing precipitate is surrounded by a diffusion field inside which the driving force for another nucleation event is lowered. To take this phenomenon into account, the MatCalc software allows disabling nucleation inside a spherical volume centered on the precipitate. The inactive radius factor gives the radius of this sphere and can usually be varied between 1 and 5 times the radius of the growing precipitate.

Calculation of the interfacial energy

The interfacial energy γ is a crucial parameter which significantly influences precipitation kinetics (especially nucleation but also growth and coarsening). In fact the critical energy for nucleus formation ΔG^* is proportional to γ^3 and ΔG^* appears in an exponential in the nucleation rate J. However this quantity is usually not known and delicate to measure. Thus it is often used as a fitting parameter to adjust the simulation results to experimental data.

In MatCalc, this quantity is evaluated by a generalized broken-bond approach for n-nearest neighbors based on thermodynamic input data [158]. A planar sharp interface between matrix and precipitate is considered and its energy is calculated as:

$$\gamma_0 = \frac{n_S.Z_{S,eff}}{N_A.Z_{L,eff}}\Delta E_{sol} \tag{4.29}$$

where ΔE_{sol} is the enthalpy of solutionizing, n_S the number of atoms per unit interface area, N_A the Avogadro number. $Z_{S,eff}$ represents the number of broken bonds across the interface per atom while $Z_{L,eff}$ stands for the number of neighbors of an atom. The subscript "eff" indicates that not only the first nearest neighbors have been taken into account but also the longer distance interactions. In ref. [158] the structural factor $Z_{S,eff}/Z_{L,eff}$ is derived up to 100 nearest-neighbor shells in fcc ($Z_{S,eff}/Z_{L,eff} \approx 0.329$) and bcc ($Z_{S,eff}/Z_{L,eff} \approx 0.328$) systems. This approach gives a good assessment of the interfacial energy in the case of large precipitates but greatly overestimates the value in the case of small precipitates (nucleation stage) due to the strong size-dependency of the parameter $Z_{S,eff}$. Thus a size correction factor was introduced to account for the effect of interface curvature [159]:

$$\gamma = \alpha(r).\gamma_0 = [1 - \frac{6}{11}\frac{r_1}{r} + 0.08921\frac{r_1^2}{r^2} + 0.045\ln(\frac{10}{3}\frac{r}{r_1})\frac{r_1^2}{r^2}].\gamma_0 \tag{4.30}$$

with r_1 being the nearest neighbor distance and r the precipitate radius. As can be seen on Figure 4.6, the correction factor $\alpha(r)$ takes values between 0.7 and 0.85 for typical cluster radii during nucleation (size between 1.5 and 3 times r_1). An additional correction factor β (<1) must be added to consider the entropic contributions from finite interface thickness [160]. This effect is particularly significant for coherent precipitates near their solvus temperature. Thus the interfacial energy γ is computed by MatCalc from the thermodynamic information of the CALPHAD databases as a temperature- and composition-dependent variable and is finally expressed as:

$$\gamma = \alpha(r).\beta.\gamma_0 \tag{4.31}$$

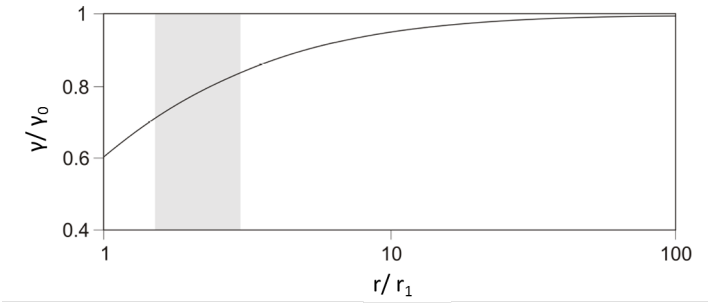

Figure 4.6: Size correction function used in MatCalc for the calculation of the interfacial energy [10].

Numerical implementation

The time integration is performed within the widely used Numerical Kampmann-Wagner (NKW) approach [161]. It consists in subdividing the precipitates population into size classes containing precipitates of identical radius and chemical composition. The global heat-treatment is also discretized into small isothermal time increments and the Euler forward integration scheme is applied to integrate the evolution equations under the constraint of mass conservation. At each time step, the nucleation rate is evaluated for each precipitate type and new size classes can be created. For each of the existing classes, the integration of the growth equations leads to an update of the radius and composition of the class. An implicit treatment of the coarsening stage is obtained by maintaining the size classes with a radius lower than r^* into the distribution. They are fully considered in the integration algorithm but are assigned a negative growth rate. If the radius of a given class decreases below a given threshold, the class is removed, allowing the total number of precipitates to decrease. And if the number of size classes exceeds a given upper limit, a rearrangement of the classes is performed by the software.

4.1.3 Coupling long-range diffusion and precipitation kinetics

Up to now very few models have attempted to include precipitation kinetics into long-range diffusion calculations. As described before (see Section 4.2.1) most of the authors have considered the precipitation rate as very high compared to the diffusion rate and have applied the assumption of local equilibrium to deduce how the precipitation state evolves into the material. Moreover, concerning experiments, measuring the particles volume fraction at different depths is a rather demanding work.

To the knowledge of the author, the challenge of coupling long-range diffusion and precipitation kinetics has been tackled by one research group only, for modeling the nitriding of FeCr alloys [120]. As depicted on the schematic of Figure 4.7, they were able to predict the gradient in precipitates parameters (mean radius, number density, volume fraction) from the surface to the interior of the material. Their results displayed a better agreement with available experimental data than previous

studies based on thermodynamic equilibrium only. Close to the surface a high density of small CrN particles was found, which results from the large driving force for precipitates nucleation due to the high nitrogen content. As nitrogen needs time to diffuse to the interior of the sample, the precipitation there starts later with a lower final density of particles and a larger mean radius. Although the model leads to a good qualitative description of the microstructural gradient across the material, several simplifications (constant interfacial energy, equilibrium nitrogen solubility, spherical shape of the precipitates, diffusion coefficient taken independent of the nitrogen content, fixed composition of the nitride CrN) may be responsible for the poor quantitative agreement with the experimental data, especially in terms of precipitate mean radius.

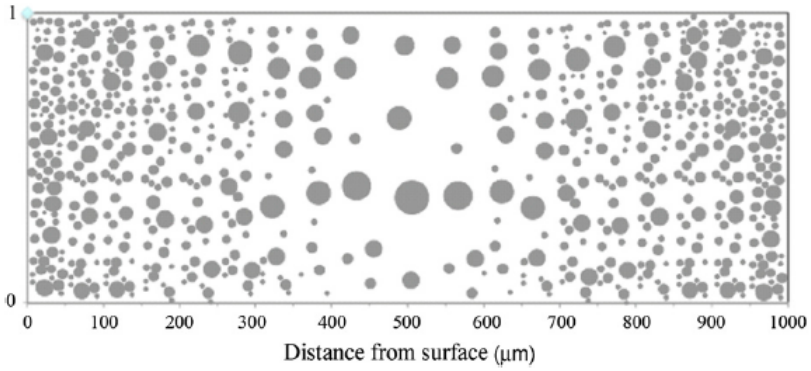

Figure 4.7: Schematic representation of the precipitate size distribution in the cross-section of a Fe-1wt.%Cr nitrided at 823K for 50400s [120].

4.2 Results

4.2.1 Coupling long-range diffusion and equilibrium precipitation

In this section, the classical approach for addressing carbon diffusion in a dissimilar weld has been applied to the 18MND5-309L interface subjected to the post-weld heat-treatment. It has resulted in building a mesoscopic thermo-kinetics model coupling long-range diffusion to equilibrium precipitation. This model has been implemented into the MatCalc software.

4.2.1.1 Design of the simulation

The region of the weld concerned by these phase transformations is considered over 1.5 mm and is divided into three adjacent zones: the base metal 18MND5, the martensitic intermediate layer with a fixed thickness of 50 μm and the 309L austenitic weld metal, each of them being characterized by an initial content in Fe, Cr, Ni and C as well as a matrix phase (see Table 4.1). The one dimensional space is split into 40 cells, their size being finer next to the interfaces between the previously described zones down to 5 μm (see schematic of Figure 4.8-a).

Table 4.1: Settings used for the diffusion/equilibrium precipitation simulation in terms of matrix phases and initial compositions.

	Matrix phase	Cr (wt.%)	Ni (wt.%)	C (wt.%)
Base metal	BCC	0.18	0.74	0.2
Martensitic layer	BCC	11	6	0.1
Weld metal	FCC	18	9	0.05

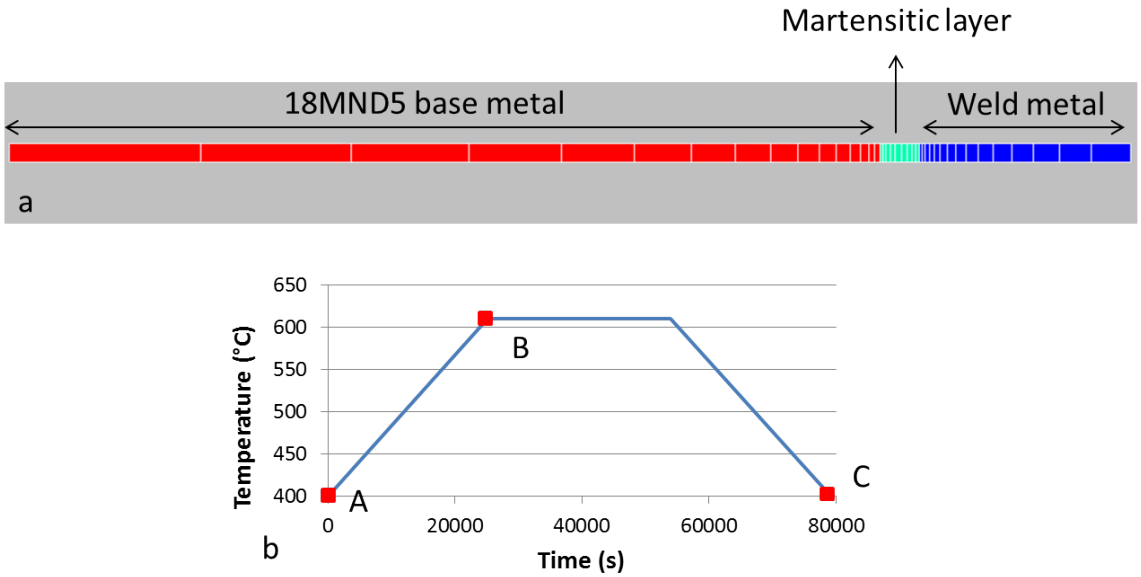

Figure 4.8: Design of the simulation: a- geometry with 1D mesh, b- heat-treatment.

The multi-component diffusion equation (see Equation 4.9) is solved with respect to the matrix content of each element by the finite differences technique. Implicit discretization is chosen leading to the following expression for the diffusion of element A in a multi-component environment in the case of variable diffusion coefficient and cell size:

$$[1+\sum_k D_{Ak}\Delta t(\frac{1}{(\Delta x_{i+1})^2}+\frac{1}{(\Delta x_{i-1})^2})]C^{t+}_{A,i}-\sum_k \frac{D_{Ak}\Delta t}{(\Delta x_{i+1})^2}C^{t+}_{k,i+1}-\sum_k \frac{D_{Ak}\Delta t}{(\Delta x_{i-1})^2}C^{t+}_{k,i-1}=C^t_{A,i} \quad (4.32)$$

$C^{t+}_{k,i}$ being the content of element k in the cell i at the time $(t+\Delta t)$, Δx_{i-1} the distance between cells i and i-1 and Δx_{i+1} between cells i and i+1. At both extremities a fixed composition is maintained as boundary condition. When calculating the diffusional fluxes between two cells with different matrix phases, the diffusion coefficient (normally taken as the mean value of the ones in each cell) is here multiplied by a trans-interface enhancement factor to mimic the effect of fast transfer across a stationary phase boundary. After the diffusion step, the thermodynamic equilibrium between the matrix phase and the precipitates is evaluated in each cell. The precipitates allowed to form are M_7C_3, $M_{23}C_6$ and M_3C with M standing for the metallic elements. By this approach, the precipitates are not considered individually as only their composition and volume fraction are made accessible. As atoms are picked up to be bound to the precipitates, changes in the matrix composition result, so these atoms do not participate to the next diffusion step. The post-welding heat-treatment was considered between 400 and 610°C with a temperature plateau at 610°C for 8 hours and heating and cooling rates of 30°C/h (see Fig. 4.8-b). Indeed significant carbon diffusion can occur in the BCC matrices even at 400°C, as shown by the values of the diffusion coefficients in Table 4.2.

Table 4.2: Carbon and chromium diffusion coefficients calculated with the thermodynamic mc-fe.tdb and kinetics mc-fe.ddb databases included in MatCalc [114] for the initial compositions displayed in Table 4.1.

Diffusion coefficients [m^2/s]	D_{CC}(400°C)	D_{CC}(610°C)	D_{CrCr}(400°C)	D_{CrCr}(610°C)
Base metal (BCC)	3.0×10^{-13}	1.4×10^{-11}	2.1×10^{-25}	9.3×10^{-20}
Martensitic layer (BCC)	1.8×10^{-13}	9.8×10^{-12}	1.9×10^{-24}	4.5×10^{-19}
Weld metal (FCC)	3.3×10^{-18}	7.2×10^{-15}	7.2×10^{-27}	1.5×10^{-21}

4.2.1.2 First results

The results of the simulation in terms of element contents, carbon chemical potential and precipitates volume fraction are displayed on Figure 4.9. In agreement with the low diffusion coefficients of substitutional elements in the temperature range of interest (see Table 4.2 for Cr) only carbon was found to significantly diffuse during the heat-treatment (see Fig. 4.9-a,b).

During the heating ramp from 400 to 610°C, some carbon diffusion already occurred in the BCC matrices from the base metal towards the martensite as expected given the values of the diffusion coefficients and the huge gap in the initial carbon chemical potential between the low-alloyed base metal and the high-alloyed martensite ($\Delta\mu \approx -68$ kJ/mol on Figure 4.9-d). As a consequence, the

base metal decarburized over 65 μm whereas carbon enrichment of the martensitic layer took place with a maximum global carbon content at 1.2 wt.% at the interface with the base metal (see Fig. 4.9-b).

This diffusion was found to go on during the temperature plateau at 610°C leading to a final decarburization distance of 166 μm in the base metal, with cementite being totally dissolved over 120 μm (see Fig. 4.9-c). Chromium-rich carbides M_7C_3 and $M_{23}C_6$ were predicted to appear in the martensitic band which is in good agreement with the nature of the precipitates identified by the Astar scans on the extraction replicas (see Section 3.3.2.1). However their volume fraction (up to 18% at the end of the heat-treatment) was slightly overestimated as a maximum of 14% was measured by FIB serial cuts (see Fig. 3.17). The main discrepancy between simulation and experimental measurements is related to the diffusion into the austenitic weld metal: it was calculated to span over less than 5 μm (see Fig. 4.9-b) whereas an increased carbon content was detected over 70 μm by both SIMS and WDS.

In order to investigate the reasons for this divergence and simplify the configuration under study, a simulation was conducted without the martensitic band, the austenitic weld metal being directly in contact with the base metal. Such a simulation was intended to outline the role played by the intermediate martensitic band in the carbon transfer from the base metal to the weld metal. As can be seen on Figure 4.10-a, without any martensitic layer, carbon was found to have diffused over 26 μm inside the austenite at the end of the heat-treatment. It is greater than in the case with the martensite but still not enough in light of the experimental measurements. In both cases (with and without martensite) the carbon content of the BCC matrix (base metal or martensite depending on the case involved) adjacent to the weld metal at the end of the heating ramp (25200 s) was very low:

- $W_{BCC}(C) = 2.6 \times 10^{-5}$ $wt.\%$ in the presence of martensite
- $W_{BCC}(C) = 1.8 \times 10^{-3}$ $wt.\%$ without any martensite

Thus there was almost no carbon available in the BCC matrix to diffuse into the FCC during the isothermal part of the heat-treatment. This is certainly due to the fact that the carbides (especially M_7C_3 and $M_{23}C_6$) are highly stable and pull all the carbon out of the solid solution as the matrix content is constrained to its equilibrium value (no supersaturation allowed).

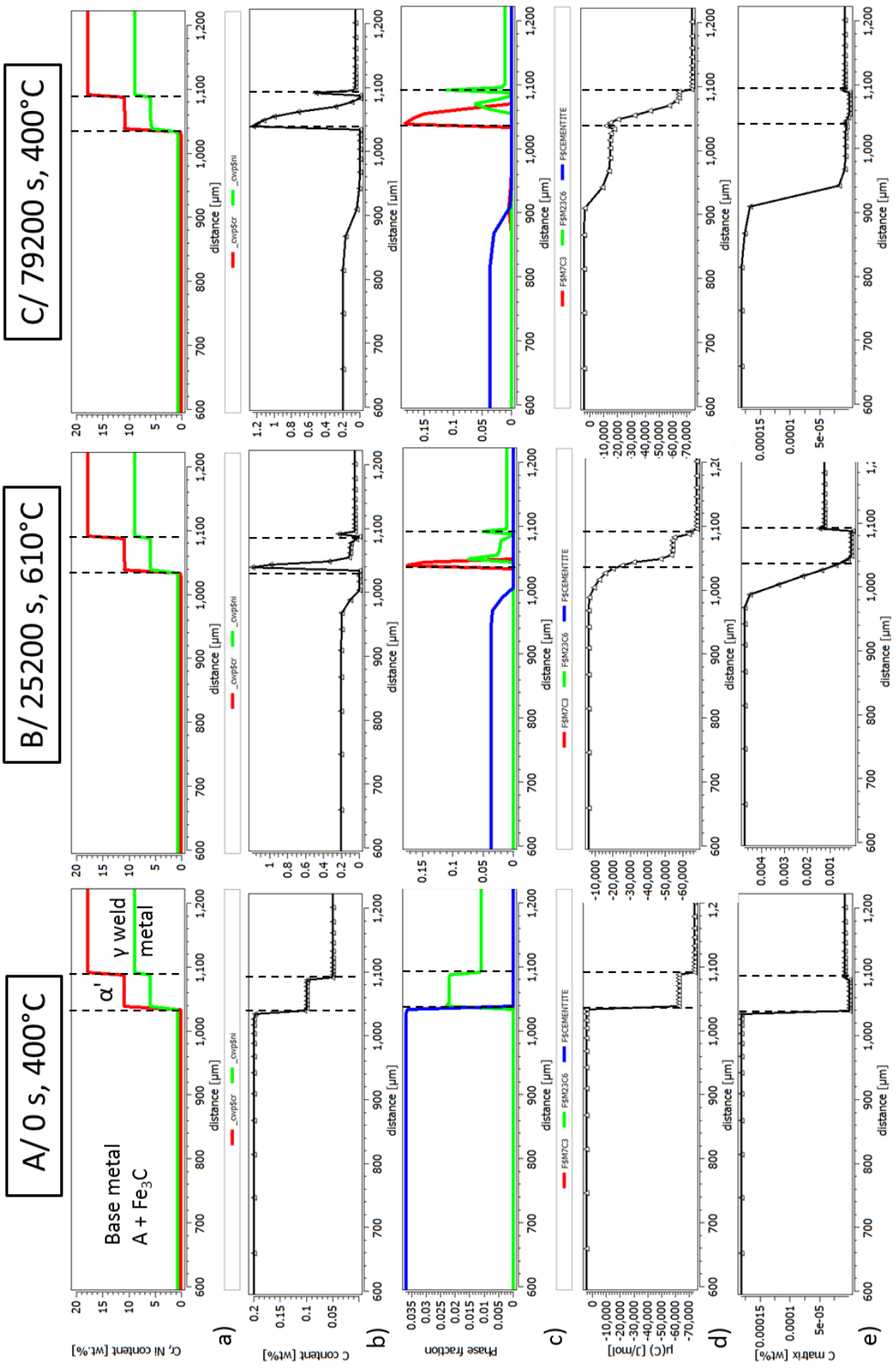

Figure 4.9: Results of a non-isothermal simulation of diffusion with equilibrium precipitation for times A, B and C on the heat-treatment of Figure 4.8-b. a- Substitutional elements content b- Carbon content c- Precipitates volume fractions d- Carbon chemical potential e- Matrix carbon content.

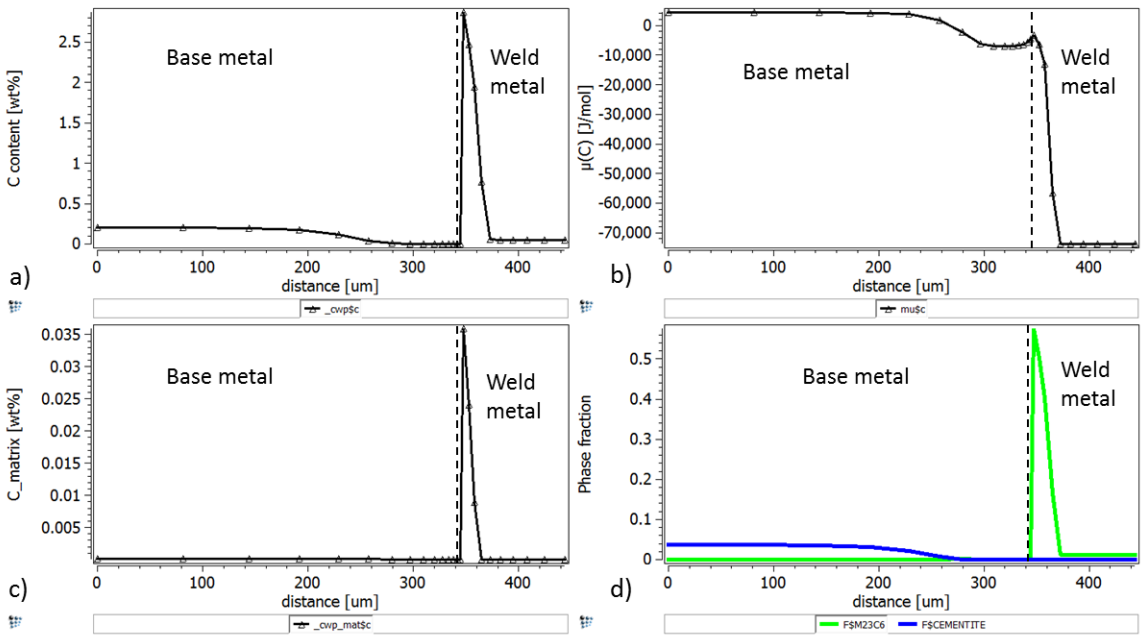

Figure 4.10: Results of a non-isothermal simulation of diffusion with equilibrium precipitation for an hypothetical weld between the base metal and the weld metal without any martensitic band a- Carbon content; b- carbon chemical potential; c- matrix carbon content; d- precipitates volume fractions at the end of the heat-treatment (time C on Fig. 4.8-b).

4.2.1.3 Diffusion enhancement

A simulation was performed with increased diffusion coefficients in order to estimate the enhancement necessary to reproduce the measured carbon profile across the weld. The best agreement was obtained by multiplying the carbon diffusion coefficient by 8 in the BCC matrices and by 400 in the FCC and can be seen on Figure 4.11 where the simulation results were compared to WDS measurements.

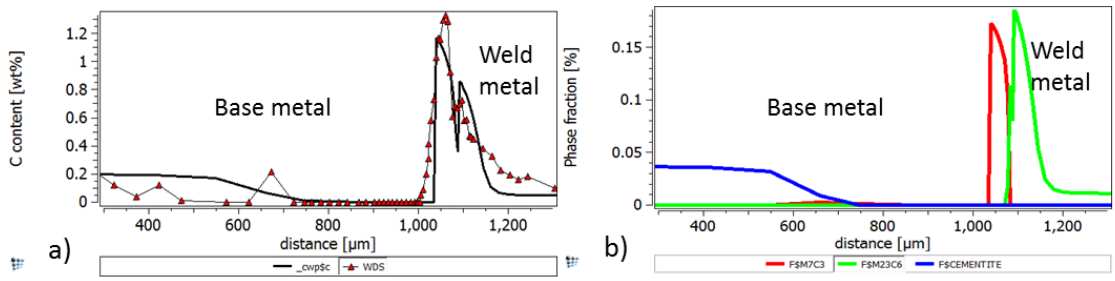

Figure 4.11: Results of a non-isothermal simulation of diffusion with equilibrium precipitation and enhanced carbon diffusion coefficients (×8 in the BCC phases and ×400 in the FCC) a- Carbon content calculated and measured by WDS b- Calculated precipitates volume fraction.

In a real microstructure, diffusion can usually be enhanced by the presence of defects such as dislocations and grain boundaries. In their neighborhood, the lattice is expanded, allowing the solute atoms to move much faster than in the undisturbed bulk crystal. These short-circuits will contribute to the total amount of diffusion according to their weighted fractions [162]:

$$M = \rho b^2 M_{dislo} + \frac{\delta}{d} M_{gb} + (1 - \rho b^2 - \frac{\delta}{d}) M_{bulk} \tag{4.33}$$

where M denotes the mobility of carbon, ρ the dislocation density, b the Burgers vector ($\approx$ 0.3 nm), δ the thickness of the grain boundary ($\approx$ 1 nm) and d the grain diameter. According to the diffusion rate theory, each mobility takes the form of:

$$M = \frac{M_0}{RT} exp(\frac{-Q}{RT}) \tag{4.34}$$

with the prefactor M_0 and the activation energy Q being considered independent of the temperature. Grain boundaries and dislocations are assumed to contribute with the same frequency factor as the bulk and a modified activation energy:

$$\begin{aligned} M_{gb} &= \frac{M_0^{bulk}}{RT} exp(\frac{-k^{GB} Q_{bulk}}{RT}) \\ M_{dislo} &= \frac{M_0^{bulk}}{RT} exp(\frac{-k^{dislo} Q_{bulk}}{RT}) \end{aligned} \tag{4.35}$$

with 0.5 and 0.8 being typical values of the energy multipliers k^{GB} and k^{dislo} respectively [163]. Extracting the bulk mobility of carbon in the martensite at 400°C ($M^C_{BCC} = 3.3 \times 10^{-17}$) and 610°C ($M^C_{BCC} = 1.3 \times 10^{-15}$) from the dedicated Calphad-type databases allows to calculate M_0^{bulk} and Q_{bulk} according to Equation 4.34 and then deduce M_{gb} and M_{dislo} from Equation 4.35. A dislocation density of $2.9 \times 10^{18}/m^2$ ($6.7 \times 10^{18}/m^2$) is found to be necessary to achieve a global carbon mobility value in the martensite 8 times higher than in the bulk at 400°C (610°C). Such values are not realistic, and even in the case of highly dislocated microstructures after welding, some recovery should happen during the heat-treatment, and consequently lowering the dislocation density. Concerning the subgrains, a width d of 571 nm (79 nm) results in an enhancement of 8 on the global mobility at 400°C (610°C). These values are realistic, especially at low temperature, as the width of the martensitic laths was measured around 400 nm. However the large enhancement factor (400) needed for the austenitic part of the weld can certainly not be explained this way because the grains are large (about 50 μm) and typical values for the dislocation density in austenite are around 10^{12} $/m^2$.

Another potential enhancement factor for carbon diffusion is the presence of stress gradients (Gorsky effect) [164]. Cases of stress-induced diffusion have been reported during the nitriding of stainless steels at low temperatures [165, 166], compressive stresses being generated by the gradient in interstitial solute fractions. The stress gradient is usually considered as an additional contribution to the driving force for diffusion $\Delta\mu$:

$$\Delta\mu(X_c, \sigma) = \Delta\mu(X_c, \sigma = 0) - V_c \Delta\sigma \tag{4.36}$$

where σ stands for the stress and V_c for the partial molar volume of carbon in the FCC matrix ($V_c = 3.78 \times 10^{-5}\ m^3/mol$). $\Delta\mu(X_c, \sigma = 0)$ is the chemical potential gradient in the absence of stresses which depends on composition only (X_c) and can be obtained from a thermodynamic database. The stress state σ is reported to be directly proportional to the amount of interstitial atoms in solid solution X_c:

$$\sigma = \lambda . X_c \tag{4.37}$$

the constant λ being estimated at approximately 200 MPa/at.% in the case of nitrogen [167], which is known to be extremely efficient for austenite strengthening. If we consider that no precipitates form and the carbon atoms in the austenite at the interface with the martensite ($w(C) = 0.8$ wt.%) are all located on the octahedral sites of the FCC matrix, the expected stress increase given by Equation 4.37 is about 7 MPa. It leads to a stress contribution to the diffusion driving force of 265 J/mol, which is negligible in comparison to the chemical driving force ($\approx$ 10 kJ/mol) and can certainly not justify the two-orders-of-magnitude difference needed on the diffusion coefficient.

Several authors [168, 169, 170] have been confronted to the accelerated diffusion of carbon in austenitic stainless steel when studying the low-temperature gas-phase carburization processes. They measured colossal supersaturation in the austenitic matrix up to 12 at.% without any carbides formation. This situation offered the unique opportunity for studying the dependence of the carbon diffusion coefficient on the carbon fraction over a large range of carbon contents. A maximum enhancement factor was found for the diffusion coefficient in comparison to the values included into the classical thermo-kinetics databases for Fe-Cr-Ni alloys [171, 136] which seem to largely underestimate the increase of D_{CC} with increasing X_c. A decrease of the activation energy for carbon diffusion was put forward to explain this unusual phenomenon. It might be due to an expansion of the atomic lattice caused by the large amount of interstitially dissolved carbon. However applying the experimental data of reference [169] to our case with a maximum carbon content of 3.5 at.% at the interface between martensite and austenite leads to $D_{CC}(470°C,FCC) = 5 \times 10^{-16}\ m^2/s$ which corresponds to an enhancement factor of 1.5 only, the accelerating effect being efficient at very high supersaturations (enhancement factor around 100 for $x(C) = 14$ at.%).

Another explanation usually provided to explain this extremely high carbon solubility into austenite is the para-equilibrium condition met at low temperatures where there is essentially no substitutional diffusion and only carbon is mobile to equilibrate its chemical potential [172, 173]. A paraequilibrium solubility of 5.5 at.% was calculated for carbon into austenite at 470°C (to be compared to the equilibrium solubility of 0.015 at.%). But the hypothesis of paraequilibrium seems not reasonable in our weld, especially at 610°C. In fact the compositions of the precipitates evaluated by both EDX-TEM and APT significantly diverge from the one of the surrounding matrix as they are particularly enriched in Cr (u-fraction up to 65 at.%). Even at lower temperatures in the tempered martensite, a significant amount of chromium is incorporated into the precipitates.

Several supplementary trials were performed to try to reproduce the correct carbon profile across

the weld after heat-treatment, while maintaining an equilibrium calculation for the precipitation. But none of them was successful:

1. Minor elements such as Si, Mn and Mo were added to each of the three layers according to their contents measured by WDS.

2. The initial step profile chosen for the compositions was replaced by the true continuous profiles measured by WDS and SIMS on the as-welded sample. As carbon diffusion was detected to already occur during welding, a carbon enrichment of both martensite and austenite in the form of a peak was initiated but had no significant influence on the subsequent diffusion.

3. The very stable Cr-rich carbides (M_7C_3 and $M_{23}C_6$) were suppressed from the martensitic layer, leading to cementite formation instead. The carbon content into the martensitic matrix was only raised from 2.5 to 3.6 $\times 10^{-5}$ wt.% which did not allow more diffusion into the austenite.

The classical approach based on equilibrium precipitation was efficient at modeling the evolution of the carbon profile through the weld of interest provided a significant increase of the carbon diffusion coefficients, especially in the austenitic weld metal. This was explained by the three-phase configuration of the weld including an intermediate layer of tempered martensite. The latter was simulated as a Cr-rich BCC phase and therefore had a very limited carbon solubility.

4.2.2 Coupling long-range diffusion and precipitation kinetics

One of the main approximation of the previously described model lies in the use of the equilibrium condition for evaluating precipitates volume fractions. Precipitation has been supposed instantaneous as soon as the local concentrations allow a reduction of the Gibbs free energy of the system by phase transformation. Such an approach usually leads to an overestimation of the precipitates volume fractions and might be the reason for the very low carbon content available into the martensitic matrix. The time needed for the particles to nucleate and grow has to be taken into account.

4.2.2.1 Design of the simulation

As previously, the long-range diffusion is calculated for the elements Cr, Ni, Fe and C in the matrix phases. The one-dimensional space is divided into 32 cells. The full heat-treatment between 400 and 610°C is considered (see Fig. 4.8-b). The equilibrium step is replaced by a precipitation kinetics calculation as implemented in the MatCalc software (see Section 4.1.2.3 for details). Thermodynamic and mobility parameters are extracted from CALPHAD-type databases. The nucleation kinetics is obtained from classical nucleation theory (CNT) extended for multicomponent

systems, the interfacial energy being calculated by the generalized nearest-neighbor broken-bond (GNNBB) approach. Once a precipitate is nucleated, its further growth is evaluated based on the evolution equations for the radius and composition according to the thermodynamic extremal principle (SFFK model). The numerical time integration is performed with the classical Kampmann-Wagner approach. The schematics of Figure 4.12 summarizes the different stages of the simulation. The numerical difficulty essentially lies in the calculation of the compositions at the interfaces between the three zones of interest (base metal, martensitic layer, austenitic weld metal). In fact, contrary to the case of carburization by an external atmosphere, the chemical potentials at the interfaces are not constant but evolve during the course of the heat-treatment, even when the temperature does not change. That is why they have to be determined at each time step, the crucial part of the simulation being reached when the carbon content of the base metal goes to very low values. In that case, the time step needs to be decreased to prevent negative values of the carbon content.

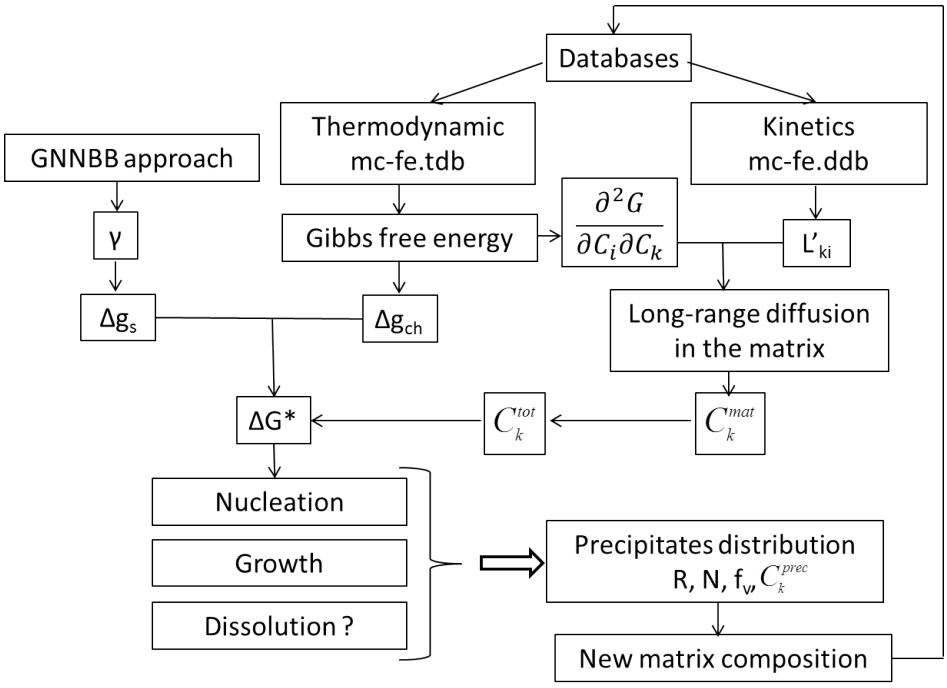

Figure 4.12: Representation of the different steps involved in the calculation coupling long-range diffusion and precipitation kinetics, L'_{ki} being the mobility coefficient of element k under a gradient of chemical potential of element i, Δg_s and Δg_{ch} the increments of surface energy and chemical energy respectively, ΔG^* the critical Gibbs free energy for nucleation, C_k^{tot} the total content of element k, C_k^{mat} and C_k^{prec} its distribution between matrix and precipitates, R, N, f_v the characteristics of the precipitates in terms of radius, number density and volume fraction respectively.

For such kind of simulation, different characteristics of the microstructure (see Table 4.3) have to be known as they will be entered as input data and play a significant role in the precipitation kinetics. Among them, one finds:

- the size and shape of grains and subgrains

- the dislocation density
- the sites where the precipitation takes place

That is why a good knowledge of the microstructures of interest is necessary. Table 4.4 presents an overview of the number of potential nucleation sites at different heterogeneous lattice positions for the three regions of the weld. Based on the equilibrium results and microstructural observations, the nature of the particles likely to form in each zone has been restrained in order to limit the computational cost: only cementite in the base metal, both $M_{23}C_6$ and M_7C_3 in the martensite, and only $M_{23}C_6$ in the weld metal. For the initial cementite population in the base metal, a Gaussian distribution with a mean value of 150 nm, a standard deviation of 0.05 and a total volume fraction of 3 % was created and imposed in each cell.

Table 4.3: Microstructural characteristics used for the kinetics simulation in the three zones of the weld. In the base metal and martensitic layer, the subgrain is the relevant geometrical feature instead of the grain.

	Base metal	**Martensitic layer**	**Weld metal**
Dislocation density	$10^{14}/m^2$	$10^{15}/m^2$	$10^{12}/m^2$
Grain/subgrain width	1 μm	400 nm	50 μm
Grain/subgrain elongation factor	20	10	1

Table 4.4: Number of potential nucleation sites in microstructures represented by tetrakaidecahedra, the microstructural features being the ones of Table 4.3.

Nucleation sites ($/m^3$)	**Base metal**	**Martensitic layer**	**Weld metal**
Bulk	8.6×10^{28}	8.6×10^{28}	8.6×10^{28}
Dislocations	4.4×10^{23}	4.4×10^{24}	4.4×10^{21}
Grain/subgrain boundaries	2×10^{25}	5.1×10^{25}	1.6×10^{24}
Grain/subgrain edges	5.9×10^{22}	3.7×10^{23}	2×10^{19}
Grain/subgrain corners	5×10^{15}	6.3×10^{16}	1.3×10^{14}

4.2.2.2 Influence of the nucleation sites

The number of nucleation sites available for precipitates to form within the martensite was found to have a significant influence on the amount of carbon transferred from the base metal to the stainless steel through the martensitic layer. The total number of nucleation sites was varied from 3.7×10^{23} $/m^3$ (corresponding to nucleation on subgrain edges) to 6.3×10^{16} $/m^3$ (subgrain corners) and the results in terms of global carbon content, precipitates volume fraction and matrix carbon content are displayed on Figure 4.13. Concerning the austenitic weld metal, nucleation was set to occur on the dislocations. In the three configurations of Figure 4.13, nothing has been changed in the

austenite. Despite this, the carbon content in the austenitic part of the weld as well as its diffusion distance are found to be highly dependent on the carbon distribution within the martensite.

In the case of a high number of nucleation sites (subgrain edges), the global carbon profile resembles the one obtained with equilibrium precipitation (see Fig. 4.9). As shown in Table 4.5, the matrix carbon content within the martensite is very low in this case, even at the end of the heating ramp ($t = 25200$ s). Decreasing the number of potential nucleation sites in the martensite led to maintain part of the carbon in solid solution during a large enough time for it to diffuse towards the austenitic part of the weld. In the case of a small number of nucleation sites (subgrain corners), carbon was found to diffuse over 70 μm into the austenite (see Table 4.6), which is in good agreement with the experimental measurements. Therefore it seems not to be necessary to increase the carbon diffusion coefficient in austenite to enhance its diffusion within this part of the weld. Since the number of nucleation sites is limited within the austenite (see Table 4.4) most of the carbon diffusing into it remains in solid solution (see Fig. 4.13-c).

Table 4.5: Carbon content within the martensitic matrix as a function of the number of nucleation sites at the end of the heating ramp ($t = 25200$ s) and at the end of the heat-treatment ($t = 79200$ s).

$\mathbf{N_0}$ ($/\mathbf{m^3}$)	**Matrix carbon content**	
	$\mathbf{t = 25200\ s}$	$\mathbf{t = 79200\ s}$
$\mathbf{3.7 \times 10^{23}}$	7.3×10^{-5} %	3.1×10^{-8} %
$\mathbf{1.85 \times 10^{20}}$	1.8×10^{-2} %	4.3×10^{-3} %
$\mathbf{6.3 \times 10^{16}}$	6.9×10^{-2} %	7.9×10^{-3} %

Moreover precipitation within the martensitic layer also has consequences on the decarburization of the base metal. The higher the volume fraction of the precipitates in the martensite is, the lower will be the content of the interstitially dissolved carbon and consequently the higher will be the driving force for carbon to diffuse from the base metal to the interfacial martensite. Considering the decarburized region as the part of the base metal with a global carbon content lower than 0.1 wt.%, the decarburization distance is found to decrease when decreasing the number of nucleation sites within the martensite. As shown in Table 4.6, the width of the decarburized region in the base metal and the one of the carburized layer in the austenitic weld metal evolve in opposite directions. In the weld under study, both the decarburized and carburized regions spread over a significant distance: 200 and 70 μm, respectively. Yet whatever the number of nucleation sites chosen for the martensite, the global amount of carbon transferred from the base metal towards the weld (both martensitic and austenitic parts) is insufficient in comparison to the one that has been experimentally measured.

Table 4.6: Size of the zones affected by carbon diffusion in both the base metal and weld metal at the end of the heat-treatment. The experimental values are recalled for comparison.

$\mathbf{N_0}$ ($/\mathbf{m^3}$)	**Decarburization distance in the base metal (exp. 200 μm)**	**Carburization distance in the γ weld metal (exp. 70 μm)**
$\mathbf{3.7 \times 10^{23}}$	133 μm	16 μm
$\mathbf{1.85 \times 10^{20}}$	61 μm	38 μm
$\mathbf{6.3 \times 10^{16}}$	0 μm	70 μm

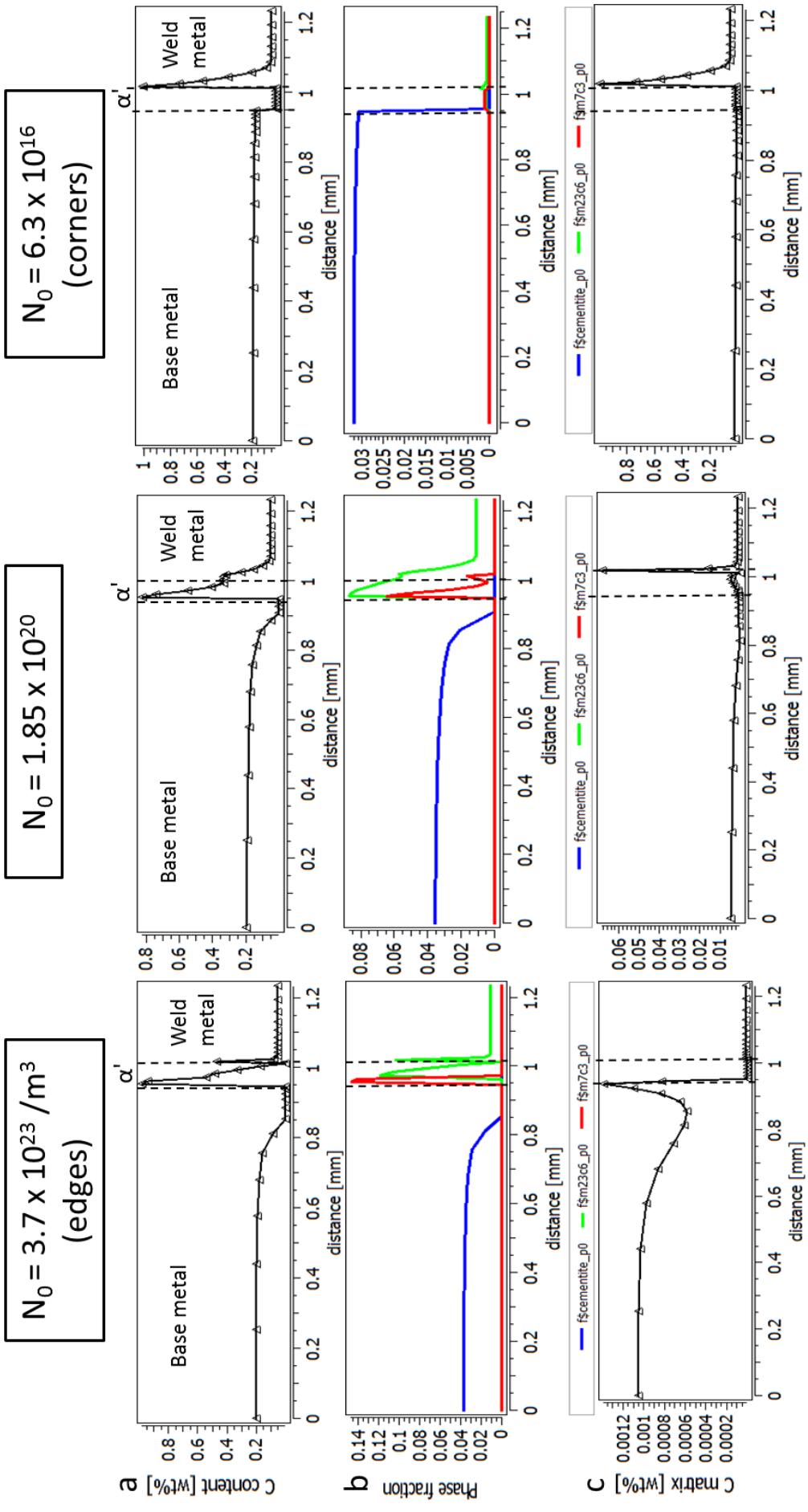

Figure 4.13: Results of a non-isothermal simulation of diffusion with precipitation kinetics for different numbers of nucleation sites within the martensite. a- Global carbon content b- Precipitates volume fractions c- Matrix carbon content.

4.2.2.3 Influence of the elastic misfit

Up to now the elastic contribution to the Gibbs energy has been neglected. Yet it enters the expressions of both the activation barrier for precipitates nucleation (see Equation 4.16) and the total Gibbs free energy of the system during growth (see Equation 4.24). Thus it can play an important role in precipitation kinetics, especially when matrix phase and precipitates have different molar volumes. As the nucleus is constrained by the surrounding matrix, the phase transformation generates elastic stresses around the inclusion. This supplementary contribution to the Gibbs energy of the system is defined as:

$$\Delta g^{el} = \frac{E^{\alpha}}{9(1-\nu^{\alpha})}(\nu^{*})^{2} \tag{4.38}$$

with E^{α} and ν^{α} being the elastic modulus and Poisson's ratio of the matrix respectively and ν^{*} representing the volumetric elastic misfit given as:

$$\nu^{*} = \frac{V_m^{\beta} - V_m^{\alpha}}{V_m^{\alpha}} \tag{4.39}$$

with V_m^{α} and V_m^{β} being the molar volumes of matrix and precipitate, respectively.

The molar volumes of both BCC matrix and precipitates at room temperature together with the resulting elastic misfit are summarized in Table 4.7. As the martensitic transformation is associated with a volume expansion, compressive residual stresses result within the martensitic layer. Therefore the matrix will constrain the growing precipitates even more. In order to investigate the influence of the elastic misfit between matrix and precipitates within the tempered martensitic layer on carbon diffusion through the weld, several values between 0.10 and 0.25 were tested for the variable ν^{*}. The nucleation sites were set to subgrain edges within the martensitic layer. For the sake of simplicity the same value of the elastic misfit was chosen for both $M_{23}C_6$ and M_7C_3 carbides. The results in terms of global carbon content, precipitates volume fraction and mean radius are displayed on Figure 4.14 for three different values of the elastic misfit.

An increase of the elastic misfit between matrix and precipitates within the martensitic region led to a similar effect as the decrease of the number of nucleation sites which was investigated in Section 4.2.2.2. Nucleation and growth became energetically less favored which led to an enhanced carbon solubility within the BCC matrix (see Table 4.8) and consequently its possible diffusion towards the austenite. As shown on Figure 4.14, carbon diffuses over a larger distance within the austenite when the elastic misfit between matrix and precipitates in the martensite is increased. However this also leads to a decrease of the global carbon content within the martensitic zone. Consequently the precipitates volume fraction and number density are smaller and the mean radius larger. This is due to the fact that, for the same Cr content, a lower C content leads to a smaller driving force for nucleation and so a smaller number of nucleation events. Carbon being highly mobile, the precipitates will then grow easily. Even in the case of the higher misfit ($\nu^{*} = 0.25$), the carbon content in solid solution within the martensite remains lower than the one experimentally measured by APT in the intermediate and heat-treated samples ($w(C) \approx 0.1$ %).

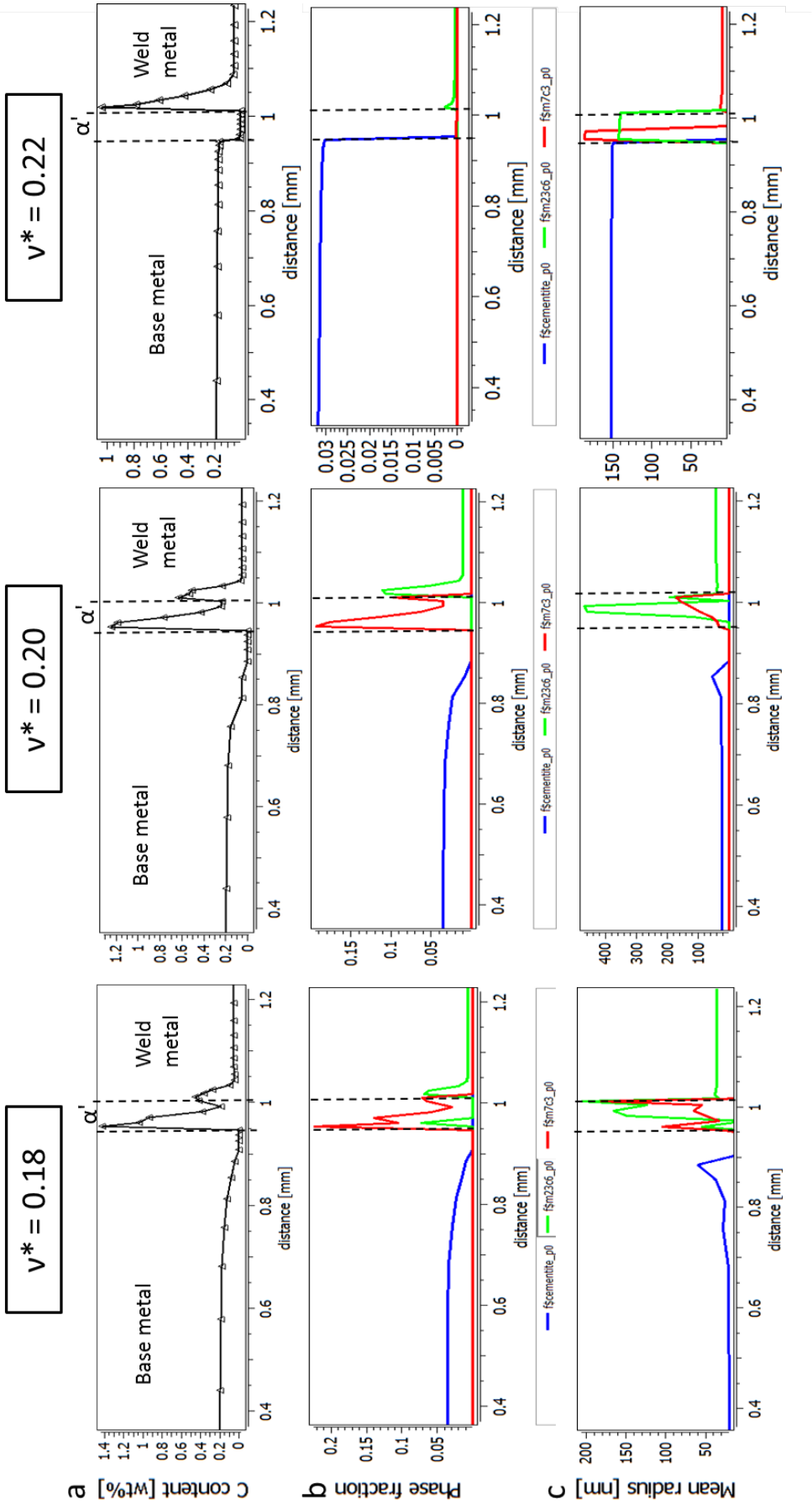

Figure 4.14: Results of a non-isothermal simulation of diffusion with precipitation kinetics for different values of the elastic misfit within the martensite. a- Global carbon content b- Precipitates volume fractions c- Precipitates mean radius.

Table 4.7: Molar volumes and resulting elastic misfit between matrix and precipitates within the martensitic layer at room temperature.

	Molar volume (cm^3/mol)	**Elastic misfit**
BCC	7.049	-
$M_{23}C_6$	7.786 [174]	0.11
M_7C_3	7.980 [175]	0.13

Table 4.8: Carbon content within the martensitic matrix as a function of the elastic misfit between matrix and precipitates at the end of the heating ramp ($t = 25200$ s) and at the end of the heat-treatment ($t = 79200$ s).

ν^*	**Matrix carbon content**	
(%)	**t = 25200 s**	**t = 79200 s**
14	1.7×10^{-4} wt.%	4.6×10^{-4} wt.%
18	1.0×10^{-4} wt.%	6.6×10^{-4} wt.%
20	6.7×10^{-3} wt.%	1.3×10^{-3} wt.%
22	2.3×10^{-2} wt.%	5.9×10^{-3} wt.%
25	2.3×10^{-2} wt.%	5.9×10^{-3} wt.%

A similar effect as the one of the elastic misfit was obtained by varying the surface energy of the precipitates within the martensite. The surface energy calculated by the GNNBB approach was multiplied by a coefficient varying between 1.2 and 2. A coefficient greater than or equal to 1.6 was found to be necessary to highly reduce precipitation within the martensitic layer (volume fraction of precipitates lower than 0.5 %) and allow carbon diffusion over 70 μm or more in the austenitic part of the weld.

By all the trials previously performed, it was possible to adjust the carbon distribution between martensite and austenite. However the global carbon quantity transferred from the low-alloyed side to the high-alloyed one remained insufficient in all cases. This was highlighted by the size of the decarburized layer that was always underestimated by the simulation in comparison to the experimental results. The latter consisted in a decrease of the global carbon content of the base metal over 500 μm with a zone without any cementite spanning over 200 μm.

4.2.2.4 Choice of one set of parameters reproducing the experimental situation

A simulation leading to results close to the experimental ones is displayed on Figure 4.15. It was calculated with a misfit of 0.19 for both $M_{23}C_6$ and M_7C_3 in the tempered martensitic layer together with an enhancement factor of 8 on the carbon diffusion coefficient in the BCC matrices. The nucleation sites were set to subgrain edges in the base metal (1 μm wide laths) and martensitic layer (400 nm wide laths), whereas precipitates were considered to nucleate on dislocations in the austenitic weld metal (dislocation density of $1 \times 10^{12}/m^2$).

Such parameters have allowed reproducing the extent of the decarburized region (200 μm of very low carbon content and a gradual increase over 300 supplementary μm) as well as the level of carbon within both carburized regions (around 1.3 wt.% in the martensite and 0.8 wt.% in the austenite). The calculated carbon profile is compared with the WDS and SIMS measurements performed on the heat-treated sample on Figure 4.15-a. Moreover mainly M_7C_3 carbides are predicted to be present in the martensitic layer at the end of the heat-treatment, which is in agreement with the identification performed with Astar software on extraction replicas (see Section 3.3.2.1). Their size (calculated between 33 and 107 nm) and number density (calculated between $2.5 \times 10^{19}/m^3$ and $1.2 \times 10^{21}/m^3$) agree well with the measurements performed by FIB cutting in Section 3.3.3.1 (mean dimension between 48 and 83 nm and density between $2.3 \times 10^{19}/m^3$ and $4 \times 10^{20}/m^3$). The main discrepancy arises from the evolution of the precipitates parameters within the martensitic layer. Indeed the increase of the number of particles together with a decrease of their mean radius when moving from the base metal / martensite interface towards the martensite / austenite one was not reproduced by the simulation. This is certainly due to the fact that the initial Cr content was taken as a constant (11 wt.%) within the whole martensitic layer. Indeed the low Cr contents in contact with the base metal are certainly responsible for a decrease of the nucleation driving force.

Concerning the austenitic weld metal, the carburization is calculated to spread over 50 μm (instead of 70 μm) and the mean radius of the precipitates is slightly overestimated (45 nm instead of 30 nm). In this case, no enhancement factor was used for the carbon diffusion within the austenite. However the cladding layers are known to be in tension because of residual stresses that persist even at the end of the heat-treatment due to the cooling of the dissimilar materials. In the case of a stretching of the FCC crystal lattice, carbon diffusion within the austenite could be enhanced. However no measurement of this local phenomenon could be performed.

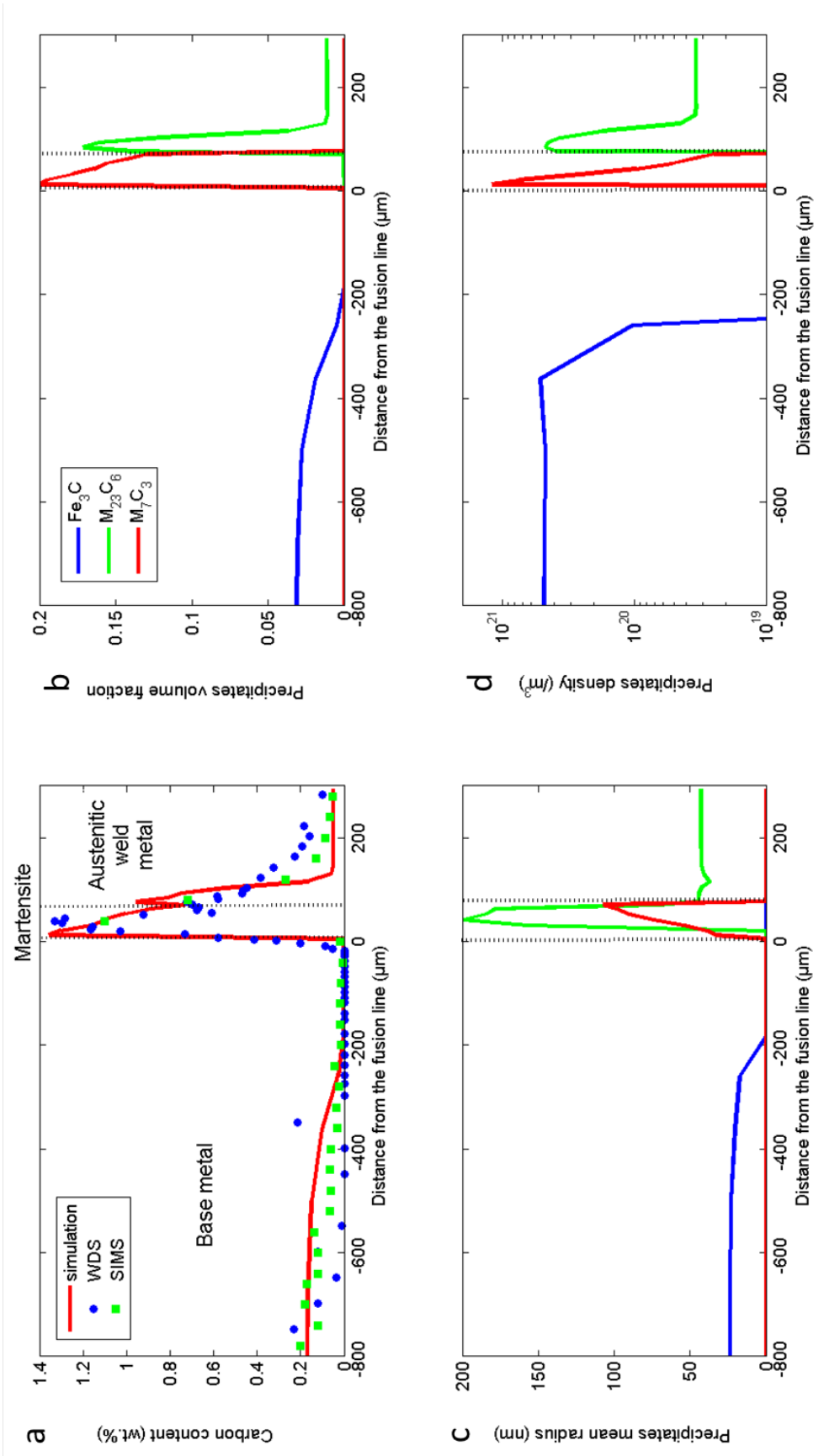

Figure 4.15: Results of a non-isothermal simulation with a full coupling between long range diffusion and precipitation. a- Global carbon content. b- Precipitates volume fraction. c- Precipitates mean radius. d- Precipitates number density.

The success of this simulation relies on the combined effect of two adjustable parameters. The first one is the elastic misfit in the martensite between precipitates and matrix that was assigned a large value (19 %). It has allowed maintaining significant carbon quantities in solid solution. According to Equation 4.38, a misfit of 19 % corresponds to an elastic energy of 900 J/cm^3, which is quite significant in comparison with the chemical driving force for nucleation. This value, higher than those calculated from the molar volumes of precipitates and matrix (see Table 4.7), could originate from the compressive residual stresses acting against precipitates nucleation and growth in the martensite. A more realistic description should thus take into account the fact that the matrix phases are certainly constrained because of mechanical incompatibility that prevents them from deforming freely.

Concerning the enhanced diffusion coefficient (×8), it was absolutely necessary to obtain a good agreement on the extent of the decarburized region in the base metal. However this value is realistic, especially when one considers the accelerating effect of the subgrain boundaries where large amounts of carbon were found to segregate (see Section 3.3.4). Using the mobility of carbon along the subgrain boundaries that has been estimated in Section 4.2.1.3 led to a diffusion coefficient of 7.2×10^{-10} m^2/s at 400°C within the lath boundaries. According to Einstein's formula ($x = 2\sqrt{Dt}$) less than 1 s is necessary at this temperature for carbon to travel along the lath boundaries through the entire thickness of the martensitic layer (50 μm). From the subgrain boundaries, carbon can diffuse towards the interior of the laths. At 400°C, with a bulk diffusion coefficient of 1.8×10^{-13} m^2/s in the BCC matrix, 55 ms are necessary for carbon to diffuse over the 200 nm which constitute the half-width of the martensitic laths. These orders of magnitude are recalled on the schematic of Figure 4.16. Since the volume diffusion length is larger than the spacing between subgrain boundaries, the volume diffusion field of neighboring subgrain boundaries should overlap extensively. This case corresponds to the A regime of the Harrison's classification [176] for polycrystals with parallel grain boundaries. Therefore a partial leakage of the diffusing species from the subgrain boundaries to the bulk and the subsequent volume diffusion around the lath boundaries is highly probable. Thus it is not surprising that the bulk value of the carbon diffusion coefficient which is included in the kinetics databases does not adequately describe diffusion in a lathy microstructure with narrow subgrains. Moreover the base metal adjacent to the martensite also has a lathy microstructure during part of the heat-treatment.

4.3 Summary and conclusions

The goal of this chapter was to develop a model able to predict carbon diffusion and the associated precipitation within a 18MND5/309L dissimilar weld corresponding to a three-phase assembly (bainitic microstructure of the low-alloy base metal / intermediate martensitic layer / austenitic weld metal) during the post-welding heat-treatment. Existing models based on coupling long-range diffusion and equilibrium precipitation were applied to the situation under study. However they failed in reproducing the significant carbon transfer that was measured from the base metal to the weld metal through the intermediate martensitic zone by both SIMS and WDS. This was attributed

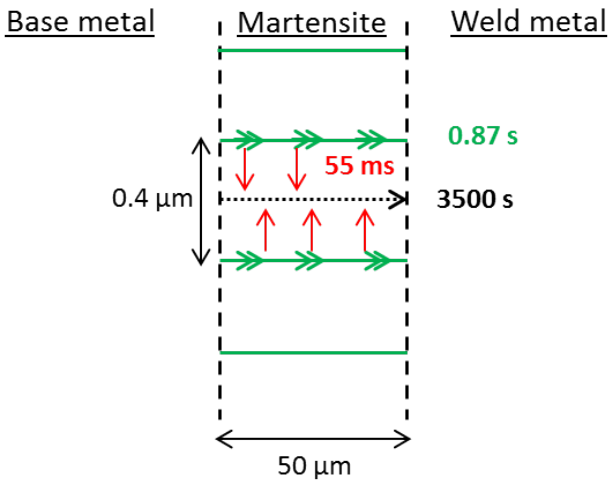

Figure 4.16: Schematic giving the orders of magnitude of both subgrain and bulk diffusion within the tempered martensite at 400°C

to the high stability of the Cr-rich carbides in the martensitic region, which resulted in a very low carbon solubility in this zone and prevented any carbon diffusion towards the austenite. This low carbon solubility was in contradiction with the significant amount of carbon (up to 0.1 wt.%) measured by APT in the martensitic matrix.

It was thus necessary to incorporate the precipitation kinetics into the model to take into account the fact that carbides nucleation and growth might not be instantaneous. A completely new approach coupling long-range diffusion to a size-class description of precipitation in conjunction with the thermodynamic and kinetics Calphad-type databases was developed.

This coupled diffusion / precipitation has allowed:

- **testing the effects of the most influential parameters (number of nucleation sites, elastic misfit between matrix and precipitates, interfacial energy, carbon diffusion coefficient) on the extent of carbon diffusion through the complex microstructure of the weld.**
- **outlining the important role of the intermediate martensitic layer in regulating the amount of carbon diffusing from the base metal towards the austenitic weld metal.**
- **identifying a set of parameters able to reproduce the carbon profile through the weld as well as the precipitates characteristics (volume fraction, mean radius, density) in the different regions. For that, it was necessary to postulate an enhanced diffusion coefficient in the lathy microstructures together with a significant elastic misfit between precipitates and matrix within the intermediate martensitic layer.**

Part III

Consequences of phase transformations on the mechanical properties around the fusion line

Chapter 5

Heterogeneities in the local elasto-plastic behavior

5.1 Introduction

As seen in Part II, the post-welding heat-treatment has a significant impact on the microstructure of the dissimilar steel weld on either side of the fusion line. As shown by the hardness profiles of Figure 5.1, most of the regions around the interface encounter microstructural changes leading to either softening or hardening:

- **18MND5 HAZ:** The bainitic microstructure of the low-alloy steel 18MND5 is tempered at 610°C. It leads to a hardness drop from 280 to 200 HV on average, although the profiles are highly disturbed due to the heterogeneities of the microstructure (bainitic laths, cementite carbides, martensite/austenite islands).

- **Decarburized region:** A supplementary decrease of hardness (down to 140 HV) is observed in the last 200 μm before the fusion line due to carbon diffusion from the base metal towards the weld. It is accompanied by carbides dissolution and ferrite grain growth, both phenomena causing softening.

- **Martensitic layer:** In this region, two opposite phenomena take place. On the one side, the as-welded microstructure is tempered, the rearrangement and annihilation of dislocations should lead to softening. On the other side, it gets carburized which should lead to hardening either by carbon in solid solution or precipitation.

- **Carburized austenite:** The first 70 micrometers after the martensitic band display a huge rise of their hardness (from 250 to 550 HV) that has to be related with carbon diffusion accompanied by precipitation of small coherent carbides into the austenitic matrix.

- **Weld metal 309L:** Only the hardness of the $\delta - \gamma$ stainless steel seems to remain unaffected by the heat-treatment. Although δ-ferrite has been found to decompose into austenite and

carbides during heat-treatment (see Section 3.3.2.3), it does not have a significant effect on the micro-hardness (global increase of about 10 HV).

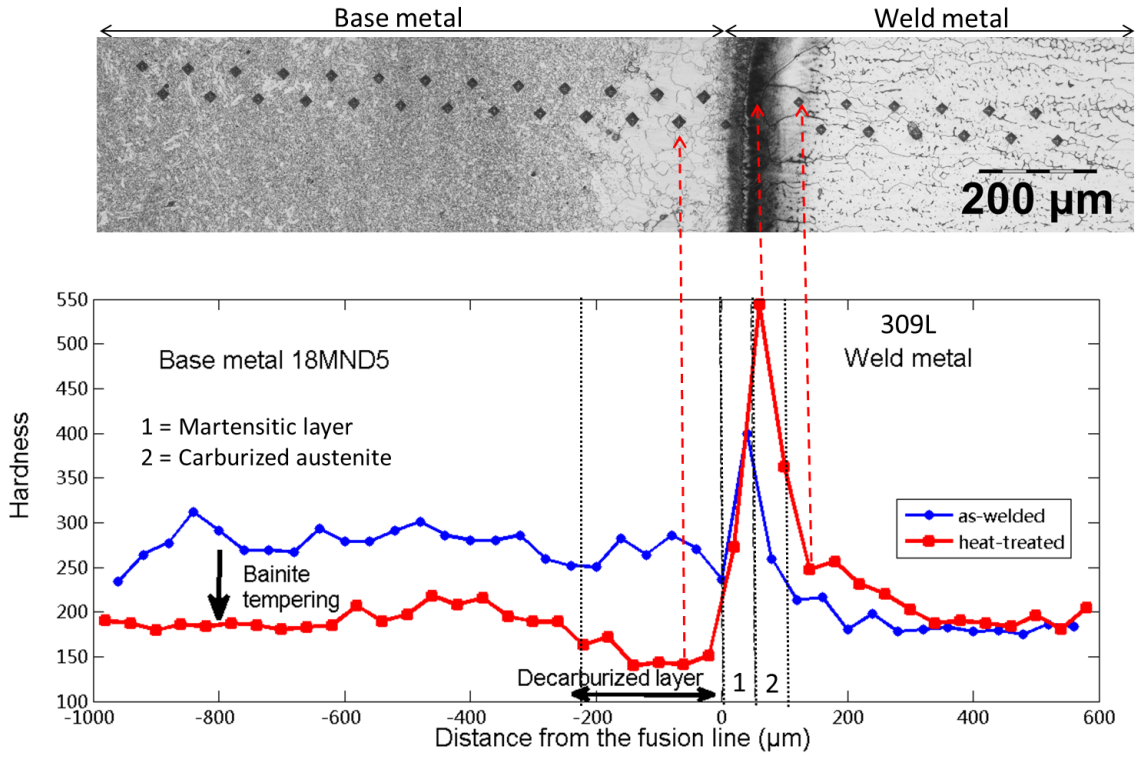

Figure 5.1: Micro-hardness profiles (100 g) on a transverse section of the weld in both the as-welded and heat-treated states, with the corresponding indent locations identified on an optical micrograph of the heat-treated sample after etching.

This chapter aims at investigating how the mechanical properties of each zone are affected by the phase transformations that take place during heat-treatment. We will try to address the following questions:

- **What are the consequences of the microstructural heterogeneities on the strain localization around the fusion line?**
- **Which elasto-plastic constitutive law can be inferred for each region of the weld?**

5.2 Experimental procedure

5.2.1 Determination of constitutive laws for each phase

5.2.1.1 Tensile tests

All the tensile tests described in this chapter were performed with a ZWICK 20kN machine at a strain rate of 10^{-3}/s. The different types of samples were obtained by electro-erosion and their geometry and dimensions are reported in Appendix C. Micro-samples (LD on Fig. 5.2) were machined parallel to the fusion interface (length and width along the LD and WD directions of Figure 5.2 respectively). Their dimensions (15 mm gauge length, 3 mm width and 0.8 mm thickness) allow to consider them as homogeneous. They were used to determine the local elasto-plastic properties in the different zones of interest: one in each stainless steel layer (309L and 308L) and two in the heat-affected zone of the base metal with their mid-thickness being located at 2 and 5 mm from the fusion line and called HAZ_2 and HAZ_5 respectively.

In addition to the classical yield strength $R_{p0.2}$ and ultimate tensile strength R_m, other characteristic parameters can be extracted from a tensile test:

- The **true strain at necking ϵ_u** corresponds to the value of the true strain (ϵ_T) when the true stress (σ_T) is maximum.
- The **hardening exponent n** is defined by:

$$n = \frac{\partial \sigma_T}{\partial \epsilon_T} \frac{\epsilon_T}{\sigma_T} \tag{5.1}$$

  where ϵ_T and σ_T are the true strain and true stress respectively. For homogeneous materials, the Considere criterion states that the hardening exponent at the onset of necking n_u should be equal to the true strain at necking ϵ_u.

- The **true fracture strain ϵ_f** can be determined on the fracture surface and is defined by:

$$\epsilon_f = ln(\frac{S_0}{S_f}) \tag{5.2}$$

  where S_0 and S_f are the initial and final sections of the tensile specimen respectively.

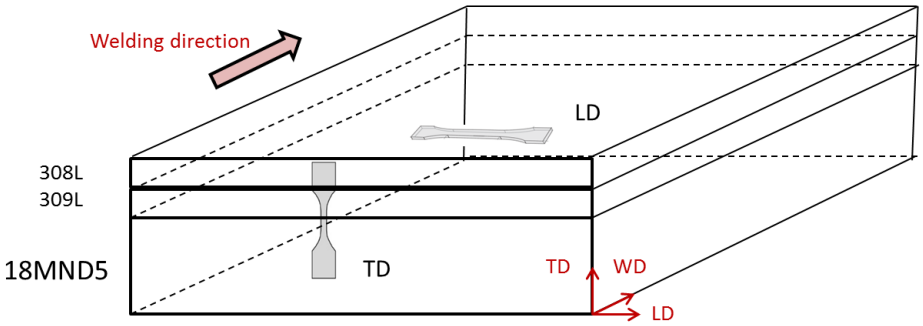

Figure 5.2: Weld geometry for locating the directions of samples machining, WD stands for welding direction, TD for transverse direction and LD for longitudinal direction.

5.2.1.2 Nanoindentation

Nanoindentation is a widespread method for probing mechanical properties at a submicron scale. A significant part of the research on nano-indentation is dedicated to create proper mechanical models for converting the raw experimental data into characteristic material properties such as hardness, Young modulus, yield stress, hardening exponent, etc.

Principle of the technique

The primary goal of nano-indentation is to extract elastic modulus E and hardness H of a specimen from the experimental load-displacement curve, an example is displayed on Figure 5.3. The depth measured during indentation includes both elastic and plastic displacements whereas only elastic recovery occurs during unloading.

According to Sneddon equation [177], the initial contact stiffness defined as the slope of the initial portion of the unloading curve $S = \frac{\partial P}{\partial h}$ gives access to the elastic modulus:

$$S = 2\beta E_r \sqrt{\frac{A_c}{\Pi}} \tag{5.3}$$

with E_r being the reduced modulus defined as

$$\frac{1}{E_r} = \frac{1-\nu^2}{E} + \frac{1-\nu_i^2}{E_i} \tag{5.4}$$

in which E and ν are the elastic modulus and Poisson's ratio of the sample, respectively, E_i and ν_i the same quantities for the indenter. β is a dimensionless correction factor whose value for Berkovich indenter lies between 1.0226 and 1.085 [104]. A_c is the projected contact area and is related to the contact depth h_c through the calibrated area function of the indenter:

$$A_c = f(h_c) = f(h_{max} - h_s) \tag{5.5}$$

The relevant characteristic depths are represented on the schematic of Figure 5.4. The displacement of the surface at the perimeter of contact h_s can be calculated from:

$$h_s = \epsilon \frac{P_{max}}{S} \tag{5.6}$$

with ϵ a geometric constant whose value should be taken at 0.75 for the three-side pyramid indenters [103]. Concerning the hardness H, it can be calculated according to the following definition :

$$H = \frac{P_{max}}{A_c} \tag{5.7}$$

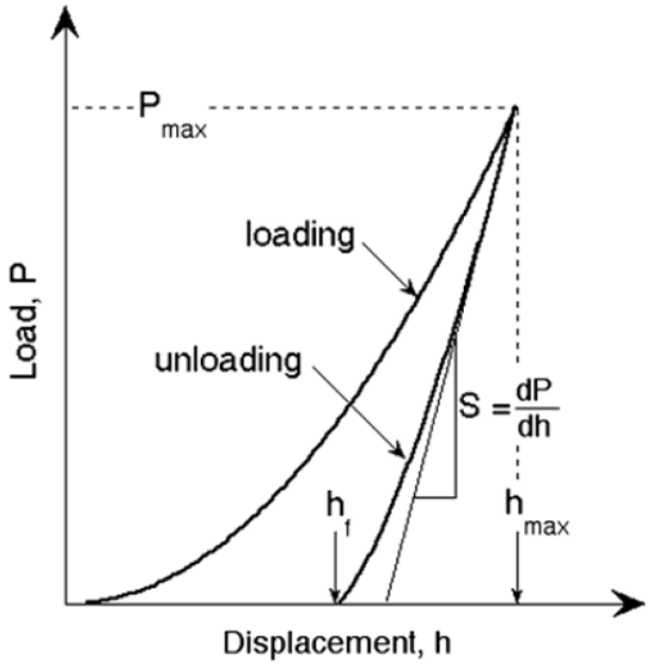

Figure 5.3: Schematic representation of a typical load-displacement curve in nanoindentation: P_{max} is the maximum load at the maximum imposed displacement h_{max}, h_f is the final displacement after complete unloading.

The Continuous Stiffness Measurement (CSM) technique allows continuously measuring the contact stiffness during loading (and not only at the maximum depth with the unloading portion) by applying a small dynamic oscillation to the force signal. Such method also provides an excellent mean of surface detection as the harmonic stiffness rises rapidly after the contact [104].

Plastic properties identification by reverse algorithm

For metallic materials, Dao et al. [178] proposed several dimensionless equations to process the raw data from nanoindentation. By means of a large number of finite element simulations, they defined a representative strain $\epsilon_{r\theta}$ at which all power-law plastic responses exhibiting the same true stress would give the same loading curvature C_θ for a fixed value of the elastic modulus:

$$\epsilon_{r\theta} = 0.105 \times cot(\theta) \tag{5.8}$$

with θ being the equivalent cone angle of the indenter.

Bucaille et al. [11] extended Dao's method and proposed a dimensionless function linking the loading curvature and the elastic modulus to the representative stress $\sigma_{r\theta}$ for an indenter of included angle θ:

$$\frac{C_\theta}{\sigma_{r\theta}} = \tan^2(\theta)\left\{0.02552[\ln(\frac{E_r}{\sigma_{r\theta}})]^3 - 0.72526[\ln(\frac{E_r}{\sigma_{r\theta}})]^2 + 6.34493[\ln(\frac{E_r}{\sigma_{r\theta}})] - 6.47458\right\} \tag{5.9}$$

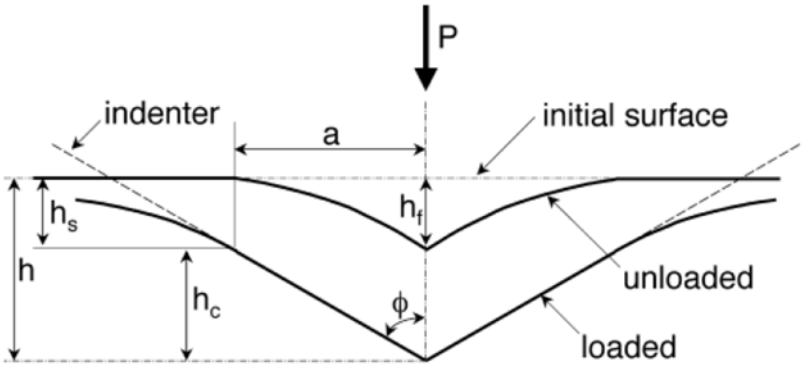

Figure 5.4: Schematic representation of a typical deformation pattern during and after indentation. It is assumed that the material around the indenter flows underneath the original contact surface, namely, the sink-in predominates.

In Bucaille's method, the elasto-plastic behavior of the material is described according to:

$$\sigma = \begin{cases} E\epsilon \text{ if } \sigma \leq \sigma_y \\ \\ K\epsilon^n \text{ if } \sigma > \sigma_y \text{ with } K = E^n \sigma_y^{1-n} \end{cases} \tag{5.10}$$

For obtaining the yield stress σ_y and the hardening exponent n, the specimen has to be indented with two different indenters, one of them being the Berkovich indenter ($\epsilon_{r\theta} = 0.033$). Afterwards the following system of equations needs to be solved:

$$\begin{cases} \sigma_{0.033} = \sigma_y (1 + \epsilon_{0.033} \frac{E}{\sigma_y})^n \\ \\ \sigma_{r\theta} = \sigma_y (1 + \epsilon_{r\theta} \frac{E}{\sigma_y})^n \end{cases} \tag{5.11}$$

However friction between diamond and the specimen surface induces an increase of the normal force F that can be expressed as:

$$\frac{\Delta F}{F} = 1 + \frac{\mu}{tan\theta} \tag{5.12}$$

where μ is the friction coefficient and θ the equivalent cone angle of the indenter. Therefore the effect of friction is even more pronounced for cube corner indenter ($\theta = 42.3°$) than Berkovich indenter ($\theta = 70.3°$). Taking a friction coefficient of 0.15, which is a classical value for the contact between diamond and metals, Bucaille [11] demonstrated that the effect of friction on the Berkovich indentation can be neglected whereas it causes an increase of the loading curvature by 16 % in the case of cube corner indentation.

Experimental set-up

Nano-indentation tests were performed using the MTS XP machine equipped with three-sided diamond pyramids as tip, either Berkovich or cube corner. The tip area functions were calibrated by indentation on a fused silica reference sample. Bucaille's method with correction for friction was applied to estimate local mechanical properties in regions of the weld where tensile specimen could

not be extracted (decarburized layer, martensitic band, carburized austenite). The penetration depth was set to 1 μm and the potential residual cold working of the specimen's surface was removed by prolonged polishing in colloidal silica suspension. Some indentations were also performed in the base metal, where the mechanical properties are known by tensile testing. Section 5.3.1.2 will detail the results that lead to the conclusion that the nanoindentation method for extracting plastic properties (yield strength and hardening exponent) is reasonably applicable to our material, except for the two-phase stainless steel region. The method requires each Berkovich indent to be associated with another cube corner indent to determine one set of plastic properties (σ_y,n). As there exists a significant scatter for the indentation curves within each group, the criterion for pairing those data was the ranking of the hardness value. The method could not be applied to the stainless steel as its microstructure made of δ-ferrite ligaments embedded in an austenitic matrix is highly heterogeneous at the scale of indentation and might lead to indentation size effects [179].

5.2.2 Processing of equivalent bulk material by decarburization experiments

Because its width is limited (200 μm) and the interfaces with adjacent regions are not planar, tensile specimens could not be extracted from the decarburized layer. The goal of this part was to find a way to create an equivalent bulk material to the decarburized layer in order to perform tensile tests on it. Thus this equivalent material should meet the following specific characteristics:

- **Large ferrite grains:** mean diameter around 40 μm
- **Low carbon content:** $w(C) \approx 0.015\%$ without any carbides
- **Soft material:** HV<150

5.2.2.1 Decarburization in wet H_2 atmosphere

Decarburized samples were obtained from the base metal 18MND5 by heat-treatment in an atmosphere with low carbon activity. The temperature was set to 660°C in order to enhance carbon diffusion while avoiding the $\alpha \rightarrow \gamma$ phase transformation. Samples, that are tensile micro-specimens (see Appendix C for the dimensions), were mechanically polished down to 2400 grit (i.e. 9 μm) prior to gas exposure. Dry hydrogen was found to be insufficient to decarburize over significant distances: only 30 μm after 72h at 660°C under a flow of 50 mL/min. The use of wet hydrogen allowed a significant increase of the decarburization kinetics, the chemical reaction $C+2H_2 \rightarrow CH_4$ being replaced by $C + H_2O \rightarrow CO + H_2$ [180].

The experimental set-up can be divided into four main parts visible on Figure 5.5:

A - The **gas control panel** which allows regulating the gas flow

B - The **water vapor partial pressure controller** which is made of two gas lines, one comprising dry gas while the other consists of humidified gas produced by passing through a water container. Both gases are mixed and a humidity probe associated with a controller allows regulating the mass flow to maintain the prescribed water vapor pressure.

C - The **tubular furnace**

D - The **pressure device** which allows controlling the pressure into the furnace through a manometer and a monitor connected to a regulation valve and a pump.

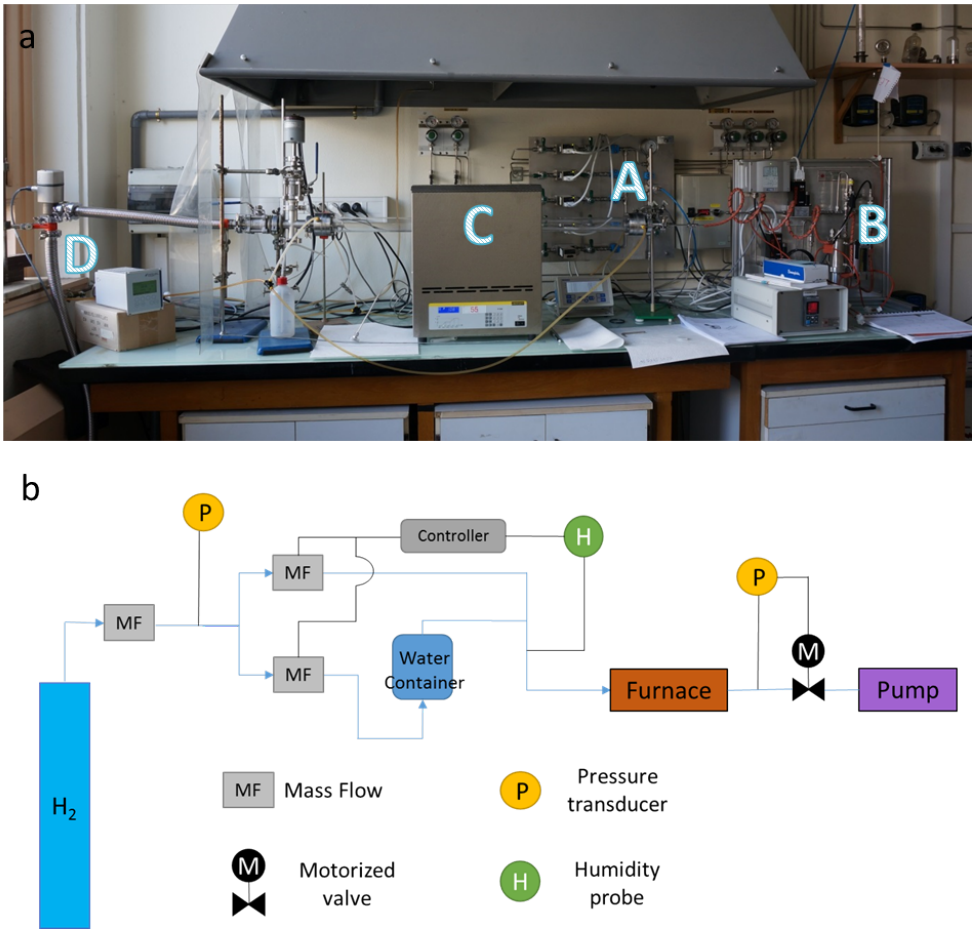

Figure 5.5: Experimental set-up for the decarburization under wet H_2 a- Picture of the device showing A- the gas control panel, B- the humidity controller, C- the tubular furnace and D- the pressure device. b- Simplified functional schematic.

Parameters which have enabled decarburizing the tensile specimens over their entire thickness (0.8 mm) are summarized in Table 5.1. 48 hours were found to be the minimum time necessary to obtain a homogeneous microstructure made of large ferrite grains without any residuals of carbon segregations, as visible on Figure 5.6. Grain boundary oxidation present on either side of the sample was certainly responsible for preventing the growth of the exterior grains. As oxide penetrations extend over less than 20 μm, they were removed by mechanical polishing of both faces before tensile testing.

Table 5.1: Parameters used for the decarburization in wet H_2 atmosphere.

Heating rate	7°C/min
Temperature plateau	660°C
Duration of the plateau	48 h
Hydrogen flow	25 mL/min
Pressure in the furnace	0.82 atm
H_2 humidity	2000 ppmv

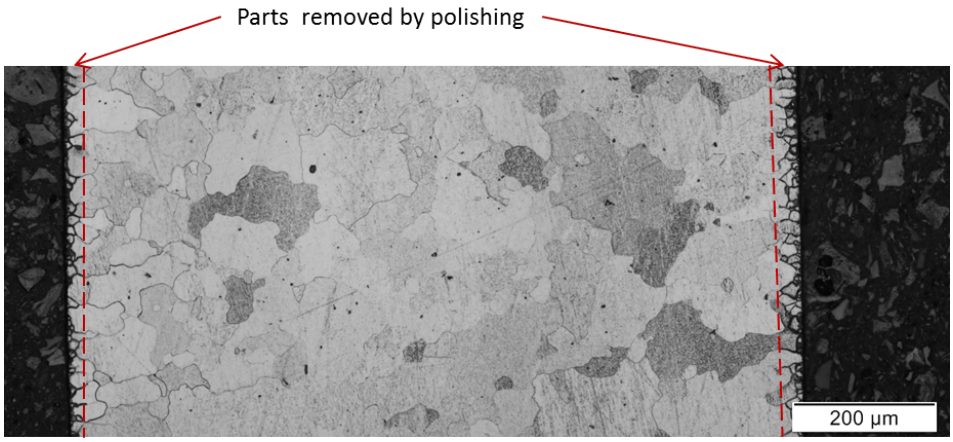

Figure 5.6: Cross-section of a specimen decarburized for 48 h at 660°C in a wet H_2 atmosphere of 2000 ppmv after Nital etching.

5.2.2.2 Decarburization by heat-treatment of diffusion couples

Diffusion couples between the low-alloy steel 18MND5 and several stainless steels (see Table 5.2) were fabricated by Hot Isostatic Pressing (HIP) in order to maintain planar interfaces and ensure a strong bonding without passing through the liquid state. Discs with a diameter of 99.3 ± 0.2 mm and a thickness of 6 ± 0.1 mm were extracted from the base metal plate by electro-wire erosion and then rectified to reach a roughness Ra below 1 μm. Afterwards, they were piled up with two discs of stainless steels (machined by laser cutting from 3 mm thick commercial plates) between each 18MND5 disc. A schematic of the assembly is presented on Figure 5.7-a and the compositions of the three stainless steels used are summarized in Table 5.2. The stack was sealed into a cylindrical container made of 304L stainless steel. It was subjected to the temperature and pressure cycle represented on Figure 5.7-b which includes a plateau of 180 ± 10 min at 1100 ± 10°C and 1200 ± 10 bar.

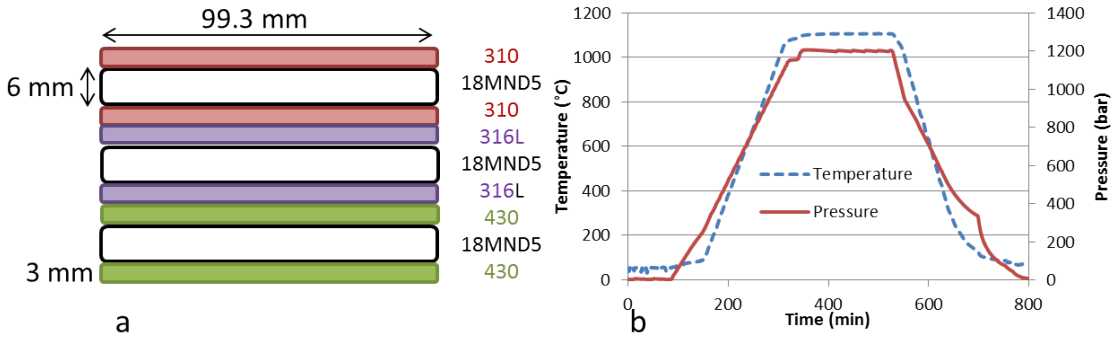

Figure 5.7: Diffusion couples made by HIP. a- Schematic of the assembly. b- Temperature and pressure cycle.

Table 5.2: Composition of the three stainless steels used in the HIP assembly.

	C (wt.%)	**Cr** (wt.%)	**Ni** (wt.%)	**Mo** (wt.%)	**Si** (wt.%)	**Mn** (wt.%)
310 (FCC)	0.12	23-26	18-21	-	1	2
316L (FCC)	0.02	16-18	10.5-13	2-2.25	1	2
430 (BCC)	0.08	16-18	0.5	-	1	1

In order to obtain decarburized 18MND5 over a significant thickness (at least 800 μm) the assembly was heat-treated after HIP at 660°C for 16 days 22 hours and 30 minutes, time that was found to be necessary to obtain extended decarburized layers. The microstructure of the diffusion couples after Nital etching can be seen on Figure 5.8 after HIP (Fig. 5.8-a) and after heat-treatment (Fig. 5.8-b). The larger decarburized layer was found in contact with 430 stainless steel. This is certainly due to the enhanced carbon diffusion into the ferritic microstructure of this steel in comparison with 316L and 310 stainless steels which consist of an austenitic matrix. However none of the fabricated decarburized layer was homogeneous, some residuals of C-rich bands that are initially present in the base metal could not be eliminated (in grey on the micrograph). Tensile micro-specimens were still machined by wire-electro erosion in the decarburized region parallel to the interface between the low-alloy steel 18MND5 and the stainless steel 430 for comparison with the mechanical properties extracted by the other techniques.

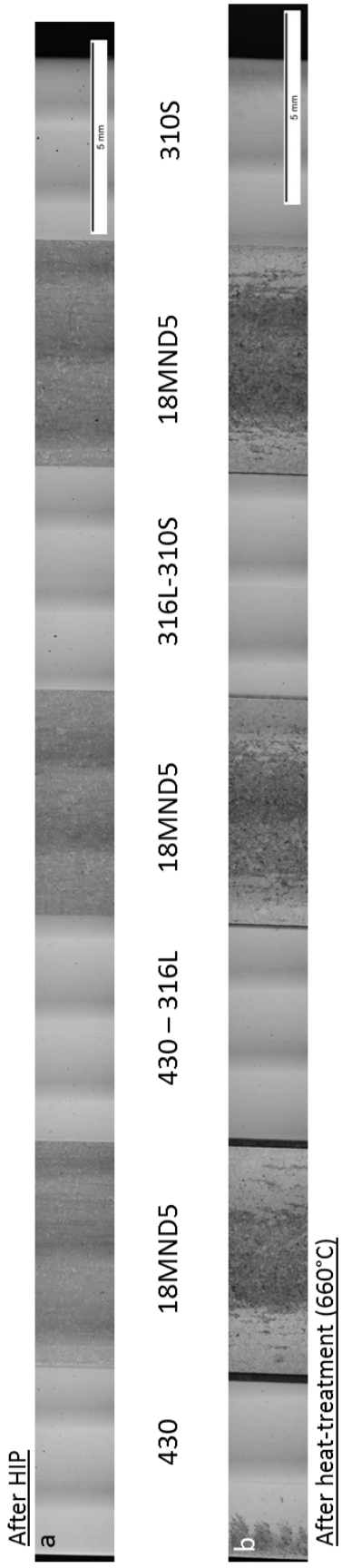

Figure 5.8: Microstructure of the diffusion couples revealed by Nital etching. a- After HIP cycle. b- After heat-treatment at 660°C for 16 days 22 hours and 30 minutes.

5.2.2.3 Comparison of the fabricated bulk materials with the decarburized layer of reference

In order to assess the reliability of the mechanical properties determined on both types of fabricated decarburized samples to represent the real mechanical behavior of the decarburized region in the weld, the samples were compared in terms of carbon content, micro-hardness and grain size. Global carbon contents were measured by combustion on both fabricated decarburized samples whereas local carbon measurements were performed by SIMS in the decarburized region of the weld. Micro-hardness was estimated for each sample from 50 indentation tests under a 100 g load, which is well-suited to the limited size of the decarburized region in the weld. Grain size was calculated by two different methods: the intercept procedure [181] which allows considering a large number of grains and the underlining of the grain boundaries followed by area measurements by image analysis. In the decarburized layer of the weld, only the second method could be applied due to the limited number of grains contained in its width.

5.2.3 Local strains measurements

As the microstructure of the dissimilar steel weld is highly heterogeneous on either side of the fusion line, it has been chosen to accurately measure local strains during tensile testing via micro-electrolithography and SEM imaging coupled with digital image correlation (DIC) to fulfill a twofold objective:

- Quantify **strain partitioning** between the different regions of the weld.
- Validate the **constitutive laws** determined for the different zones by the previously described techniques.

5.2.3.1 Microgrids deposition using electron beam lithography

The procedure employed to create the regular microgrids pattern on top of the specimen is schematically shown in Figure 5.9 with the main steps being summarized below:

a - The sample's surface was polished with a final step in colloidal silica suspension in order to reveal the main microstructural features.

b - A 4% PMMA resin in Anisole (A4) was then spin-coated on the specimen's surface at 1500 rpm for 60 s in order to obtain a film of uniform thickness. The sample was then baked at 140°C for 30 minutes in order to promote resin adhesion.

c - The coated sample was irradiated with the electron beam of a SEM (Sigma Zeiss FEG-SEM equipped with the Nanometer Pattern Generation System [182]) following a microgrid pattern.

d - The irradiated regions of the PMMA polymer was then dissolved in a solution consisting of 75% Isopropanol and 25% MethylEthylKetone for 60 s.

e - A 5 nm thick chromium layer was first evaporated (Plassys e-beam evaporator) in order to improve the adhesion of the microgrids to the steel substrate, followed by a 25 nm thick layer of gold. The advantages of gold are its good ductility and a strong contrast relative to iron when imaging with back-scattered electrons.

f - Finally, the sample was ultrasonically cleaned in acetone for 10 minutes to remove the unexposed resin.

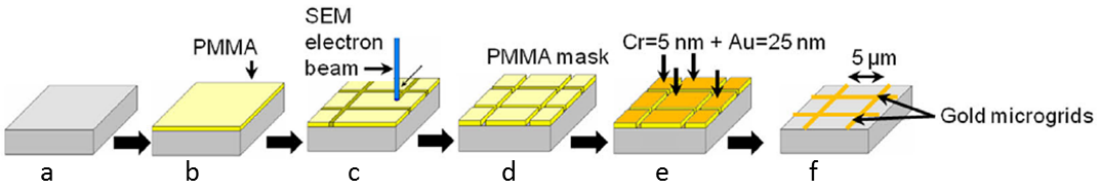

Figure 5.9: The main steps for fabricating microgrids by electron beam lithography [183].

An example of the result of this procedure is displayed on Figure 5.10. In total three areas of 800 x 800 μm^2 were covered with a fiducial microgrid having a step size of 5 μm and a line width of 300 nm, which allowed measuring strain with a fine resolution on both sides of the fusion line.

5.2.3.2 Mechanical testing and microgrids imaging

Macro-samples (see Appendix C for dimensions) were extracted perpendicularly to the fusion interface (length and width along the TD and LD directions of Figure 5.2 respectively). They are heterogeneous and allow characterizing the global mechanical behavior of the weld, which we tried to reproduce by Finite Element (FE) simulations based on experimental inputs.

The microgrids were deposited on the macro-sample in the heat-treated state and an interrupted tensile test was conducted at room temperature using a ZWICK 20kN machine under a strain rate of 10^{-3}/s. The sample was sequentially deformed and unloaded to 0.48 mm, 0.90 mm, 1.89 mm and 2.39 mm overall displacement. Low-magnification high-resolution (4096 x 3072 pixels) back-scattered electrons images of the microgrids were acquired with a SEM-FEG Zeiss Ultra55 between each increment of displacement. For each grid of 800 x 800 μm^2 four images were necessary, they were then aligned and merged to create an image of the entire area.

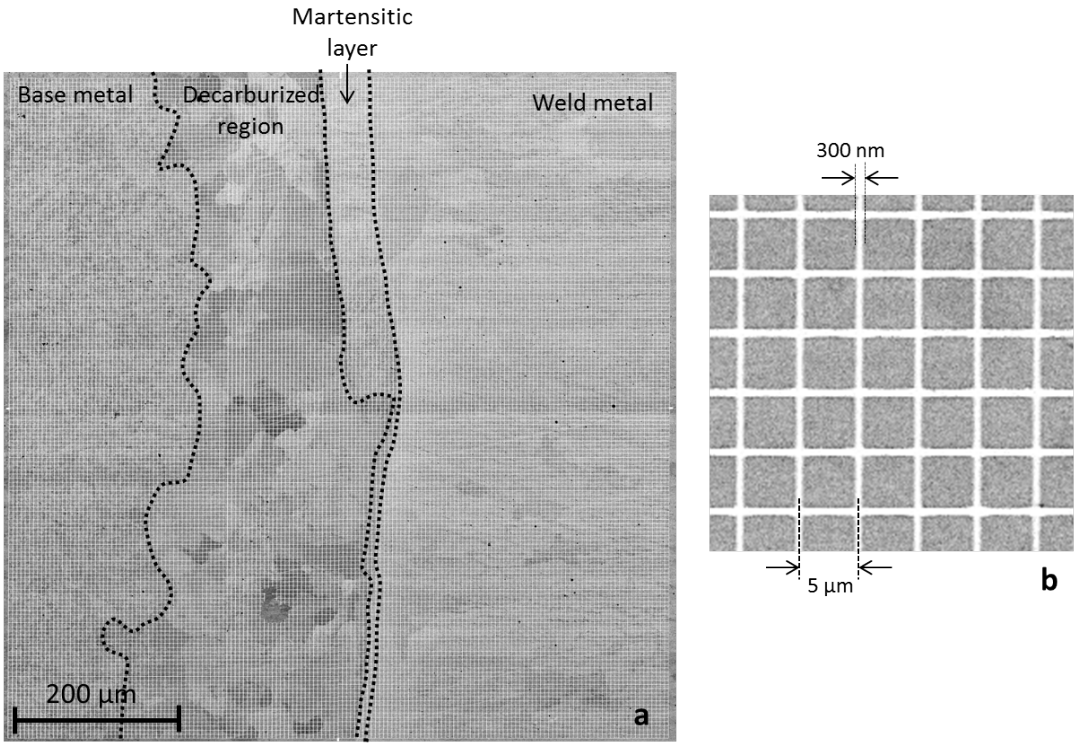

Figure 5.10: Example of microgrids fabricated by electron beam lithography a- SEM micrograph showing a global view of the microgrid (800 x 800 μm^2) covering the 18MND5/309L interface, two other equivalent grids were deposited on each side on the interface (one entirely in the base metal, and the other in the weld metal). b- Magnified SEM micrograph showing the grid step and line width.

5.2.3.3 Strain distribution mapping using Digital Image Correlation

Comparison between the microgrid intersections in the undeformed and deformed states allowed for quantitative measurements of the in-plane displacement field. For this, digital image correlation was employed with the CMV (CorrelManuV) software developed at the LMS laboratory [184, 185]. A 30 x 30 pixel correlation subset together with a search domain of 15 x 15 pixels were used for DIC. From the in-plane displacement components at each grid intersection, the local deformation gradient tensor was computed as the average over a small surface around the grid intersection. In the present study, a eight-neighbor integration scheme was chosen for the calculation of the logarithmic strain components in order to provide a good compromise between spatial resolution and accuracy on the measured strain. More details about the derivation of the logarithmic strain tensor components can be found in [184] and in Appendix D.

Mapping of the height variations on the specimen's surface was also achieved by means of a Taylor Hobson mechanical profilometer in order to obtain an order of magnitude of the displacements perpendicular to the surface of observation. The high resolution (16 nm in depth and 0.5 μm laterally) was particularly suitable for measuring the height of the step which is created at the interface between the soft decarburized region and the hard martensitic layer.

5.3 Results and discussion

5.3.1 Local mechanical properties

5.3.1.1 Constitutive laws from tensile micro-specimens

The true stress-strain curves obtained from the tensile specimens (LD type, see Fig. 5.2) machined parallel to the fusion interface in the different regions of the heat-treated weld are displayed in Figure 5.11 and the main mechanical characteristics that can be extracted from these tensile tests are gathered in Table 5.3.

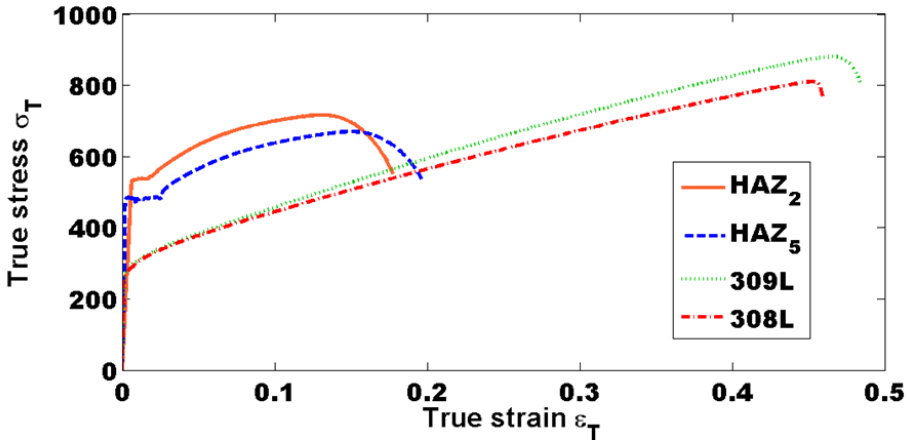

Figure 5.11: True stress-strain curves for the different regions of the weld where tensile micro-samples (LD type) could be extracted.

Table 5.3: Characteristic quantities extracted from the tensile tests on the micro-samples.

	$R_{p0.2}$	R_m	ϵ_u	ϵ_f	n_u
HAZ_5	470 MPa	670 MPa	0.15	1.17	0.13
HAZ_2	529 MPa	716 MPa	0.13	1.19	0.11
309L	281 MPa	880 MPa	0.47	1.10	0.45
308L	274 MPa	810 MPa	0.45	1.00	0.43

The difference in terms of mechanical behavior between the ferritic and austenitic sides of the weld is clearly visible: the micro-samples from the low-alloy steel side have a higher yield point but a limited strengthening capacity whereas plasticity initiates at lower stresses in the stainless steels followed by a large ductility. Although their yield points are equivalent, 309L stainless steel hardens slightly more than 308L before final failure. It is worth noticing that the hardening exponent at the onset of necking n_u and the true fracture strain at necking ϵ_u are in good agreement as predicted by the Considere criterion. This confirms that the micro-tensile specimens have been appropriately extracted from the welds and are sufficiently homogeneous. Indeed, if significant imperfections of the micro-tensile specimens were present, necking would occur earlier than the Considere criterion. Hutchinson et al. [186] showed that tiny geometrical or material inhomogeneities cause premature failure.

The flat part visible after the yield point on the 18MND5 curves corresponds to the propagation of Lüders bands (strain softening instability). They are due to interstitially dissolved carbon pinning the dislocations by formation of Cottrell atmospheres around them [187]. The difference in yield point between the 18MND5 sample at 2 mm from the fusion line and the one at 5 mm can be explained by microstructural evolutions inside the heat-affected zone as shown on Figure 5.12. The martensite-austenite islands (in white on Figure 5.12) are more coalesced at 5 mm and consequently do not constitute a continuous network of hard phases decorating most of the ferritic grain boundaries as it is the case at 2 mm.

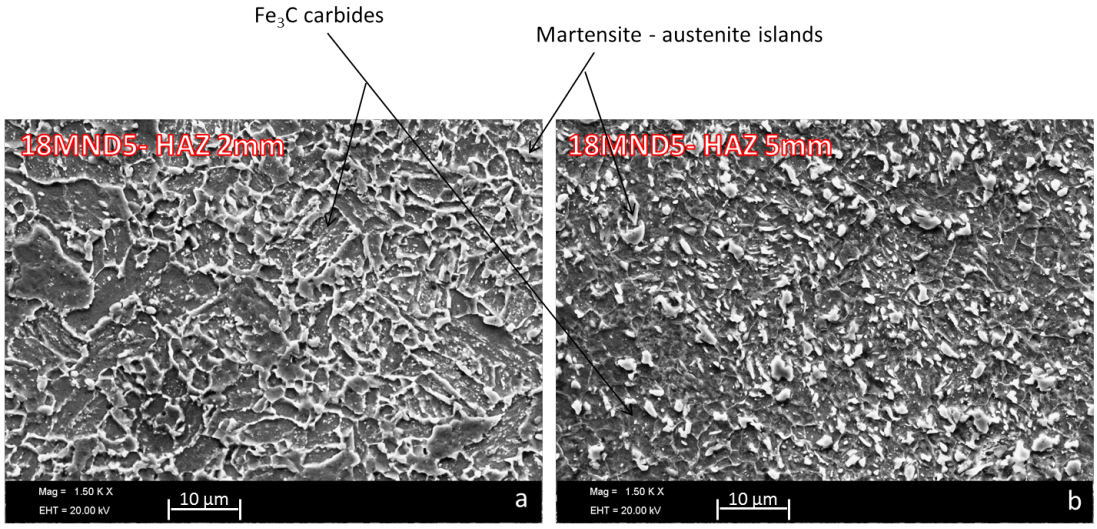

Figure 5.12: Microstructure of the 18MND5 in the HAZ revealed by Nital etching a- at 2 mm b- at 5 mm from the fusion line.

5.3.1.2 Elasto-plastic properties from nanoindentation tests

The H/E dimensionless parameter obtained by nanoindentation in the different zones of interest has been plotted on Figure 5.13 as a function of the penetration depth of the indenter. It represents the critical strain from which plastic deformation occurs. All the tests performed in a same zone give similar results. However we had to divide the carburized stainless steel into two subregions, depending on the distance to the martensitic band. An important drop of hardness occurs when moving in the stainless steel away from the martensite/austenite boundary. The martensite is found to have an intermediate H/E ratio between both austenitic regions. Such a plot allows highlighting the huge effect of carburization on the mechanical behavior of the affected zones. However the difference between the base metal and the decarburized zone is less significant: only a slight decrease of H/E is visible.

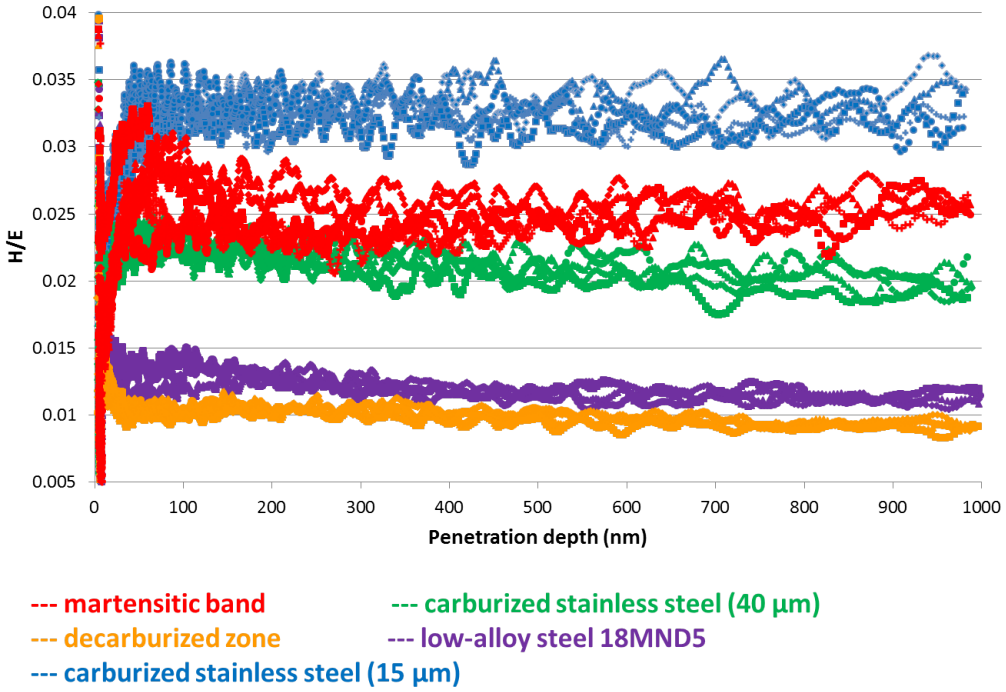

Figure 5.13: H/E ratio as a function of the penetration depth during nanoindentation test with a Berkovich indenter in the different regions of the weld.

The results obtained by Bucaille's method with two indenters are summarized in Figure 5.14 and Table 5.4. The carburized stainless steel is characterized by a huge gradient in mechanical properties: σ_y varying from 2300 to 1000 MPa and n from 0 to 0.12 over less than 30 μm. In accordance with the hardness plots of Figure 5.1, intermediate values are obtained for the yield strength of the martensitic band. The base metal serves as a region of reference as the mean values obtained by nanoindentation (493 MPa for σ_y and 0.10 for n) can be compared with the results from the tensile testing of sample HAZ_2 (529 MPa for σ_y and 0.11 for n). A difference of 7 % on the mean yield stress and of 9 % on the mean hardening exponent is evaluated. Furthermore, the error bars are large for the nanoindentation results and the tensile test results are within these error bars. Hence, the use of nanoindentation to extract plastic properties seems reasonable for the regions of interest around the fusion line. Concerning decarburization, it leads to a decrease of σ_y down to 345 MPa and a slight increase of n up to 0.13.

Table 5.4: Mechanical properties from nanoindentation by Bucaille's method.

	Representative stress		Yield strength	Hardening exponent
	Berkovich	Cube corner	σ_y (MPa)	n
Base metal	637-678	643-838	417-627	0.006-0.16
Decarb. layer	510-521	579-656	294-385	0.10-0.17
Martensite	1472-1797	1173-1575	1472-1797	0
Carb. austenite (15 μm)	2166-2509	1743-1911	2166-2509	0
Carb. austenite (40 μm)	1280-1326	1465-1564	964-1021	0.11-0.13

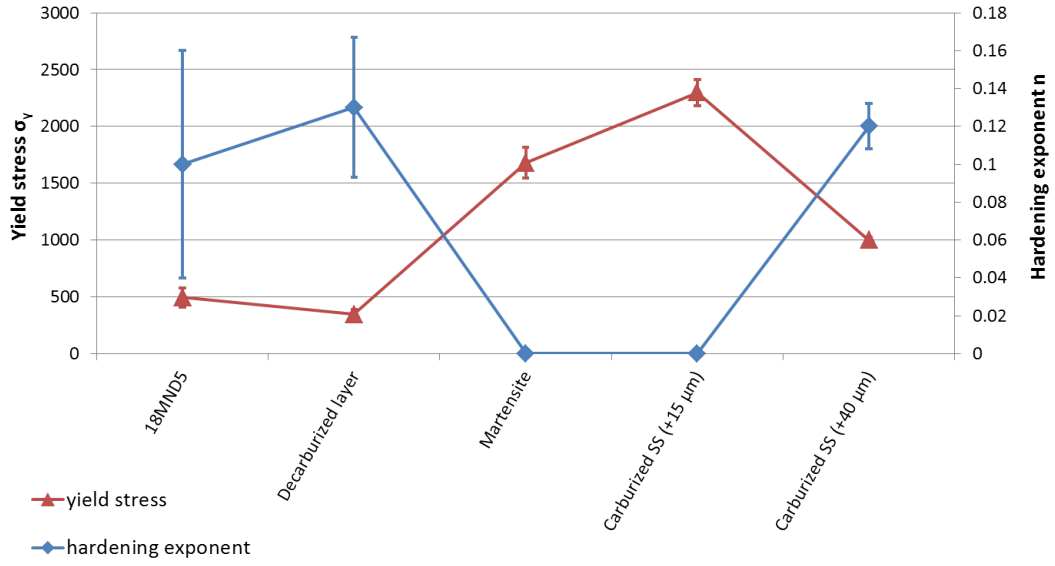

Figure 5.14: Yield strength and strain hardening exponent determined by nanoindentation via Bucaille's method [11]. The error bars represent the standard deviation of the mean value calculated over all the different tests performed in a same zone.

As shown by the error bars of Figure 5.14 and by the ranges displayed in Table 5.4, the results are highly dispersed. Several reasons can be put forward to explain the scatter of the data:

- **The pairing of the indents:** As Bucaille's method requires two indents for determining one set (σ_y,n) of mechanical properties, each Berkovich indent needed to be paired with a cube corner one. This relies on the assumption that the material under each indent is perfectly identical, which is difficult to guarantee owing to the small size of the indents (<10 μm).
- **The non-ideality of the indenter tip:** The dimensionless functions proposed by Bucaille originate from FE simulations performed with perfectly shaped indenters. However the real indenters are not ideal and present some imperfections such as rounding of the tip or deviation of the cross-sectional shape from ideal triangles, that can strongly affect the curvature of the loading curve.
- **The heterogeneities of the microstructure:** In the case of the base metal, some heterogeneities with a size comparable to the one of the indent (martensite/austenite islands, C and Mn segregations from solidification) could be responsible for the scatter of the indentation curves.

Concerning the decarburized layer, accurately determining its mechanical properties is quite challenging as it is a narrow band with a coarse microstructure. With nanoindentation, only one grain can be probed at the same time and the orientation effects cannot be neglected. It is equivalent to testing a single crystal, which is known to overestimate the yield strength in comparison to a polycristalline microstructure. Nevertheless, with micro-indentation, the influence of the hard adjacent layers cannot be avoided which will also lead to an increase of the apparent hardness.

5.3.1.3 The special case of the decarburized layer

Tensile tests were performed on the bulk decarburized samples fabricated either by decarburization in wet H_2 atmosphere or by heat-treatment of diffusion couples. As shown by the true stress-strain curves of Figure 5.15, both decarburization methods led to a drastic reduction of the yield point together with an increased ductility (see values of ϵ_f in Table 5.5). For each method, two samples were tested and they perfectly agree with each others in terms of elasto-plastic properties, except from the premature failure of sample "decarb H_2 1". The latter is certainly due to the presence of a defect in the material whose size is significant in regard of the tiny dimensions of the specimen [186]. Even if the Lüders band part of the curves has been reduced in comparison with the base metal, the effect of carbon in solid solution remains visible at the onset of yielding. Although both methods have led to a slight difference in terms of stresses (see Table 5.5 for a comparison of yield strengths $R_{p0.2}$ and ultimate tensile strengths R_m), the shape of the curves is identical, which is confirmed by similar values for the hardening exponent. The 30 MPa higher yield point for the "decarb HIP" samples can certainly be related to the carbon segregations that could not be eliminated in these samples (see Figure 5.8), leading to isolated hard areas.

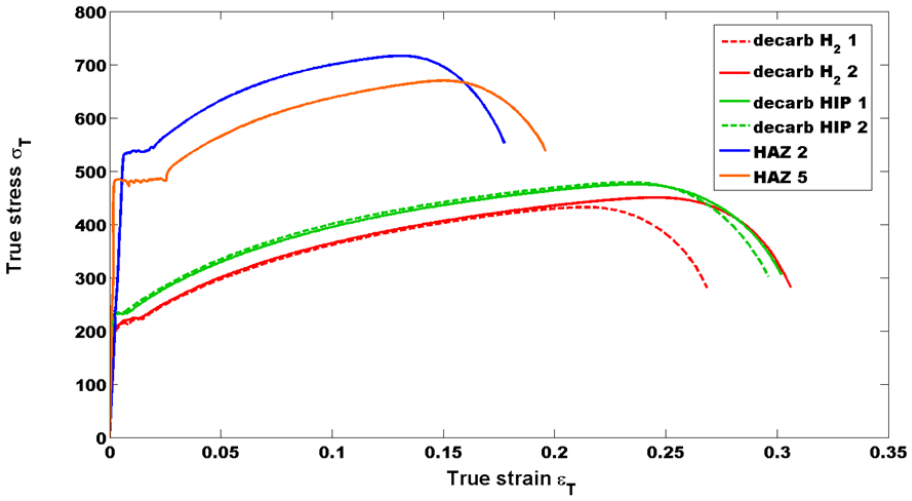

Figure 5.15: True stress-strain curves for the decarburized samples (LD type, see Fig. 5.2), decarb H_2 stands for the samples decarburized in wet H_2 atmosphere whereas decarb HIP corresponds to the ones decarburized by heat-treatment of diffusion couples. The curves for the base metal 18MND5 (HAZ 2 and HAZ 5 at 2 and 5 mm from the fusion line, respectively) have been added as a reminder.

A detailed comparison between the fabricated samples and the decarburized layer of the weld is provided in Table 5.6. The main objective is to decide on the applicability of the constitutive laws determined on the bulk decarburized samples for describing the mechanical behavior of the thin decarburized layer of the weld. In terms of carbon content, micro-hardness and grain size, the "decarb HIP" sample is the closest to the decarburized layer. However one should keep in mind that its microstructure was found to be heterogeneous, as confirmed by the high value of the standard deviation obtained on the micro-hardness measurements.

Table 5.5: Characteristic quantities extracted from the tensile tests on the decarburized samples.

	$\mathbf{R_{p0.2}}$	$\mathbf{R_m}$	$\epsilon_\mathbf{u}$	$\epsilon_\mathbf{f}$	$\mathbf{n_u}$
decarb H_2 1	203 MPa	432 MPa	0.22	2.61	0.19
decarb H_2 2	206 MPa	450 MPa	0.25	2.51	0.21
decarb HIP 1	232 MPa	476 MPa	0.24	2.48	0.20
decarb HIP 2	232 MPa	479 MPa	0.24	2.50	0.19

If one refers to the "decarb H_2" sample as best simulation of the decarburized layer of the weld, an increased yield point is expected due to a higher carbon content in the weld compared to the "decarb H_2" sample (see Table 5.6). Indeed, carbon is known to be a powerful hardening element when interstitially dissolved. According to [188], a hardening coefficient of 5014 MPa/wt.% is reported which should lead to an additional contribution of 65 MPa on the yield stress compared to the "decarb H_2" sample. However the difference in grain size should also be considered, as the larger grains of the decarburized layer of the weld should contribute to softening according to the well-known Hall-Petch equation:

$$\sigma_y = \sigma_0 + \frac{k}{\sqrt{d}} \tag{5.13}$$

d being the average grain size, k the strengthening coefficient and σ_0 the intrinsic stress of the lattice. With a Hall-Petch coefficient k of 17 $MPa.mm^{1/2}$ typical of low-carbon steels [189, 190], the yield strength should be decreased by 21 MPa.

Table 5.6: Comparison of the decarburized samples with the decarburized layer of the weld in terms of carbon content, micro-hardness and grain size.

	Carbon content wt.%	Hardness HV_{100g}	Grain size by the intercept method	Grain size by image analysis
decarb H_2	0.002	124 ±5	30 μm	26 μm
decarb HIP	0.011	137 ±16	59 μm	54 μm
decarburized layer	0.015	136 ±9	-	41 μm

The previous corrections lead to an estimation of the yield strength of the decarburized layer around 247 MPa which is below the values obtained by nanoindentation (294-385 MPa). A potential further increase could be attributed to the residual stresses accumulated in the weld during the cooling subsequent to the post-welding heat-treatment. Due to the difference in thermal expansion coefficient between the ferritic and austenitic part of the weld ($\alpha(18MND5) = 11.5 \times 10^{-6}/K$ whereas $\alpha(309L) = 14.4 \times 10^{-6}/K$), stresses are generated in the WD and LD directions. An order of magnitude of the level of residual stresses can be obtained by $\sigma = \frac{E\Delta\alpha\Delta T}{2(1-\nu)}$, which leads to 280 MPa for the weld of interest. Such stresses can cause plastic flow and isotropic hardening and result in an increase of the initial yield stress by creation of new dislocations. These stresses are not

present in the bulk fabricated specimens as they are made of only one material and do not present the "differential thermal dilatation effect" responsible for potential local plasticity and hardening.

With the fabrication of model bulk materials equivalent to the decarburized layer we had to face the problem of decarburizing over a sufficient thickness for making tensile specimen machining possible without loosing too much carbon. The sample "decarb H_2" was decarburized homogeneously over 1 mm but its global carbon content was too low.

Therefore it was not possible to determine a unique set of elasto-plastic properties (σ_y, n) for the decarburized layer. Instead we obtained lower (200 MPa by tensile tests on bulk materials) and upper (350 MPa by nanoindentation) bounds for the yield stress. Both extreme values will have to be tested in the finite element simulations in the next sections. Comparison in terms of tensile curve and local strain values will help discriminate between them. Concerning the hardening capacity, the one found in the tensile tests on bulk specimens will be retained as it was similar (n≈0.2) for both fabricated samples having different carbon content and grain size (see Table 5.5).

5.3.2 Global mechanical properties

5.3.2.1 Tensile testing

Effect of the post-welding heat-treatment

An example of tensile curves obtained on the macro-samples machined perpendicular to the fusion interface (TD type, including the different regions of the weld) in the as-welded and heat-treated states is presented on Figure 5.16-a. In both cases and in a reproductible way, final failure always occurs in the 308L layer.

Surprisingly a reduction in yield strength (from 400 to 300 MPa) is observed in the case of the heat-treated sample. Although the ferritic part of the weld was subjected to tempering by the heat-treatment (see micro-hardness profiles of Figure 5.1), its yield stress remains far above the one of the stainless steel layers, as shown by the curves of Figure 5.11. The yield point of the weld should be determined by the softer zone, namely the stainless steel layers whose engineering stress-strain curves in the heat-treated state are compared to those in the as-welded state on Figure 5.16-b and -c. In both cases (309L and 308L) the yield point is slightly lower in the heat-treated state but the hardening capacity is increased which lead to an ultimate tensile strength slightly higher in the heat-treated state. This small difference in yield strengths is unlikely to explain a disparity of 100 MPa on the yield point of the weld in the heat-treated and as-welded states. The hypothesis of a softening of the austenitic matrix by carbon depletion during the ferrite decomposition taking place at 610°C was also disregarded as nanoindentation profiles across the ferrite residuals did not reveal any local hardness decrease of the surrounding matrix. As it will be emphasized later, the decarburized layer, by its limited width, cannot induce such a global softening. The only probable

hypothesis remains the residual stresses accumulated during the welding process and that will then be released during the isothermal part of the heat-treatment. As calculated in [191], the austenitic cladding is found to be in tension with longitudinal stresses (direction LD on Figure 5.2) around 350 MPa at the end of the welding cycle. Then, at the end of the heat-treatment, cooling occurs from 610°C only and consequently the residual stresses decrease. Such stresses disappear during the machining of the micro-samples extracted parallel to the fusion interface in an homogeneous zone. From now and for the following of this section, we will concentrate on the heat-treated sample that corresponds to the state of the weld in service conditions.

The softening singularity visible on the heat-treated curve of the global weld for a displacement around 1 mm (see Figure 5.16-a) has to be related with the Lüders bands phenomenon that develops within the base metal and that was already identified on the micro-samples extracted from the heat-affected zone.

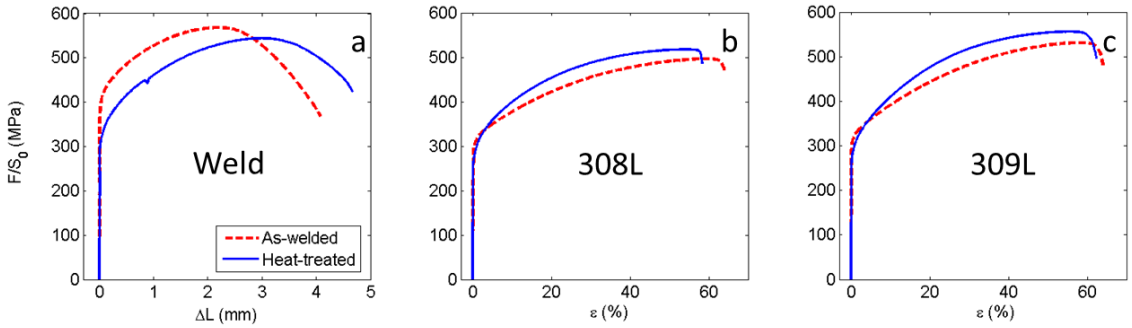

Figure 5.16: Tensile curves in the as-welded and heat-treated states a- for the weld (TD-type sample), b- for the 308L layer (LD-type), c- for the 309L layer (LD-type).

Anisotropic behavior of the stainless steels

A tensile specimen was machined in the heat-treated state perpendicularly to the fusion interface with only stainless steels along its gauge length (same positioning as the macro-samples with a shift towards the austenitic layers). It allowed investigating the mechanical properties of the stainless steel layers in the same direction as the one tested on the macro-sample of the weld. Figure 5.17 reveals that the behavior of the stainless steels is highly anisotropic in terms of strengthening. The yield point of the transverse sample is quite similar to the ones of the 309L and 308L longitudinal samples but it has a higher hardening capacity. The directional solidification during welding is responsible for the strong texture of both cladding layers. The <001> direction of the cubic structure is preferentially oriented along the thermal gradient, which means perpendicular to the fusion interface. Such preferential crystallographic orientation is clearly visible on pole figures obtained by X-Ray diffraction [192] or EBSD and is responsible for the hardening observed along the TD direction, which is also confirmed by the micro-hardness tests on both surfaces (see Table 5.7). This anisotropic behavior of the stainless steel was already evidenced by micro-hardness measurements in [18]. Therefore the stainless steels do not have the same mechanical properties in the tensile direction chosen for the weld (TD direction) and in the one chosen for the machining of

the micro-samples (LD direction) which were supposed to provide the constitutive laws to be used for each region within the weld. In what follows, the properties determined in the TD direction will be kept to represent a mean behavior of the stainless steel layers when loaded in the transverse direction.

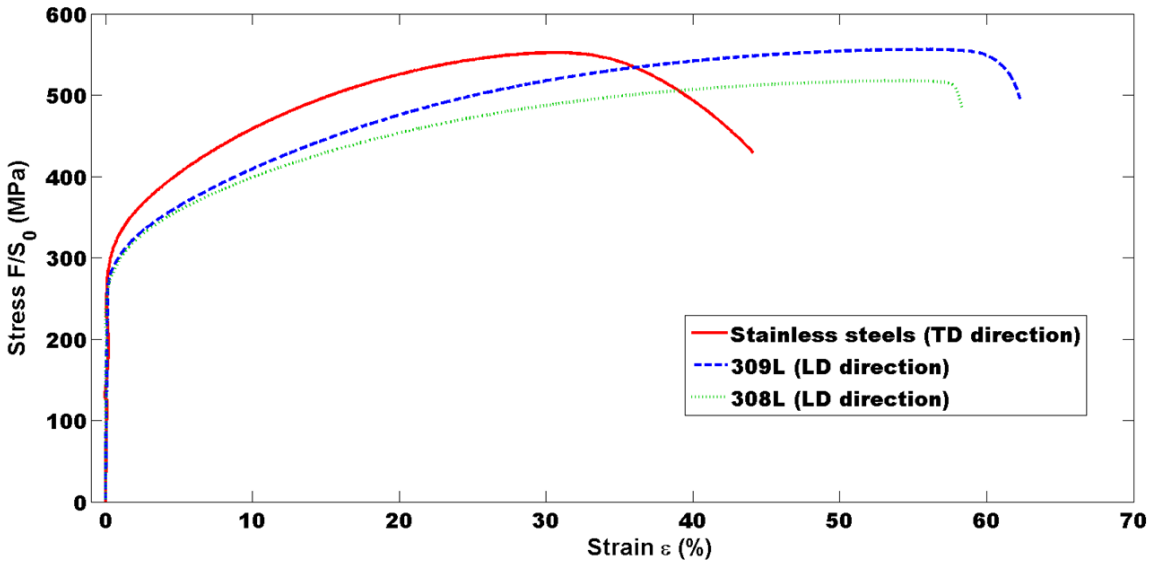

Figure 5.17: Engineering stress-strain curve of the stainless steel layers in the TD direction, the curves for the 309L and 308L stainless steels in the LD direction have been added as a reminder.

Table 5.7: Comparison of the micro-hardness of the stainless-steel layers in the different directions.

	309L		**308L**	
Surface	TD-LD	WD-LD	TD-LD	WD-LD
Micro-hardness HV_{1kg}	171	157	173	155

5.3.2.2 Elasto-plastic modeling

Model description

The goal of this section is to model the global transverse tensile behavior of the weld using the general purpose finite element code Abaqus [193] assuming J2 isotropic plasticity. The main characteristics in terms of geometry and boundary conditions are represented on Figure 5.18.

Two symmetry planes (TD-WD and TD-LD) were considered to reduce the computational time. The mesh was refined in both the narrow layers (mesh size of 5 μm in the decarburized region) and in the region where the final fracture takes place, namely the extremity of the 308L layer. Figure 5.19 shows the constitutive laws that were introduced in the different regions:

- A **power law** (see equation 5.10) was used for the **carburized regions** (martensite and both austenitic layers) with σ_y and n taken as the mean values determined by **nanoindentation.**

- The **experimental stress-strain curves** from the tensile tests on the micro-samples were introduced point by point up to the onset of necking for the **austenitic cladding** (309L and 308L). They were further extrapolated using a **Swift law:**

$$\sigma = \sigma_y(1 + k\epsilon_P)^n \tag{5.14}$$

where σ_y is the yield stress, ϵ_P the true plastic strain, n and k two constants taken as 0.42 and 27 respectively.

- Concerning the **base metal**, the experimental curves from the HAZ were fitted by a **stress plateau followed by a power law** of type $\sigma = K\epsilon_P^n$ to take into account the initial strain instability.

- For the **decarburized layer**, constitutive laws were constructed from the tensile curve of the **"decarb H_2" specimen:** the yield stress was varied between 200 and 350 MPa while maintaining the same strain hardening capacity as those experimentally measured.

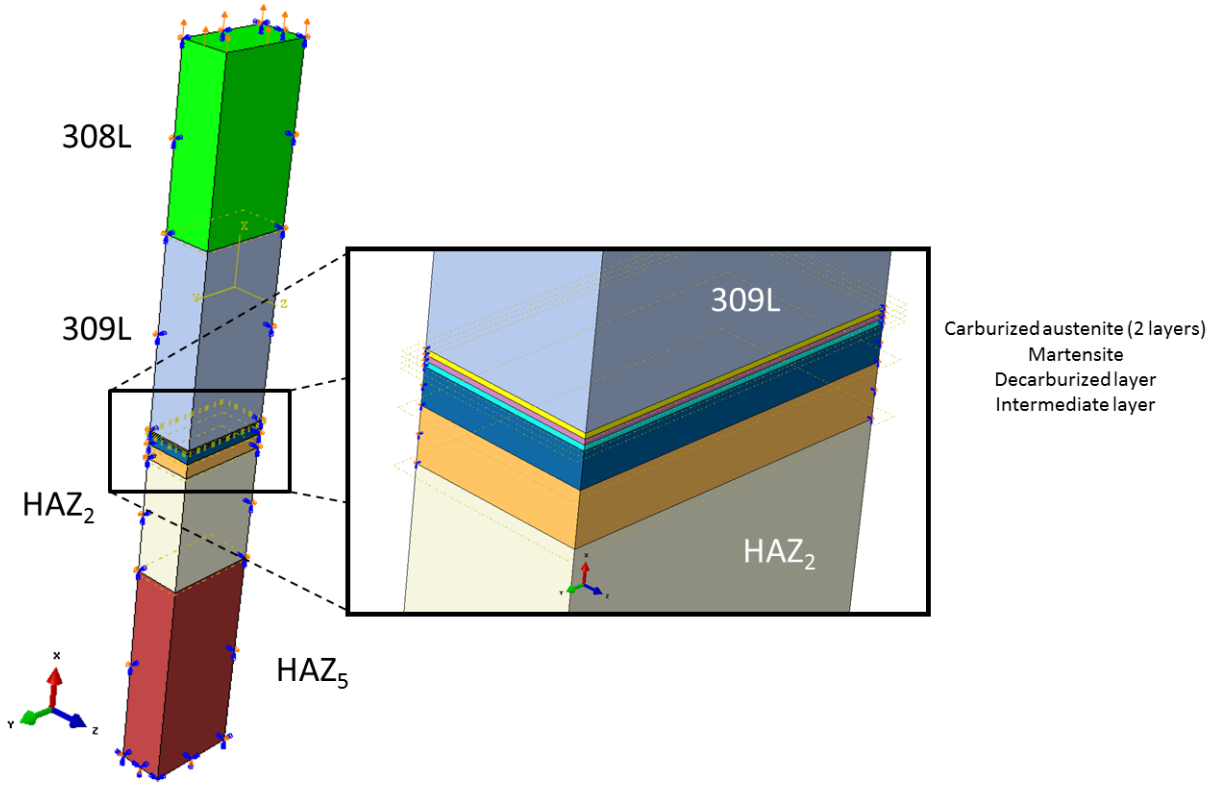

Figure 5.18: Geometry and boundary conditions for the FE simulation of a tensile test on the weld macro-specimen.

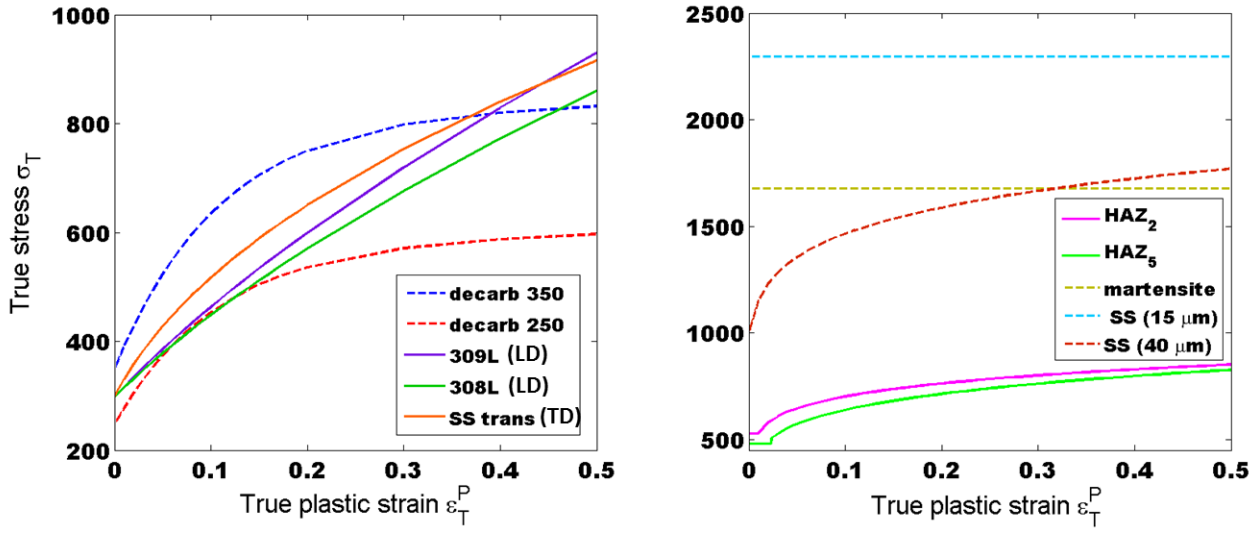

Figure 5.19: Local constitutive laws used in the different regions for the FE simulation of a tensile test on the weld macro-specimen. SS trans refers to the properties determined by the tensile test on the stainless steel layers in the transverse direction, whereas SS stands for carburized stainless steel

Assessment of the model

Figure 5.20 compares the predicted tensile curves to the experimental one. When the constitutive laws from the micro-samples in the longitudinal direction (curves 309L and 308L of Figure 5.19-a) were used for the stainless steel layers, the stress level was under-estimated (see curve simulation - longitudinal 309L+308L). When they were both replaced by the mean properties determined in the transverse direction on a stack of several stainless steel layers (curve SS trans of Figure 5.19-a), the agreement with the experiment was better (see curve simulation - transverse SS). The remaining discrepancy arises from the fact that both layers could not be considered separately due to their small thickness (4 mm). To reach a better agreement an anisotropic law specific of each cladding layer should be used.

The strain instability (black circles on Fig. 5.20) was reproduced by the simulation even though its localization on the stress-strain curve does not match exactly. This can be attributed to the fact that the base metal was discretized in only two regions whereas its properties may evolve more continuously within the heat-affected zone. As shown on Figure 5.21, the strain instability that occurs at step 28 in the simulation corresponds to the onset of plastic deformation in the HAZ_5 region of the base metal. When the yield point of this region is reached, it suddenly plastically deforms allowing a global displacement (from 0.93 to 0.97 mm between steps 28 and 29) without any increase of the stress (478 MPa at steps 28 and 29). It was also noticed that the properties introduced for the decarburized layer did not affect the shape of the global tensile curve, certainly because of its reduced width (200 μm) in comparison to the gauge length (15 mm). Likewise the variation of the thickness of the martensitic layer did not have any particular effect at the global scale.

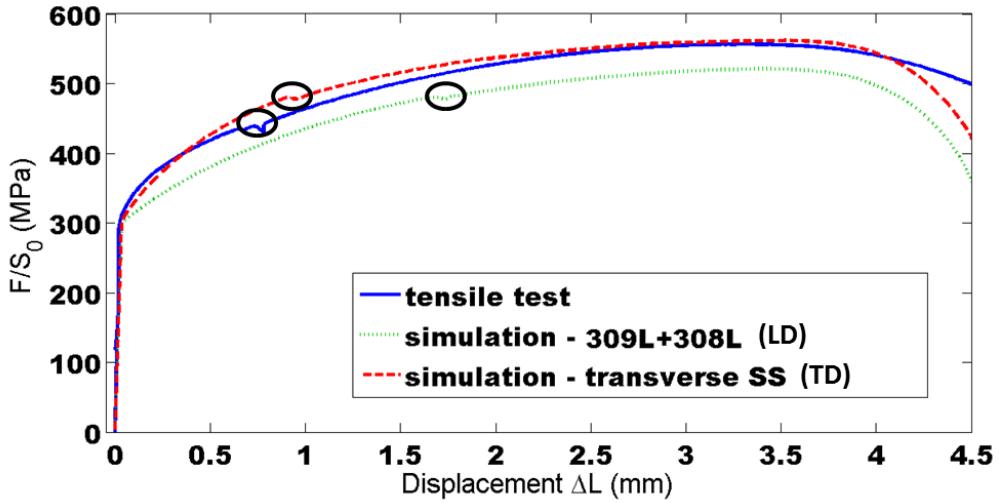

Figure 5.20: Comparison of the experimental engineering stress-displacement curve with the calculated ones. The black circles allow locating the strain instabilities.

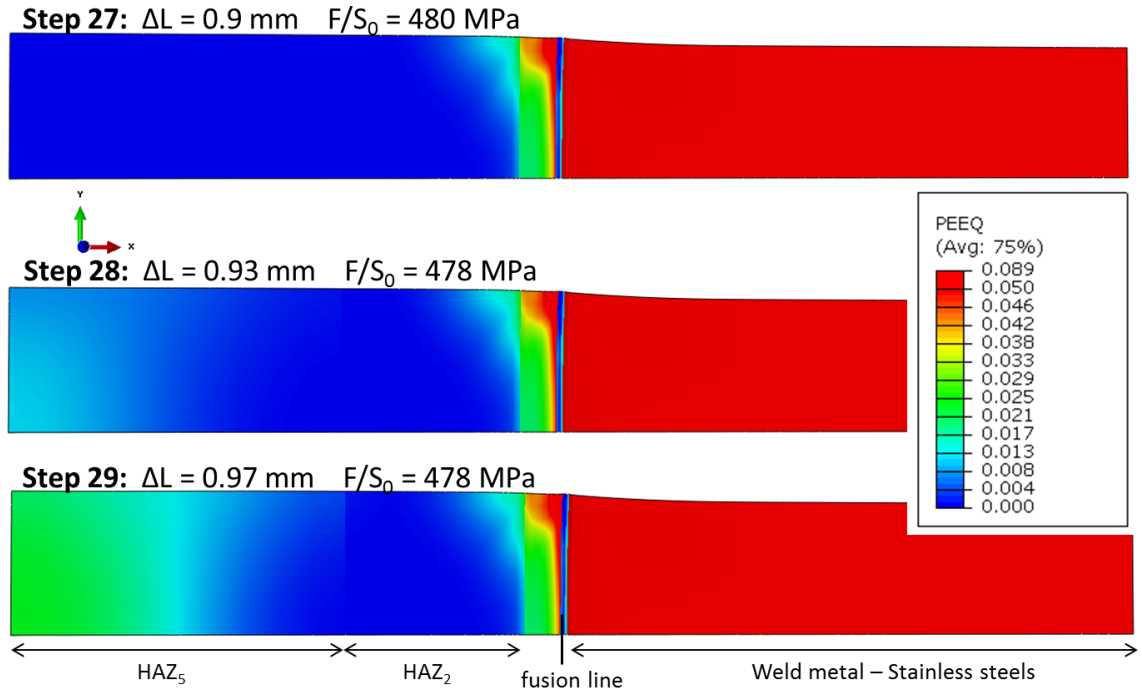

Figure 5.21: 3D mapping of the equivalent plastic strain (PEEQ) on one half of a specimen for successive increments of displacement when the HAZ_5 region of the base metal begins deforming plastically.

5.3.3 Strain partitioning

Figure 5.22 shows the results from the digital image correlation performed on the weld during tensile testing: the magnitude of the logarithmic strain component along the tensile direction ϵ_{11} is mapped over a surface of 2400 x 800 μm^2 around the fusion line for different increments of displacement. The plots of Figure 5.23 have been made by averaging the ϵ_{11} strain of all the subsets located at the same distance from the fusion line (in black on Figure 5.22) and those of Figure 5.24 represents the standard deviation of this mean strain as a function of the distance from the fusion line. The following elements are worth noting:

- High levels of strain are found in the stainless steel, which is in agreement with its low yield strength and high ductility highlighted by the micro-samples machined from this region of the weld. However the strain is not homogeneous along the tensile axis because the part close to the fusion line is highly constrained by the hard adjacent layers (martensite and carburized austenite). Therefore carburization is responsible for the gradient of strain observed in the stainless steel from the fusion line towards the specimen's extremity.

- In between the decarburized layer (200 μm wide) and the base metal with limited deformation ($<$5% in the last increment) an intermediate zone with moderate strain levels is found over 300 μm. It can be correlated to the decarburization which is gradual and spreads over 300 supplementary micrometers towards the base metal with neither complete carbides dissolution nor grain growth (see carbon profile on Figure 3.3). It leads to think that intermediate mechanical properties between those of the decarburized band and the base metal are encountered in this region. Such intermediate layer has been introduced into the simulation with a yield stress between 300 and 350 MPa and the same hardening capacity as the "decarb H_2" sample. It plays an important role as it directly influences the level of stresses that act on the decarburized layer.

- A high strain is found to appear at low stresses at the interface between the martensite and the decarburized ferrite and then spread into the soft layer. This tendency for strain localization in contact with a hard layer is unexpected as it is a highly constrained region. It has to be related with the step that is created at the ferrite/martensite interface in the early deformation stages and whose depth was measured by profilometry (see Figure 5.26). Indeed, for the first increment of displacement (0.48 mm), the step height is already found to be around 4 μm (see Fig. 5.26-a). This step increases with increasing the global displacement (around 20 μm for 2.39 mm, see Fig. 5.26-b). Therefore the measured strain along the tensile axis could be biaised because of this out-of-plane displacement at the interface.

- As confirmed by the plot of Figure 5.24, the deformation within the decarburized layer is highly dispersed with red (maximum strain) and blue (minimum strain) subsets adjacent to each others on the maps of Figure 5.22. It can be attributed to microstructural effects as grains are coarse in this region and may preferentially deform according to their crystallographic orientation.

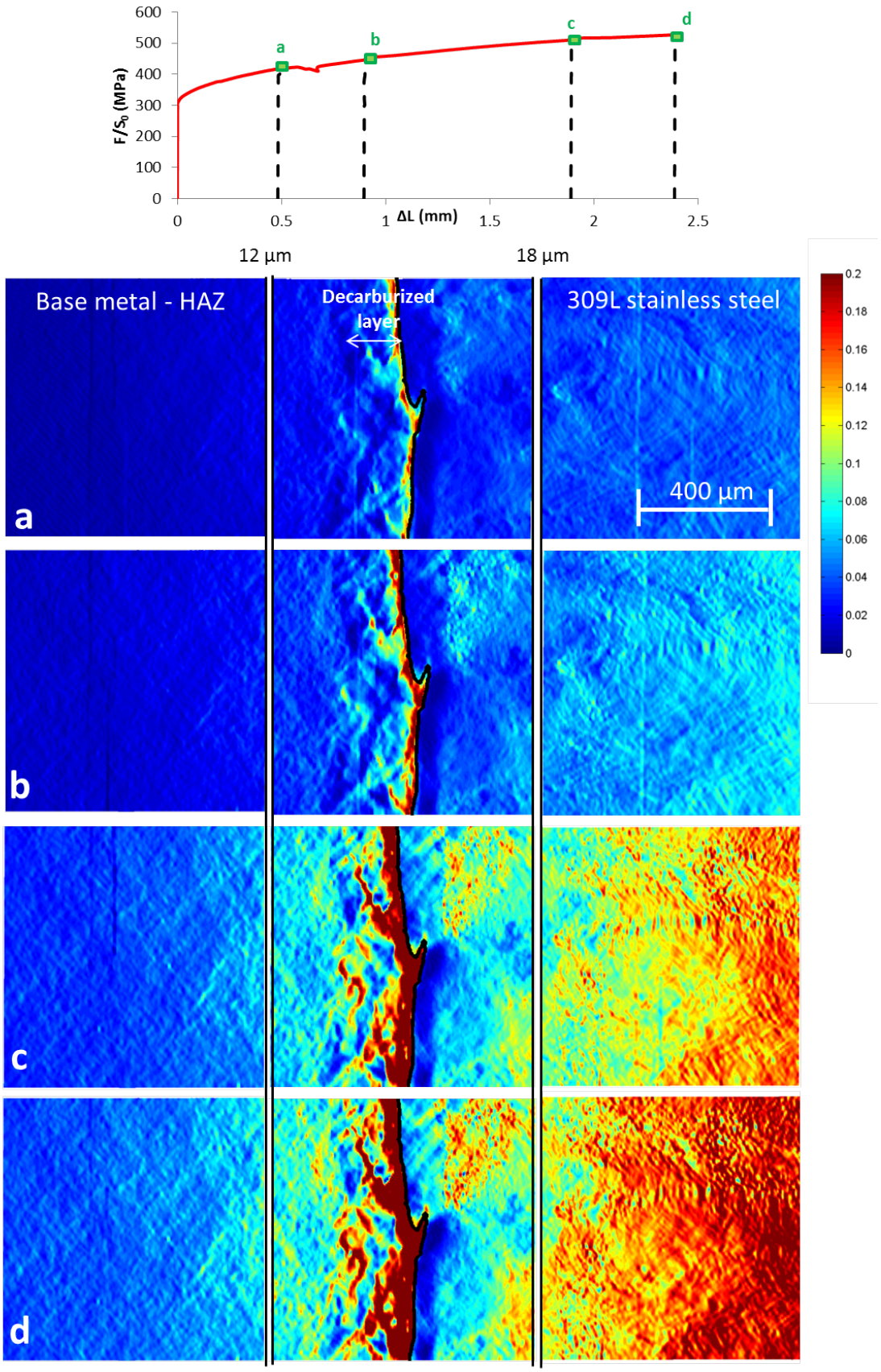

Figure 5.22: Logarithmic tensile strain maps determined by digital image correlation at different positions on the stress-strain curve of the weld: a- $\Delta L = 0.48$ mm, $\sigma = 421$ MPa; b- $\Delta L = 0.90$ mm, $\sigma = 480$ MPa; c- $\Delta L = 1.89$ mm, $\sigma = 534$ MPa; d- $\Delta L = 2.39$ mm, $\sigma = 548$ MPa. The fusion interface has been highlighted in black.

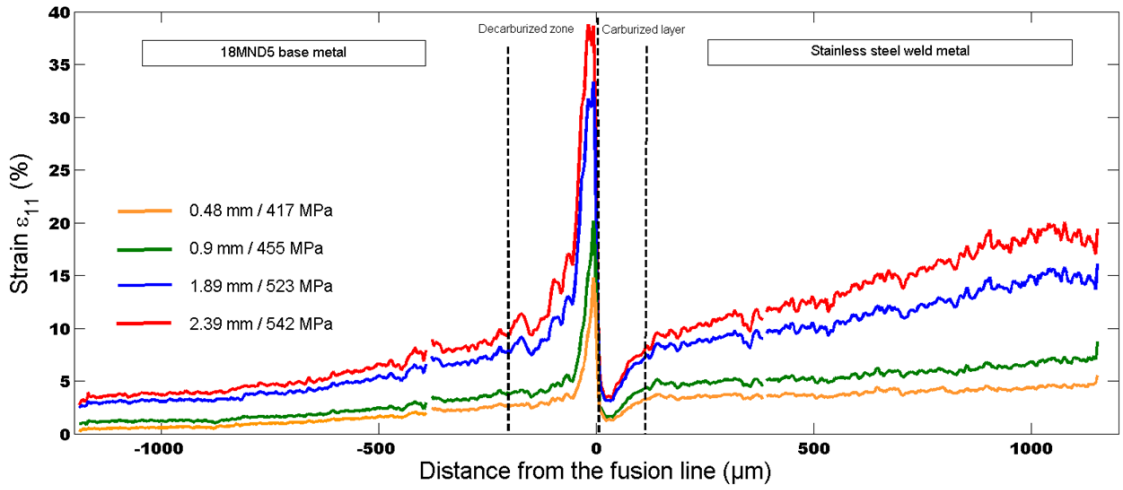

Figure 5.23: Logarithmic strain along the tensile axis as a function of the distance from the fusion line for different increments of displacement.

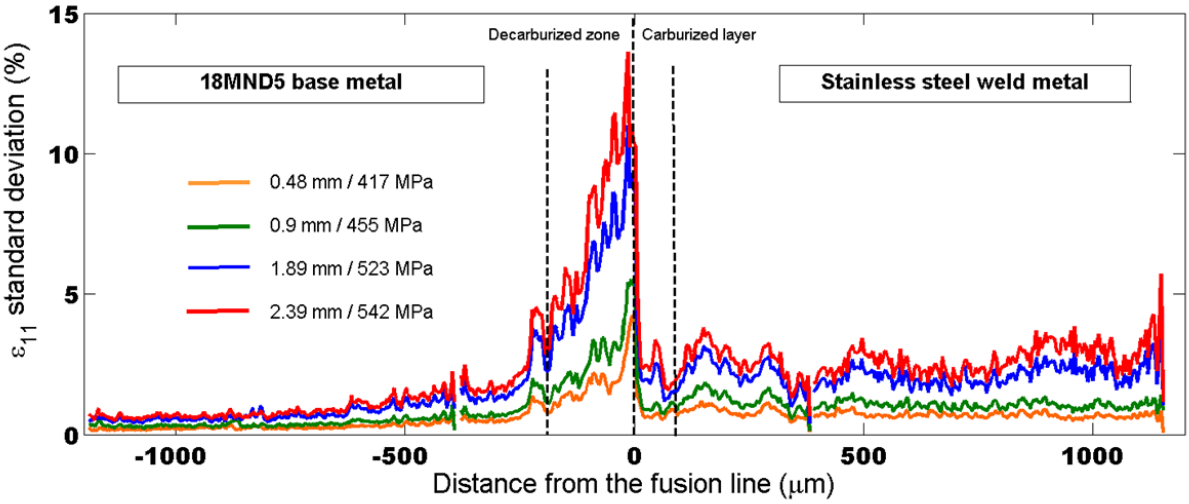

Figure 5.24: Standard deviation of the logarithmic strain along the tensile axis as a function of the distance from the fusion line for different increments of displacement.

Several values of the yield stress for both the intermediate and decarburized regions were tested in the FE simulations and were compared with the experimental measurements of the local strains by DIC. The best general agreement was obtained with a yield stress of 250 MPa in the decarburized layer and the addition of an intermediate layer with a yield strength of 300 MPa over 300 μm in between the decarburized layer and the heat-affected zone of the base metal. Such a change does not affect the global tensile curve but allows reproducing the significant strain levels measured by DIC between 200 and 500 μm from the fusion line on the base metal side. The strain along the tensile direction calculated by FE modeling is mapped on Figure 5.27 for the 250/300 MPa couple. A good agreement is obtained for nearly all regions with similar levels of strain measured by DIC and calculated by FE simulation (see plots of Figure 5.25 for a direct comparison).

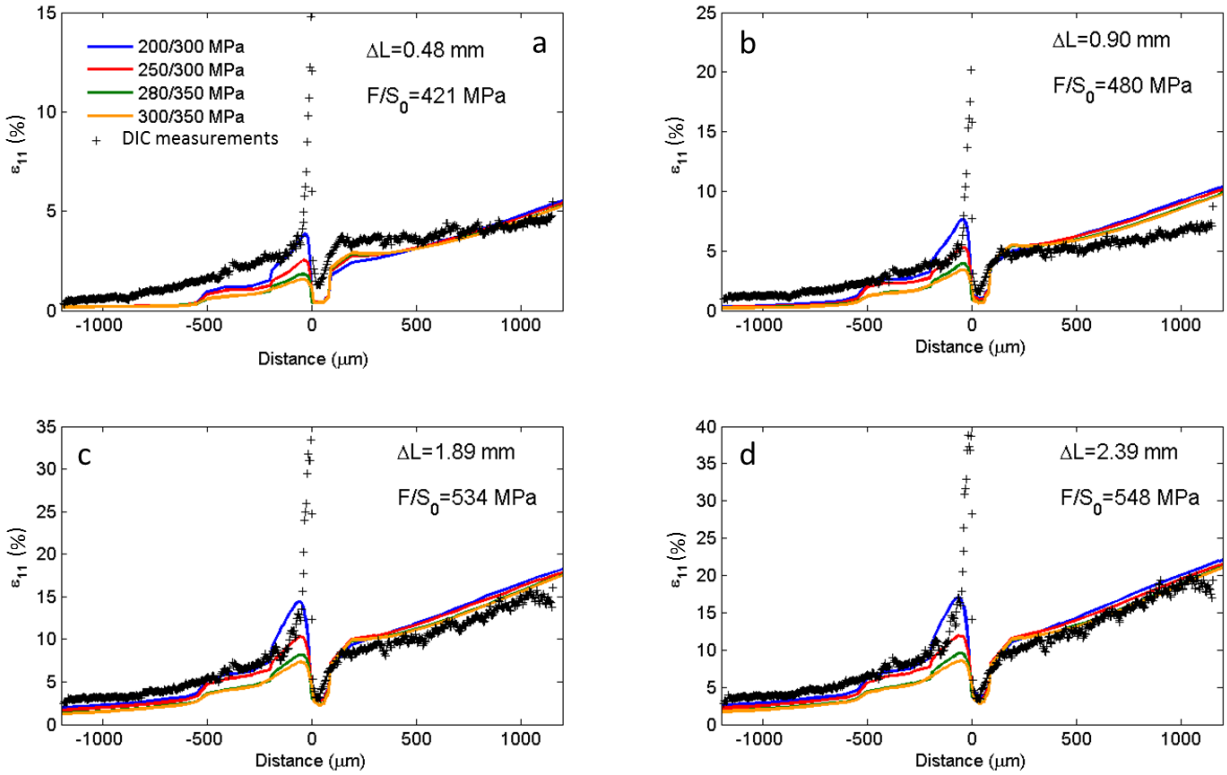

Figure 5.25: Comparison between DIC measurements and FE simulations in terms of logarithmic strain along the tensile direction for different values of the yield stress of both the decarburized and intermediate regions. a- $\Delta L = 0.48$ mm, $\sigma = 421$ MPa; b- $\Delta L = 0.90$ mm, $\sigma = 480$ MPa; c- $\Delta L = 1.89$ mm, $\sigma = 534$ MPa; d- $\Delta L = 2.39$ mm, $\sigma = 548$ MPa.

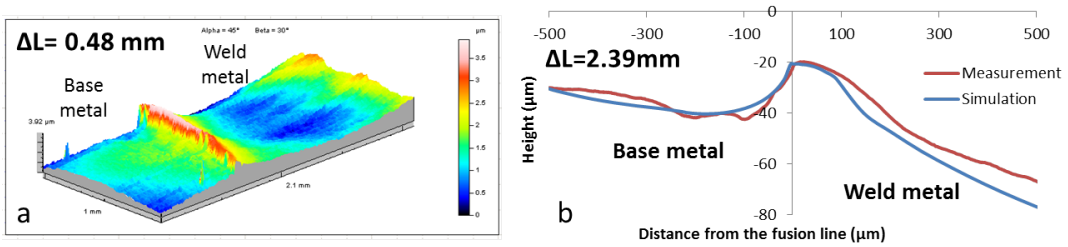

Figure 5.26: Measurement of the variations of specimen's height by profilometry: a- 3D mapping around the interface for a global displacement of 0.48 mm. b- Comparison between elasto-plastic simulation and profilometry measurements in terms of height of the specimen surface after a global displacement of 2.39 mm ; 0 corresponds to the initial position of the surface before deformation.

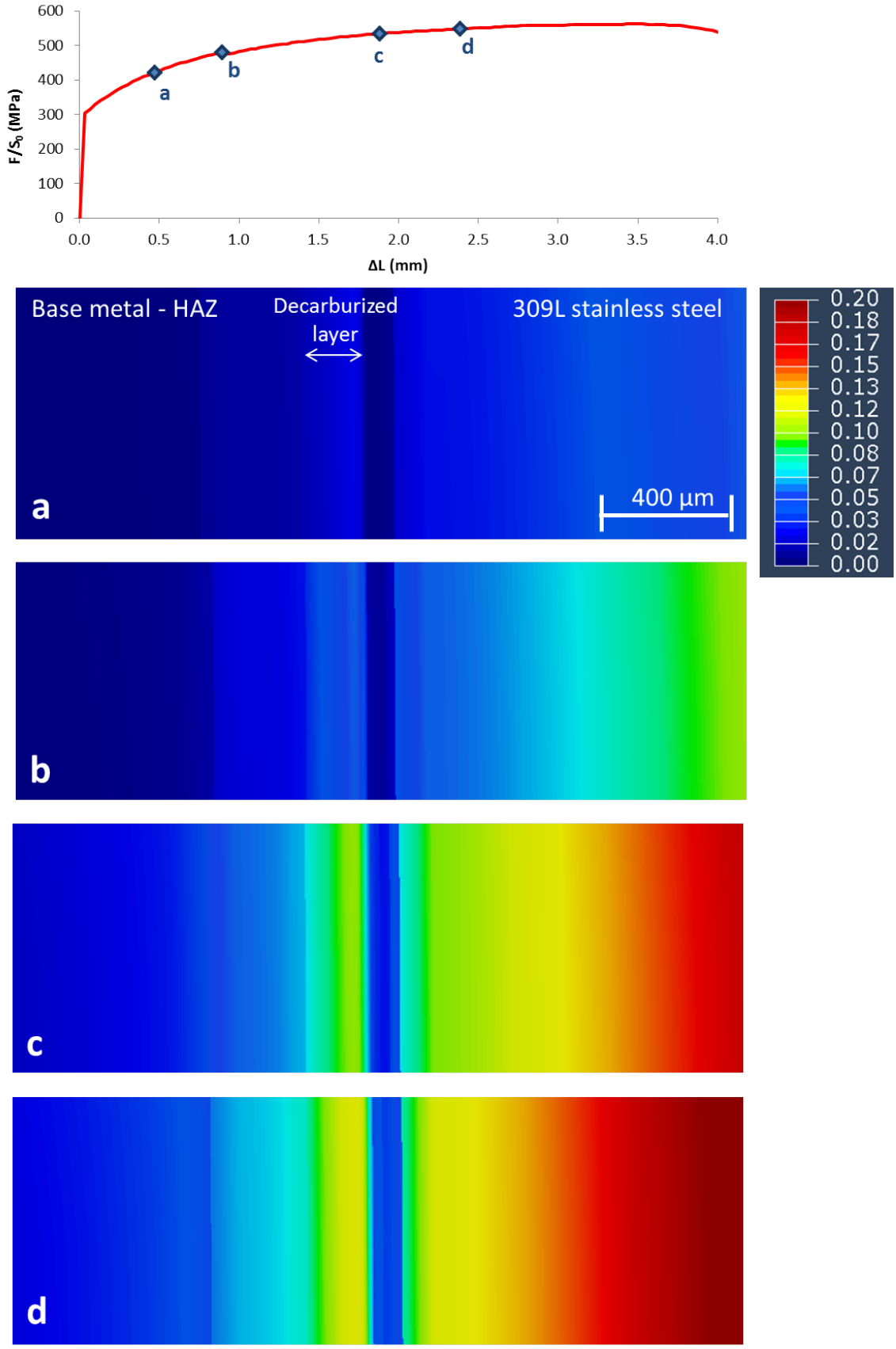

Figure 5.27: Logarithmic strain mapping by FE calculation of a tensile test on the weld at different positions on the global stress-strain curve: a- $\Delta L = 0.48$ mm, $\sigma = 421$ MPa; b- $\Delta L = 0.90$ mm, $\sigma = 480$ MPa; c- $\Delta L = 1.89$ mm, $\sigma = 534$ MPa; d- $\Delta L = 2.39$ mm, $\sigma = 548$ MPa.

However the large strain measured in the right part of the decarburized layer in contact with the martensite was not reproduced by the simulation. Up to 38% was measured for ϵ_{11} at the fourth increment of deformation whereas the maximum reached in the simulation in this zone was of 15%. This large discrepancy can be attributed to the out-of-plane displacements which cannot be neglected in this particular region. As shown by the schematics of Figure 5.28 and confirmed by the step measured at the fusion line by profilometry (see Fig. 5.26), the shear component in the interface's plane ϵ_{13} is particularly high, even at the early stages of deformation (see Fig. 5.28-a). In this region, the principal strain direction does not lie along the tensile axis as normally expected during a tensile test. Shear perpendicular to the tensile axis dominates as a result of the necessary strain adaptation in presence of a large gradient of mechanical properties. Not only shear in this plane was not accessible by a 2D measurement by DIC but it could also have disturbed the estimation of the in-plane components. As shown by Figure 5.26-b, a good agreement was obtained between simulation and measurements by profilometry for the shape of the deformed free surface, exactly at the location where DIC was achieved for the last increment of deformation.

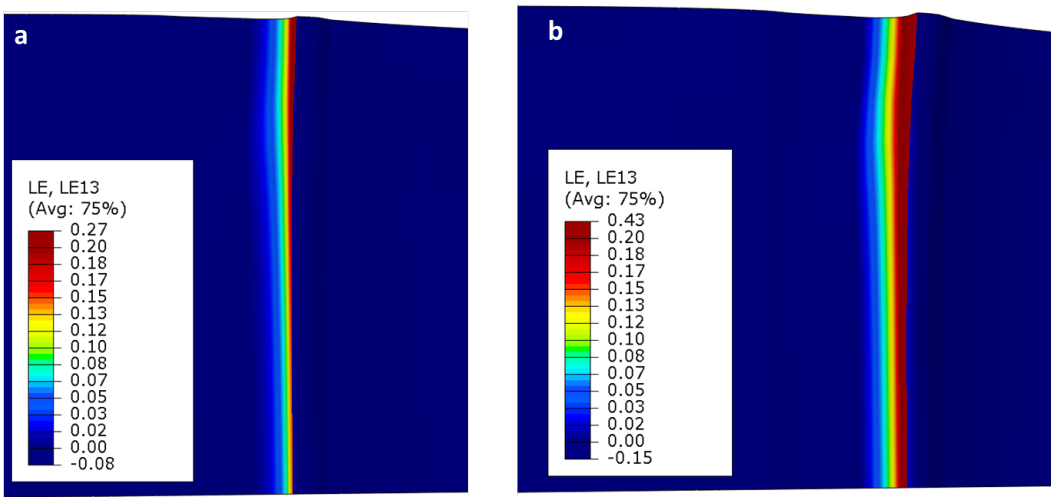

Figure 5.28: Mapping of the calculated shear strain in the plane of the fusion interface ϵ_{13}. a- $\Delta L = 0.9$ mm / $\sigma = 480$ MPa b- $\Delta L = 2.39$ mm / $\sigma = 548$ MPa.

5.4 Conclusion

In this chapter several methods have been employed to estimate the mechanical properties of the different regions of the weld:

- **Micro-samples parallel to the fusion line** were appropriate for regions wider than 1 mm (HAZ of the base metal and stainless steel cladding layers).
- **Nanoindentation** allowed probing the thinner areas, especially the carburized regions both in the martensite and austenite.
- A particular attention was devoted to the decarburized layer with **two attempts of fabricating an equivalent bulk material:** the first one using gaseous wet H_2 and the second one via a diffusion couple with stainless steel.

From comparison of the experimental results with FE elasto-plastic simulations, both in terms of tensile curves and strain distribution mapping, the main following facts could be deduced:

- **Both stainless steel cladding layers have an anisotropic behavior** due to their directional solidification. That is why the local properties determined via micro-samples parallel to the fusion interface did not allow reproducing the correct global stress-strain curve. Instead mean properties determined on a transverse specimen with several SS layers were used and provided a better agreement up to the onset of necking.
- Concerning the base metal, the **discretization of the HAZ in only two layers** is of course rough but sufficient. The effect of the strain softening instability was identified on the stress-strain curve and reproduced by the simulation. A more accurate description of the HAZ could be obtained by approximating it by a continuous gradient of mechanical properties.
- A **unique set (σ_y = 250 MPa, n = 0.2)** has been identified to describe the mechanical behavior of the decarburized layer. On the one side, the fabricated bulk materials were used for determining its strengthening capacity together with a lower bound of the yield strength. On the other side, nanoindentation provided an upper bound of the yield point. Eventually comparison between simulations and strain measurements led to choose a yield point at 250 MPa for the decarburized layer and to introduce an intermediate layer before the base metal with a yield stress of 300 MPa and the same hardening capacity as the decarburized zone.
- The **very high strain level detected at the martensite/ferrite interface** could not be reproduced. Several reasons can be invoked:

    1. non homogeneous properties within the decarburized layer with a very soft zone adjacent to the martensite, but surprisingly not detected by nanoindentation profiles.
    2. too strong constraints applied by the adjacent regions on the decarburized layer. This could be the case if we had overestimated the strength of the hard interfacial regions by nano-indentation. Being softer they would allow more deformation in both the

decarburized layer and the adjacent stainless steel. One has to keep in mind that mean properties have been used for the stainless steels instead of specific properties for each layer in the present case because of a lack of experimental data in the direction of interest. Indeed the 309L was found to be have a larger hardening capacity than the 308L.

3. an overestimation of the strain along the tensile axis because of out-of-plane displacements which may produce misleading results with 2D measurements by DIC.

This chapter has allowed determining a constitutive law for each of the regions of the dissimilar weld, that could now be used as input data for various mechanical models involving different geometries and/or loadings. The results in terms of plastic properties (both yield stress and hardening capacity) of the different zones of the weld are summarized in Figure 5.29 and highlight the high variability that is created around the fusion line as a consequence of carbon diffusion and precipitation during the post-welding heat-treatment.

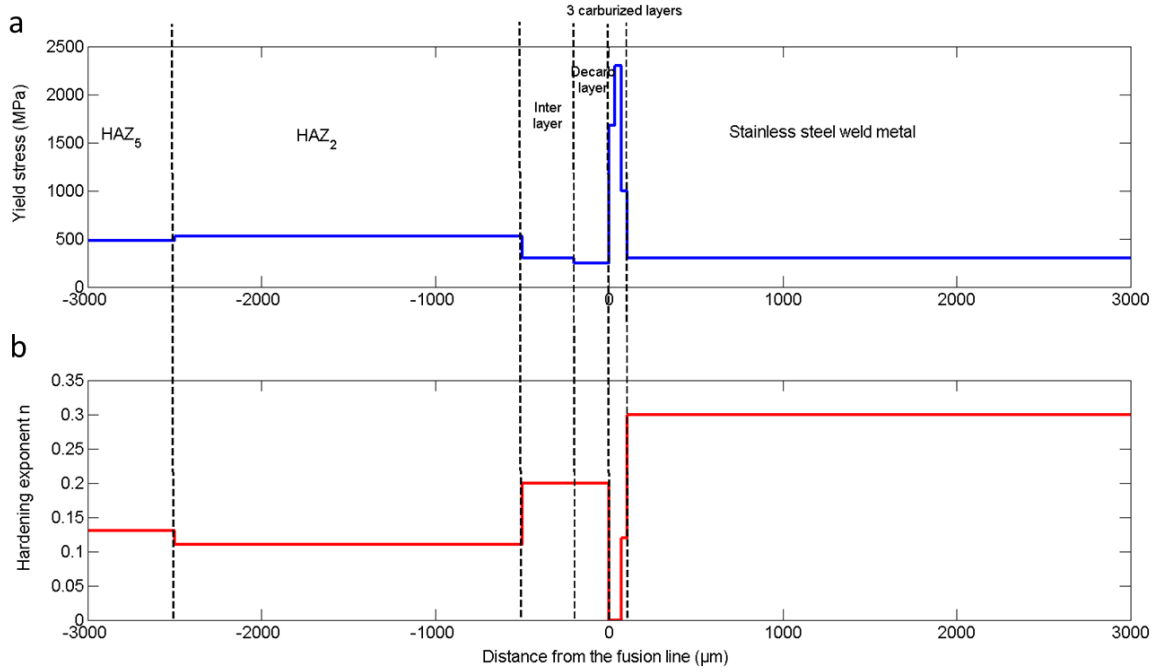

Figure 5.29: Summary of the evolution of the plastic properties around the fusion line in the heat-treated weld in terms of a- yield stress and b- hardening exponent.

Chapter 6

Investigation of the damage mechanisms in the soft regions

6.1 Introduction

The constitutive laws established in the previous chapter for the different regions of the assembly can now be used to predict both the elasto-plastic behavior of the weld in different configurations together with the ultimate plastic localization leading to final failure. This chapter will be focused on ductile fracture as it is the most common mechanism of failure at room and service temperatures for the different metals involved in the weld of interest. Besides, no other mode of failure such as cleavage or grain boundaries embrittlement was ever evidenced in our study.

The observation of fracture surfaces subsequent to Charpy impact tests carried out at different temperatures with the notch located on either side of the fusion line revealed that damage in these regions consisted of voids nucleation followed by a phase of damage growth and coalescence driven by plastic deformation. However the values for the impact energy were very scattered as the crack path was highly irregular and often went through several regions having different mechanical properties. Of particular interest was the fact that the size and density of voids varied strongly over small distances. Figure 6.1-a is a SEM micrograph of a fracture surface from an impact test at 300°C on a heat-treated sample with the notch initially located at 0.5 mm from the fusion line on the weld metal side. Three distinct zones can be seen:

- On the top of Figure 6.1-a (zone b), **voids of a few micrometers** have grown into the **purely austenitic zone.** It is worth noting that these voids are larger in the region in contact with the martensitic layer which indicates the presence of a high growth rate in this particular region.

- In the middle of Figure 6.1-a (zone c), numerous voids are present in the **martensitic zone.** They have **a very limited size (around 300 nm)** that can be related with the high density of carbides whose mean diameter is around 100 nm and mean spacing around 225 nm.

- At the bottom of Figure 6.1-a (zone d), **very large voids with a diameter around 30 μm**

are visible in the **decarburized layer.** Such cavities can be induced by either an extremely high growth rate or a very limited number of nucleation sites, and both phenomena may be involved simultaneously. In this region, the mean spacing between the centers of the cavities after failure is of the order of 40 μm.

The main goal of this chapter is to determine the mechanisms that control the weld ductility. For that, attention was focused on the final stage of tensile tests conducted on both flat and notched specimens.

We will try to answer to the following questions:

- **How does ductile failure take place in the soft regions of the weld, that is to say the decarburized layer and the stainless steel? What are, in each regions, the inclusions responsible for damage nucleation? What is the growth rate of the cavities and when does coalescence occur?**
- **What are the consequences of the microstructural changes taking place during the post-welding heat-treatment on the ductility of the different regions? In fact, phase transformations can either change the nature and/or number of nucleation sites or modify the mechanical properties (softening/hardening) of one given zone or of the neighboring regions that act directly on it.**

It is important to keep in mind that, because of its strong dependance on triaxiality, ductile fracture depends both on **local properties (such as nucleation sites)** and on **non local ones (such as heterogeneous plastic flow).**

6.2 Preliminary observations

6.2.1 In the decarburized layer

A region of high stress triaxiality

Stress triaxiality (T) defined as the ratio of the absolute value of the hydrostatic pressure (σ_h) to the equivalent Von Mises stress (σ_{eq})

$$T = \frac{\sigma_h}{\sigma_{eq}} = \frac{\sigma_{11} + \sigma_{22} + \sigma_{33}}{3\sigma_{eq}} \tag{6.1}$$

is the key parameter controlling damage kinetics. In the Rice and Tracey model [194], the growth rate of a spherical cavity located inside an infinite perfectly plastic material is expressed as:

$$\frac{dR}{R} = 0.283 \ exp(\frac{2}{3}\frac{\sigma_h}{\sigma_{eq}}) \ d\epsilon_{eq} \tag{6.2}$$

where R is the cavity radius and $d\epsilon_{eq}$ the increment of plastic strain. The value of the triaxiality is highly dependent on the strength gradient that exists between the soft and hard zones together

with the size of the soft zone, especially its confinement degree. In the case of the heat-treated weld, the decarburized layer is subjected to high levels of stress triaxiality because it is surrounded by the hard base metal on one side and the even harder carburized layers on the other side. Figure 6.2 displays a map of the stress triaxiality inside a flat tensile specimen together with plots extracted at different locations in the height of the specimen. In the case of an homogeneous tensile specimen, the stress triaxiality should be constant and equal to 1/3. Here, levels of stress triaxiality higher than one are found within the decarburized region adjacent to the martensitic layer. Then, it decreases with plastic straining as can be seen on the plots of Figure 6.2 taken at different increments of deformation. It is worth noticing that the stress triaxiality state is complex: first it evolves with increasing deformation and secondly, it is heterogeneous through sample's width within the decarburized layer. This will certainly make the damage analysis more complex. The values of triaxiality encountered within the stainless steel adjacent to the carburized layers are lower than those in the decarburized region. It can certainly not be explained by a large difference in terms of mechanical properties ($\sigma_y = 300$ MPa and $n = 0.3$ versus 250 MPa and 0.2 for the decarburized layer). They are rather due to the larger width of the stainless steel region which spreads to the extremity of the sample and therefore guarantees the absence of confinement.

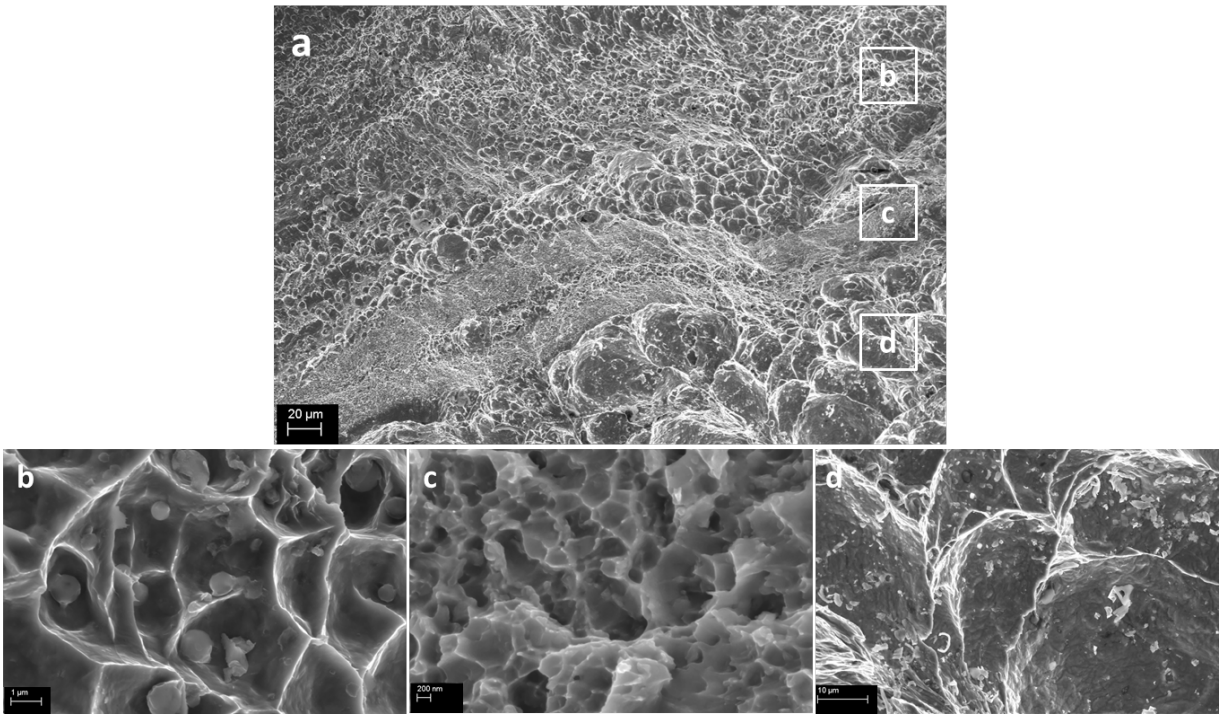

Figure 6.1: SEM micrograph of a fracture surface from a Charpy impact test at 300°C on a heat-treated sample with the notch initially located at 0.5 mm from the fusion line on the weld metal side. a- General view around the fusion line. Voids b- in the purely austenitic zone, c- in the martensitic layer, d- in the decarburized layer.

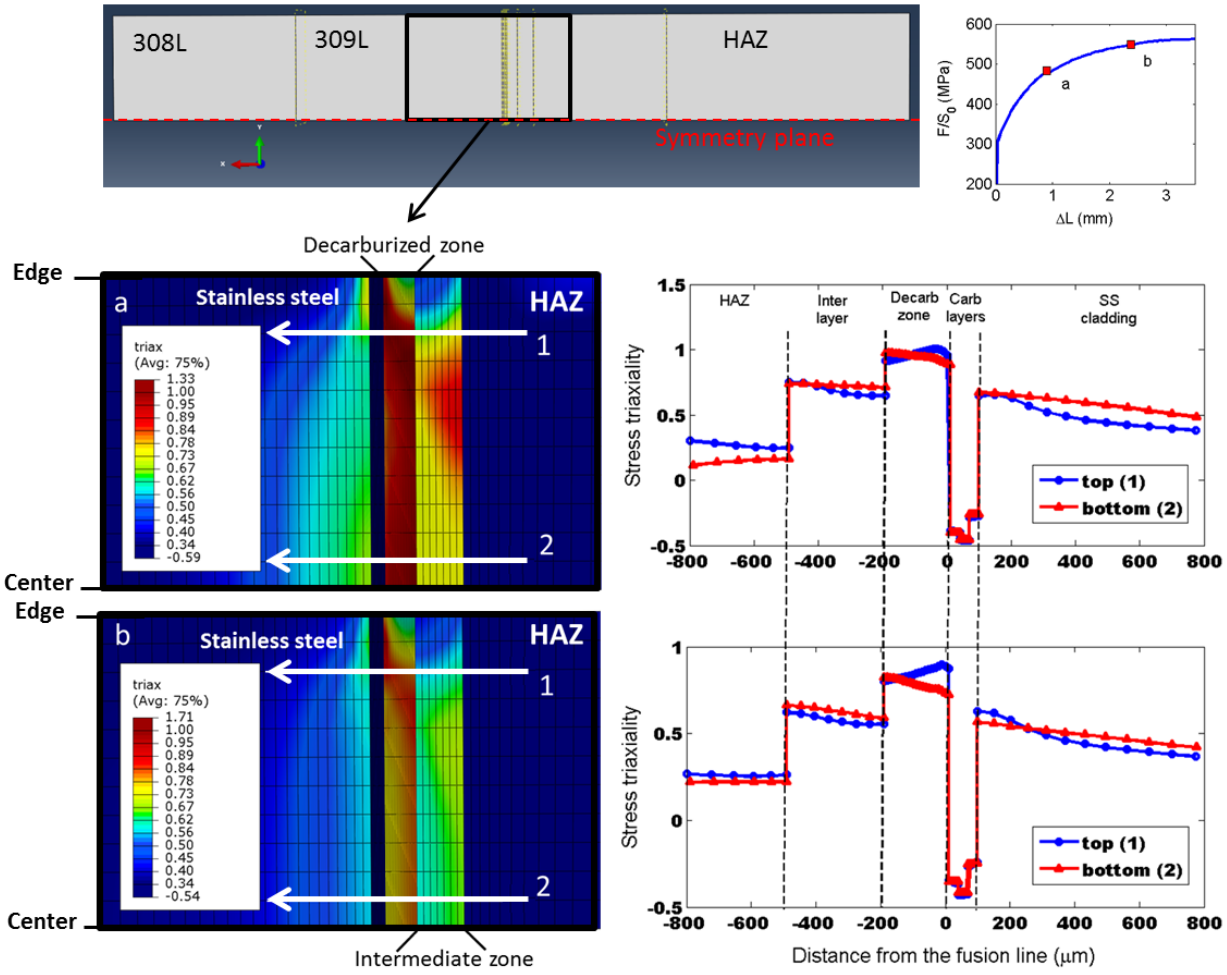

Figure 6.2: Mapping of the stress triaxiality within a tensile specimen for different increments of displacement, a- $\Delta L = 0.90$ mm, $\sigma = 480$ MPa; b- $\Delta L = 2.39$ mm, $\sigma = 548$ MPa.

Damage nucleation sites

For ductile failure to take place, sites are necessary for damage initiation. In general, voids nucleate on inclusions either by interface's decohesion or particle's fracture. The decarburized layer is particularly "clean" in terms of inclusions. In fact, decarburization has resulted in cementite dissolution and the only remaining particles are the manganese sulfides MnS. They have been quantified by SEM image analysis, the results being presented in Table 6.1. Franklin's formula [195] is also widely used to estimate their volume fraction for a given steel's composition:

$$f_v(MnS) = 0.054(w\%(S) - \frac{0.001}{w\%(Mn)}) + 0.05w\%(O) = 0.007\% \tag{6.3}$$

By both methods the quantity of MnS obtained is very low. They have a rounded shape and relatively small dimensions.

Table 6.1: Results for the quantification of the MnS particles by SEM image analysis.

Mean dimension (nm)	**Number density** $(/m^2)$	**Surface fraction (%)**
420	4.83×10^8	0.012

Tensile tests on notched specimens

In order to force failure to occur in the decarburized layer, semi-circular notches with a diameter of 1 mm were machined on the SEM tensile specimens (see dimensions in Appendix C), the center of the notch being located in the middle of the 200 micrometers of decarburized zone. In-situ tensile tests were performed under an optical microscope until final failure. Optical images were preferred to SEM ones because they were free of distorsions at low magnification and so allowed precise measurements. Moreover they could be taken at many regular spaced displacements without interrupting the tensile test. The global level of deformation that appears on the micrographs of Figure 6.3 was obtained by measuring the evolution of the distance between the notch ends. It allowed to focus on the strains around the fusion line only. As can be seen on the micrographs of Figure 6.3 and in Table 6.5, deformation is not concentrated in the ferritic part of the weld only. Although the specimen section including the austenitic part of the weld is larger, it is subjected to some amount of strain and participates therefore to the global elongation of the notch.

Table 6.2: Deformation ratios between the austenitic and ferritic parts of the weld calculated on the micrographs of Figure 6.3.

Global deformation	**Ferrite deformation** ϵ_{fer} (%)	**Austenite deformation** ϵ_{aus} (%)	**Deformation ratio** $\epsilon_{aus}/\epsilon_{fer}$
$\epsilon = 0.46$ %	0.74	0.15	0.20
$\epsilon = 2.2$ %	2.6	1.3	0.51
$\epsilon = 4.6$ %	5.2	2.8	0.54
$\epsilon = 6.6$ %	7.7	5.2	0.68
$\epsilon = 12.6$ %	14.7	9.0	0.61

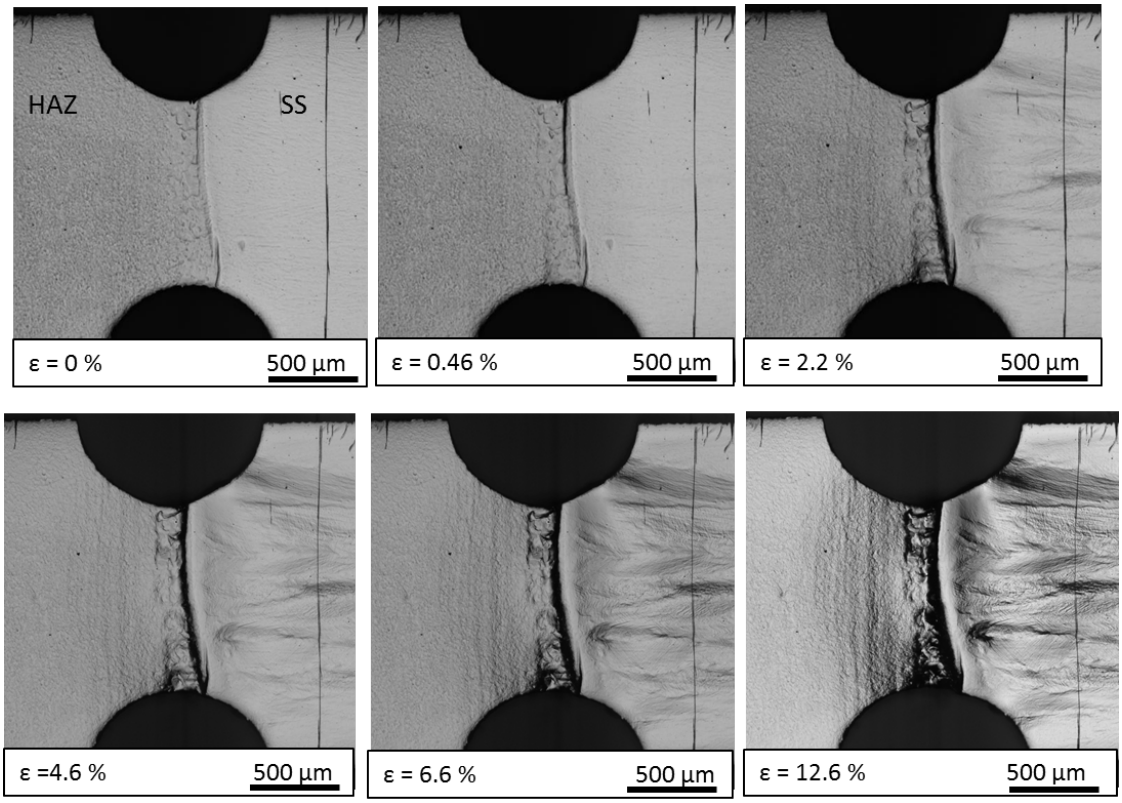

Figure 6.3: a- Optical micrographs taken during an in-situ tensile test on a specimen with notches in the decarburized region.

Influence of the width of the martensitic band

Among the tested samples, the main variable parameter was the width of the martensitic band. It spanned from 5 to 120 μm, so representing the high variability encountered in a single weld resulting from the turbulent nature of the fluid flow in the weld pool. As shown on Figure 6.4, increasing the martensite width seems to lead to a decrease of the true fracture strain and therefore a drop in ductility. A larger martensitic layer, while maintaining the same mechanical properties (especially σ_y), is expected to produce a higher constraint on the adjacent soft zones. It should result in a higher stress triaxiality in the decarburized region, and so a higher driving force for cavities nucleation, growth and coalescence. As visible on the fracture surfaces of Figure 6.4, the voids are more numerous but smaller in the case of the large martensite. The higher stress triaxiality might have induced nucleation in many locations and finally promoted coalescence by voids linking after a smaller increment of growth.

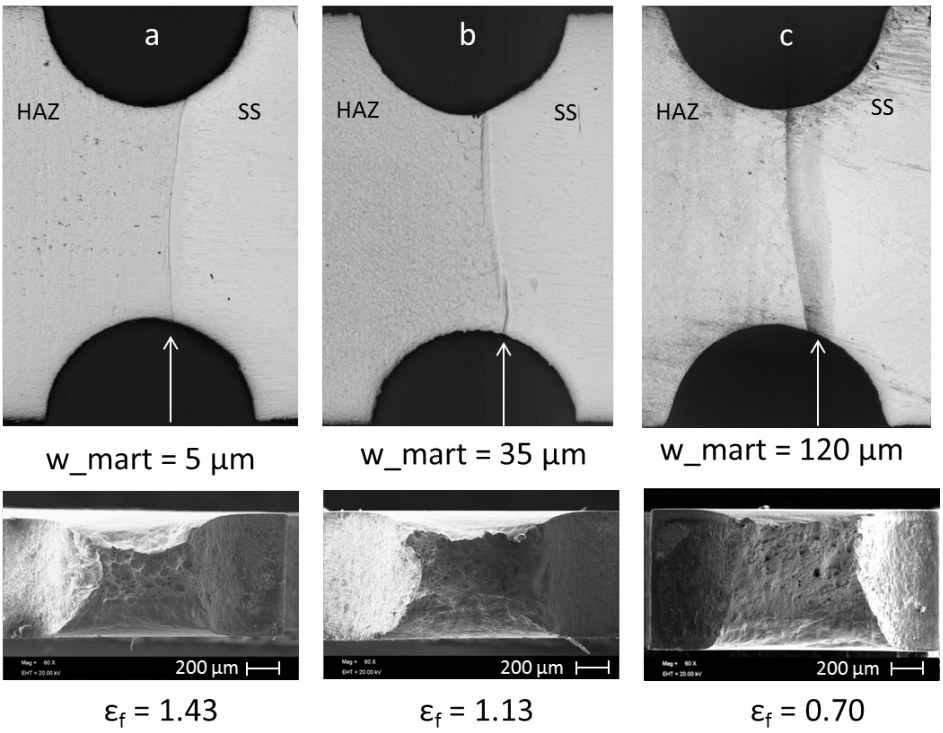

Figure 6.4: Fracture surfaces of notched samples in the decarburized layer for different width of the martensitic band, a- 5 μm b- 35 μm c- 120 μm.

6.2.2 In the stainless steel

In the absence of notch, all the samples broke in the 308L layer, away from the constrained ferritic/austenitic interface. By contrast with the decarburized region, both stainless steel layers contain a large number of inclusions that may serve as nucleation sites for damage initiation:

- **the oxides:** They are rounded particles with a large variety of sizes (mean diameter between 250 nm and 5 μm). They have a low-melting point and form from the last droplets of liquid during the solidification of the weld metal. They are enriched in oxygen, manganese, titanium and aluminum.
- **the $\delta - \gamma$ interfaces:** The δ-ferrite ligaments embedded into the austenitic matrix are elongated and numerous with a volume fraction up to several percents. As shown in Section 3.3.2.3, the δ-ferrite decomposes during the post-welding heat-treatment, resulting in numerous $M_{23}C_6$ carbides which decorate the $\delta - \gamma$ interfaces.

A quantification of the different particles in both stainless steel layers was performed by image analysis on pictures obtained either by optical microscopy (δ-ferrite) or scanning electron microscopy (oxides). The carbides were quantified by TEM using Automated Crystal Orientation Maps (ACOM) that allowed estimating the percentage of δ-ferrite that had been transformed into carbides. Knowing the total amount of ferrite in the as-welded state for each stainless steel layer and assuming the transformation to take place similarly for each ferrite residual, the fraction of carbides could be

calculated (see Section 3.3.2.3). The results are displayed in Table 6.3. Interestingly, the fraction of inclusions (both oxides and carbides) is found to be larger in the 308L layer than in the 309L one. In the 308L, the smaller degree of completion for the decomposition reaction of ferrite than in the 309L is compensated by the larger initial volume fraction of ferrite.

Table 6.3: Results of the quantification of the inclusions in the stainless steel layers.

	Oxides			**δ-ferrite**	**Carbides**
	Fraction	**Mean diameter**	**Number density**	**(as-welded)**	**(heat-treated)**
309L	0.5%	700 nm	$1 \times 10^{10}/m^2$	5.9%	1.1%
308L	0.8%	860 nm	$9 \times 10^{9}/m^2$	14%	1.5%

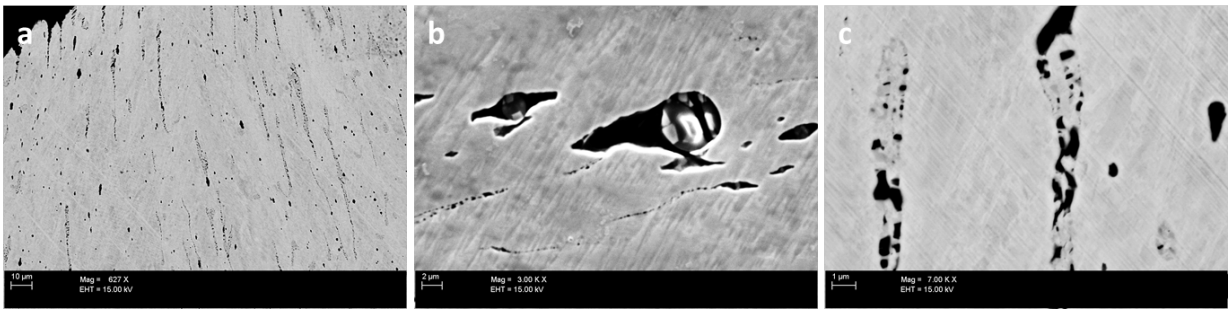

Figure 6.5: SEM micrographs of a longitudinal cut at mid-thickness of a fractured tensile specimen in the heat-treated state showing voids. a- General view. b- Cavities nucleated at oxides, c- at carbides/matrix interfaces.

Comparing the fracture surfaces of samples in the as-welded and heat-treated states revealed a significant decrease of the true fracture strain due to the post-welding heat-treatment[1] (see Fig. 6.6): 1.50 $\pm$ 0.036 for the as-welded samples versus 1.11 $\pm$ 0.13 for the heat-treated ones. In addition to the spherical cavities associated with oxides, elongated voids are visible in the heat-treated specimens and absent from the as-welded ones (see Fig. 6.6). They can be attributed to decohesions of the $\delta - \gamma$ interfaces under the weakening effect of the carbides. SEM observations performed at mid-thickness within a broken specimen in the heat-treated state (see Fig. 6.5) allowed imaging voids nucleated at both oxides (either by particle fracture or interface decohesion) and carbides (interface decohesion only).

Such a loss in ductility by carbides precipitation at the $\delta - \gamma$ interfaces has already been reported in the literature [196, 197]. In the case where the carbides form a quasi-continuous film along the $\delta - \gamma$ boundaries, closely spaced microvoids which match the distribution of the $M_{23}C_6$ particles have been observed in 304L weldments aged for one hour at 720°C [119]. A drop in impact energy of 75 J was even measured for type 316 weld metals after 300 hours at 700°C that had led to the transformation of 55 % of the δ-ferrite into carbides [196].

[1] The dissimilar steel interfaces are the only welds of a nuclear power plant to be heat-treated after welding. The specifications to be obtained in terms of mechanical properties always apply to the state after heat-treatment.

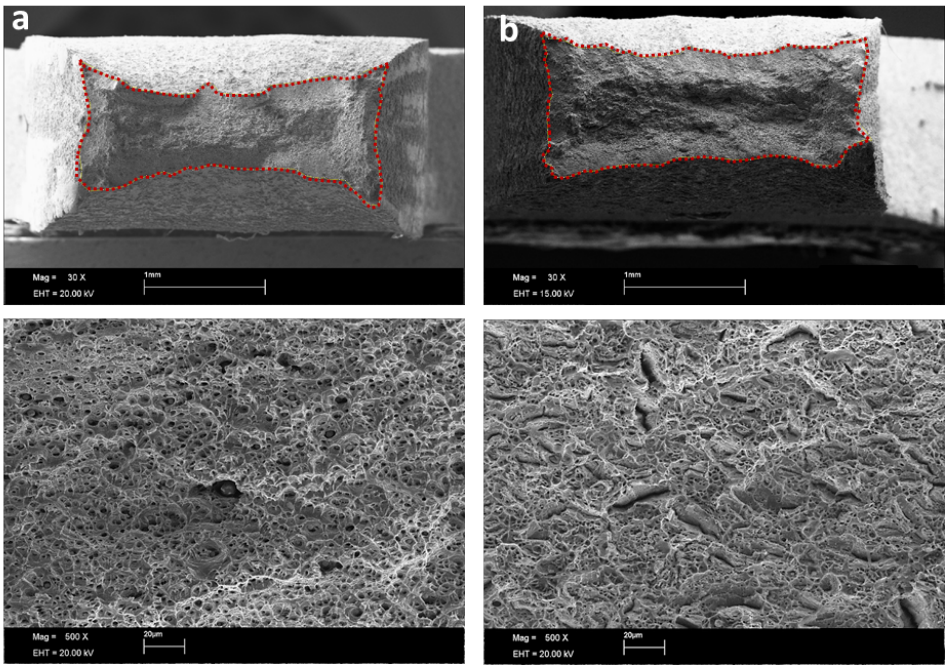

Figure 6.6: Fracture surfaces of tensile specimens a- in the as-welded and b- heat-treated states.

6.3 Damage model description

Ductile fracture is composed of consecutive and overlapping phenomena of nucleation, growth and coalescence of voids (see Fig. 6.7). In the present study, we made use of a micro-mechanics based model which allowed computing the local fracture strain. Developed by Pardoen et al. [12, 13], this model is an extension of the well-known Gurson model [15] enhanced by Tvergaard et al. [?], Needleman et al. [198], Thomason [16] (for the voids coalescence condition), Gologanu et al. [199] (for the voids morphology), Benzerga et al. [200] and Lassance et al. [201] (for improvements in the voids coalescence condition). This model has been extensively described in the publications of Thomas Pardoen group [12, 13, 202, 203, 204] at UCL (Université Catholique de Louvain-la-Neuve) and the following text is highly inspired from their model description.

6.3.1 Void nucleation

The void nucleation criterion used in the present damage model is the one originally proposed by the Beremin group [14]. The nucleation of voids, either by interface or particle fracture, is assumed to occur when the maximum principal stress in the particle or at the interface reaches a critical value σ_c:

$$\sigma_{princ}^{particle\ max} = \sigma_c \tag{6.4}$$

This critical value varies depending on the nature of the inclusion and the mechanism responsible for voids formation. Based on Eshelby theory [205] and the secant modulus extension to plastically deforming matrix proposed by Berveiller and Zaoui [206], the maximum principal stress in an elastic inclusion (and at the interface) $\sigma_{princ}^{particle\ max}$ can be related to the overall stress state by the following

equation:

$$\sigma_{princ}^{particle\ max} = \sigma_{princ}^{max} + k(\sigma_e - \sigma_0) \tag{6.5}$$

where σ_{princ}^{max} is the maximum overall principal stress, σ_e the overall effective Von Mises stress, σ_0 the yield stress of the matrix and k a parameter of the order of unity which is a function of the inclusion shape and loading direction.

The larger the particle, the smaller the nucleation stress should be, as there is a higher probability for large defects in the particle or at the interface with the matrix. Therefore σ_c corresponds to the critical nucleation stress at the larger particles, whereas nucleation continues on smaller ones when the matrix hardening increases. That is why the rate of change of the void volume fraction due to nucleation of new voids is taken as a function of the plastic strain rate:

$$\dot{f}_{nuc} = g(\bar{\epsilon}^P)\dot{\bar{\epsilon}}^P \tag{6.6}$$

where $\dot{\bar{\epsilon}}^P$ is the effective plastic strain rate of the matrix and g a polynomial function. When the criterion of Equation 6.5 is fulfilled, nucleation starts and takes place during a given range of strain $\Delta\bar{\epsilon}^P$.

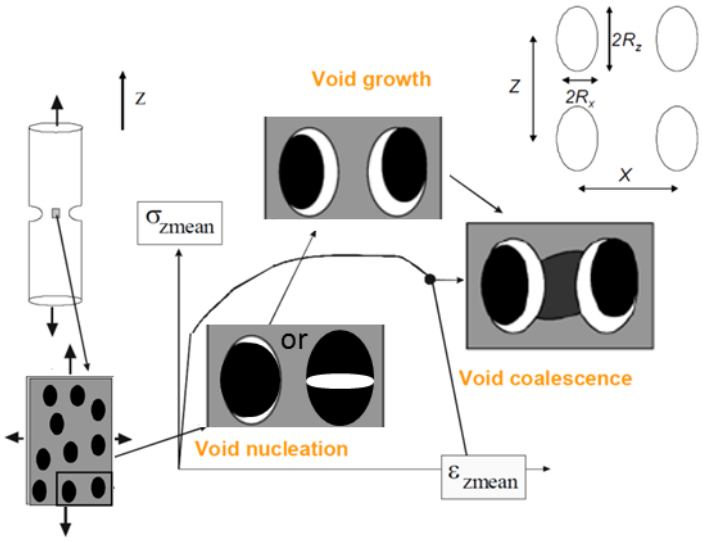

Figure 6.7: Schematic description of the sequence of damage mechanisms leading to ductile failure in metallic alloys, adapted from [207].

6.3.2 Void growth

Both void growth and nucleation contribute to the total rate of increase of porosity through:

$$\dot{f} = \dot{f}_{nuc} + \dot{f}_{growth} \tag{6.7}$$

The accumulation of plastic deformation results in voids enlargement and so increases the total void volume fraction. By assuming volume conservation, one writes:

$$\dot{f}_{growth} = (1 - f)\dot{\epsilon}_{ii}^P \tag{6.8}$$

where $\dot{\epsilon}_{ij}^P$ are the ij components of the overall plastic strain rate tensor. In addition to their volume fraction f, the voids that are assumed to be spheroidal, are characterized by their aspect ratio W (see Fig. 6.7) defined by:

$$W = \frac{R_z}{R_{x,y}} \tag{6.9}$$

The evolution law for S=ln(W) was derived by Gologanu et al. [199] through a micro-mechanical analysis of the growth of spheroidal voids in a J_2 perfectly plastic material:

$$\dot{S} = \frac{3}{2}(1+h_1)(\dot{\epsilon}^P - \frac{\dot{\epsilon}_{kk}^P}{3}\delta) : P + h_2\dot{\epsilon}_{kk}^P \tag{6.10}$$

with h_1 and h_2 being functions of S and f, P a projector tensor defined by $\epsilon_z \otimes \epsilon_z$ and δ the Kronecker tensor. The hardening behavior of the matrix is related to the overall stress and plastic strain rate through the energy balance initially proposed by Gurson [15]:

$$\sigma_y \dot{\bar{\epsilon}}^P (1-f) = \sigma \dot{\epsilon}^P \tag{6.11}$$

with the mean yield stress of the matrix material σ_y which is a function of $\dot{\epsilon}^P$ via the constitutive law. An associated flow rule, stating that the plastic strain rate is normal to the flow potential ϕ, allows calculating the evolution of f, S and σ_y as well as the stress state σ:

$$\dot{\epsilon}_{ij}^P = \dot{\gamma}\frac{\partial \Phi}{\partial \sigma_{ij}} \tag{6.12}$$

Φ is the flow potential proposed by Gologanu et al. [199] for a porous material involving spheroidal voids:

$$\Phi = \frac{C}{\sigma_y^2} \mid\mid \sigma' + \eta\sigma_h^g X \mid\mid^2 + 2q(g+1)(f+g)cosh(\kappa\frac{\sigma_h^g}{\sigma_y}) - (g+1)^2 - q^2(g+f)^2 = 0 \tag{6.13}$$

where:

- σ' is the deviatoric part of the Cauchy stress tensor.
- σ_h^g is a generalized hydrostatic stress defined by $\sigma_h^g = \sigma : J$ with J a tensor associated to the void axis and defined by:

$$J = (1-2\alpha_2)e_z \otimes e_z + \alpha_2 e_x \otimes e_x + \alpha_2 e_y \otimes e_y \tag{6.14}$$

- X is a tensor also associated with the void axis and defined by:

$$X = \frac{2}{3}e_z \otimes e_z - \frac{1}{3}e_x \otimes e_x - \frac{1}{3}e_y \otimes e_y \tag{6.15}$$

- $\mid\mid\ \mid\mid$ is the Von Mises norm.
- C, η, g, κ, α_2 are analytical functions of the state variables S and f.
- q is a parameter that has been calibrated as a function of f_0 (initial void fraction), W_0 (initial void aspect ratio) and n [199].

The stresses are then calculated from:

$$\dot{\sigma}_{ij} = L_{ijkl}(\dot{\epsilon}_{kl} - \dot{\epsilon}^P_{kl}) \tag{6.16}$$

where the L_{ijkl} are the elastic moduli.
This void growth model has been validated in [199, 12] and then applied to several cases of damage development [208, 202, 203], especially in aluminium alloys.

6.3.3 Void coalescence

The process of voids growth driven by relatively homogeneous plastic deformation of the matrix surrounding the voids is, at some point, interrupted by the localization of the plastic flow in the ligament between the voids. This point corresponds to the onset of coalescence and the following stage is quite similar to an internal necking process at the microscale. Thomason [16] proposed the following condition for the onset of coalescence:

$$\frac{\sigma_{zz}}{\sigma_y(1-\chi^2)} = \frac{2}{3}[\alpha(\frac{1-\chi}{\chi W})^2 + 1.24\sqrt{\frac{1}{\chi}}] \tag{6.17}$$

where α has been fitted as a function of the average value of the strain hardening exponent n [12]:

$$\alpha(n) = 0.1 + 0.22n + 4.8n^2 \tag{6.18}$$

Criterion 6.17 states that coalescence occurs when the stress normal to the localization plane reaches a critical value. This critical value decreases as the voids open (W increases) and get closer to each other (χ increases). The relative void spacing χ defined as:

$$\chi = (\frac{f}{\gamma}\frac{\lambda}{W})^{1/3} \tag{6.19}$$

is the dominant parameter controlling the transition from growth to coalescence. λ is the particle distribution factor and γ a geometric factor depending on the arrangement of voids. The meanings of the different parameters describing voids shape and distribution are summarized on the schematics of Figures 6.8 and 6.9. In the present study we considered uniformly distributed spherical voids on a periodic hexagonal mesh, leading to values of 1, 1 and 0.605 for W, λ and γ respectively (box in Fig. 6.9). The amount of porosity affects the coalescence indirectly as it enters the expression for the void spacing χ and also through its softening effect on the applied stress σ_{zz}. Equation 6.17 assumes that coalescence occurs in a band normal to the main void axis, which remains here parallel to the main loading direction z. In the present study, the fracture strain is assumed to correspond to the onset of coalescence in the most damaged region, which means that the extra overall deformation required after the onset of coalescence to break the specimen is considered as being small.

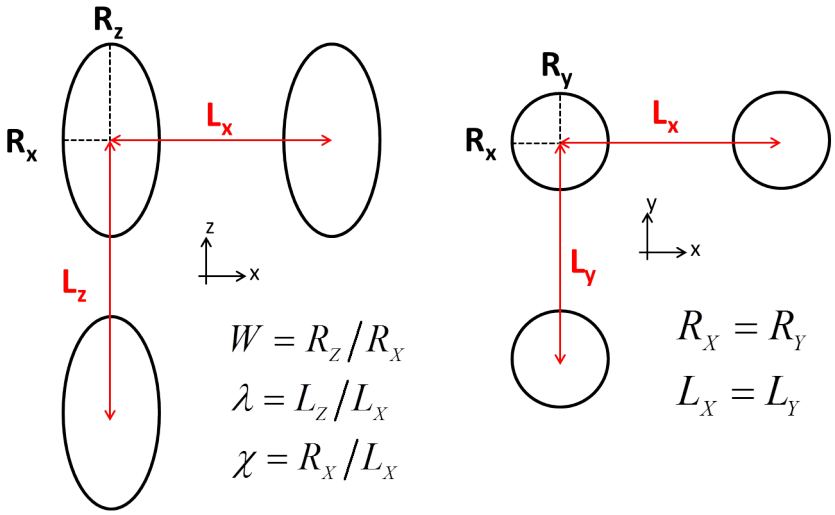

Figure 6.8: Schematic of the spheroidal voids geometry defining the parameters W, λ and χ.

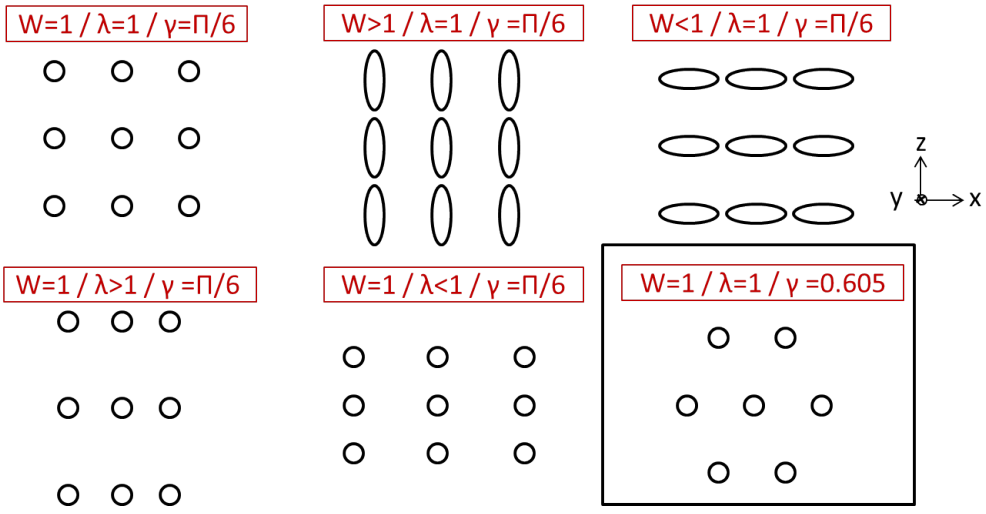

Figure 6.9: Schematic of the different parameters describing voids shape and distribution.

6.3.4 The different steps of the calculation

The specificity of the approach implemented here is that flow and damage were decoupled to reduce computational time. Although the previously described model was implemented into Abaqus as a user-defined material subroutine by Pardoen et al., it was chosen here to proceed in two steps. Such method which neglects the coupling between the mechanical fields and the damage was shown to be acceptable up to the point of fracture initiation and to provide a good estimation of the macroscopic fracture strain [209, 204].

First, the elasto-plastic calculation without any damage was conducted with Abaqus (Fig. 6.10-a) and provided on request the evolution of strain and triaxiality in the different elements of the

mesh. Then, the damage model was run in "post-processing" with axisymmetric loading conditions (Fig. 6.10-c). This means that, for a given element, the history of stress triaxiality as a function of equivalent plastic strain served as input data for the damage model (Fig. 6.10-b). The latter one allowed predicting the local plastic strain at the onset of coalescence ϵ_P^{coal}. The last step consisted in comparing experiments and simulations through the global fracture strain ϵ_f, defined from the reduction of cross-sectional area measured on broken samples (see Equation 5.2). This macroscopic mechanical parameter could be extracted from the elasto-plastic calculation at the step where coalescence occurs (Fig. 6.10-d). This step was determined by the local maximum plastic strain calculated by the damage model in the most critical element (identified a priori). When the location of fracture was not obvious, the damage calculation was performed for several elements in the region of interest and the one giving the smaller fracture strain was considered as the most damaged.

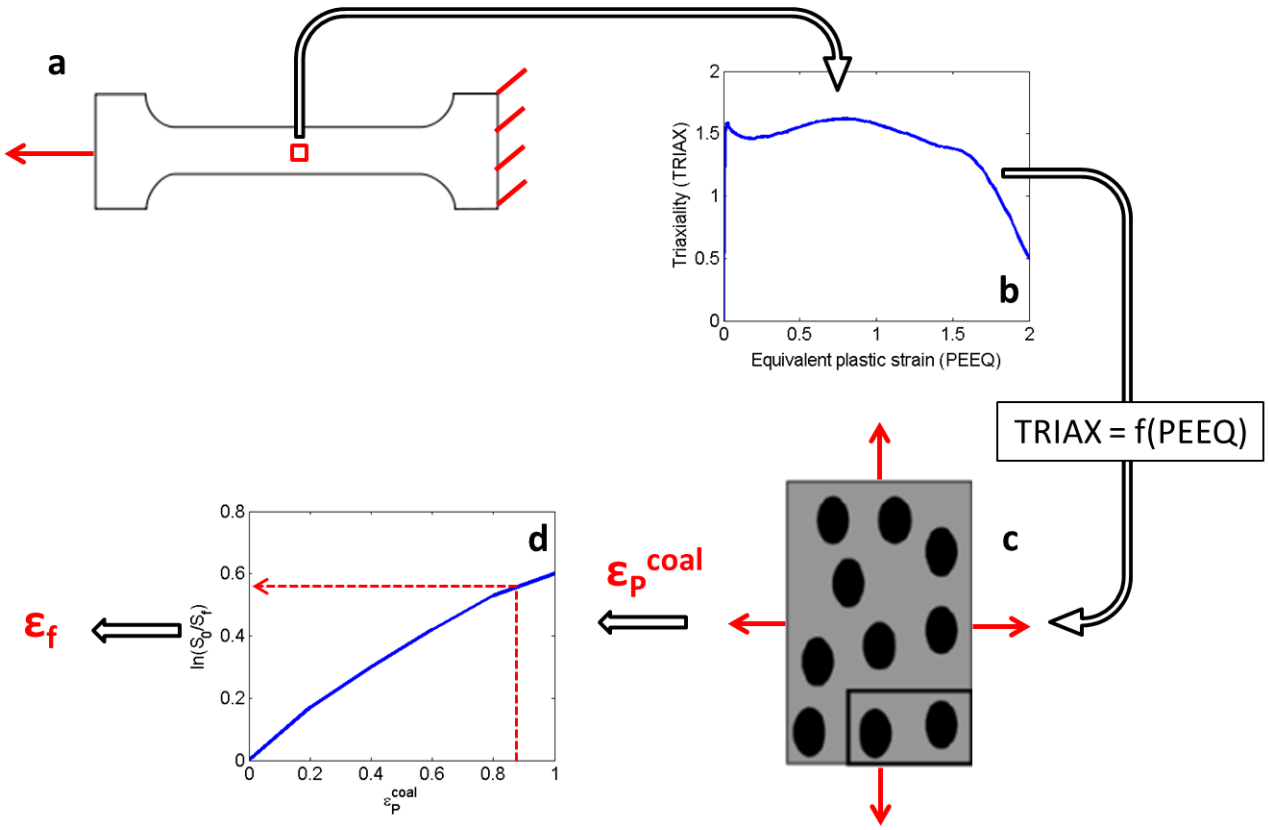

Figure 6.10: The different steps of the damage evaluation: a- 3D elasto-plastic calculation on the whole sample; b- Extracting stress triaxiality (TRIAX) and equivalent plastic strain (PEEQ) for the most critical element. c- Axi-symmetric damage calculation which provides the microscopic plastic deformation at the onset of coalescence. d- Evaluation of the macroscopic fracture strain by linking the microscopic strain at coalescence to the section reduction from the initial elasto-plastic model.

6.4 Application of the model to ductile failure in the soft regions

6.4.1 Ductile failure in the decarburized layer

6.4.1.1 Elasto-plastic constitutive laws

As the center of the notches were located in the decarburized layer, its elasto-plastic properties and the ones of the adjacent regions (intermediate zone and 309L stainless steel) had a direct influence on the mechanical response of the specimen, which was not the case in the macro-samples. For the present study dedicated to failure in the decarburized zone, it is important to know the plastic behavior of the regions of interest beyond the onset of necking. Indeed the tensile tests on decarburized micro-samples did not provide any information for a strain higher than 0.2 whereas constitutive laws that serve as inputs for the elasto-plastic modeling need to be entered up to larger strains (typically around 1). For that, the curves experimentally obtained and used previously for the comparison with DIC measurements (see Section 5.3.2.2) were extrapolated at large strains by using a law of Voce [210] including a stage IV hardening:

$$\sigma(\epsilon_P) = \sigma_y + \theta_{IV}\epsilon_P + \frac{\theta}{\beta}exp(-\beta\epsilon_P) \tag{6.20}$$

The meaning and value of the different parameters used in Equation 6.20 are summarized in Table 6.4 for both the decarburized and intermediate layers. Large strain experiments [211, 212] have demonstrated that the usual decrease of the hardening rate is interrupted by a constant hardening stage, named stage IV. At the microstructural scale, it corresponds to the increasing misorientation among the dislocation cells that have been built during stage III.

Concerning the 309L stainless steel, the averaged mechanical properties determined by means of a transverse tensile test including several layers were retained. As in Section 5.3.2.2, a Swift law was chosen for the extrapolation beyond necking. The deformation ratio between the austenitic and ferritic parts of the weld under the notches was calculated and a good agreement was found between the experimental and numerical values for different increments of global deformation (see Table 6.5).

Table 6.4: Parameters used in the Voce law for the decarburized and intermediate layers and comparison with the shear modulus μ.

	Yield stress σ_y (MPa)	**Dynamic recovery rate β**	**Dislocation storage rate θ (MPa)**	**Stage IV hardening θ_{IV} (MPa)**
Decarb.	248	9.49	3102 $\approx \mu/28$	50 $\approx \mu/1770$
Inter.	297	9.42	3726 $\approx \mu/24$	50 $\approx \mu/1770$

Table 6.5: Comparison of the deformation ratios between the austenitic and ferritic parts of the weld.

Global	$\epsilon_{\mathbf{fer}}$ (%)		$\epsilon_{\mathbf{aus}}$ (%)		$\epsilon_{\mathbf{aus}}/\epsilon_{\mathbf{fer}}$ (%)	
deformation	**exp.**	**sim.**	**exp.**	**sim.**	**exp.**	**sim.**
$\epsilon = 2.2$ %	2.6	2.8	1.3	1.4	51	52
$\epsilon = 4.6$ %	5.2	5.3	2.8	3.5	54	66
$\epsilon = 6.6$ %	7.7	7.5	5.2	5.2	68	69
$\epsilon = 12.6$ %	14.7	15.1	9.0	8.9	61	59

6.4.1.2 Role of the inclusions properties

Following the elasto-plastic calculation, the damage model described in Section 6.3 was applied to several elements of the decarburized layer by extracting, for each of them, the history of the stress triaxiality as a function of the equivalent plastic strain. The element encountering the earliest voids coalescence was considered as the weakest point of the weld and allowed determining the step at which the true fracture strain should be computed.

Nucleation stress

The critical stress for voids nucleation is the main adjustable parameter of the damage model. Values between 800 and 1100 MPa were reported in the literature for MnS particles in low-alloy steels [14]. In our case this value was adjusted to reproduce the true fracture strain in the case of the notched sample with a 35 μm thick martensitic layer, that is to say 1.13. The width of the strain range during which nucleation takes place was kept constant and equal to 1%, assuming that nucleation is quasi-instantaneous once the critical nucleation stress has been reached. The results of the parametric study are reported on Figure 6.11. A high value of the nucleation stress, around 1800 MPa, was necessary to obtain such a large ductility. Nevertheless this order of magnitude is realistic as the MnS particles invoked in the literature are usually larger (several micrometers), so that they can be observed by optical microscopy [14]. In the present case, the MnS inclusions, owing to their reduced shape, are closer to the rounded cementite particles or titanium carbides, for which Argon and Im [213] have identified critical nucleation stresses of 1650 and 1820 MPa respectively. If the particles would have been larger with a nucleation stress around 800 MPa, as mentioned in the literature [14], the true fracture strain would have been reduced by 42% for the same plastic properties of the matrix. Therefore the ductility of the decarburized layer is found to highly depend on the critical stress for voids nucleation, that is to say on the size of the inclusions.

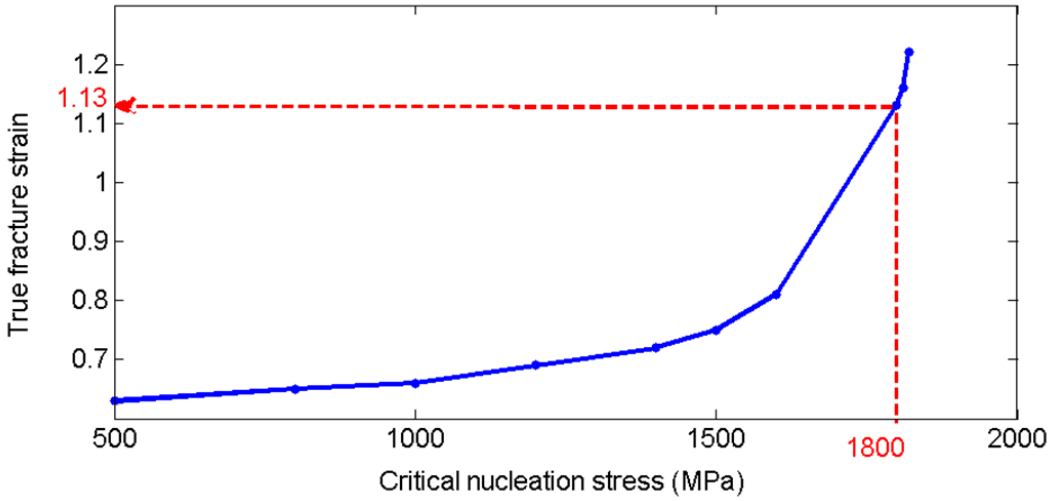

Figure 6.11: Results of the parametric study giving the true fracture strain as a function of the critical nucleation stress.

Particles volume fraction

The low-alloy steel plate used for this study had a low sulphur content ($w(S) = 1.9 \times 10^{-3}$ %) and consequently, a low volume fraction of MnS particles was found in all regions of the heat-affected zone. According to the RCC-M specifications, the sulphur content of the bainitic steel used for the fabrication of nuclear components can reach a maximum of 1.2×10^{-2} wt.% [214], which lead to 0.067 % for the MnS volume fraction by application of Franklin's formula [195]. The influence of the particles volume fraction on the true fracture strain was investigated for a given nucleation stress set to 1800 MPa, the results being displayed on Figure 6.12-a. Keeping the nucleation stress constant, while increasing the volume fraction of particles, is equivalent to an increase of the number density of inclusions while maintaining a constant size. In the case of the maximum allowed sulfur content, the ductility would be reduced by only 8.8 %.

Particles shape

When subjected to straining, the voids both elongate in the loading direction and contract in the transverse direction (see Fig. 6.5-b), leading to needle-like shapes. The MnS particles are usually elongated and their fracture or debonding result in penny-shape voids. However, in the present case, the inclusions were rather spherical, certainly because they were broken during the rolling of the metal sheet, which might be less frequent for forged products. The influence of the initial shape of the particles on the ductility was investigated by performing simulations with different initial void aspect ratios varying between 1/10 and 10, while keeping the nucleation stress constant (1800 MPa). The results displayed on Figure 6.12-b show a reduction of the ductility when the voids are oblate, which means oriented perpendicularly to the tensile direction. However the critical nucleation stress will generally be influenced by the initial shape of the particles. The void shape effect is known to be less pronounced at high stress triaxiality [12].

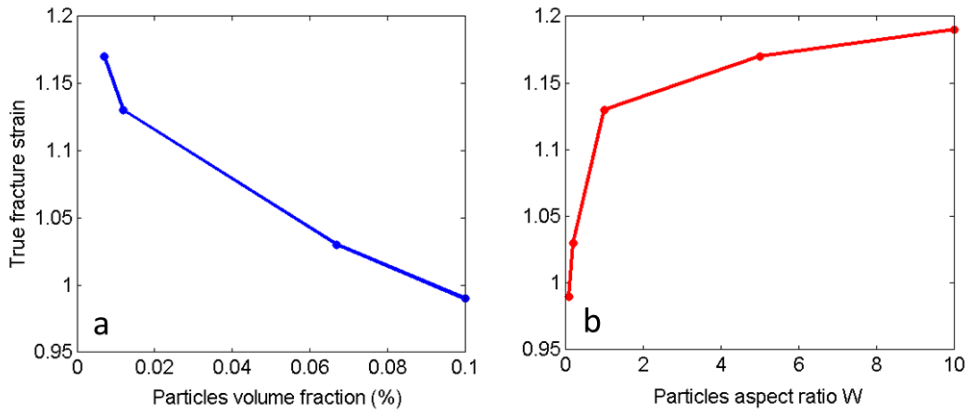

Figure 6.12: True fracture strain as a function of the characteristics of the inclusions: a- Particles volume fraction, b- Particles aspect ratio.

Among all the parameters that were varied, the critical stress for voids nucleation, which is related to both particles size and shape, was found to highly influence the ductility of the decarburized region.

6.4.1.3 Effect of the size of the martensitic band

Three specimens with different martensite's width were simulated, all the other parameters being kept constant (size of the other regions, elasto-plastic properties of the different zones, characteristics of the inclusions). The results from the elasto-plastic calculation in terms of stress triaxiality as a function of equivalent plastic strain are plotted in Figure 6.14 for two elements at different locations within the decarburized layer (see elements A and B on Figure 6.13). As expected, an increased width of the martensitic band resulted in a higher stress triaxiality. However this effect was only pronounced for the elements of the decarburized region adjacent to the martensite (example of element A on Fig. 6.13). In the case of the large martensite layer, triaxiality was found to reach values higher than 3. Nevertheless these elements located in a highly constrained area encounter a small equivalent plastic strain. For the elements subjected to a higher plastic deformation (example of element B on Fig. 6.13), the influence of the martensite's width is more limited, as shown by the curves of Figure 6.14-b.

Whatever the size of the martensite, the strain and triaxiality distributions are very similar and resemble the ones displayed in Figure 6.13. At the surface of the notch where the deformation can develop freely, regions of large strain are adjacent to the martensite whereas inside the specimen they are shifted away from the hardened layer. Concerning stress triaxiality, the higher values are localized in the center of the specimen in contact with the martensitic region, where strain is very limited. The damage model applied to the three configurations led to similar results. The weak element was always identified to be initially located around 150 μm from the interface with the martensitic band. At this position, which is likely to be the region of failure, the history of stress

triaxiality is very weakly dependent on the martensite layer width. Therefore, this explains that, with our model, we expect a weak dependance of the macroscopic fracture strain on the martensite layer thickness. In fact, the computed true fracture strains were of the same order of magnitude. Although the fracture strain was found to decrease when increasing the martensite's width, the effect was very limited (a mere 10 %, between 1.19 and 1.08, see Table 6.6) in comparison to what had been experimentally observed (a factor 2, between 1.43 and 0.7).

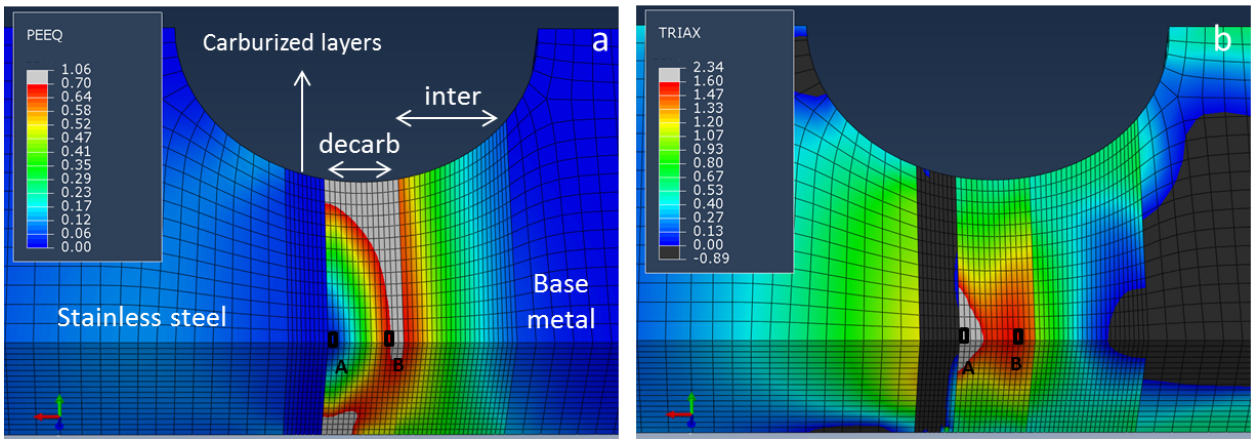

Figure 6.13: Equivalent plastic strain and triaxiality maps for a notched sample with a 35 μm wide martensitic layer at a global strain $\epsilon = 30$ %, the strengths of the carburized regions being those of Fig. 5.29.

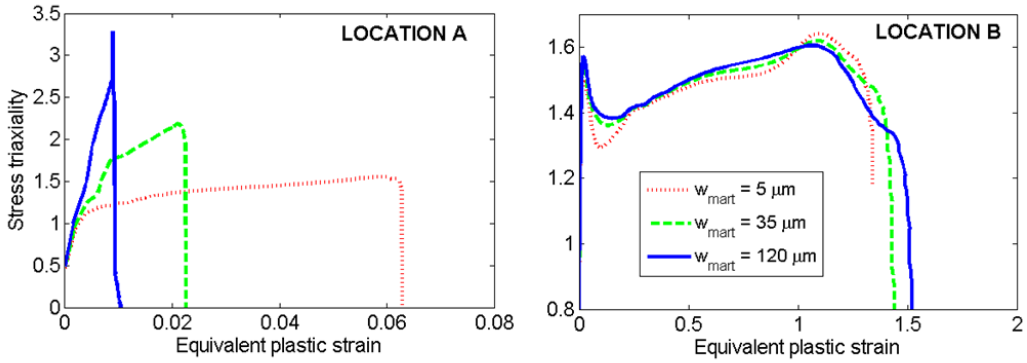

Figure 6.14: Evolution of the stress triaxiality within the decarburized layer of a notched sample for different width of the martensitic band: A- in the first element adjacent to the martensite (A in Fig. 6.13), B- for the element initially located at 150 μm from the martensite (B in Fig. 6.13).

Table 6.6: Comparison of the experimental and simulated true fracture strain obtained for different widths of the martensitic band.

	True fracture strain	
	ϵ_f **exp.**	ϵ_f **sim.**
$w_{mart} = 5\ \mu m$	1.43	1.19
$w_{mart} = 35\ \mu m$	1.13	1.13
$w_{mart} = 120\ \mu m$	0.7	1.08

As the variation of the width of the martensitic band seemed to be insufficient to explain the large reduction of fracture strain observed, other realistic parameters, related to the plastic properties of the different regions of the weld involved in the notch deformation during loading, will be varied in the next sections.

6.4.1.4 Effect of the strength of the carburized layers

The effect of the strength of the hard zones was investigated. In fact, their mechanical properties are known only approximately as they were determined by nanoindentation with a large scatter in the results. One could expect a lower yield point in the case of a large martensite as carbon will need to diffuse through a larger width before reaching the austenite, where the strengthening effect is really pronounced. That is why their yield point was varied between 1000 and 2000 MPa, while keeping all the other parameters constant, which encompasses the size of the carburized zone (105 μm in the present case) together with the mechanical properties of all the other regions and the characteristics of the inclusions (volume fraction at 0.012% and nucleation stress at 1800 MPa).

The reduction of the strength of the carburized layers was found to impact both the triaxiality and strain distribution within the soft decarburized layer (see Figure 6.15 where the strength of these layers was reduced to 1000 MPa). The same color scale as in Figure 6.13 was kept for comparison. The main difference was the location of the most damaged element which was slightly shifted towards the hard layers (see position of element C in Figure 6.15). Failure was predicted to occur at about 120 μm instead of 150 μm from the interface with the martensite in the original configuration but the true fracture strain was only slightly affected (1.22 instead of 1.13).

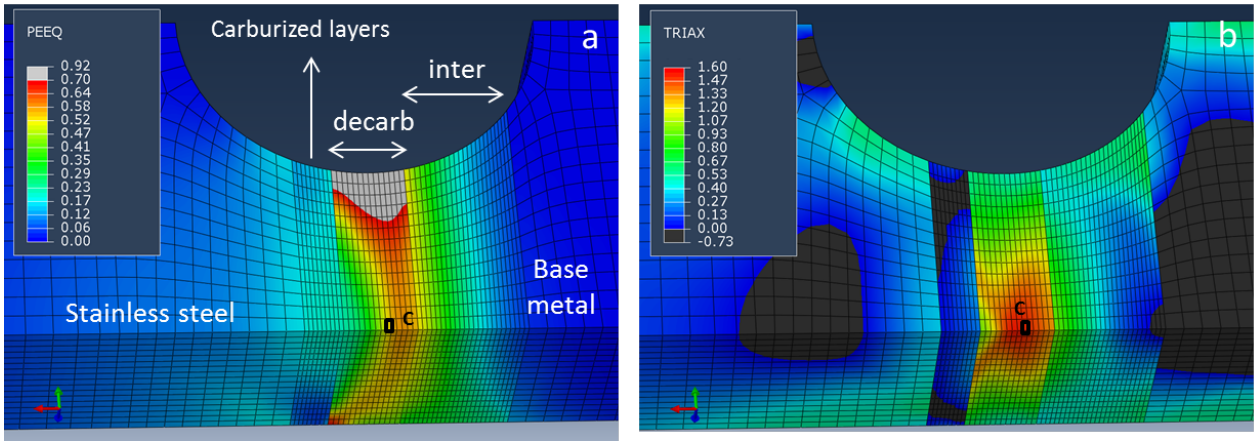

Figure 6.15: Equivalent plastic strain and triaxiality maps for a notched sample with the yield point of the carburized layers reduced to 1000 MPa and a notch deformation of 30%. The same color scale as in Figure 6.13 has been maintained for comparison. The element marked C is the location of final failure.

As can be seen on the plot of Figure 6.16-a where the strength of the carburized layer was varied between 1000 and 2000 MPa, the maximum of plastic deformation was shifted away from the ferrite/martensite interface (towards the left of the plot) when the strength was increased. This is in agreement with the fact that the distance (measured in the initial configuration) between the martensite and the element where coalescence starts increases with the strength of the carburized layer (see Table 6.7). Concerning the stress triaxiality, the high level of constraints produced by a high strength in the carburized layers (between 1500 and 2000 MPa) is responsible for increasing the triaxiality in a 70 μm wide band adjacent to the martensite (see Fig. 6.16-b). However, similarly to the case of an increase of the martensite's width, this region with extremely high stress triaxiality (T>1.5) is associated to a low strain which prevents fracture from happening there. On the stainless steel side (right part of the plots), the triaxiality increases gradually when increasing the strength of the carburized zone. The difference of behavior between both soft layers is related to the presence of constraints on only one side of the stainless steel.

Concerning the stress-strain curves, they were only slightly affected, but exhibited, as expected, an increase of the ultimate tensile strength when the strength of the carburized layers was increased (see Table 6.7). A decrease of the hard layers strength results in an increased ductility: up to 1.60 for the true fracture strain in the case of a 1000 MPa yield stress. However, as shown in Table 6.7, a huge increase of the strength would be necessary in the model to significantly reduce the fracture strain: even with a yield point at 2000 MPa over 105 μm, the experimentally observed value of 0.70 for the reduction of area could not be reproduced. The increase of stress triaxiality seems to be systematically counter-balanced by the displacement of the region with large strains. This explains that only small variations of the fracture strain were obtained for a yield point varying between 1200 and 2000 MPa in the carburized regions. Such an increase in yield stress cannot find a reasonable explanation based on physical grounds.

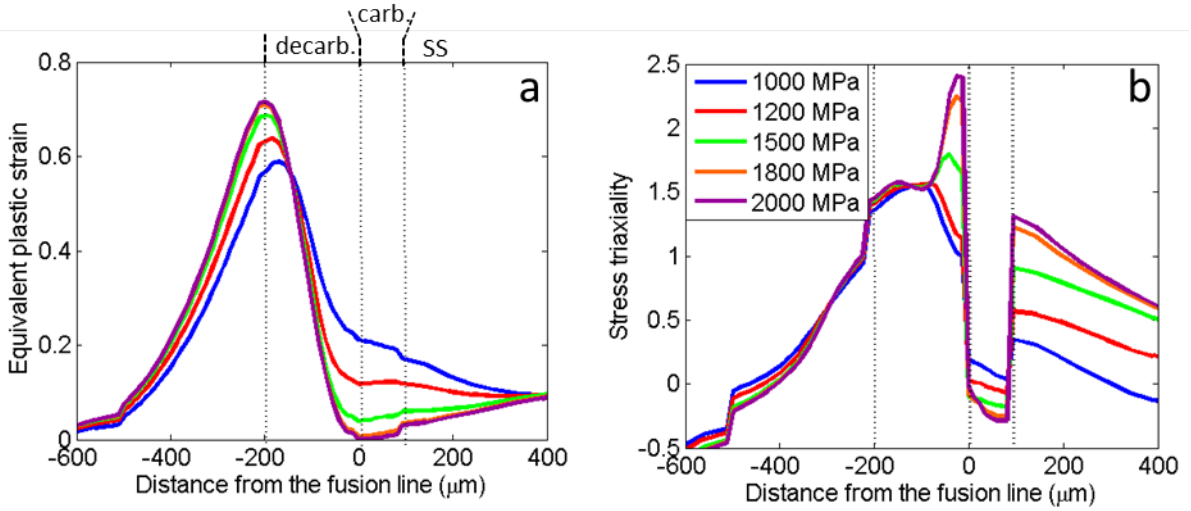

Figure 6.16: Influence of the strength of the carburized zone on a- the equivalent plastic strain, b- the stress triaxiality across the fusion line for a notch deformation of 30%.

Table 6.7: Influence of the strength of the carburized zone on the true fracture strain, the ultimate tensile strength and the failure position relative to the interface with martensite in the initial state.

	True fracture strain	**Failure position**	**Maximum stress**
σ_y = **1000 MPa**	1.61	122 μm	615 MPa
σ_y = **1200 MPa**	1.27	129 μm	628 MPa
σ_y = **1500 MPa**	1.16	136 μm	637 MPa
σ_y = **1800 MPa**	1.20	143 μm	640 MPa
σ_y = **2000 MPa**	1.14	143 μm	641 MPa

6.4.1.5 Influence of the plastic properties of the decarburized region

Since low carbon contents are particularly difficult to measure (see Section 3.3.1) and slight variations are known to have a drastic effect on the yield stress, plastic properties of the soft regions (both decarburized and intermediate zones) will be varied in this section. Indeed, an accurate measurement of the carbon content within the decarburized layer could only be performed by SIMS in the case of a medium-sized martensite (around 50 μm). One could expect that a larger martensite would result in a higher driving force for carbon to leave the low-alloy side of the weld and so create a more pronounced depletion. However, the size of the decarburized layer with large ferritic grains was found to be unchanged and equal to 200 μm whatever the size of the adjacent martensite.

Three couples of yield points were investigated, the hardening exponent being kept constant and equal to 0.2: 200/300 MPa, 250/300 MPa and 300/350 MPa for the decarburized and intermediate layers respectively. The results in terms of true fracture strain and fracture location are displayed in Table 6.8 for two values of the nucleation stress: 1800 and 1400 MPa. 1400 MPa corresponds to the nucleation stress which allows reproducing the redution of ductility experimentally observed in the case of a 120 μm wide martensite. Changing the yield point of the soft regions essentially affects

the location of the element where coalescence starts, with lower yield points leading to failure closer to the hard layers. However, for a given nucleation stress, the true fracture strain was only slightly modified (see Table 6.8). In the case of the 200/300 MPa couple and a nucleation stress of 1800 MPa, no value could be reported as the voids never nucleated. It is due to the stress levels that were too low for the nucleation condition to be fulfilled (Equations 6.4 and 6.5).

Table 6.8: Influence of the strength of the decarburized and intermediate zones on the true fracture strain and failure position relative to the interface with martensite in the initial state.

Nucleation stress	σ_{nuc} **= 1800 MPa**			σ_{nuc} **= 1400 MPa**		
Yield points (MPa)	200/300	250/300	300/350	200/300	250/300	300/350
True fracture strain	-	1.13	1.21	0.57	0.72	0.74
Failure position (μm)	-	136	157	114	150	157

Thus, none of the changes investigated (size of the martensite, strength of the hard layers, yield stress of the decarburized and intermediate zones) was efficient to explain the large variations of ductility encountered when performing tensile tests on notched specimens: from 1.43 to 0.70 when the martensite's width was increased from 5 to 120 μm. Changing the nucleation stress (from 1800 to 1400 MPa) while maintaining all other parameters constant (size and strength of the different regions of the weld) was the only way to cover a wide range of ductility. However, the MnS particles, which serve as nucleation sites for damage to initiate, originate from the solidification of the initial base material and are not affected by carbon diffusion during the heat-treatment. There is no physically acceptable explanation for the strength of the particles/matrix interface or the size of the particles to change with the width of the interfacial martensitic band.

The only admissible explanation for a drastic drop of the ductility when increasing the martensite's width could be that the high level of stress triaxiality would induce nucleation in other sites that were not considered here, such as triple junctions of grain boundaries or small impurities. These supplementary sites could be activated only under high stress levels that are reached in the vicinity of the martensitic band, especially when its width is significant. Thus it could lead to premature failure without a need for a significant growth of cavities. This argument is in agreement with the fracture surfaces of Figure 6.4 where the voids are more numerous and smaller in the case of the 120 μm wide martensite.

6.4.2 Ductile failure in the stainless steel

6.4.2.1 Two populations of inclusions

Contrary to the case of the decarburized zone with few nucleation sites, the stainless steel layers contain many inclusions that can serve to initiate damage. The main nucleation sites are the oxides as they can reach sizes of several micrometers and present a large mismatch of properties with the metallic matrix. The δ-γ interfaces are also known to be prone to damage initiation [215] as the difference in phase properties influences the local stress triaxiality which serves as driving force for interface decohesion [216]. In the case of the heat-treated sample, these interfaces are certainly weakened as they are decorated by an important density of carbides, which will enhance void nucleation. It is thus necessary to consider two populations of voids, each of them being characterized by an initial volume fraction and a critical nucleation stress. For the void aspect ratio, a rule of mixture was applied [202]:

$$W_0 = \frac{f_0^A W_0^A + f_0^B W_0^B}{f_0^A + f_0^B} \tag{6.21}$$

Although both particles are quasi-spherical ($W_0^A = W_0^B = 1$), the voids at the carbides will appear later (higher critical nucleation stress), with a global void aspect ratio being higher than 1 because the primary voids nucleated on the oxides will have already elongated in the loading direction. For this reason, it was necessary to transform the initial porosity of the second population into an effective porosity [202]:

$$f_0^{B,eff} = \frac{W}{W_0^B} f_0^B \tag{6.22}$$

where W corresponds to the value of the void aspect ratio at the nucleation strain. The effective porosity $f_0^{B,eff}$ is then used in Equation 6.21.

6.4.2.2 Results in terms of fracture strain

In this section, we will consider ductile failure of flat tensile specimens machined either perpendicular to the fusion interface and including the entire weld or parallel to it in a given stainless steel layer. In order to trigger necking in the simulation of homogeneous tensile specimens a small initial width reduction (linear over 0.75 mm with a maximum reduction of 2% at mid-width) was introduced in the cross-section located on the symmetry plane of the sample. As shown in Figure 6.17, the absence of both notch and confinement led to triaxiality values in the stainless steel lower than those previously encountered in the decarburized layer.

The difficulty of predicting ductile failure in metallic alloys with different kinds of particles lies in the determination of the appropriate nucleation stress for each family of inclusions. In the present study, we decided to optimize these values for the case of an homogeneous 308L tensile specimen machined parallel to the fusion interface in both the as-welded and heat-treated states (see stress-strain curves of Fig. 5.16-c). The selected values for each nucleation sites are reported in Table 6.9. As cavities along the δ-γ interfaces were also observed in the as-welded state of the 308L sample, the possibility of nucleating voids in this region, even in the absence of carbides, had to be

considered. Of course, the weakening effect of the $M_{23}C_6$ particles present at the δ-γ boundaries in the post-weld heat-treated condition, was taken into account by lowering the nucleation stress (from 3000 to 2300 MPa) at this location and so allowing voids to appear earlier in the course of deformation. Among the different sources of voids, the oxides, which present both a large size and a high crystallographic mismatch with the matrix, were the first to be activated ($\sigma_{nuc} = 1500$ MPa).

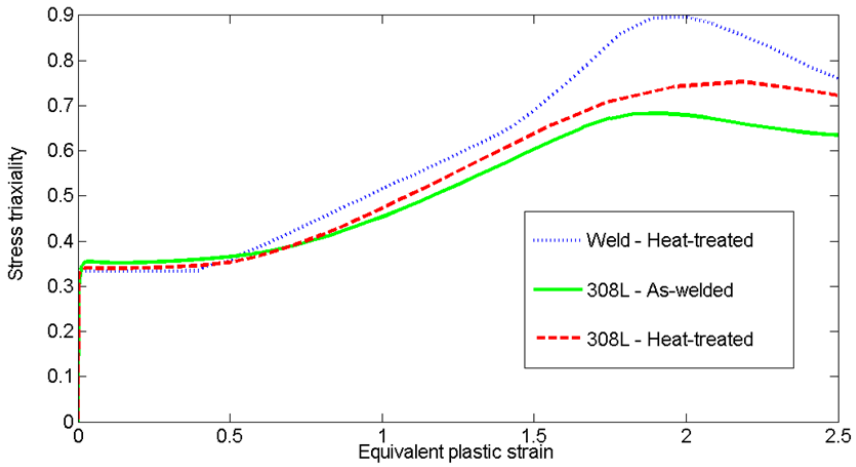

Figure 6.17: Stress triaxiality as a function of equivalent plastic strain for the element located in the center of the most damaged region in flat tensile specimens.

Table 6.9: Values of the nucleation stress used in the damage model for each site.

	Nucleation stress
Oxides	1500 MPa
As-welded δ-γ interfaces	3000 MPa
Carbides in the heat-treated state	2300 MPa

Once the nucleation stresses were selected, the damage model was then applied to predict ductile failure in homogeneous 309L specimens in both the as-welded and heat-treated states and in the complete weld (heterogeneous sample with the loading axis perpendicular to the fusion interface). The results in terms of macroscopic fracture strain are summarized in Table 6.10.

The reduction of ductility due to the post-weld heat-treatment is correctly reproduced and there is a good agreement for both the homogeneous specimens and the complete weld. Higher ductility is predicted in the 309L samples than in the 308L ones, as expected given both a lower volume fraction of inclusions and a larger hardening capacity. As the constitutive laws for all the different regions of the weld were not precisely known in the as-welded state, the same triaxiality history as in the heat-treated state was applied to the damage model when dealing with the as-welded state of the entire weld. Only the inclusions were adapted to correspond to the ones quantified in the as-welded 308L. Despite this approximation, the agreement between experimental and simulated fracture strains is good (around 1.5). It is also important to note that the damage calculation for the weld sample in the as-welded state led to coalescence before the maximum principal stress at

the δ-γ had reached the critical value of 3000 MPa. Therefore voids could not nucleate at the δ-γ interfaces whereas they appear in the homogeneous 308L and 309L samples before failure. This is in agreement with the fact that no elongated cavities were observed on the fracture surface of the as-welded assembly whereas they were present in the case of 308L and 309L samples in the as-welded condition. It can also explain the higher ductility (1.5 versus 1.27 and 1.25) obtained for the weld than for the longitudinal and homogeneous specimens.

Table 6.10: Comparison between experimental tensile tests and damage modeling in terms of true fracture strain.

	True fracture strain	
	ϵ_f **exp.**	ϵ_f **sim.**
308L as-welded	1.27	1.35
308L heat-treated	1.00	1.10
309L as-welded	1.25	1.39
309L heat-treated	1.10	1.23
Weld as-welded	1.50	1.55
Weld heat-treated	1.10	1.21

6.5 Conclusion

This chapter dedicated to damage mechanisms has been focused on the two soft regions of the weld (yield points lower than 300 MPa) that were identified in Chapter 5: the stainless steel layers and the decarburized zone. Both regions are subjected to transformations during the post-welding heat-treatment:

- **The decarburized layer** corresponds to a 200 μm wide region of the HAZ of the base metal subjected to **carbides dissolution, carbon depletion and grain growth**.
- The **austenitic cladding layers** contain ferrite residuals which decompose at 610°C and lead to the **formation of carbides at the δ - γ interfaces.**

Flat tensile specimens were sufficient to study damage in the stainless steels whereas notches had to be machined on the weld to force failure to occur in the narrow decarburized layer. The main differences between both regions are the **confinement degree** and the **quantity of potential nucleation sites.** The latter are numerous in the stainless steels, especially in the heat-treated state where the carbides present along the δ - γ interfaces complement the oxides formed during the solidification of the weld. On the contrary, the decarburized region is rather "clean" with only few and small MnS inclusions that can serve as nucleation sites.

3D elasto-plastic calculations allowed to evaluate the levels of plastic deformation and stress triaxiality within the different regions of interest. In addition, a **micro-mechanics based damage model** was applied to the critical element of the mesh in the different configurations in order to predict the true fracture strain. This model, where the critical stress for voids nucleation is the only adjustable parameter, allowed to **quantitatively predict the reduction of ductility observed in the stainless steel layers after heat-treatment** due to the weakening effect of the carbides on the δ - γ interfaces. However, in the case of the decarburized zone, **it failed in reproducing the variation of true fracture strain with the width of the adjacent martensitic layer.** As expected, higher levels of stress triaxiality were obtained in the case of a large hard zone but they were limited to a band of 70 μm adjacent to the martensite and associated with a small plastic strain. This was responsible for a displacement of the failure location towards the base metal where both plastic strain and triaxiality were weakly influenced by the size of the martensitic band. A detailed parametric study was carried out (strength of hard and soft zones especially) but none of the sets of parameters within a reasonable range of variations led to sufficiently large changes in ductility as observed experimentally. Nucleation on other sites in the case of high stress levels (large martensite) was invoked to explain the drop of ductility measured experimentally. An extended experimental campaign would be necessary to confirm the tendency observed, especially on thicker samples such as compact tension specimens.

Chapter 7

Conclusions

The dissimilar steel welds between a low-alloy steel and a stainless steel are widely encountered in industrial applications. They are known to be the place of several complex phase transformations that occur in the vicinity of the dissimilar interface during fabrication and/or service. Both these microstructural evolutions and their potential consequences on the mechanical behavior of the assembly were still poorly understood. That is why further studies were necessary to accurately quantify the extent of these evolutions and become able to predict their effects on both microstructure and mechanical properties.

7.1 Overview of the work

This PhD thesis has been divided into three main parts, each of them corresponding to a different condition of the weld, that is to say the as-welded state, the post-weld heat-treated one and the one in service.

- **Part I** was dedicated to the **solidification of the dissimilar interface** and the **origin of the resulting microstructures**. Microstructural observations (OM, SEM, WDS, EBSD) were combined with thermo-kinetics calculations. The main objective was to explain why the metastable γ phase formed in a narrow layer ($\approx 70\ \mu m$) from the base metal and how two successive transitions in the solidification mode allowed to recover the δ-γ microstructure typical of austenitic stainless steels.

- **Part II** was focused on the **phase transformations** that occur during the **post-weld heat-treatment** at 610°C. The latter were the subject of an in-depth investigation, both experimentally and theoretically. First, several characterization techniques were associated in order to:

  - measure the carbon diffusion through the weld (WDS, SIMS).
  - identify the precipitates that form in the carburized regions (ACOM-TEM) together with their preferential nucleation sites (FEG-SEM, TEM).

- quantify the carbides in terms of volume fraction, number density and size as a function of their distance from the fusion line (FIB serial cutting, TEM).
- measure the precipitates composition (EDX-TEM) as well as the chemical elements solubility within the matrix phases (APT).

Then, in a second chapter, a **mesoscopic thermodynamic and kinetics model** developed to fully couple diffusion in a multi-component system with precipitates nucleation, growth and coarsening was presented. The numerical Kampmann-Wagner approach was adopted for precipitation whereas the Onsager's equation with the chemical potential as driving force was used for calculating long-range diffusion. A parametric study allowed understanding the role played by each microstructural feature in the carbon transfer from the base metal towards the weld. The conditions necessary for an extensive carburization of the austenitic part of the weld in agreement with the experimental measurements were highlighted.

- **Part III** was intended to investigate how the phase transformations that occur during the post-weld heat-treatment impact the **local mechanical behavior around the dissimilar interface.** The purpose of the first chapter was to determine a **constitutive law** (yield stress and hardening capacity) for each type of microstructure encountered in the vicinity of the fusion line. For that, several experimental techniques were used (micro-tensile specimens, nanoindentation) and a particular attention was paid to the decarburized layer with two trials aiming at creating an equivalent bulk material. Digital image correlation at the micro-scale allowed validating the mechanical behavior chosen for each region. **Ductile failure** in the two soft regions (stainless steel and decarburized layer) was the topic of the second chapter. Experimental observations were combined with a micro-mechanics based damage model to identify the mechanisms that may cause a loss of ductility of the weld.

7.2 Specific contributions

The salient features of this study, that provide new inputs for the understanding of the microstructural and mechanical evolutions of the dissimilar steel welds, are listed below:

- **Influence of the fluid flow in the weld pool**

  A region of compositional gradients was detected by WDS on the weld metal side. Segregations during solidification were calculated and were found to be insufficient to create such an extended gradient. Insufficient mixing of the molten base metal with the liquid weld metal was pointed out as the cause of the compositional heterogeneities. Therefore, the fluid flow in the weld pool, and consequently the welding parameters were evidenced as responsible for the diversity of the microstructural features encountered at the fusion line, especially the variable width of the martensitic layer. As shown by the tensile tests on notched samples, these particular features at the interface stemming from the solidification, may play a significant role when dealing with ductile failure in the decarburized layer.

- **Origin of the purely austenitic zone**

  The purely austenitic zone had already be mentioned as a common feature in the dissimilar welds between a ferritic low-alloy steel and an austenitic stainless steel. However no clear explanation had been given so far for its formation. In this study, it was proven that this 100 μm wide zone resulted from the metastable solidification of the weld as primary austenite and that this out-of-equilibrium solidification took place in epitaxy on the solid base metal: such findings imply the metastable fusion of the base metal.

- **The post-weld heat-treatment cannot be assimilated to a simple temperature plateau**

  The post-weld heat-treatment is often, but wrongly, designed by its holding time at 610°C. However the heating and cooling rates being low (30°C/h), the assembly spends a significant amount of time at intermediate temperatures (between 400 and 610 °C) where changes can occur at the scale of the microstructure. The study of an intermediate sample, for which the heat-treatment had been interrupted at the end of the heating ramp, has shown that some carbon diffusion from the base metal to the martensitic layer has already taken place before the temperature plateau. This diffusion was accompanied by precipitates nucleation and growth together with carbon segregation to the subgrain boundaries within the tempered martensite. It would be a mistake to limit the post-weld heat-treatment to a temperature plateau at 610°C and not to consider the effects of the lower temperatures on the weld microstructure.

- **Model coupling long-range diffusion to precipitation kinetics**

  Up to now, modeling carbon diffusion within a dissimilar steel weld was always achieved under the hypothesis of equilibrium precipitation. In the present case, this classical approach was unable to reproduce the carbon profile measured through the weld, especially the extent of the carbon diffusion in the austenite. To face this problem, a model combining precipitation kinetics to long-range diffusion was built. Its specificity lies in:

  – the use of Calphad-type databases to calculate the thermodynamic and kinetics parameters at each node and each time step.
  – the consideration of the chemical potential gradient instead of the concentration gradient as the driving force for precipitation.
  – the calculation of the full precipitates distribution at each node via a numerical Kampmann-Wagner approach instead of only the mean radius.
  – the possibility of taking into account several types of precipitates that may compete against each others together with the dissolution of some of them.
  – the estimation of the interfacial energy of the precipitates through the GNNBB approach.

  Such a model can be applied to different combinations of alloys involved in a diffusion couple but also to heat-treatments in a gaseous atmosphere such as in nitriding and carburizing processes.

- **Role of the martensitic layer in the carbon diffusion from the low-alloyed side to the high-alloyed one**

  The accumulation of carbon within the interfacial martensitic layer has been found to be responsible for carbon penetration over 70 μm within the austenitic weld metal. The experimental measurements together with the thermo-kinetics modeling have shown the dual nature of this region: on the one hand, part of the carbon precipitates and gives rise to large carbides; on the other hand, significant quantities of carbon remain in solid solution and are available to diffuse towards the austenite. For the modeling to reproduce experimental measurements, it has been necessary to destabilize the Cr-rich carbides via the elastic stresses to enable the dissolution of a sufficient amount of carbon within the matrix.

- **Ageing of the dissimilar interface**

  The study of the samples aged at 400°C for 5000 and 10000 hours has revealed the stability of both the microstructure and the mechanical properties of the dissimilar weld in service conditions. Thus the post-weld heat-treated state has been considered as representative of the weld that would be encountered in today's nuclear power plants. That is why the whole mechanical study (Part III) has been focused on this state. More details concerning the microstructural and mechanical investigations that were conducted on aged samples can be found in Appendix B.

- **δ-ferrite decomposition at 610°C and significant consequences on the weld ductility**

  The dissimilar steel welds are the only welds of a pressurized water reactor involving austenitic stainless steels to be post-weld heat-treated. Microstructural observations at different scales have evidenced the decomposition of the δ-ferrite residuals into austenite and $M_{23}C_6$ carbides at 610°C. As a result, the δ-γ interfaces in both 309L and 308L cladding layers are decorated by cuboïd carbides which constitute potential sites for voids nucleation. A drop of ductility associated with the presence of elongated voids on the fracture surface has been found when comparing the weld in the heat-treated state to the one in the as-welded condition. The weakening effect of the carbides on the δ-γ interfaces has been taken into account and the damage model was able to reproduce the order of magnitude of the decrease in fracture strain.

- **Microstructural and mechanical characterization of the decarburized region**

  Although generally associated with a low hardness and the absence of carbides, the decarburized layer that exists on the low-alloy side of a dissimilar steel weld was poorly documented both in terms of microstructural and mechanical characteristics. In the present study, a quantitative method using reference samples with a known carbon concentration has been developed in SIMS in order to estimate the low carbon content of the decarburized layer. Concentrations between 0.0043 and 0.02 wt.% have been detected within the large grains ferritic region. Then, equivalent bulk materials with similar microstructure and carbon

content were fabricated in two different ways: by decarburization of the base metal in wet H_2 atmosphere and by heat-treatment of diffusion couples obtained by HIP. This allowed accurately determining the mechanical properties of this particular region: yield stress of 200 MPa and hardening exponent of 0.2. A thorough knowledge of the properties and behavior was achieved through this work and can now be used for other studies involving dissimilar steel welds, especially numerical simulations.

- **Clear evidence of an intermediate zone between the decarburized region and the unaffected base metal**

  The decarburized layer which results from the carbon depletion of the base metal was often associated with the 200 μm wide ferrite layer adjacent to the fusion line. However meticulous carbon measurements by both WDS and SIMS have shown that the carbon depletion actually extends over 500 μm, which include the region with large ferritic grains but are not limited to it. The supplementary 300 μm correspond to a gradual decrease of the carbon content from the one of the base metal (0.2 wt.%) to about 0.015 wt.%. In this intermediate zone, some carbides are still present. On a mechanical point of view, this zone, also highlighted by DIC, was subjected to intermediate levels of strain during tensile testing. A yield point of 300 MPa together with a hardening exponent of 0.2 have been attributed to it. This region is of particular importance as it directly acts on the soft ferritic region and allows to reduce its confinement degree and consequently its triaxiality.

7.3 Perspectives

Several new aspects have been raised but could not be addressed in this study due to time constraints. It would be of great interest to include them if an extension of the present work is considered. Therefore some future tasks will be suggested below to complement the three topics that have been investigated in this PhD thesis.

7.3.1 Solidification of the dissimilar interface

- **Influence of the nature of the base metal on the formation of the purely austenitic zone:**

  It was shown that the metastable fusion of the 18MND5 base metal was responsible for the solidification of the weld as primary austenite in the first 100 μm. It would be of great interest to replace the 18MND5 by another base metal with a δ-ferrite domain spreading over a larger range of temperatures in its phase diagram. This means choosing an alloy with a higher content in ferrite stabilizer elements (Cr,Mo) and/or a lower content in austenite stabilizer elements (C,Ni,Mn). And this should result in eliminating the metastable melting of the substrate and consequently lead to a primary ferrite solidification of the weld over its entire height. Such experiment would constitute a direct evidence to confirm the scenario we have proposed in Part I.

- **Effect of the welding speed on the metastable melting of the base metal:**

  A Time-Resolved X-Ray Diffraction (TRXRD) experiment was conducted in a synchrotron to study the influence of the heating rate on the nature of the 18MND5 melting. It aimed at determining a critical heating rate above which the melting would be metastable and proceed in only one step ($\gamma \rightarrow$Liquid) without any δ-ferrite formation. However several technical difficulties were encountered (reproducibility of the high rate temperature cycles, failure of the sapphire crucibles, carbon evaporation, grain growth) and prevented us from drawing unambiguous conclusions. It would be necessary to improve the experimental set-up to achieve the initial goal and completely validate the hypothesis of a metastable melting at high heating rates.

- **Multi-physics modeling of the submerged arc welding process:**

  The thickness of the boundary layer was estimated by simple and approximate calculations (see Section 2.4.1 and Appendix A for more details). Yet a good order of magnitude similar to the extent of the region with compositional gradients measured by WDS was obtained. To go further, it would be interesting to build a multi-physics model to accurately calculate the fluid flow in the weld pool and its consequences on the mixing of the elements from the filler metal with the molten base metal under both convection and diffusion. A parametric study based on the welding characteristics could allow optimizing the mixing and proposing different solutions to reduce the extent of the intermediate mixed zone. Up to now, no numerical model has been developed to simulate dissimilar welding by SAW.

7.3.2 Phase transformations during the post-welding heat-treatment

- **Improvements of the carbon measurements:**

  This study had to cope with the difficulty of measuring low carbon contents in regions of reduced size. In-depth profiles with SIMS were successful to quantify carbon within the decarburized layer of the heat-treated sample but failed in the case of the as-welded specimen because of their limited lateral resolution. A quantitative approach with SIMS in the image mode (area of $100 \times 100\ \mu m^2$) is currently under development at the Centre Public Gabriel Lippman in Luxembourg. It should enable in a near future a quantification of both the decarburization and carburization which take place during the welding process. Moreover APT measurements could also be performed in the decarburized regions in order to determine how the residual carbon is distributed within the matrix and evaluate the level of segregations at the grain boundaries.

- **Simplification of the diffusion/precipitation problem:**

  Modeling the coupling between long-range diffusion and precipitation turned out to be far more difficult than initially expected. The difficulty arose from the non-isothermal heat-treatment, the complexity of the three-phase configuration of the weld with the presence of an intermediate layer of martensite at the interface, and the phase competition between several precipitates. To correctly assess the validity of the model developed, it would be particularly relevant to test it on simple cases, for which experimental data will thus be needed. Diffusion couples could be realized by HIP and subjected to various isothermal heat-treatments. As the alloys in contact will not melt, mixing of elements will only occur by solid-state diffusion, preventing from the formation of any extended IMZ and its subsequent transformation into martensite. By varying the duration of the heat-treatment and/or the composition of the alloys, different states in terms of decarburization and carburization could be achieved. However an extensive characterization campaign would be necessary to quantify not only the carbon evolution through the weld but also the nature and characteristic parameters of the precipitates. Then, the simulation could be extended to more sophisticated situations, including the effect of the thickness of the intermediate martensitic layer.

- **A better thermodynamic and kinetics description of the tempered martensite:**

  Despite a significant chromium content (around 11 wt.%), high levels of carbon in supersaturation within the matrix of the tempered martensite (around 0.1 wt.%) were measured by APT in the as-welded, intermediate and heat-treated states. In the modeling step, it was necessary to highly destabilize the precipitates to maintain such a large quantity of dissolved carbon. This enhanced solubility turned out to be the key parameter allowing carbon to diffuse within the austenitic part of the weld. These findings give strong hints that the current description of the tempered martensite as an alloyed BCC phase is certainly not correct. For the moment no specific thermodynamic and kinetics database has been developed for such microstructures. In the present case, the specific and dual role of the subgrain boundaries as both shortcuts for diffusion and segregation places allowing precipitates to nucleate and grow has been highlighted. Fischer et al. [217] have proposed a new approach to deal with trapping of diffusing interstitial components by dislocation cores, substitutionnal impurities or other sorts of traps such as incoherent interfaces. Their method based on local thermodynamic equilibrium between the atoms on the different lattice positions and the derivation of a non-linear diffusion equation is currently under implementation in the MatCalc software. It was already shown to greatly reduce cementite precipitation in steels with a large dislocation density. A critical step in the improvement of the current model of diffusion/precipitation in a dissimilar steel weld would be to include trapping in the tempered bainitic and martensitic parts of the weld, especially at the lath boundaries. The enthalpy of this kind of traps and its evolution with the temperature should be determined and combined with an enhanced diffusion coefficient along them.

7.3.3 Mechanical behavior of the dissimilar weld

- **Effect of the residual stresses:**

  The residual stresses resulting from non-uniform heat distributions and phase transformations within the assembly during welding can have a significant impact on both diffusion and precipitation as well as on mechanical behavior. Finite element simulations [191] showed that the post-weld heat-treatment of the dissimilar weld was efficient at reducing the level of stresses within the HAZ but did not have any effect on the cladding layer that are found to be in tension. However these calculations were performed with a coarse mesh (element size around 1 mm) which did not allow capturing fine evolutions in the vicinity of the fusion line. Measurements at the micron scale, by means of either neutron diffraction in a synchrotron or FIB milling and image correlation in a SEM, would certainly be interesting to evaluate the levels of residual stresses with a fine lateral resolution adapted to the size of the microstructures around the dissimilar interface.

- **Mechanical behavior of the different regions at large strains:**

  Tensile testing on micro-samples were mainly used to determine the constitutive laws that characterize each region of the weld. However such method only gives valuable information up to the onset of necking. When dealing with failure, high levels of strain can be achieved locally and it becomes necessary to extrapolate the previously determined laws. An efficient way to assess the mechanical behavior at large strains would be to perform compression or torsion tests on samples extracted from the different regions of the weld.

- **Anisotropic mechanical behavior of the stainless steel cladding layers:**

  The anisotropic behavior of the stainless steel cladding layers has been evidenced by tensile testing in different directions. Not only the yield point was found to vary in the different directions, but also the hardening capacity appeared to be anisotropic. To correctly take into account this specificity into the elasto-plastic modeling, it would be necessary to calculate the constitutive law in the transverse direction using a crystal plasticity model together with an homogenization scheme. Indeed the thickness of the cladding layers is too small (4 mm) to machine a tensile specimen in it. The Von Mises yield criterion would have to be replaced by the Hill one. Anisotropy of the mechanical properties is also known to influence the cavity growth in ductile failure [200] and this aspect was not considered in the present study.

- **Correction of the out-of-plane displacements near the dissimilar interface:**

  In order to accommodate the mechanical mismatch that exists between the carburized and decarburized regions in the heat-treated sample, significant out-of-plane displacements occurred at the fusion line during tensile testing on the entire weld. Such out-of-plane displacements that were confirmed by profilometry prevented from a correct measurement of the local strains in the decarburized region near the hard martensite by 2D image correlation. It would be first necessary to scan the specimen's surface by profilometry after each increment

of strain and then, similarly to what was done in [218], to recalculate the deformation gradient according to the real out-of-plane displacements and deduce the exact value of the in-plane strain components. Such correction would allow a complete comparison of the levels of strain obtained by simulation and experimental measurements, even at the fusion line.

- **Critical stress for voids nucleation:**

  The critical stress for voids nucleation is the main adjustable parameter of the damage model. Its value was evidenced to have a profound effect on the final fracture strain. Combining elasto-plastic finite element simulations with interrupted tensile tests on notched specimens would allow assessing this critical value for the various types of particles encountered in the different regions of the weld [14]. Concerning the decarburized region, MnS particles were considered in this study as the main damage initiation sites. However the level of stress triaxiality could have a pronounced effect on cavity nucleation that could initiate at multiple locations, especially at grain boundary triple junctions. Interrupted tensile tests could also be suggested as a way to address this point and remove uncertainty on that topic.

- **Supplementary mechanical testing and modeling in the decarburized layer:**

  The effect of the martensitic layer on the ductility of the decarburized region that was experimentally observed could not be reproduced by damage modeling. This point first needs confirmation, which requires an extensive experimental campaign. Thoughness measurements by means of Compact Tension specimens with a fatigue crack located within the decarburized region could be suggested to experimentally assess the ease for a crack to propagate within this confined region. Tests at 300°C would also be necessary to mimic the conditions of service. If the tendency for ductility loss is experimentally confirmed, the modeling approach will have to be improved. For failure in the decarburized region to be influenced by the size of the martensitic layer, it has to take place in the vicinity of the fusion line. It was not the case in the present simulations based on the well-known Gurson model, in which both stress triaxiality and plastic deformation govern the growth of cavities. Second-gradient models [219, 220] including the gradient of stress as driving force for damage development might be more adapted to cause failure in the vicinity of the interface, as it was observed experimentally. However such models are computationally expensive and convergence of the elasto-plastic iterations often remains difficult.

Bibliography

Bibliography

[1] C. Cayron, B. Artaud, and L. Briottet. Reconstruction of parent grains from EBSD data. *Materials Characterization*, 57:386–401, 2006.

[2] C. Cayron. ARPGE: a computer program to automatically reconstruct the parent grains from electron backscatter diffraction data. *Journal of Applied Crystallography*, pages 1183–1188, 2007.

[3] W. Kurz, B. Giovanola, and R. Trivedi. Theory of microstructural development during rapid solidification. *Acta Metallurgica*, 34:823–830, 1986.

[4] M. Bobadilla, J. Lacaze, and G. Lesoult. Influence des conditions de solidification sur le droulement de la solidification des aciers inoxydables austnitiques. *Journal of Crystal Growth*, 89:531–544, 1988.

[5] M. Rappaz, S.A. David, J.M. Vitek, and L.A. Boatner. Analysis of solidification microstructures in Fe-Ni-Cr single-crystal welds. *Metallurgical Transactions A*, 21A:1767–1782, 1990.

[6] K. Bongartz, W. Quadakkers, R. Schulten, and H. Nickel. A mathematical model describing carburization in multielement alloy systems. *Metallurgical and Materials Transactions A*, 20:1021–1028, 1989.

[7] A. Engström, L. Höglund, and J. Ägren. Computer simulation of diffusion in multiphase systems. *Metallurgical and Materials Transactions A*, 25:1127–1134, 1994.

[8] T. Helander, J. Ägren, and J-O. Nilsson. An experimental and theoretical investigation of diffusion across a joint of two multicomponent steels. *ISIJ international*, 11:1139–1145, 1997.

[9] J. Svoboda, F.D. Fischer, P. Fratzl, and E. Kozeschnik. Modeling of kinetics in multi-component multi-phase systems with spherical precipitates I- Theory. *Materials Science and Engineering A*, 385:166–174, 2004.

[10] E. Kozeschnik. *Modeling solid-state precipitation*. Momentum Press, 2013.

[11] J.L. Bucaille, S. Stauss, E. Felder, and J. Michler. Determination of plastic properties of metals by instrumented indentation using different sharp indenters. *Acta Materialia*, 51:1663–1676, 2003.

[12] T. Pardoen and J.W. Hutchinson. An extended model for void growth and coalescence. *Journal of the Mechanics and Physics of Solids*, 48:2467–2512, 2000.

[13] T. Pardoen and J.W. Hutchinson. Model for trends in toughness of ductile metals. *Acta Materialia*, 51:2467–2512, 2003.

[14] F.M. Beremin. Cavity formation from inclusions in ductile fracture of A508 steel. *Metallurgical Transactions A*, 12:723–731, 1981.

[15] A.L. Gurson. Continuum theory of ductile rupture by void nucleation and growth: Part I-Yield criteria and flow rules for porous ductile media. *Journal of Engineering Materials and Technology*, 99:2–15, 1977.

[16] P.F. Thomason. *Ductile fracture of metals.* Pergamon Press, 1990.

[17] www.nrc.gov.

[18] B. Yrieix. Caractéristiques mécaniques locales des liaisons bimétalliques 16MND5/309L/308L. Technical report, EDF R&D HT-42/95/028/B, 1996.

[19] K. Easterling. *Introduction to the Physical Metallurgy of Welding.* Butterworth-Heinemann, 1992.

[20] R.L. Klueh and J.F. King. Austenitic stainless steel - ferritic steel weld joint failures. *Welding Journal*, 61:302–311, 1982.

[21] J.N Dupont and C.S. Kusko. Technical note : martensite formation in austenitic/ferritic dissimilar alloy welds. *Welding Journal*, pages 51–54, 2007.

[22] Z. Sun and T. Moisio. Weld metal/ferritic steel interface in laser welded austenitic/ferritic dissimilar steel joints. *Journal of Materials Science Letters*, 13:802–805, 1994.

[23] F. Ornath, J. Soudry, and B.Z. Weiss. Weld pool segregation during the welding of low alloy steels with austenitic electrodes. *Welding Journal*, 60:227–230, 1981.

[24] T. Doody. Intermediate mixed zones in dissimilar metal welds for sour service. *Welding Journal*, 55:55–60, 1992.

[25] N. Murugan and R.S. Parmar. Effect of welding conditions on microstructure and properties of type 316L stainless steel submerged arc cladding. *Welding Research Supplement*, pages 210s–217s, 1997.

[26] W.F. Savage, E.F. Nippes, and E.S. Szekeres. A study of weld interface phenomena in a low alloy steel. *Welding Journal*, 55:s260–s268, 1976.

[27] Y. Cui, C.L. Xu, and Q. Han. Effect of ultrasonic vibration on unmixed zone formation. *Scripta Materialia*, 55:975–978, 2006.

[28] R. Dehmolaei, M. Shamanian, and A. Kermanpur. Effect of electromagnetic vibration on the unmixed zone formation in 25Cr-35Ni heat resistant steel/alloy 800 dissimilar welds. *Materials Characterization*, 59:1814–1817, 2008.

[29] S. Kou and Y.K. Yang. Fusion-boundary macrosegregation in dissimilar-filler welds. *Welding Journal*, 86:303–312, 2007.

[30] G. Faber and T. Gooch. Assemblages soudntre aciers inoxydables et aciers faiblement alli Etat de la question. *Soudage et Techniques connexes*, pages 109–115, 1983.

[31] H. Ikawa, S. Shin, M. Inui, Y. Takeda, and A. Nakano. On the martensitic-like structure at weld bond and the macroscopic segregation in weld metal in the welded dissimilar metals of α-steels and γ-steels. *IIW Database*, pages 1–33, 1972.

[32] T. Ishida. Formation of stainless steel layer on mild steel by welding arc cladding. *Journal of Materials Science*, 26:6431–6435, 1991.

[33] Y.K. Yang and S. Kou. Weld-bottom macrosegregation caused by dissimilar filler metals. *Welding Journal*, 86:379s–387s, 2007.

[34] T. Gandhi and D.K. Aidun. Effects of enhanced convection on the microstructure of dissimilar welds. In *Proceedings of the 7th International Conference*, 2005.

[35] M.F. Gittos and T.G. Gooch. The interface below stainless steel and nickel-alloy claddings. *Welding Research Supplement*, pages 461s–472s, 1992.

[36] F. Gauzzi and S. Missori. Microstructural transformations in austenitic-ferritic transition joints. *Journal of Materials Science*, 23:782–789, 1988.

[37] T.G. Kravtsov, V.I. Ikonnikov, and N.K. Solyanik. Structure of the metal in the fusion zone in depositing austenitic steel on pearlitic steel. *Welding International*, 3:200–202, 1989.

[38] C. Pan, R. Wang, and J. Gui. Direct TEM observation of microstructures of the austenitic/carbon steels welded joint. *Journal of Materials Science*, 25:3281–3285, 1990.

[39] K. Rajasekhar, C.S. Harendranath, R. Raman, and S.D. Kulkarni. Microstructural evolution during solidification of austenitic stainless steel welds metals: a color metallographic and electron microprobe analysis study. *Materials Characterization*, 38:53–65, 1997.

[40] J.C. Lippold and W.F. Savage. Solidification of austenitic stainless steel weldments: Part 2 - The effect of alloy composition on ferrite morphology. *Welding Research Supplement*, pages 48s–58s, 1980.

[41] N. Suutala. Effect of solidification conditions on the solidification mode in austenitic stainless steels. *Metallurgical Transactions A*, 14:191–197, 1983.

[42] J.M. Vitek, A. Dasgupta, and S.A. David. Microstructural modification of austenitic stainless steels by rapid solidification. *Metallurgical Transactions A*, 14:1833–1841, 1983.

[43] W.T. Delong. Ferrite in austenitic stainless steel weld metal. *Welding Journal*, 52:273s–286s, 1974.

[44] J.A. Dantzig and M. Rappaz. *Solidification*. EPFL Press, 2009.

[45] S. Fukumoto and W. Kurz. The δ to γ transition in Fe-Cr-Ni alloys during laser treatment. *ISIJ International*, 37:677–684, 1997.

[46] S. Fukumoto and W. Kurz. Prediction of the δ to γ transition in austenitic stainless steels during laser treatment. *ISIJ International*, 38:71–77, 1998.

[47] T. Hashimoto, H. Terasaki, and Y. Komizo. Effect of the solidification velocity on weld solidification process of alloy tool steel. *Science and Technology of Welding and Joining*, 13:409–414, 2008.

[48] S.S. Babu, J.W. Elmer, J.M. Vitek, and S.A. David. Time-resolved X-ray diffraction investigation of primary weld solidification in Fe-C-Al-Mn steel welds. *Acta Materialia*, 50:4763–4781, 2002.

[49] T.W. Nelson, J.C. Lippold, and M.J. Mills. Nature and evolution of the fusion boundary in ferritic-austenitic dissimilar metal welds - Part 2 : On-cooling transformations. *Supplement to the Welding Journal*, pages 267s–277s, 2000.

[50] Y. Wu and B.M. Patchett. Formation of crack-susceptible structures of weld overlay of corrosion resistant alloys. *Proceeding of the international symposium on materials performance: sulphur and energy*, pages 283–295, 1992.

[51] J.L. Pouchou and F. Pichoir. Basic expression of "PAP" computation for quantitative epma. $11^{th} ICXCOM$, 1986.

[52] C. Cayron. Genova: a computer program to generate orientational variants. *Journal of Applied Crystallography*, 40:1179–1182, 2007.

[53] B. Sundman, B. Jansson, and J-O. Andersson. The Thermo-Calc databank system. *Calphad*, 9:153–190, 1985.

[54] www.thermocalc.com.

[55] O. Grong and N. Christensen. Effects of weaving on temperature distribution in fusion welding. *Materials Science and Technology*, 2:967–973, 1986.

[56] P. Dupas and F. Waeckel. Recueil bibliographique de caractéristiques thermomniques pour l'acier de cuve, les revêtements inoxydables et les alliages 182 et 600. Technical report, EDF/DER HI-74/93/087-HT-26/93/058/A, 1994.

[57] H. Granjon. *Bases métallurgiques du soudage.* 1989.

[58] S. Kou. *Welding Metallurgy.* John Wiley and Sons, 2003.

[59] W. Steven and A.G. Haynes. The temperature of formation of martensite and bainite in low-alloy steel. *JISI*, 183:349–359, 1956.

[60] H. Finkler and M. Schirra. Transformation behaviour of high temperature martensitic steels with 8-14% chromium. *Materials technology, Steel research*, 67:328–342, 1996.

[61] J.P. Cunat. Aciers inoxydables, crits de choix et structure. *Techniques de l'Ingeur, Traittaux Mlliques*, MB4, 2000.

[62] J.W. Elmer, S.M. Allen, and T.W. Eager. Microstructural development during solidification of stainless steel alloys. *Metallurgical Transactions A*, 20A:2117–2131, 1989.

[63] A.B. Greninger and A.R. Troiano. The mechanism of martensite formation. *Metals Transactions*, 185:590–598, 1949.

[64] G. Kurdjumov and G. Sachs. Uber den Mechanismus des Stahlhartung. *Zeitschrifft fr Physik*, 64:325–343, 1930.

[65] Z. Nishiyama. *Sci. Rep. Tohoku Imp. Univ.*, 23:637–664, 1934.

[66] D-W. Cho, W-H. Song, M-H. Cho, and S-J. Na. Analysis of submerged arc welding process by three-dimensional computational fluid dynamics simulations. *Journal of Materials Processing Technology*, 213:2278–2291, 2013.

[67] S. Kou and D.K. Sun. Fluid flow and weld penetration in stationary arc welds. *Metallurgical Transactions A*, 16A:203–213, 1985.

[68] Y. Fautrelle. Ecoulement dans les bains mlliques en procédé de souadge TIG. *Soudage et techniques connexes*, pages 12–19, 1985.

[69] A.E.P. Veldman. *Boundary layers in fluid dynamics.* University of Groningen, 2011-2012.

[70] M. Carin and E. Favre. Numerical simulation of fluid flow during arc welding. In *Proceedings of the COMSOL Multiphysics User's Conference*, 2005.

[71] M.E. Glicksman. *Principles of Solidification.* Springer, 2011.

[72] S.A. David and J.M. Vitek. Correlation between solidification parameters and weld microstructures. *International Materials Reviews*, 34:213–245, 1989.

[73] W. Kurz and D.J. Fischer. *Fundamentals of Solidification.* Trans Tech Publications, 1986.

[74] D.E. Coates, S.V. Subramanian, and G.R. Purdy. Solid-liquid interface stability during solidification of dilute ternary alloys. *Trans AIME*, 242:800–810, 1968.

[75] M. Rettenmayr, O. Warkentin, M. Rappaz, and H.E. Exner. Simulation of solutal remelting. *Acta Materialia*, 49:2499–2510, 2001.

[76] G.P. Ivantsov. The temperature field around a spherical, cylindrical and needle-shaped crystal, growing in a pre-cooled melt. *Doklady Akad. Nauk SSSR*, 58:567–569, 1947.

[77] W.W. Mullins and R.F. Sekerka. Stability of a planar interface during solidification of a dilute binary alloy. *Journal of Applied Physics*, 35:444, 1964.

[78] N. El-Kaddah, M. Arenas, and V.L. Acoff. Heat transfer and fluid flow in stationary GTA welding of γ-TiAl based alloys: effect of thermocapillarity flow. In *Second International Conference on CFD in the Minerals and Process Industries*, 1999.

[79] J. Sopousek, R. Foret, and V. Jan. Simulation of dissimilar weld joints of steel P91. *Science and Technology of Welding and Joining*, 9:59–64, 2004.

[80] J.M. Race and H.K.D.H Bhadeshia. Carbon migration across dissimilar steel welds. *International Trends in Welding Science and Technology*, pages 315–319, 1992.

[81] X. Gomez and J. Echeberria. Microstructure and mechanical properties of low alloy steel T11-austenitic stainless steel 347H bimetallic tubes. *Materials Science and Technology*, 16:187–193, 2000.

[82] C.C. Silva, H.E. Miranda, H.B. de Sant'Ana, and J.P. Farias. Austenitic and ferritic stainless steel dissimilar weld metal evaluation for the applications as coating in the pretroleum processing equipment. *Materials and Design*, 47:1–8, 2013.

[83] R. Foret, B. Slamal, and J. Sopousek. Structural stability of dissimilar weld between two Cr-Mo-V steels. *Supplement to the Welding Journal*, pages 211s–217s, 2006.

[84] L.S. Darken. Diffusion of carbon in austenite with a discontinuity in composition. *Trans AIME*, pages 430–438, 1948.

[85] R.J. Christoffel and R.M. Curran. Carbon migration in welded joints at elevated temperatures. *Welding Journal*, 35:457s–468s, 1956.

[86] J.M. Race and H.K.D.H Bhadeshia. Precipitation sequences during carburisation of Cr-Mo steel. *Materials Science and Technology*, 8:875–882, 1992.

[87] E. Kozeschnik, P. Polt, S. Brett, and B. Buchmayr. Dissimilar 2.25Cr/9Cr and 2Cr/0.5CrMoV steel welds - Part 1: Characterization of weld zone and numerical simulation. *Science and Technology of Welding and Joining*, 7:63–68, 2002.

[88] M. Huang and L. Wang. Carbon migration in 5Cr-0.5Mo/21Cr-12Ni dissimilar metal welds. *Metallurgical and Materials Transactions A*, 29:3037–3046, 1998.

[89] S.K. Albert, T.P.S. Gill, A.K. Tyagi, S.L. Mannan, S.D. Kulkarni, and P. Rodriguez. Soft zone formation in dissimilar welds between two Cr-Mo steels. *Welding Research Supplement*, pages 135s–142s, 1997.

[90] E. Kozeschnik, P. Warbichler, I. Letofsky-Papst, S. Brett, and B. Buchmayr. Dissimilar 2.25Cr/9Cr and 2Cr/0.5CrMoV steel welds - Part 2: Identification of precipitates. *Science and Technology of Welding and Joining*, 7:69–76, 2002.

[91] C.D. Lundin. Dissimilar metal welds - Transition Joints Literature Review. *Welding Journal*, 61:58–63, 1982.

[92] K. He, A. Brown, R. Brydson, and D.V. Edmonds. Analytical electron microscope study of the dissolution of the Fe_3C iron carbide phase (cementite) during a graphitisation anneal of carbon steel. *Journal of Materials Science*, 41:5235–5241, 2006.

[93] C. Scott and J. Drillet. A study of carbon distribution in retained austenite. *Scripta Materialia*, 56:489–492, 2007.

[94] N. Valle, J. Drillet, O. Bouaziz, and H.-N. Migeon. Study of carbon distribution in multi-phase steels using the NanoSIMS 50. *Applied Surface Science*, 252:7051–7053, 2006.

[95] J. Laigo, F. Christien, R. Le Gall, F. Tancret, and J. Furtado. SEM, EDS, EPMA-WDS and EBSD characterization of carbides in HP type heat resistant alloys. *Materials Characterization*, 59:1580–1586, 2008.

[96] L. Lan, C. Qiu, D. Zhao, X. Gao, and L. Du. Analysis of martensite-austenite constituent and its effect on toughness in submerged arc welded joint of low carbon bainitic steel. *Journal of Materials Science*, 47:4732–4742, 2012.

[97] Y.J. Li, P. Choi, C. Borchers, Y.Z. Chen, S. Goto, D. Raabe, and R. Kirchheim. Atom probe tomography characterization of heavily cold drawn pearlitic steel wire. *Ultramicroscopy*, 111:628–632, 2011.

[98] C. Garcia-Mateo, F.G. Caballero, M.K. Miller, and J.A. Jimenez. On measurement of carbon content in retained austenite in a nanostructured bainitic steel. *Journal of Materials Science*, 47:1004–1010, 2012.

[99] F. Seidel, H.R. Stock, and P. Mayr. Glow discharge optical spectroscopy depth profiles of ion-implanted steel, titanium and titanium nitride coatings. *Thin Solid Films*, 308-309:425–429, 1997.

[100] S. Mandl, B. Fritzsche, D. Manova, D. Hirsch, H. Neumann, E. Richter, and B. Rauschenbach. Wear reduction in AISI 630 martensitic stainless steel after energetic nitrogen ion implantation. *Surface and Coatings Technology*, 195:258–263, 2005.

[101] Iso 16592: Analyse par microfaisceaux - Analyse par microsonde électronique (microsonde de Castaing) - Lignes directrices pour le dosage du carbone dans les aciers par la droite d'lonnage.

[102] F. Robaut, A. Crisci, M. Durand-Charre, and D. Jouanne. Practical aspects of carbon content determination in carburized steels by EPMA. *Microscopy and Microanalysis*, 12:1–4, 2006.

[103] W.C. Oliver and G.M. Pharr. An improved technique for determining hardness and elastic modulus using load and displacement sensing indentation experiments. *Journal of Materials Research*, 7:1564–1583, 1992.

[104] W.C. Oliver and G.M. Pharr. Measurement of hardness and elastic modulus by instrumented indentation: Advances in understanding and refinements to methodology. *Journal of Materials Research*, 19:3–20, 2004.

[105] Gatan. Ion beam etching applications in materials characterization. Technical report.

[106] E. Rauch and A. Duft. Orientation maps derived from TEM diffraction patterns collected with external CCD camera. *Materials Science Forum*, pages 197–202, 2005.

[107] E. Rauch and M. Véron. Orientation and phase mapping in TEM microscopy (EBSD-TEM like): applications to materials science. In 14^{th} *International Conference on Electron Microscopy*, 2012.

[108] P. Moeck, S. Rouvimov, E. Rauch, M. Véron, H. Kirmse, I. Hausler, W. Neumann, D. Bultreys, Y. Maniette, and S. Nicolopoulos. High spatial resolution semi-automatic crystallite orientation and phase mapping of nanocrystals in transmission electron microscopes. *Crystal Research and Technology*, 46:589–606, 2001.

[109] D.V. Shtansky, K. Nakai, and Y. Ohmori. Decomposition of martensite by discontinuous-like precipitation reaction in an Fe-17Cr-0.5C alloy. *Acta Materialia*, 48:969–983, 2000.

[110] R. Berkane, J.C. Gachon, J. Charles, and J. Hertz. A thermodynamic study of the chromium-carbon system. *Calphad*, 11:375–382, 1987.

[111] D.V. Shtansky, K. Nakai, and Y. Ohmori. Crystallography and interface boundary structure of pearlite with M_7C_3 carbide lamellae. *Acta Materialia*, 47:1105–1115, 1999.

[112] P. Villars and K. Cenzual. Pearson's crystal data: Crystal structure database for inorganic compounds. *ASM International®*.

[113] E. Kozeschnik and B. Buchmayr. MatCalc - a simulation tool for multicomponent thermodynamics, diffusion and phase transformations. *Mathematical modelling of weld phenomena*, 5:349–361, 2001.

[114] www.matcalc.tuwien.ac.at.

[115] F.C. Hull. Effect of δ-ferrite on the hot cracking of stainless steel. *Welding Journal*, 46:399s–409s, 1967.

[116] J.A. Brooks, A.W. Thompson, and J.C. Williams. A fundamental study of the beneficial effects of δ ferrite in reducing weld cracking. *Supplement to the Welding Journal*, pages 71s–83s, 1984.

[117] J. Foulds and J. Moteff. Carbide formation in a low-ferrite austenitic stainless steel weld metal at 649°C. *Metallurgical Transactions A*, 13:173–174, 1982.

[118] R.A. Farrar and R.G. Thomas. The microstructure and phase transformations in duplex 316L submerged arc weld metals. *Journal of Materials Science*, 18:3461–3474, 1983.

[119] C.C Tseng, Y. Shen, S.W. Thompson, M.C. Mataya, and G. Krauss. Fracture and the formation of sigma phase, M23C6, and austenite from δ-ferrite in an AISI 304L stainless steel. *Metallurgical and Materials Transactions A*, 25A:1147–1158, 1994.

[120] H.P. Van Landeghem, M. Gouné, and A. Redjaimia. Nitride precipitation in compositionally heterogeneous alloys: nucleation, growth and coarsening during nitriding. *Journal of Crystal Growth*, 341:53–60, 2012.

[121] A. Maheshwari and A.J. Ardell. Morphological evolution of coherent misfitting precipitates in anisotropic elastic media. *Physical Review Letters*, 70:2305–2309, 1993.

[122] C.H. Su and P.W. Voorhees. The dynamics of precipitate evolution in elastically stressed solids - II- Particle alignment. *Acta Materialia*, 44:2001–2016, 1996.

[123] U. Rolander and H.O. Andr'en. On atom-probe analysis of cubic MX-type carbides and carbonitrides. *Journal de Physique*, 49:299–304, 1988.

[124] M. Thuvander, J. Weidow, J. Angseryd, L.K.L. Falk, F. Liu, M. Sonestedt, K. Stiller, and H.O. Andr'en. Quantitative atom probe analysis of carbides. *Ultramicroscopy*, 111:604–608, 2011.

[125] A.J. Clarke, M.K. Miller, R.D. Field, D.R. Coughlin, P.J. Gibbs, K.D. Clarke, D.J. Alexander, K.A. Powers, P.A. Papin, and G. Krauss. Atomic and nanoscale chemical and structural changes in quenched and tempered 4340 steel. *Acta Materialia*, 77:17–27, 2014.

[126] D.W. Saxey. Correlated ion analysis and the interpretation of atom probe mass spectra. *Ultramicroscopy*, 111:473–479, 2011.

[127] P.M. Hekker, H.C.F. Rozendaal, and E.J. Mittemeijer. Excess nitrogen and discontinuous precipitation in nitrided iron-chromium alloys. *Journal of Materials Science*, 20:718–729, 1985.

[128] L. Onsager. Reciprocal relations in irreversible processes. II. *Phys. Rev.*, pages 2265–2279, 1931.

[129] A.D. Smigelskas and E.O. Kirkendall. Zinc diffusion in alpha brass. *Trans AIME*, pages 130–142, 1947.

[130] G. Inden. Diffusion and phase transformations in multi-component systems. *Defect and Diffusion Forum*, 263:11–20, 2007.

[131] J.O. Andersson and J. Ägren. Models for numerical treatment of multicomponent diffusion in simple phases. *Journal of Applied Physics*, 72:1350–1355, 1992.

[132] A. Schneider and G. Inden. Simulation of the kinetics of precipitation reactions in ferritic steels. *Acta Materialia*, 53:519–531, 2005.

[133] N. Saunders and A.P. Miodownik. *CALPHAD (Calculation of Phase Diagrams): A Comprehensive Guide*. Elsevier, 1998.

[134] H. Lukas, S.G. Fries, and B. Sundman. *Computational Thermodynamics The Calphad Method*. Cambridge University Press, 2007.

[135] O. Redlich and A.T. Kister. Algebraic Representation of Thermodynamic Properties and the Classification of Solutions. *Industrial and Engineering Chemistry*, 40:345–348, 1948.

[136] B Jönsson. Assessment of the mobility of carbon in FCC C-Cr-Fe-Ni alloys. *Z. Metallkd.*, 85:502–509, 1994.

[137] T. Turpin, J. Dulcy, and M. Gantois. Carbon diffusion and phase transformations during gas carburizing of high-alloyed stainless steels: Experimental study and theoretical modeling. *Metallurgical and Materials Transactions A*, 36:2751–2760, 2005.

[138] C. Sudha, N. Sivai Bharasi, R. Anand, H. Shaikh, R.K. Dayal, and M. Vijayalakshmi. Carburization behavior of AISI 316LN austenitic stainless steel : Experimental studies and modeling. *Journal of Nuclear Materials*, 402:186–195, 2010.

[139] H. Du and J. Ägren. Gaseous nitriding iron : evaluation of diffusion data of N in γ' and ϵ phases. *Z. Metallkd.*, 86:522–529, 1995.

[140] T. Helander and J. Ägren. Computer simulation of multicomponent diffusion in joints of dissimilar steels. *Metallurgical and Materials Transactions A*, 28:303–308, 1997.

[141] A. Engström and J. Ägren. Simulation of diffusion in multicomponent and multiphase systems. *Defect and Diffusion Forum*, 143-147:677–682, 1997.

[142] S-J. Lee, D. K. Matlock, and C. J. Van Tyne. An empirical model for carbon diffusion in austenite incorporating alloying element effects. *ISIJ International*, 51:1903–1911, 2011.

[143] A. Borgenstam, A. Engström, L. Höglund, and J. Ägren. Dictra, a tool for simulation of diffusional transformations in alloys. *Journal of Phase Equilibria*, 21:269–280, 2000.

[144] H. Larsson and A. Engström. A homogenization approach to diffusion simulations applied to $\alpha + \gamma$ Fe-Cr-Ni diffusion couples. *Acta Materialia*, 54:2431 – 2439, 2006.

[145] H. Larsson and L. Höglund. Multiphase diffusion simulations in 1D using the DICTRA homogenization model. *Calphad*, 33:495 – 501, 2009.

[146] K.G.F. Janssens, D. Raabe, E. Kozeschnik, M.A. Miodownik, and B. Nestler. *Computational Materials Engineering: An Introduction to Microstructure Evolution*. Elsevier Academic Press, 2007.

[147] J.B. Zeldovich. On the theory of new phase formation; cavitation. *Acta Physicochim.*, 18:1–22, 1943.

[148] C.M. Zener. Theory of growth of spherical precipitates from solid solution. *Journal of Applied Physics*, 20:950–953, 1949.

[149] D.V. Shtansky and G. Inden. Phase transformation in Fe-Mo-C and Fe-W-C steels -I The structural evolution during tempering at 700°C. *Acta Materialia*, 45:2861–2878, 1997.

[150] A. Schneider and G. Inden. Computer simulation of diffusion controlled phase transformations. *Continuum Scale Simulation of Engineering Materials*, 2004.

[151] Q. Chen, J. Jeppsson, and J. Ägren. Analytical treatment of diffusion during precipitate growth in multicomponent systems. *Acta Materialia*, 56:1890–1896, 2008.

[152] Thermo-Calc Software AB. *TC-PRISMA User's Guide and Examples Version 2.0*, 2013.

[153] L. Onsager. Reciprocal relations in irreversible processes I. *Phys. Rev.*, 37:405–426, 1931.

[154] J. Svoboda, I. Turek, and F.D. Fischer. Application of the thermodynamic extremal principle to modeling of thermodynamic processes in material sciences. *Philosophical Magazine*, 85:3699–3707, 2005.

[155] E. Kozeschnik, J. Svoboda, and F.D. Fischer. Modified evolution equations for the precipitation kinetics of complex phases in multi-component systems. *CALPHAD*, 28:379–382, 2004.

[156] M. Perez. Gibbs-Thomson effects in phase transformations. *Scripta Materialia*, 52:709–712, 2005.

[157] E. Kozeschnik, J. Svoboda, P. Fratzl, and F.D. Fischer. Modelling of Kinetics in Multi-Component Multi-Phase Systems with Spherical Precipitates II- Numerical Solution and Application. *Materials Science and Engineering A*, 385:157–165, 2004.

[158] B. Sonderegger and E. Kozeschnik. Generalized nearest-neighbor broken-bond analysis of randomly oriented coherent interfaces in multicomponent FCC and BCC structures. *Metallurgical and Materials Transactions A*, 40:499–510, 2009.

[159] B. Sonderegger and E. Kozeschnik. Size dependence of the interfacial energy in the generalized nearest-neighbor broken-bond approach. *Scripta Materialia*, 60:635–638, 2009.

[160] Y.W. Lee and H.I. Aaronson. Anisotropy of coherent interphase boundary energy. *Acta Metallurgica*, pages 539–548, 1980.

[161] R. Kampmann and R. Wagner. Kinetics of Precipitation in Metastable Binary Alloys - Theory and Applications to Cu-1.9at%Ti and Ni-14at%Al. *Decomposition of Alloys : the early stages, Proceedings of the* 2^{nde} *Acta-Scripta Metallurgica Conference*, pages 91–103, 1983.

[162] J. Philibert. *Atom movements diffusion and mass transport in solids.* EDP Sciences, 1995.

[163] Dictra user's guide version 26. Technical report, ThermoCalc AB.

[164] J. Philibert. Diffusion and stresses. *Defect and Diffusion Forum*, 129-130:3–8, 1996.

[165] A. Galdikas and T. Moskalionieve. Modeling of stress induced nitrogen diffusion in nitrided stainless steel. *Surface and Coating Technology*, 205:3742–3746, 2011.

[166] T. Moskalionieve and A. Galdikas. Stress induced and concentration dependent diffusion of nitrogen in plasma nitrided austenitic stainless steeel. *Vacuum*, 86:1552–1557, 2012.

[167] T. Christiansen and M. Somers. Avoiding ghost stress on reconstruction of stress- and composition- depth profiles from destructive X-ray diffraction depth profiling. *Materials Science and Engineering A*, 424:181–189, 2006.

[168] Y. Cao, F. Ernst, and G.M. Michal. Colossal carbon supersaturation in austenitic stainless steels carburized at low temperature. *Acta Materialia*, 51:4171–4181, 2003.

[169] F. Ernst, A. Avishai, H. Kahn, X. Gu, G.M. Michal, and A.H. Heuer. Enhanced carbon diffusion in austenitic stainless steel carburized at low temperature. *Metallurgical and Materials Transactions A*, 40:1768–1780, 2009.

[170] T. Christiansen and M. Somers. Stress and composition of carbon stabilized expanded austenite on stainless steel. *Metallurgical and Materials Transactions A*, 40:1791–1798, 2009.

[171] B-J. Lee. On the stability of Cr carbides. *Calphad*, 16:121–149, 1992.

[172] G.M. Michal, F. Ernst, and A.H. Heuer. Carbon paraequilibrium in austenitic stainless steel. *Metallurgical and Materials Transactions A*, 37:1819–1824, 2006.

[173] N. Agarwal, H. Kahn, A. Avishai, G. Michal, F. Ernst, and A.H. Heuer. Enhanced fatigue resistance in 316L austenitic stainless steel due to low-temperature paraequilibrium carburization. *Acta Materialia*, 55:5572–5580, 2007.

[174] M. Lassus, R. Riviere, and G. Monnier. Chimie minérale - Sur la structure et l'évolution des paramètres cristallins de la solution solide $(Cr, Fe)_7C_3$. *Compte rendus des Séances de l'Académie des Sciences*, 264, 1967.

[175] H.L. Yakel. Atom distributions in Tau-carbide phases: Fe and Cr distributions in $(Cr_{(23-x)}Fe_xC_6)$ with x = 0, 0.74, 1.70, 4.13, and 7.36. *Acta Crystallographica*, 43, 1987.

[176] L.G. Harrison. Influence of dislocations on diffusion kinetics in solids with particular reference to the alkali halides. *Transactions of the Faraday Society*, 57:1191–1199, 1961.

[177] I.N. Sneddon. The relation between load and penetration in the axisymmetric Boussinesq problem for a punch of arbitrary profile. *International Journal of Engineering Science*, 3:47–56, 1965.

[178] M. Dao, N. Chollacoop, K.J. Van Vliet, T.A. Venkatesh, and S. Suresh. Computational modeling of the forward and reverse problems in instrumented sharp indentation. *Acta Materialia*, 49:3899–3918, 2001.

[179] M. Delincé, P.J. Jacques, and T. Pardoen. Separation of size-dependent strengthening contributions in fine-grained Dual-Phase steels by nano-indentation. *Acta Materialia*, 54:3395–3404, 2006.

[180] J.L. Snoek. On the decarburization of steel and related questions. *Physica VIII*, 7:734–744, 1941.

[181] ASTM E112-13 Standard test methods for determining average grain size.

[182] www.jcnabity.com.

[183] G. Martin, C.W. Sinclair, and R.A. Lebensohn. Microscale plastic strain heterogeneity in slip dominated deformation of magnesium alloy containing rare earth. *Materials Science and Engineering A*, 603:37–51, 2014.

[184] L. Allais, M. Bornert, T. Bretheau, and D. Caldemaison. Experimental characterization of the local strain field in a heterogeneous elastoplastic material. *Acta Metallurgica and Materialia*, 42:3865–3880, 1994.

[185] P. Doumalin, M. Bornert, and J. Crépin. Characterisation of the strain distribution in heterogeneous materials. *Mécanique et Industries*, 4:607–617, 2003.

[186] J.W. Hutchinson and K.W. Neale. Influence of strain-rate sensivity on necking under uniaxial tension. *Acta Metallurgica*, 25:839–846, 1977.

[187] Y. Bréchet, G. Canova, and L.P. Kubin. Strain softening, slip localization and propagation: from simulations to continuum modelling. *Acta Materialia*, 44:4261–4271, 1996.

[188] F.B. Pickering. *Physical metallurgy and the design of steel.* Applied Science Publishers LTD., 1978.

[189] W.B. Morrison. The effect of grain size on the stress-strain relationship in low carbon steel. *Trans ASM*, 59:824–846, 1966.

[190] H. Asahi, A. Yagi, and M. Ueno. Effects of strengthening mechanisms on sulfide stress cracking resistance of low strength steels. *ISIJ International*, 33:1190–1195, 1993.

[191] EC2-MS. Simulation numque du soudage, Revêtement des cuves REP. Technical report, EDF SEPTEN.

[192] Projet Durée de vie des cuves REP II - Caractérisations métallurgique et ultrasonore d'une maquette de réparation de virole de cuve - H-T27-2011-02688-FR. Technical report, EDF R&D, 2011.

[193] *Abaqus, Version 6.13, 2013, User's Manual (online version), Providence RI.*

[194] J. Rice and D. Tracey. On the ductile enlargement of voids in triaxial stress fields. *Journal of Mechanics and Physics of Solids*, 17:201–217, 1969.

[195] A. Franklin. Comparison between a quantitative microscope and chemical methods for assessment of non-metallic inclusions. *Journal of the Iron and Steel Institute*, pages 181–186, 1969.

[196] R.A. Farrar, C. Huelin, and R.G. Thomas. Phase transformation and impact properties of type 17-8-2 austenitic weld metals. *Journal of Materials Science*, 20:2828–2838, 1985.

[197] J.J. Smith and R.A. Farrar. Influence of microstructure and composition on mechanical properties of some AISI 300 series weld metals. *International Materials Reviews*, 38:25–51, 1993.

[198] A. Needleman and V. Tvergaard. An analysis of ductile rupture in notched bars. *Journal of Mechanics and Physics of Solids*, 32:461–490, 1984.

[199] M. Gologanu, J-B. Leblond, G. Perrin, and J. Devaux. *Recent extensions of Gurson's model for porous ductile metals.* Continuum Micromechanics Berlin: Springer-Verlag, 1995.

[200] A.A. Benzerga, J. Besson, and A. Pineau. Anisotropic ductile fracture: Part II: Theory. *Acta Materialia*, 52:4639–4650, 2004.

[201] D. Lassance, F. Scheyvaerts, and T. Pardoen. Growth and coalescence of penny-shaped voids in metallic alloys. *Engineering Fracture Mechanics*, 73:1009–1034, 2006.

[202] D. Lassance, D. Fabrègue, F. Delannay, and T. Pardoen. Micromechanics of room and high temperature fracture in 6xxx Al alloys. *Progress in Materials Science*, 52:62–129, 2007.

[203] K.L. Nielsen, T. Pardoen, V. Tvergaard, B. de Meester, and A. Simar. Modelling of plastic flow localisation and damage development in friction stir welded 6005A aluminium alloy using physics based strain hardening law. *International Journal of Solids and Structures*, 47:2359–2370, 2010.

[204] A. Simar, Y. Brechet, B. de Meester, A. Denquin, C. Gallais, and T. Pardoen. Integrated modeling of friction stir welding of 6xxx series Al alloys: Process, microstructure and properties. *Progress in Materials Science*, 57:95–183, 2012.

[205] J.D. Eshelby. The determination of the elastic field of an ellipsoïdal inclusion and related problems. *Proceeding of the Royal Society*, A241:376–396, 1957.

[206] M. Berveiller and A. Zaoui. An extension of the self-consistent scheme to plastically flowing polycrystals. *Journal of Mechanics and Physics of Solids*, 26:325–340, 1979.

[207] A. Pineau and T. Pardoen. *Comprehensive Structural Integrity*, chapter Failure of Metals, pages 686–783. Elsevier, 2008.

[208] G. Huber, Y. Bréchet, and T. Pardoen. Predictive model for void nucleation and void growth controlled ductility in quasi-eutectic cast aluminium alloys. *Acta Materialia*, 53:2739–2749, 2005.

[209] C. Gallais, A. Simar, D. Fabrègue, A. Denquin, G. Lapasset, B. de Meester, Y. Bréchet, and T. Pardoen. Multiscale analysis of the strength and ductility of AA 6056 aluminum friction stir welds. *Metallurgical and Materials Transactions A*, 38:964–981, 2007.

[210] E. Voce. Practical strain-hardening function. *Acta Metallurgica*, 51:219–226, 1955.

[211] U.F. Kocks and H. Mecking. Physics and phenomenology of strain hardening: the FCC case. *Progress in Materials Science*, 48:171–273, 2003.

[212] E. Nes. Modelling of work-hardening and stress saturation in FCC metals. *Progress in Materials Science*, 41:129–193, 1998.

[213] S.A. Argon and J. Im. Separation of second phase particles in spheroidized 1045 steel, Cu-0.6pctCr alloy and maraging steel in plastic straining. *Metallurgical Transactions A*, 6:825–837, 1975.

[214] P. Bocquet, D. Buisine, and L. Durand-Roux. Les facteurs métallurgiques de la ténacité de l'acier de cuve. *Endommagement des matériaux dans les centrales nucléaires u pressurisée, Matériaux*, pages 121–152, 1997.

[215] G. Martin, S.K. Yerra, Y. Bréchet, M. Véron, J.D. Mithieux, B. Chehab, L. Delannay, and T. Pardoen. A macro- and micromechanics investigation of hot cracking in duplex steels. *Acta Materialia*, 60:4646–4660, 2012.

[216] S.K. Yerra, G. Martin, M. Véron, Y. Bréchet, J.D. Mithieux, L. Delannay, and T. Pardoen. Ductile fracture initiated by interface nucleation in two-phase elasto-plastic systems. *Engineering Fracture Mechanics*, 102:77–100, 2013.

[217] F.D. Fischer, J. Svoboda, and E. Kozeschnik. Interstitial diffusion in systems with multiple sorts of traps. *Modelling and simulation in Materials Science and Engineering*, 21, 2013.

[218] E. Soppa, P. Doumalin, P. Binkele, T. Wiesendanger, M. Bornert, and S. Schmauder. *Computational Materials Science*, 21:261–275, 2001.

[219] K. Enakoutsa and J-B. Leblond. Numerical implementation and assessment of the glpd micromorphic model of ductile rupture. *European Journal of Mechanics - A/ Solids*, 28:445–460, 2009.

[220] J-M. Bergheau, J-B. Leblond, and G. Perrin. A new numerical implementation of a second-gradient model for plastic porous solids, with an application to the simulation of ductile rupture tests. *Computer Methods in Applied Mechanics and Engineering*, 268:105–125, 2014.

[221] M. Blat. Etude métallurgique de soudures hrogs réalisées par dépôt électrode sur un acier ferritique (10 CD 9-10) de différents alliages austénitiques (acier inoxydable 24-12 et alliages base nickel). Master's thesis, CNAM, 1989.

[222] M. Bornert. *Morphologie microstructurale et comportement mnique; caractérisations expérimentales, approche par bornes et estimations autocohntes généralisées.* PhD thesis, Laboratoire de Mécanique des Solides, Ecole Polytechnique, 1996.

[223] P. Doumalin. *Microextensométrie locale par corrélation d'images numériques.* PhD thesis, Laboratoire de Mécanique des Solides, Ecole Polytechnique, 2000.

Appendices

Appendix A

Weld pool boundary layer

In the present appendix, the different steps for the calculation of the thickness of the solutal boundary layer will be explained in details. We consider the fluid flow in the weld pool when surfacing a 18MND5 plate by SAW. As the liquid pool is covered by a blanket of granular flux, the top surface is not free and so there is no Marangoni shear stress acting on it. The dominant force is the electromagnetic one [66]. The weld pool geometry is visible on the macrographs of Figure A.1 and is schematically represented on Figure A.2.

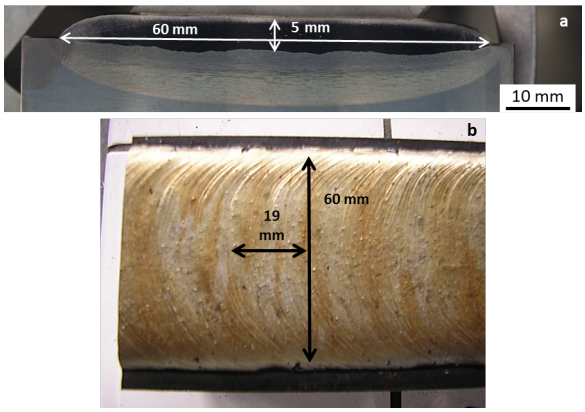

Figure A.1: Macrographs of the mono-layer weld: a- longitudinal section; b- top view.

A.1 Electromagnetic force

The weld pool surface shape was approximated by an ellipse and the current density j through it was calculated by:

$$j = \frac{I}{S} = \frac{I}{\Pi ab} = 2 \times 10^5 \ \ A/m^2 \tag{A.1}$$

where I is the current intensity (= 750 A), S the top surface of the weld pool, a and b the minor and major axes of the ellipse equal to 20 and 60 mm respectively. The magnitude of the magnetic field B is given by:

$$B = \frac{\mu_0 I}{C} = 3.5 \times 10^{-3} \ \ T \tag{A.2}$$

where μ_0 is the vacuum magnetic permeability ($= 1.256 \times 10^{-6}$ H/m) and C the circumference of the ellipse (≈ 268 mm). The electromagnetic force $\vec{F_M}$ is the cross product of the current density and the electromagnetic field and its norm can thus be evaluated by:

$$\left\|\vec{F_M}\right\| = j \times B = 700 \ \ N/m^3 \tag{A.3}$$

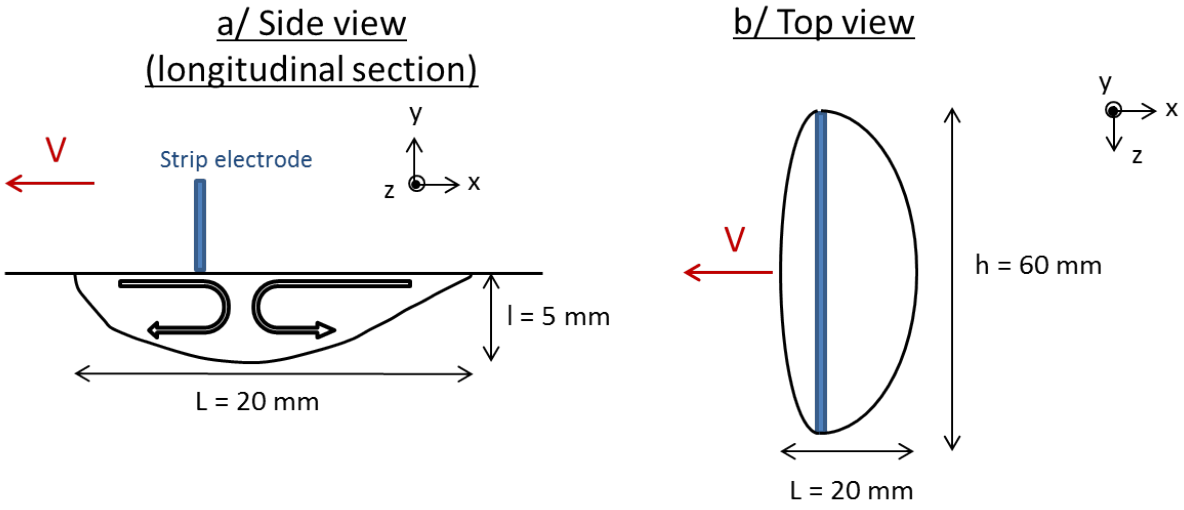

Figure A.2: Schematic representation of the weld pool geometry: a- side view, b- top view.

A.2 Fluid velocity within the weld pool

Neglecting the viscous forces and applying the Navier-Stokes equation in the stationary regime allows expressing the previously calculated electromagnetic force as a function of the fluid velocity U, the density of the liquid steel ρ and a characteristic dimension of the weld pool L:

$$\left\|\vec{F_M}\right\| = \frac{\rho U^2}{L} \tag{A.4}$$

Depending of the choice of the characteristic length L (20 or 60 mm), it leads to a steady-state velocity between 47 and 81 mm/s.

A.3 Hydrodynamic and diffusive boundary layers

The hydrodynamic boundary layer is a thin layer in contact with a solid in which the effects of viscosity are significant. As a consequence the fluid velocity decreases when approaching the bottom of the weld pool, as shown on the schematic velocity profile of Figure A.3-a. An order of magnitude for the thickness of this layer is given by [69]:

$$\delta_v \approx \sqrt{\frac{\nu L}{U}} \tag{A.5}$$

where ν is the kinematic viscosity of liquid steel ($= 3.9 \times 10^{-7} \ m^2/s$ [70]) and L a characteristic length of the solid present in the liquid flow. Depending of the value chosen for this characteristic

length (20 or 60 mm), the hydrodynamic boundary layer can be estimated between 408 and 536 μm.

As shown on the schematic of Figure A.3-b, the diffusive boundary layer, in which convection is negligible and mixing of species occurs mainly by diffusion, is included within the hydrodynamic one. Solute transport in the liquid pool is governed by Equation 2.2 which includes both diffusion and convection:

$$\frac{\partial C}{\partial t} = D\nabla^2 C - \vec{U}.\vec{\nabla C} \tag{A.6}$$

where C is the solute content and U the velocity of the fluid. If we consider the permanent regime for solute transport ($\frac{\partial C}{\partial t} = 0$), diffusive and convective terms have to be equal leading to:

$$D\frac{C}{\delta_c^2} = U_1\frac{C}{L} \tag{A.7}$$

where U_1 is the fluid velocity at the top of the diffusive boundary layer where the convective and diffusive contributions are equal. As shown on the schematic of Figure A.3-b, the velocity profile within the hydrodynamic boundary layer was considered as linear which leads to the following expression for the velocity U_1 for $y = \delta_c$:

$$U_1 = \frac{\delta_c U}{\delta_v} \tag{A.8}$$

Combining Equations A.7 and A.8 allows calculating an order of magnitude for the thickness of the diffusive boundary layer:

$$\delta_c = (\frac{DL}{U} \times \delta_v)^{1/3} \tag{A.9}$$

For L between 20 and 60 mm, the diffusive boundary layer is estimated between 64 and 84 μm. This order of magnitude is in good agreement with the width of the zone with compositional gradients measured by WDS on a transverse section of the weld (see Section 2.3.2).

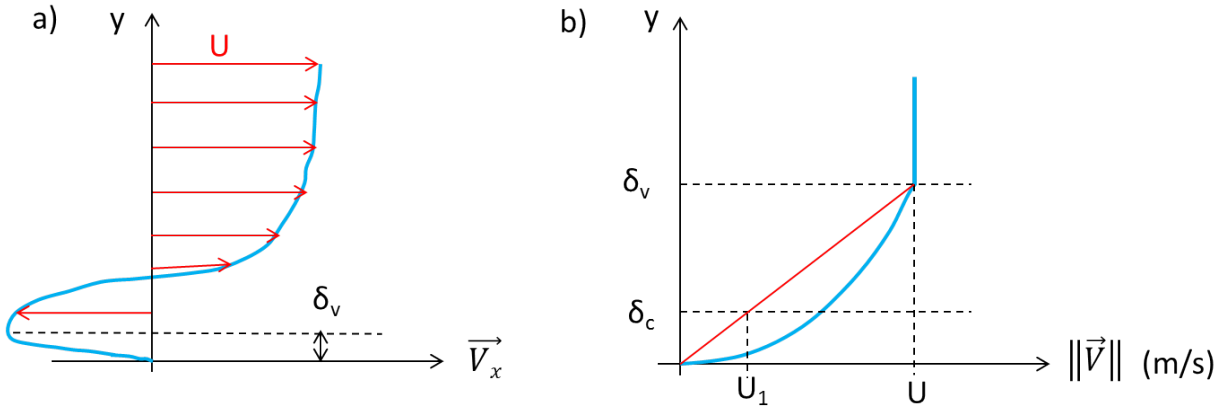

Figure A.3: a- View cut (plane y-z) within the weld pool showing the fluid velocity field along the x-axis. b- Enlargement near the weld pool bottom allowing to define the hydrodynamic δ_v and diffusive δ_c boundary layers.

Appendix B

Thermal ageing of the dissimilar weld

B.1 Introduction

As mentioned in Section 1.2, two of the heat-treated samples were subjected to an accelerated isothermal aging treatment at 400°C: one specimen (id.:248V1) for 5000 hours and the other one (id.:248V2) for 10000 hours. Although the service temperatures are lower ($T_{max} = 330$°C), 400°C was chosen in order to represent a long-term operation of several decades by a heat-treatment of reasonable duration. These two specimens were compared with the post-weld heat-treated one in terms of both microstructural and mechanical evolutions. In the context of the sodium-cooled fast reactor Super-Phénix, ageing treatments between 100 and 3000 hours at 600°C had already been studied for welds between the ferritic steel 10CD9-10 and the austenitic 309L stainless steel [221]. For 3000 h at 600°C, a decarburization of the ferritic steel over 1200 μm together with a carburization of the 309L over 600 μm were measured by WDS. These affected zones were significantly reduced by replacing the austenitic filler metal by a nickel-base alloy (alloys 82 and 182).

The goal of this study was to answer to the following questions: Does the carbon diffusion from the low-alloy base metal to the stainless steel weld metal go on after the post-welding heat-treatment at the low temperatures of service? Has thermal aging at 400°C any influence on the microstructures observed on both sides of the welding interface? Does the assembly encounter a degradation of its mechanical properties?

B.2 Microstructural observations

As shown on the micrographs of Figure B.1, the aged samples were first observed by optical microscopy after a two-step etching procedure with first Nital and then electro-chromic solutions. The resulting microstructures are very similar to the one of the sample after post-welding heat-treatment displayed on Figure 3.2-b. The dark region which encompasses both the martensite and the carburized austenite did not extend further into the weld metal. The width of the decarburized layer with large ferritic grains was measured at 25 different locations every 3 mm along the fusion line for each aging condition. The results have been compiled into Table B.1. Only a slight increase of the width of the ferritic zone was measured for the sample aged for 5000 h in comparison with the

one only post-weld heat-treated. No further increase was observed for 5000 supplementary hours at 400°C. These variations do not seem meaningful since they are included within the scatter of the experimental measurements.

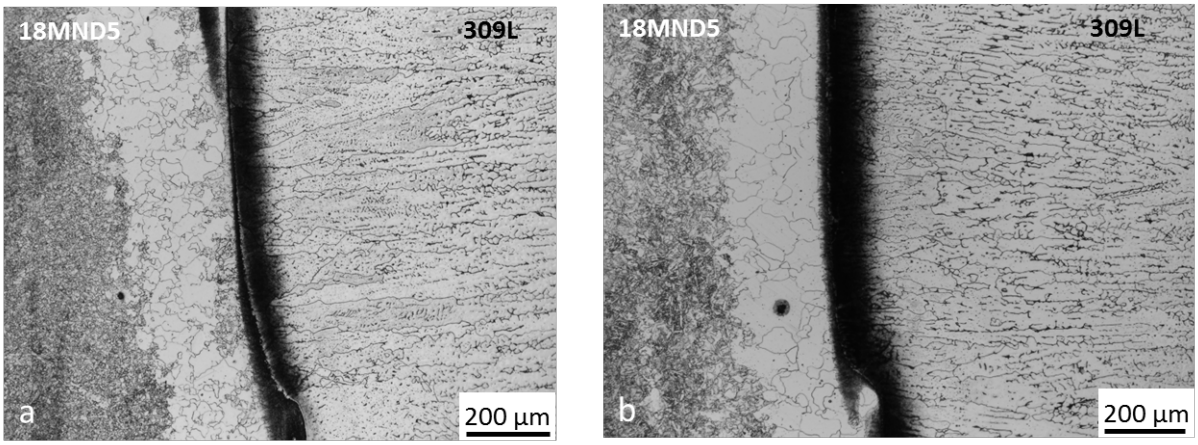

Figure B.1: Optical micrograph of the dissimilar interface after a two-step etching : Nital (5% HNO_3 in methyl alcohol) and electro-chromic (10 g CrO_3 in H_2O, 6V, $1A/cm^2$). Aged for a- 5000 h at 400°C and b- 10000 h at 400°C.

Table B.1: Evolution of the width of the decarburized region subsequent to aging at 400°C.

	Width of the ferritic decarburized layer			
Aging time at 400°C	**Mean**	**Standard deviation**	**Max.**	**Min.**
0 h	194 μm	52 μm	259 μm	83 μm
5000 h	249 μm	55 μm	354 μm	151 μm
10000 h	235 μm	46 μm	323 μm	114 μm

The measurements of the carbon content through the weld by WDS confirmed the absence of significant long-range diffusion at 400°C (see Figure B.2). The carbon profiles on the samples with and without aging treatment were performed in regions with a similar martensite's width (around 35 μm) and led to practically superimposed results. Neither any extension of the low carbon content region on the ferritic side nor any continuation of the carbon diffusion within the austenitic weld could be detected.

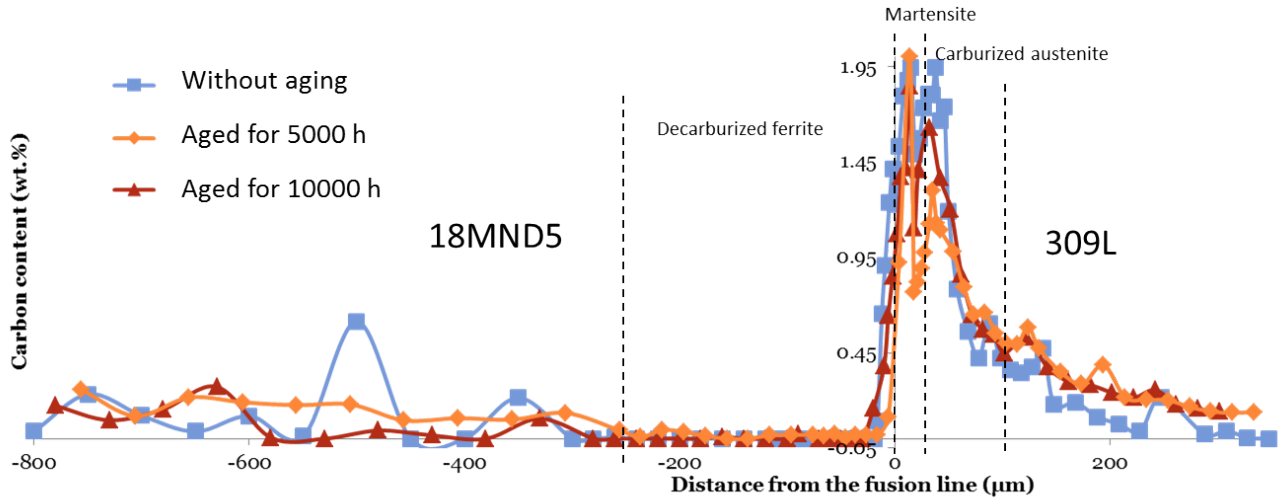

Figure B.2: Carbon content as a fonction of the distance from the fusion line measured by WDS on aged and non-aged samples.

Then the precipitates were observed by SEM and TEM. Although the previously described WDS measurements did not show any significant long-range diffusion of carbon through the weld at 400°C, the precipitates formed during the post-welding heat-treatment might evolve by diffusion of elements over short distances, that is to say from the surrounding matrix to the precipitates and vice versa. New precipitates might nucleate and the existing ones might grow or dissolve during the isothermal aging treatment, which would have an influence on the local mechanical hardening. However such changes were not observed, neither in the martensitic layer nor in the austenitic weld metal. As shown on the SEM images of Figure B.3, carbides similar in size and density were observed on the subgrain boundaries and within the laths in the aged samples as well as in the non-aged one. TEM observations such as the one of Figure B.4-a confirmed that the carbides dimensions (around 150 nm) did not significantly evolve during aging. As in the post-weld heat-treated conditions, the carbides in the 70 μm of carburized austenite display after aging a cubic shape and a regular alignment along particular directions of the matrix (see Fig. B.4-b in the case of an aging time of 5000 hours). Their dimensions (mean diameter around 50 nm) do not significantly evolve at 400°C. Carbides that formed at the δ - γ interfaces during the post-welding heat-treatment were also investigated after aging. The ferrite decomposition initiated at 610°C did not continue at lower temperatures and therefore the fraction of these carbides at the phase interfaces was maintained constant during the aging treatment.

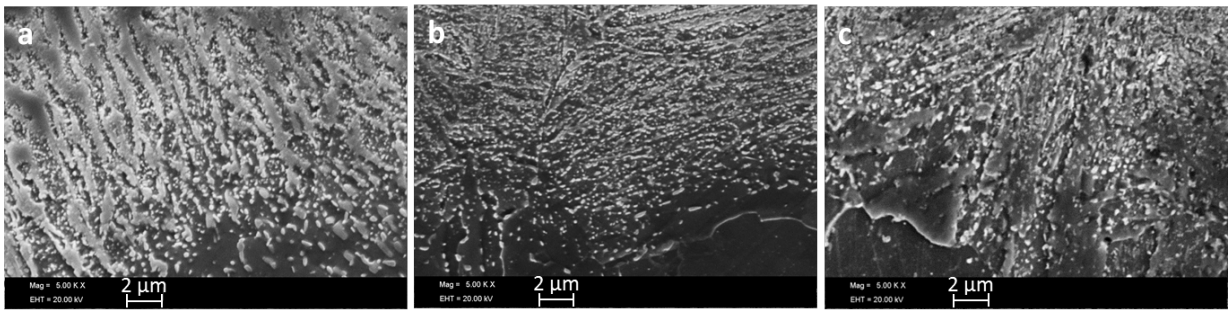

Figure B.3: SEM images of the carbides in the martensitic layer after Nital etching in a- the non-aged, b- aged for 5000 h and c- aged for 10000 h conditions.

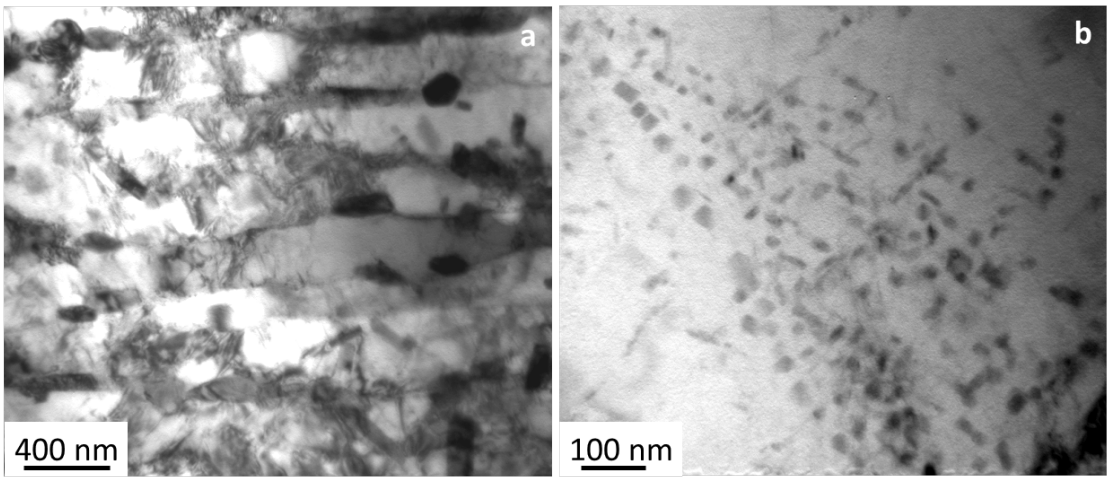

Figure B.4: TEM images of the carbides in a sample aged for 5000 h at 400°C a- in the martensitic layer b- in the carburized austenite.

B.3 Hardness measurements

Both micro and nano-hardness measurements were performed on the aged samples. For the Vickers micro-hardness profiles of Figure B.5-a, a 100 g load was used (same conditions as in Figure 5.1) which allowed determining the width of both softened and hardened regions. Despite the intrinsic variability that exists within a given weld, the results for both aged and non-aged samples were similar and did not reveal any evolution of the local mechanical properties.

In order to probe the mechanical behavior at a smaller scale, nanoindentation was also used in two different ways: either as profiles (Figure B.5-b) or as individual indentations (Figure B.6). The first ones require a reduced step (4 μm) together with a small indentation depth (200 nm) in order to track the evolutions that may occur over short distances. The individual indentations were performed within the different regions of the weld for the three conditions of interest. They allowed a larger indentation depth (500 nm) and consequently a more accurate determination of the bulk Young modulus and hardness without being disturbed by any surface artifact. Both methods led to an equivalent conclusion: aging at 400°C did not produce any significant effect on the local

mechanical properties in the different regions of the dissimilar weld. This result is in agreement with the fact that no microstructural transformation was found at the different scales of observation. The slight softening of the decarburized region measured by the profile performed on the sample aged for 10000 hours was not considered as significant as it was not confirmed by both micro-indentation and the individual nano-indents. Moreover the two hardness peaks detected by nanoindentation in the 309L of the aged sample correspond to the profile crossing austenitic grain boundaries that are known to be enriched in carbon as they constitute shortcuts for diffusion.

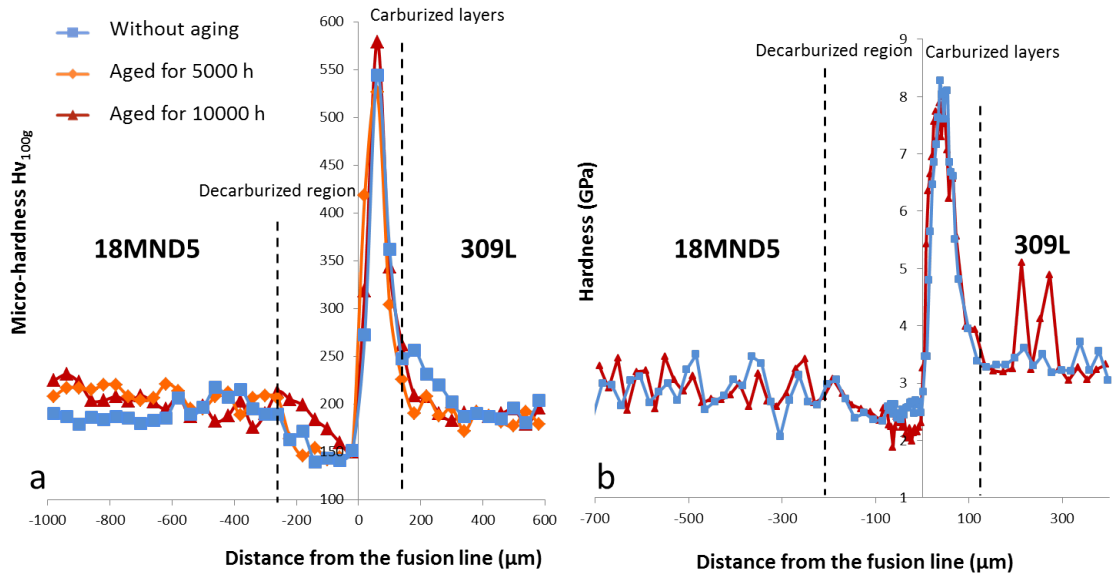

Figure B.5: Hardness evolution during aging at 400°C measured by a- Vickers micro-indentation, b- nanoindentation.

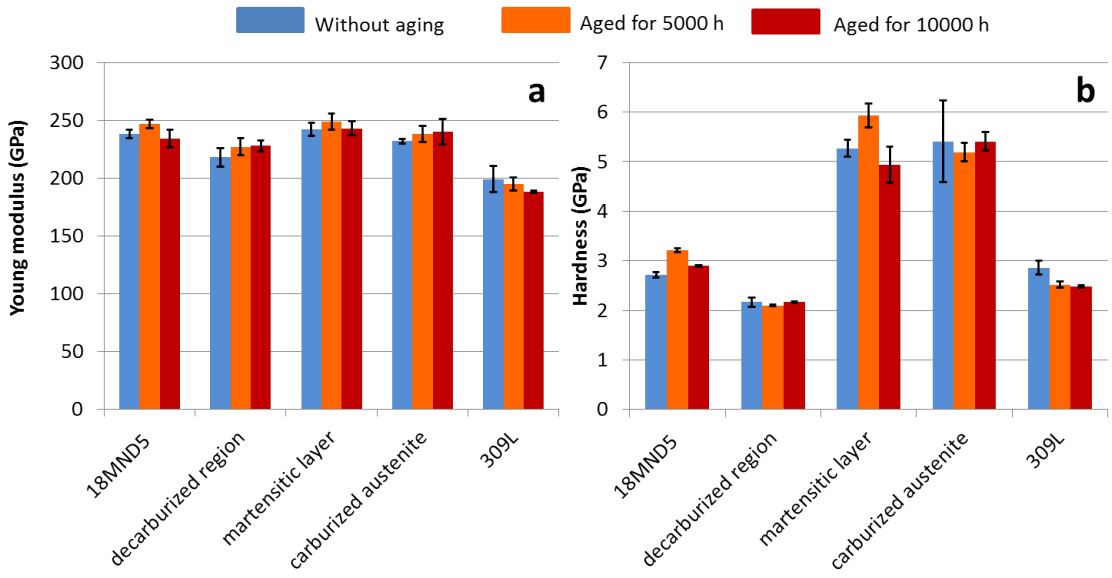

Figure B.6: Nanoindentation measurements on aged and non-aged samples: a- Young modulus b- Hardness.

B.4 Conclusion

All microstructural and mechanical investigations performed on samples aged for 5000 and 10000 hours at 400°C showed that no significant evolution took place in comparison to the post-weld heat-treated condition. Observations at various scales in the different regions of interest combined with hardness measurements by micro- and nanoindentation revealed a high similarity between the three states of the weld that have been studied. Even if this study should be complemented by mechanical testing at a larger scale (for example toughness with a pre-crack in the decarburized layer), it seems judicious to consider the state of the weld after post-weld heat-treatment as representative of the dissimilar interface in normal service conditions. Indeed all the phase transformations which impact microstructure and local mechanical properties on both sides of the fusion line were found to take place during the post-weld heat-treatment at 610°C and not to go on at a temperature of 400°C. That is why this PhD work was dedicated to the dissimilar weld in the post-weld heat-treated condition to accurately quantify and understand the microstructural changes that occur during the heat-treatment and that will deeply modify the 18MND5-309L interface before the nuclear power plant starts operating.

Appendix C

Tensile specimens dimensions

C.1 Macro-samples

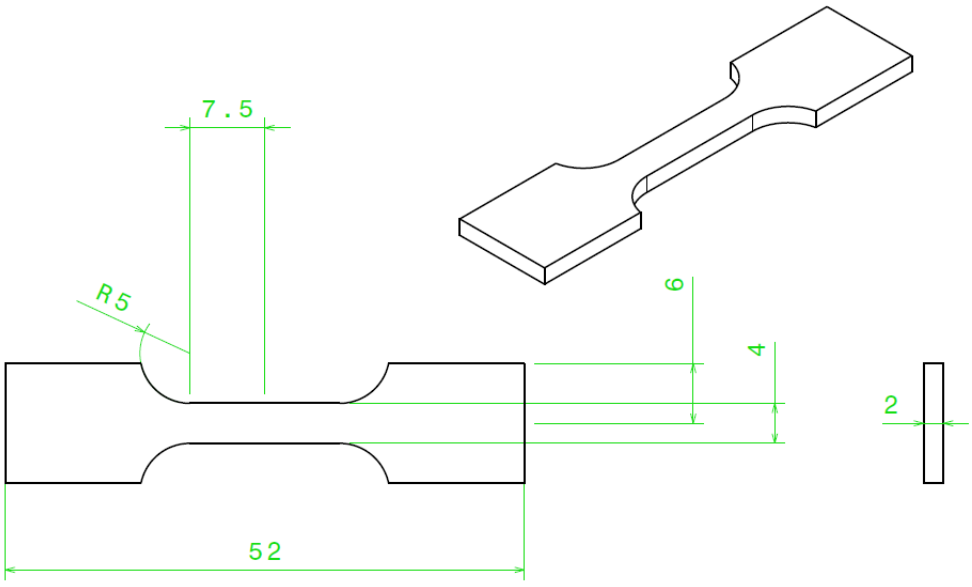

C.2 Micro-samples

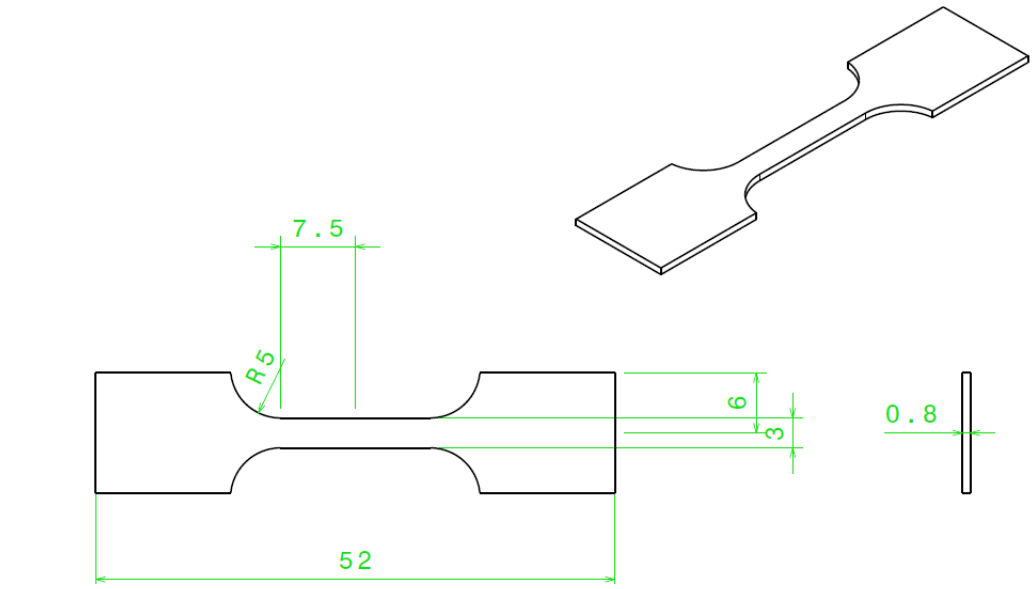

C.3 SEM samples

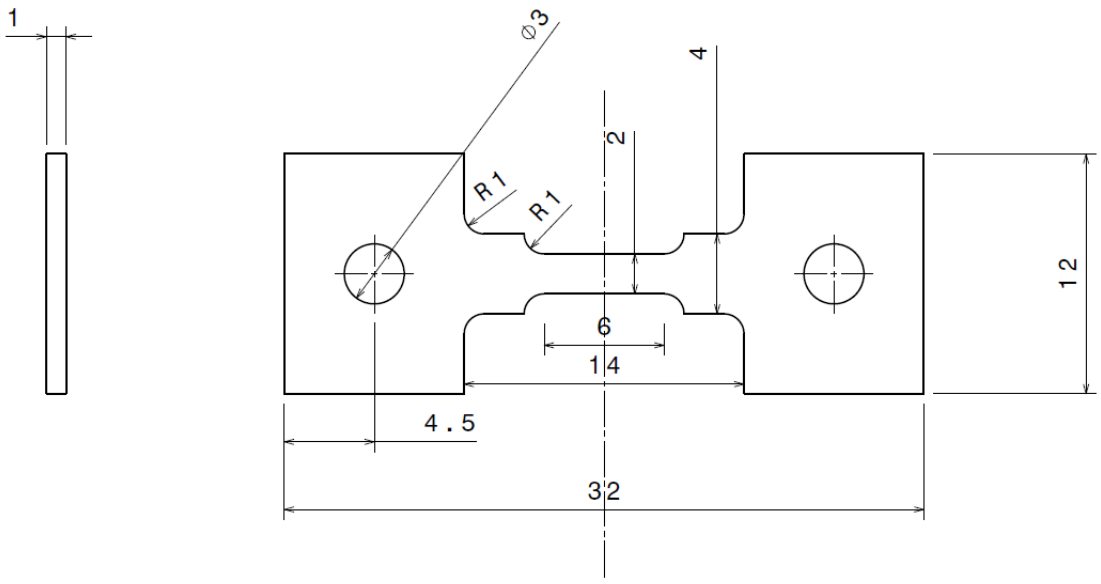

C.4 SEM samples with notch

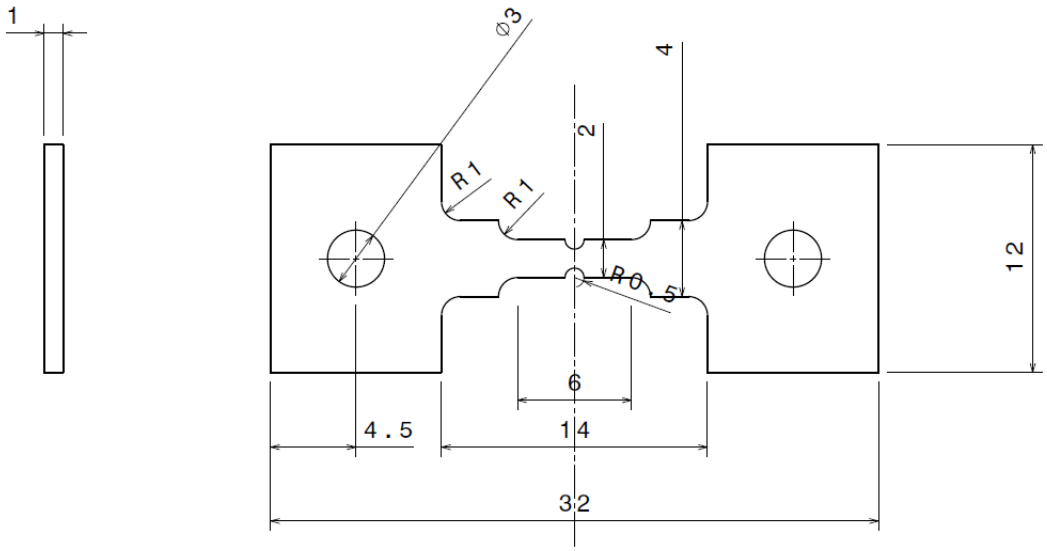

Appendix D

Strain computation

This appendix aims at providing details about the computation of the different components of strain by the CorrelManuV software that was used in this study for DIC. All the calculations presented below can be found in references [184] and [222].

D.1 Definition of the local transformation gradient

$\underline{X}$ denotes the position in a reference orthonormal coordinate system of a material point in the initial configuration of a three dimensional continuous medium and $\underline{x}$ its position in the same reference system in the deformed configuration. The gradient of the mechanical transformation $\overline{\overline{F}}$ at $\underline{X}$ is given by:

$$\overline{\overline{F}} = \frac{\partial \underline{x}}{\partial \underline{X}} \tag{D.1}$$

where $\underline{X} = \begin{pmatrix} X \\ Y \\ Z \end{pmatrix}$

and $\underline{x} = \begin{pmatrix} x \\ y \\ z \end{pmatrix}$

The displacement tensor can be expanded as follows:

$$\overline{\overline{F}} = \begin{bmatrix} F_{11} & F_{12} & F_{13} \\ F_{21} & F_{22} & F_{23} \\ F_{31} & F_{32} & F_{33} \end{bmatrix} \tag{D.2}$$

In the CorrelManuV software developed by Bornert and Doumalin [223], the in-plane components of the local transformation gradient tensor (F_{11}, F_{22}, F_{12} and F_{21}) are calculated at each microgrid intersection. Additional assumptions need to be made to estimate the unknown gradient components (F_{13}, F_{23}, F_{31}, F_{32} and F_{33}):

1. Direction 3 (the one orthogonal to the image plane) is a principal direction for the transformation.

2. There is no rotation outside the image plane $(\underline{e_1}, \underline{e_2})$. Thus $F_{i3} = F_{3i} = 0$ for $i = [1; 2]$.

3. In the present study the hypothesis of incompressibility (that is to say no volume change during deformation) was chosen to calculate the F_{33} component. Let F_1, F_2 and F_{33} be the eigenvalues of the gradient tensor:

$$\begin{aligned} det(\overline{\overline{F}}) &= F_1 F_2 F_{33} = 1 \\ F_{33} &= \tfrac{1}{F_1 F_2} \end{aligned} \tag{D.3}$$

D.2 Computation of the in-plane components of the logarithmic strain

In the present study, the logarithmic definition of the strain was chosen as it is the one conventionally used by the metallurgists. The displacement gradient may be decomposed into a rigid-body rotation tensor $\overline{\overline{R}}$ and a symmetric stretch tensor $\overline{\overline{U}}$:

$$\overline{\overline{F}} = \overline{\overline{R}}.\overline{\overline{U}} \tag{D.4}$$

$\overline{\overline{R}}$ gives the in-plane rotation angle of the transformation. The stretch tensor $\overline{\overline{U}}$ can be diagonalized in an orthogonal base as:

$$\overline{\overline{U}} = \overline{\overline{Q^t}}.\overline{\overline{D}}.\overline{\overline{Q}} \tag{D.5}$$

where $\overline{\overline{D}}$ is a diagonal tensor, $\overline{\overline{Q}}$ a tensor giving the orientation of the principal directions of the stretch and $\overline{\overline{Q^t}}$ the transpose tensor of $\overline{\overline{Q}}$. The logarithmic strain tensor can then be computed from Equation D.6:

$$\overline{\overline{\epsilon^{log}}} = \overline{\overline{Q^t}}.ln\overline{\overline{D}}.\overline{\overline{Q}} \tag{D.6}$$

$$\text{where } \overline{\overline{Q}} = \begin{bmatrix} cos(\theta) & sin(\theta) & 0 \\ -sin(\theta) & cos(\theta) & 0 \\ 0 & 0 & 1 \end{bmatrix}$$

$$\text{and } \overline{\overline{D}} = \begin{bmatrix} F_1 & 0 & 0 \\ 0 & F_2 & 0 \\ 0 & 0 & F_3 \end{bmatrix}$$

By developing Equation D.6, one gets the expression for the logarithmic strain tensor:

$$\overline{\overline{\epsilon^{log}}} = \begin{bmatrix} \ln F_1 \cos^2(\theta) + \ln F_2 \sin^2(\theta) & \sin(\theta)\cos(\theta)\ln(F_1/F_2) & 0 \\ \sin(\theta)\cos(\theta)\ln(F_1/F_2) & \ln F_1 \sin^2(\theta) + lnF_2 \cos^2(\theta) & 0 \\ 0 & 0 & \ln F_3 \end{bmatrix} \tag{D.7}$$

The principal axes of the symmetric stretch tensor $\overline{\overline{U}}$ are those of $\overline{\overline{F}}$. Let λ_i be the eigenvalues of $\overline{\overline{U}}$. The logarithmic deformation tensor has the same principal axes as $\overline{\overline{U}}$ and its eigenvalues are $\ln(\lambda_i)$. The equivalent Von Mises strain can then be calculated thanks to Equation D.8:

$$\epsilon_{eq}^{VonMises} = \sqrt{\frac{2}{3}(\epsilon_{11}^2 + \epsilon_{22}^2 + \epsilon_{33}^2 + 2\epsilon_{12}^2)} \tag{D.8}$$

D.3 Average strain over a domain

The previously described method cannot be applied directly to compute the local strains. Indeed the displacements are only known in a discrete way through the grid intersections, so that their local derivatives can not be computed exactly. For overcoming this issue, the local transformation gradient at a given grid intersection p is computed as the average of the true local gradient over a small volume Ω_p around the grid intersection. The chosen volume is a cylinder with its axis orthogonal to the surface of the sample, his height e arbitrarily small and a polygonal upper surface Σ_p whose vertices are neighbors of the considered grid intersection (see Figure D.1). Let $\partial\Sigma_p$ be the boundary of Σ_p, S_{Σ_p} its area and $\underline{n}_{\Sigma_p}$ its normal. Σ_{p^-} is the lower surface of the cylinder.

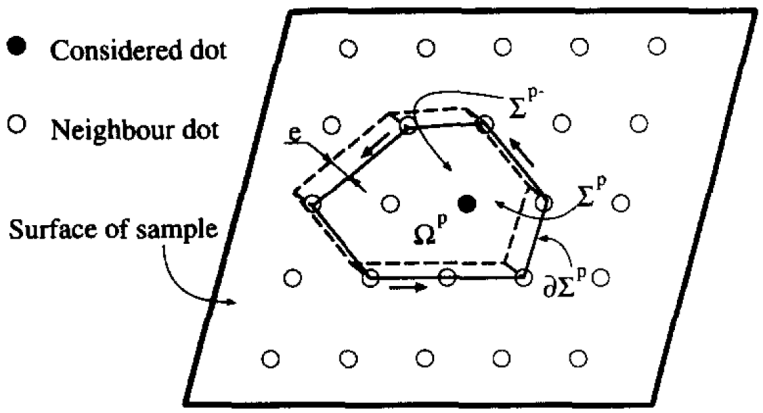

Figure D.1: Averaging volume for local strains computation [184].

The average transformation gradient over Ω_p is given by:

$$\left\langle \overline{\overline{F}} \right\rangle_{\Omega_p} = \frac{1}{V_{\Omega_p}} \int_{\Omega_p} \overline{\overline{F}} dV_{\Omega_p} \tag{D.9}$$

The previous volume integral may be transformed into a surface integral according to Green's formula:

$$\left\langle \overline{\overline{F}} \right\rangle_{\Omega_p} = \frac{1}{V_{\Omega_p}} \int_{\partial\Omega_p} \underline{x} \otimes \underline{n} ds \tag{D.10}$$

The detailed derivation of F_{xx}, F_{xy}, F_{yx} and F_{yy} from Equation D.10 can be found in [184] and leads to:

$$\begin{cases} F_{xx} = \frac{1}{2S_{\Sigma_p}} . \sum_{q=1}^{N} (x^q + x^{q+1})(Y^{q+1} - Y^q) \\ F_{xy} = \frac{1}{2S_{\Sigma_p}} . \sum_{q=1}^{N} -(x^q + x^{q+1})(X^{q+1} - X^q) \\ F_{yx} = \frac{1}{2S_{\Sigma_p}} . \sum_{q=1}^{N} (y^q + y^{q+1})(Y^{q+1} - Y^q) \\ F_{yy} = \frac{1}{2S_{\Sigma_p}} . \sum_{q=1}^{N} -(y^q + y^{q+1})(X^{q+1} - X^q) \end{cases} \tag{D.11}$$

The area of the polygon S_{Σ_p} may be computed as:

$$S_{\Sigma_p} = \frac{1}{2} . \sum_{q=1}^{N} \begin{vmatrix} X^n & X^{n+1} \\ Y^n & Y^{n+1} \end{vmatrix} \tag{D.12}$$

The previous summations are performed over the N neighbors and depend on the choice of the surface of integration Σ_p. The CorrelManuV software includes several possible choices for Σ_p (see Figure D.2). "Scheme a" has the smallest possible averaging surface, but it is not centered on the considered grid intersection. "Scheme b" has the smallest centered averaging surface. "Schemes c and d" have larger averaging surfaces, so that they may smooth out local strain heterogeneities but their accuracy is better. Note that when the considered grid intersection is close to the edge of the region of interest, these schemes must be truncated to the available neighbor grid intersections. In the present study, "Scheme c" was chosen for the local strain calculations.

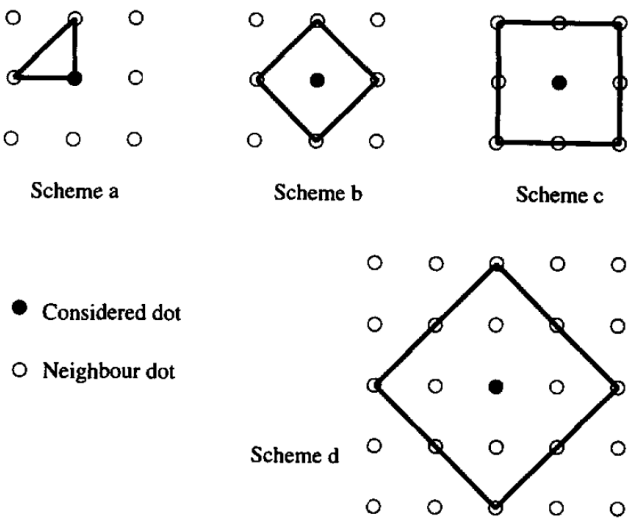

Figure D.2: Several possible integration schemes [184].

Appendix E

Strain components measured by DIC

E.1 In-plane shear strain ϵ_{12}

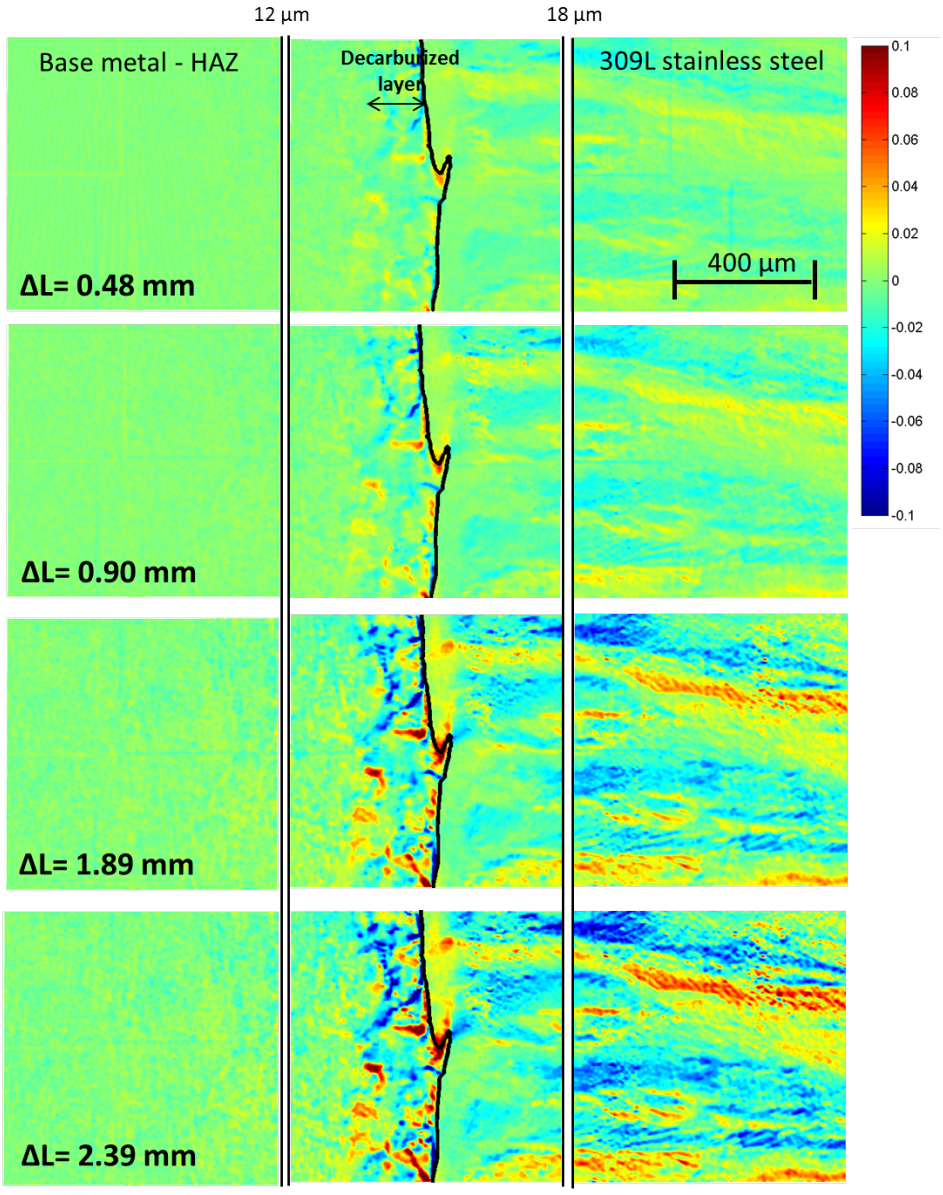

E.2 Strain perpendicular to the tensile direction ϵ_{22}

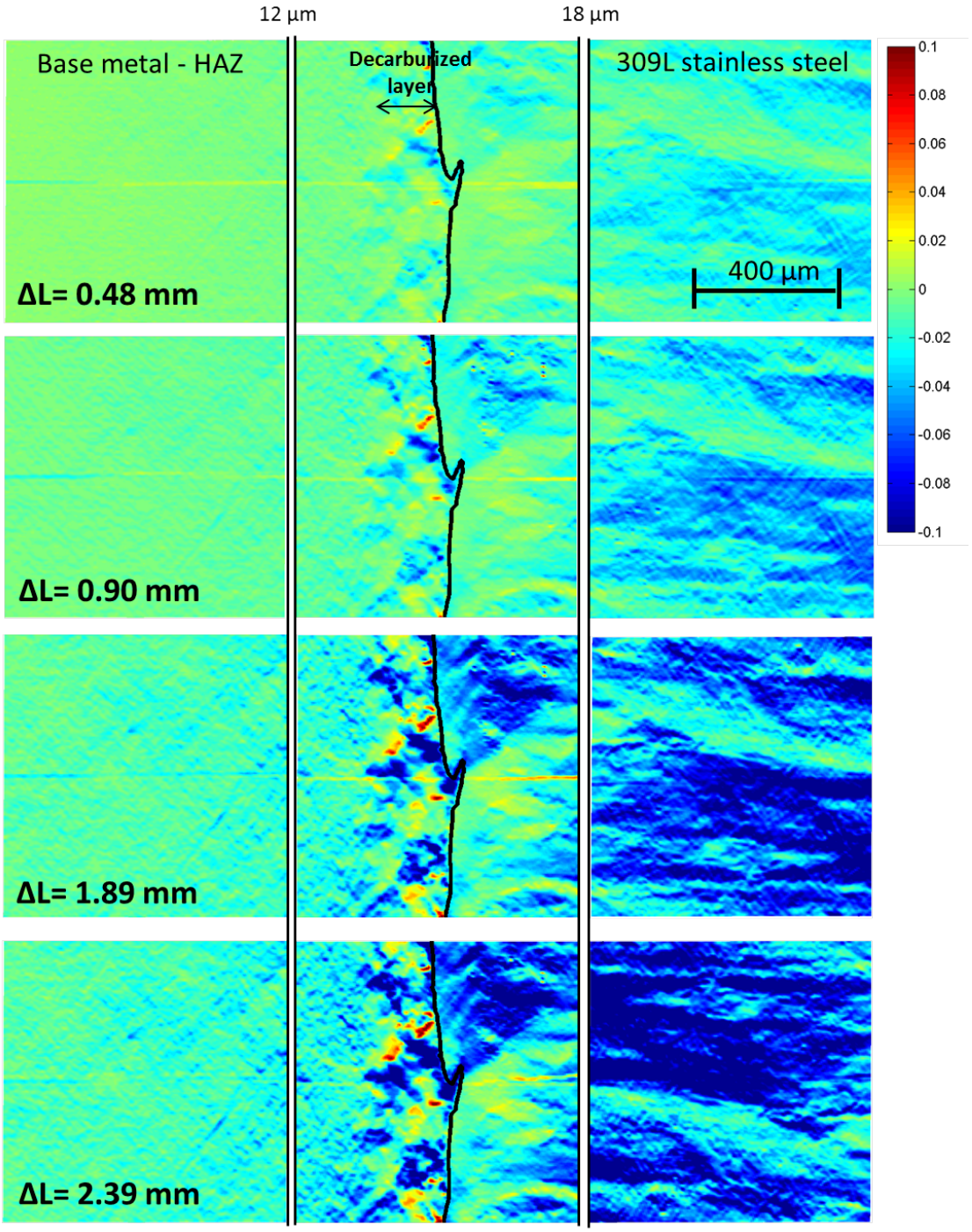

E.3 Equivalent Von Mises strain

$$\epsilon_{eq} = \sqrt{\frac{2}{3}(\epsilon_{11}^2 + \epsilon_{22}^2 + \epsilon_{33}^2 + 2\epsilon_{12}^2)}$$

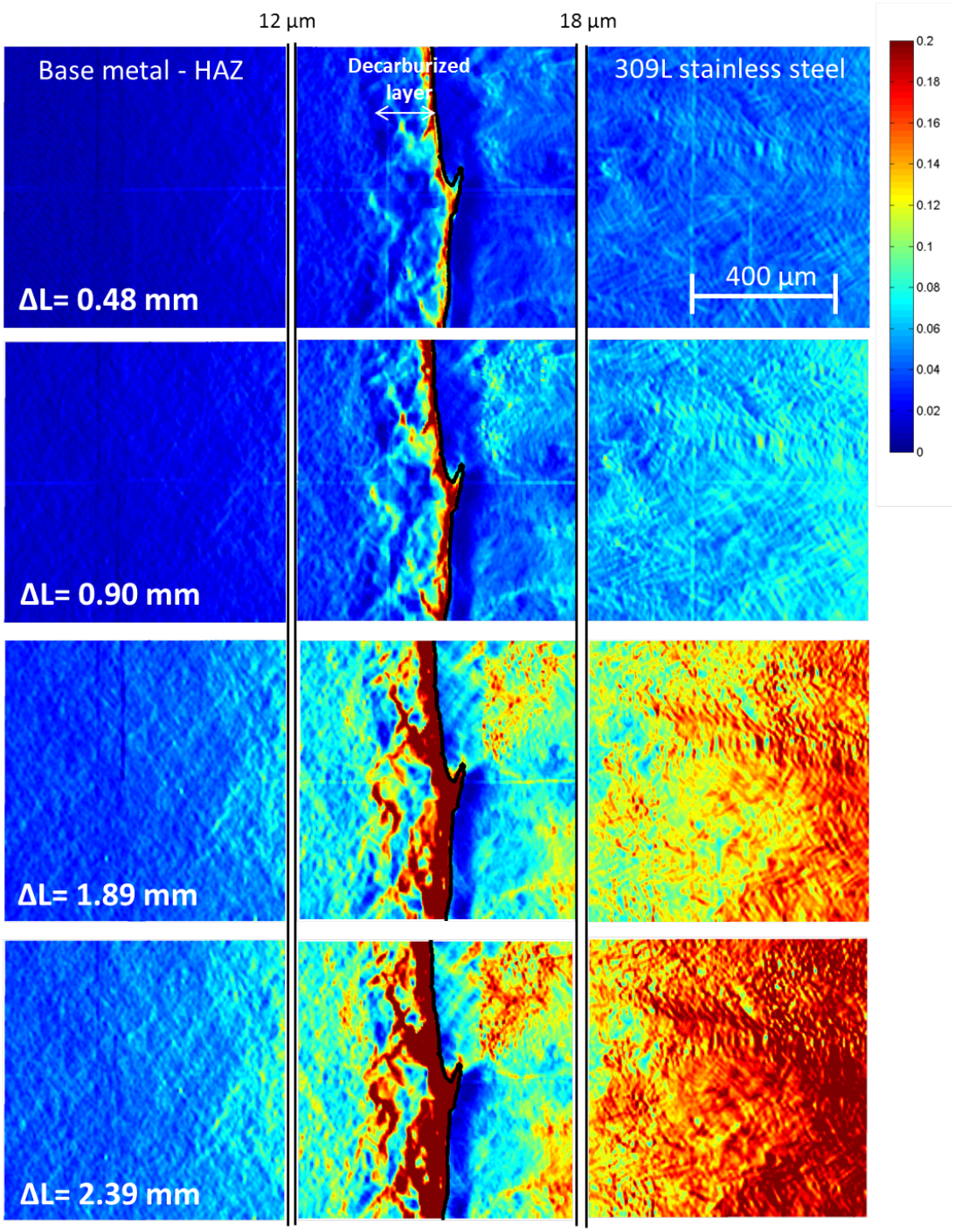

Résumé :
Les liaisons bimétalliques entre acier faiblement allié et acier inoxydable sont nombreuses au sein des réacteurs nucléaires français où elles assurent la connexion entre les principaux composants et les tuyauteries du circuit primaire. Le revêtement interne de cuve réalisé par soudage feuillard-flux est un autre cas de soudure dissimilaire dont le rôle est d'assurer une bonne protection contre la corrosion. Ce travail de thèse a notamment pour but de comprendre la genèse des microstructures complexes se formant à l'interface entre les deux aciers pendant le soudage. Il étudie d'autre part leur évolution durant le traitement thermique post-soudage à 610°C ainsi que les conséquences de ces transformations sur le comportement mécanique du joint soudé. Partant du métal de base, on rencontre successivement une fine bande de martensite, une zone purement austénitique puis la microstructure biphasée δ/γ de l'acier inoxydable. Des techniques de microscopie (MEB, EDS, EBSD) combinées à des calculs thermo-cinétiques (modèle de Scheil-Gulliver, surfusion en pointe de dendrite) ont permis d'expliquer le gradient de microstructure et les raisons des transitions de phases observées. Au cours du traitement thermique de détensionnement à 610°C, le gradient de potentiel chimique du carbone à travers l'interface de fusion cause la dissolution de la cémentite et la croissance des grains du côté faiblement allié. On observe également la diffusion du carbone à travers l'interface et la précipitation de carbures riches en Cr dans le liseré martensitique et la zone austénitique. Une caractérisation détaillée des profils de composition et de la précipitation a été réalisée à différentes échelles (depuis le millimètre jusqu'au niveau atomique). Un modèle mésoscopique, s'appuyant sur des bases de données thermodynamiques et cinétiques, a été développé pour coupler la diffusion à longue distance dans un milieu multi-constitué à la germination et croissance des précipités (approche de type Kampmann-Wagner). Il a permis de prévoir la teneur en carbone ainsi que la fraction volumique et la distribution de taille des précipités en fonction de la distance à l'interface. Les conséquences de la forte variabilité de microstructure sur le comportement mécanique local ont été analysées dans la dernière partie de ce travail, en particulier les aspects de déformation localisée et de rupture ductile. Des lois de comportement élasto-plastique ont été déterminées pour chacune des régions de l'assemblage à l'état détensionné. L'étude des mécanismes de rupture ductile dans les zones les plus faibles de la soudure, c'est-à-dire le métal de base décarburé et les couches de revêtement austénitique a donné lieu à des observations in-situ et une modélisation de l'endommagement.

Abstract:
Dissimilar welds between low-alloy steel and stainless steel are numerous within the French nuclear power plants where they enable connecting the main components to the primary circuit pipes. The internal cladding (in stainless steel) of the pressure vessel (in bainitic steel) made by submerged arc welding is another case of dissimilar weld whose goal is the protection against corrosion. This PhD work aims at understanding the complex microstructures which form at the interface between both steels during welding together with their evolution during the post-weld heat-treatment at 610°C and their consequences on the mechanical behavior of the welded assembly. Starting from the base metal, one meets successively a thin layer of martensite, a fully austenitic zone and the two-phase δ/γ microstructure of the stainless steel. Microscopy techniques (SEM, EDS, EBSD) combined with thermo-kinetics calculations (Scheil-Gulliver model, dendrite tip undercooling) have allowed explaining the graded microstructure and the reasons for the observed phase transitions. During the post-weld heat-treatment, the large gradient of carbon chemical potential across the fusion line leads to cementite dissolution and grain growth on the low-alloyed side. Carbon diffusion through the interface and Cr-rich carbides precipitation in both the martensitic layer and the austenitic weld have also been observed. An in-depth characterization has been performed at different scales (from the millimeter to the atomic level) to quantify the extent of carbon diffusion and carbides precipitation during the phase transformations. A mesoscopic thermodynamic and kinetic model based on Calphad databases has been developed to fully couple long-range diffusion in a multi-component system with precipitates nucleation and growth (Numerical Kampmann-Wagner approach). It allowed a prediction of the carbon content, volume fraction and size distribution of the precipitates at any distance from the fusion line. The consequences of the high variability of microstructures on the local mechanical behavior have been examined in the last part of this work, in particular the localization of deformation and the ductile failure. Elasto-plastic constitutive laws were determined for each region of the dissimilar weld in the heat-treated state. Ductile failure mechanisms in the weak zones of the weld, namely the decarburized base metal and the stainless steel cladding layers, were investigated through in-situ observations and damage modeling.